

**Spin Noise Correlations in  
Multispecies Hot Atomic Vapors**

PhD Thesis, University of Crete

*Konstantinos Mouloudakis*

*Heraklion, 2020*

**Advisor : *Prof. Dr. Iannis Kominis***

UNIVERSITY OF CRETE

PHD THESIS

---

# Spin Noise Correlations in Multispecies Hot Atomic Vapors

---

*Author:*

Konstantinos Mouloudakis

*Advisor:*

Prof. Dr. Iannis Kominis



A DISSERTATION  
PRESENTED TO THE FACULTY  
OF UNIVERSITY OF CRETE  
IN CANDIDACY FOR THE DEGREE  
OF DOCTOR OF PHILOSOPHY

Department of Physics

January 13, 2021



This research is co-financed by Greece and the European Union (European Social Fund- ESF) through the Operational Programme « Human Resources Development, Education and Lifelong Learning » in the context of the project “ Strengthening Human Resources Research Potential via Doctorate Research ” (MIS-5000432), implemented by the State Scholarships Foundation (IKY).



# Abstract

---

UNIVERSITY OF CRETE

## Spin Noise Correlations in Multispecies Hot Atomic Vapors

Department of Physics

Spin-exchange collisions in alkali-metal vapors underlie several fundamental and applied investigations such as nuclear structure studies and tests of fundamental symmetries, ultrasensitive atomic magnetometers, magnetic resonance, and biomagnetic imaging. The effect of spin-exchange collisions on the atomic system is very rich and it can vary depending on the conditions: it can cause decoherence and produce spin noise, or it can transfer spin-polarization and coherences without contributing to spin relaxation. Recently, with the development of quantum measurements and quantum technology in general, spin-exchange collisions have attracted a lot of interest as a resource for quantum metrology and as a potential source of quantum noise.

We have performed a precision experiment regarding spin-noise correlations in multispecies hot alkali vapors. In particular, we observe non-zero spin-noise correlations and coherence transfer effects in equilibrium between overlapping  $^{133}\text{Cs}$  and  $^{87}\text{Rb}$  spin ensembles, having different gyromagnetic ratios. Both observations stem from the spontaneous and incessant spin-exchange collisions that tend to couple the two atomic species through the coherent exchange of spin-polarization.

We investigate the behaviour of the spontaneous spin-noise correlations both in a strong coupling regime at low magnetic fields where the spin-exchange rate is larger than the difference of the Larmor frequencies and in a weak coupling regime, at higher fields, where the fast Larmor precession tends to rapidly contract the formatted correlations.

On theoretical grounds, we develop a quantum-trajectory picture of spin-exchange collisions, consistent with their long-standing ensemble description using density matrices. We then use quantum trajectories to reveal the nature of spin-noise correlations that spontaneously build up in multispecies atomic vapors, frequently utilized in the most sensitive spin measurements.

Finally, we show that spin-exchange collisions in hot alkali vapors naturally produce strong bipartite entanglement, which we explicitly quantify using the tools of quantum information science. This entanglement is shown to have a lifetime at least as long as the spin-exchange relaxation time, and to directly affect measurable spin noise observables. We present a formal theoretical demonstration that a hot and dense atomic vapor can support longlived bipartite and possibly higher-order entanglement.

Deeper understanding of spin-noise exchange in dual-species hot alkali vapors may advance the operation of atomic devices like for example atomic magnetometers and atomic gradiometers and it may also contribute to the development of new quantum protocols and devices.



# Acknowledgements

---

I would first like to thank my supervisor prof. Iannis Kominis. I am sincerely grateful that I was given the opportunity to work next to Iannis for almost a decade, since my undergraduate studies. He is a really enterprising person and I feel that his influence on me is definitely multidimensional and indelible. First of all, as a supervisor, he was always there, constantly available for any kind of discussion and he was always the one who would certainly come up with ingenious solutions to the toughest problems I have faced in this thesis. His physical intuition and his ability to explain the physics in the most elegant and simple way, in combination with his constant and tireless passion for studying science in general, constitute the characteristics that were mostly stimulating and encouraging me to develop as a physicist, but also the ones that provided me a concrete training through these years. I want to deeply express my gratitude for teaching me the importance of a precision measurement and for his insistence to a better measurement.

Aside from a good supervisor, he is also a good friend and a good mentor. We've spent together a lot of constructive time inside and outside the lab and I appreciate his efforts to encourage me in many difficult situations. Additionally, I would like to thank him for being the first to bring the amazing physics of alkali spin measurements in Greece and providing lavishly students the opportunity to be part of this world, but also for his invaluable efforts to initiate the modern world of quantum technologies. On the whole, I would like to thank Iannis for his support, his enthusiasm and his counseling throughout these years.

I would also like to give great thanks to Georgios Vasilakis for being in the right place at the right time and deliver priceless guidance and assistance. I would like to express my gratitude for being next to me in the last year of my PhD studies and for being always willingful to explain in detail any aspect of our work. I thank him for making me appreciate the value of the details of an experimental setup and last but not least, I would like to thank him for all the delightful discussions we've exchanged on the topics of quantum noise that have been always sparking my interest.

I would like also to sincerely thank David Petrosyan who read the final form of the thesis in great detail and contributed with his comments and his corrections to the advancement of the quality of the thesis.

The environment in the lab could not have been more friendly and more warm thanks to my very good friends and colleagues with whom we've spent endless hours

accompanied with moments of intense emotions. First of all, I would like to thank G.Anyfantaki and A.Margaritakis for spending most of our time together, working as a team, sharing everything and being always there for one-another. I appreciate their work in optics and fibers and in computer engineering, respectively, and I am very glad that I've worked next to such talented young scientists. Additionally, I would like to acknowledge A.Margaritakis for his 3D printing skills that made my life easier.

We have also shared a lot of beautiful moments with D.Dolapsakis, D. Pantazopoulou, D.Giarikanis and G.Garidis who have been the silent power from the back and always provide a helping hand when needed. Of course, I would like to thank K. Vitalis for assisting me in my first steps on numerical simulations and for the endless discussions we've found ourselves into. S.Travlos and E.Kardamaki were delivering great assistance in our first attempts to build homemade diode lasers and K.Saliaris was always watchful, controlling the appropriate lab operation. Moreover, I deeply thank A.Margaritakis, E.Chrysafi and K.Archaki for the funny moments during the endless coil-wrapping! Sorry for that!

I won't miss to mention G.Vlachakis, N.Tsatrafyllis, K.Tsampourakis, K.Kessing, T.Ilias, K.Gratsea, G.Magkos, M.Kritsotakis and M.Petrakakis for exchanging thoughts and ideas during our overlap in the lab and for being great colleagues. Special thanks to E.Köse for being in Crete as a visiting student in our group and we've spent the summer of 2019 having fun with some optical pumping experiments. Finally, I would like to express sincere thanks to the members of my examining committee P. Rakitzis and D. Charalambidis for the comprehensive discussions we have exchanged during these years.

Apart from the colleagues, I would like to thank G.Komis and A.Pavlis for the endless discussions about the PhD journey and for being the friends that understand better than anyone the peculiarities of it. I also thank them for the beautiful moments we have shared throughout the years in the physics department and for the funny moments we have been into. I cannot miss to mention Agathi, Marina, Mike and Stefanos (aka "Urban Vibes"), our beautiful band, being a relaxing break and a happy tune during weekends. Furthermore, I would like to thank D.Domalakis and M.Gemistos for being true friends that I can rely on, and for being always a source of joy and reassurance.

Finally, I would like to express my love to my family, Louisa, George and Bill for their support and their unlimited love which follows me in life. For the above reasons, I dedicate this thesis to them.



# Contents

|   |             |
|---|-------------|
| <b>Abstract</b>   | <b>i</b>    |
| <b>Acknowledgements</b>   | <b>iii</b>  |
| <b>Contents</b>   | <b>viii</b> |
| <b>List of Figures</b>  | <b>xi</b>   |
| <b>List of Tables</b>   | <b>xii</b>  |
| <b>1 Introduction</b>   | <b>1</b>    |
| 1.1 Noise in Quantum Systems . . . . .                              | 1           |
| 1.2 Spin noise and atomic magnetometry . . . . .                    | 2           |
| 1.3 Thesis contents . . . . .                                       | 7           |
| <b>2 Atoms and Light</b>  | <b>10</b>   |
| 2.1 The Atomic Hilbert Space . . . . .                              | 10          |
| 2.2 The Density Matrix . . . . .                                    | 11          |
| 2.3 Irreducible Components of the Density Matrix . . . . .          | 13          |
| 2.3.1 Spin Operators . . . . .                                      | 15          |
| 2.4 Alkali Atoms in Magnetic Field . . . . .                        | 16          |
| 2.4.1 Time Evolution in the Magnetic Field . . . . .                | 20          |
| 2.5 Atom-Light Interaction . . . . .                                | 22          |
| 2.5.1 Light Propagation I . . . . .                                 | 24          |
| 2.5.2 The Dipole Interaction . . . . .                              | 26          |
| 2.5.3 Ground State Hamiltonian and Polarizability . . . . .         | 27          |
| 2.5.4 Velocity Average . . . . .                                    | 28          |
| 2.5.5 Irreducible Components of the Polarizability Tensor . . . . . | 31          |
| 2.5.6 Scalar Polarizability . . . . .                               | 32          |
| 2.5.7 Vector Polarizability . . . . .                               | 35          |
| 2.5.8 Vector Interaction Hamiltonian . . . . .                      | 36          |
| 2.5.9 Light Propagation II . . . . .                                | 38          |
| 2.6 Stokes Parameters and Polarimetry . . . . .                     | 40          |

|          |  |           |
|----------|--|-----------|
| 2.7      | Spin-Projection Noise . . . . .                            | 42        |
| 2.8      | Bloch Equations . . . . .                                  | 44        |
| 2.8.1    | Dual Species Spin-Exchange . . . . .                       | 51        |
| 2.8.2    | Uncorrelated Noise Terms . . . . .                         | 53        |
| 2.8.3    | Anti-correlated Noise Terms . . . . .                      | 54        |
| 2.9      | Quantum Back-action Noise - Light Shift Noise . . . . .    | 55        |
| <b>3</b> | <b>Spin-Exchange and Spin Relaxation Processes</b>         | <b>58</b> |
| 3.1      | Spin-Exchange Collisions . . . . .                         | 58        |
| 3.1.1    | Spin-1/2 Particles Without Nuclear Spin . . . . .          | 61        |
| 3.1.2    | Spin-Exchange Properties . . . . .                         | 66        |
| 3.1.3    | Spin-Exchange in Alkali Atoms . . . . .                    | 67        |
| 3.1.4    | Spin-Exchange Master Equation . . . . .                    | 69        |
| 3.1.5    | Spin-Temperature Distribution . . . . .                    | 71        |
| 3.2      | Transit-Time Broadening . . . . .                          | 71        |
| 3.3      | Relaxation due to Wall Collisions . . . . .                | 72        |
| 3.4      | Relaxation due to Magnetic Field Inhomogeneities . . . . . | 73        |
| 3.5      | Radiation Trapping and Quenching . . . . .                 | 75        |
| 3.6      | Complete Density Matrix Evolution . . . . .                | 76        |
| <b>4</b> | <b>Spin-Noise Cross-Correlations Experiment</b>            | <b>77</b> |
| 4.1      | Introduction . . . . .                                     | 77        |
| 4.2      | Photodetectors . . . . .                                   | 79        |
| 4.3      | Balanced Polarimeter . . . . .                             | 81        |
| 4.3.1    | Standard Quantum Limit . . . . .                           | 83        |
| 4.3.2    | Schottky's formula for Shot Noise . . . . .                | 84        |
| 4.3.3    | Balanced Polarimeter-Stokes Representation . . . . .       | 86        |
| 4.3.4    | Quantum Description: Homodyne Detection . . . . .          | 88        |
| 4.4      | Stationary Stochastic Processes . . . . .                  | 91        |
| 4.4.1    | Sampling . . . . .   | 93        |
| 4.5      | Vapor Cells and Oven . . . . .                             | 95        |
| 4.5.1    | Vapor Cells . . . . .                                      | 95        |
| 4.5.2    | Oven . . . . .   | 96        |
| 4.5.3    | Faraday Rotation from Oven Optical Elements . . . . .      | 99        |
| 4.6      | Lasers and Optical Fibers . . . . .                        | 100       |
| 4.7      | Absorption Measurements . . . . .                          | 104       |



|          |  |            |
|----------|--|------------|
| 4.8      | Magnetic Shield . . . . .  | 111        |
| 4.8.1    | Degaussing . . . . .   | 114        |
| 4.8.2    | Fluxgate Magnetometer . . . . .  | 115        |
| 4.9      | Data Acquisition . . . . .   | 116        |
| 4.9.1    | Cross-Talk . . . . .   | 118        |
| 4.10     | Spin-noise Spectrum and Spin-noise Broadening . . . . .                                  | 120        |
| 4.11     | Spin-noise Correlations . . . . .  | 127        |
| 4.12     | Dual Balanced Polarimeter Scheme . . . . .   | 136        |
| 4.13     | Diamagnetic Faraday Rotation . . . . .   | 140        |
| 4.14     | Wavelength Measurement . . . . .   | 149        |
| <b>5</b> | <b>Quantum Trajectory Theory in Spin-Exchange Collisions</b>                             | <b>153</b> |
| 5.1      | Phase-Jump Toy Model . . . . .   | 156        |
| 5.2      | Overview of Quantum Trajectory Theory . . . . .  | 159        |
| 5.3      | Quantum Trajectories and Spin-Exchange Dynamics . . . . .                                | 164        |
| 5.4      | Lindblad dynamics for Alkali Spin-Exchange Interaction . . . . .                         | 176        |
| <b>6</b> | <b>Entanglement in Spin-Exchange Collisions</b>  | <b>181</b> |
| <b>7</b> | <b>Conclusions</b>   | <b>190</b> |
| <b>A</b> | <b>Spin Operators and Density Matrix</b>   | <b>192</b> |
| A.1      | Spin Operators . . . . .   | 192        |
| A.1.1    | Relations Between Spin Operators and Irreducible Spherical<br>Tensor Operators . . . . . | 194        |
| A.2      | Density Matrix Decomposition . . . . .   | 196        |
| <b>B</b> | <b>Gaussian Beams and Fresnel Equations</b>  | <b>199</b> |
| B.1      | Gaussian beams . . . . .   | 199        |
| B.2      | Fresnel Equations . . . . .  | 200        |
| <b>C</b> | <b>Atom-Light General Derivations</b>  | <b>201</b> |
| C.1      | The Wigner-Eckart Theorem . . . . .  | 201        |
| C.1.1    | Wigner-Eckart Expansion . . . . .  | 201        |
| C.2      | Interaction Picture . . . . .  | 202        |
| C.2.1    | Small Mathematical Trick . . . . .   | 203        |



---

|   |            |
|---|------------|
| <b>D Atomic Polarizability</b>  | <b>204</b> |
| D.1 Adiabatic Elimination and Derivation of the Polarizability Tensor . . . . | 204        |
| D.2 Irreducible Components of the Polarizability Tensor . . . . .             | 206        |
| <b>Bibliography</b>   | <b>223</b> |



# List of Figures

---

|      |  |     |
|------|--|-----|
| 1.1  | Schematic of an Atomic Magnetometer . . . . .            | 4   |
| 1.2  | Spin Signal . . . . .                                    | 6   |
| 2.1  | Atomic Energy Levels . . . . .                           | 11  |
| 2.2  | Breit-Rabi Energy Levels . . . . .                       | 19  |
| 2.3  | Quantum Revival Beats . . . . .                          | 21  |
| 2.4  | Lorentz Model . . . . .                                  | 33  |
| 2.5  | Poincaré Sphere . . . . .                                | 40  |
| 2.6  | Coherent and Squeezed Spin States . . . . .              | 43  |
| 3.1  | Singlet-Triplet Energy Curves . . . . .                  | 60  |
| 4.1  | Experimental Setup . . . . .                             | 78  |
| 4.2  | Balanced Polarimeter . . . . .                           | 81  |
| 4.3  | Shot Noise . . . . .                                     | 86  |
| 4.4  | Quantum Polarimeter . . . . .                            | 89  |
| 4.5  | Vapor Cell . . . . .                                     | 96  |
| 4.6  | Vapor Cells . . . . .                                    | 97  |
| 4.7  | Oven . . . . .   | 98  |
| 4.8  | Oven Temperatures . . . . .                              | 99  |
| 4.9  | Lasers . . . . .   | 100 |
| 4.10 | Beam Diameter Measurement . . . . .                      | 102 |
| 4.11 | Absorption Spectrum Scheme . . . . .                     | 105 |
| 4.12 | Absorption Spectrum . . . . .                            | 108 |
| 4.13 | Magnetic Shield . . . . .                                | 112 |
| 4.14 | Shield Coil Calibration . . . . .                        | 113 |
| 4.15 | Magnetic Field vs Position . . . . .                     | 113 |
| 4.16 | Magnetic Field Noise . . . . .                           | 114 |
| 4.17 | Analog Low-Pass Filters . . . . .                        | 117 |
| 4.18 | Electronic Noise . . . . .                               | 119 |
| 4.19 | Cross-Talk . . . . .                                     | 120 |
| 4.20 | Spin-Noise Spectrum at $T = 100^\circ\text{C}$ . . . . . | 121 |

|  |     |
|--|-----|
| 4.21 Spin-Noise Spectrum at $T = 140^\circ\text{C}$ .                | 122 |
| 4.22 Spin-Noise Broadenings  | 123 |
| 4.23 Power Broadening  | 124 |
| 4.24 Scaling of Spin-Noise Power with Atomic Number Density          | 125 |
| 4.25 Cross-Correlation in Time-domain                                | 128 |
| 4.26 Cross-Correlation in Frequency-domain                           | 129 |
| 4.27 Effects of the Low Frequency Noise on the Cross-Correlation PSD | 130 |
| 4.28 Dependence of the Cross-Correlation on the Detuning             | 132 |
| 4.29 Cross-Correlation vs Magnetic Field                             | 133 |
| 4.30 Histograms of Cross-Correlation ( $\tau = 0$ ) vs Laser Power   | 135 |
| 4.31 Cross-Correlation vs Laser Power                                | 135 |
| 4.32 Experimental Setup of Dual Polarimeter Scheme                   | 136 |
| 4.33 Dual Polarimeter Spin-Noise                                     | 137 |
| 4.34 Dual Polarimeter Spin-Noise Log-Plot                            | 138 |
| 4.35 Experimental Setup for Density Measurement                      | 141 |
| 4.36 Solenoid Coil   | 142 |
| 4.37 Field-Current   | 143 |
| 4.38 RLC Circuit   | 144 |
| 4.39 First Harmonic  | 147 |
| 4.40 Faraday Rotation  | 148 |
| 4.41 Number Density vs Temperature                                   | 149 |
| 4.42 Wavelength Meter  | 150 |
| 4.43 Wavemeter Experimental Setup                                    | 151 |
| 4.44 Laser Frequency Stability                                       | 152 |
| 5.1 Simulation of SE Master Equation I                               | 154 |
| 5.2 Simulation of SE Master Equation II                              | 155 |
| 5.3 Spin-Exchange Phase-Jumps  | 157 |
| 5.4 Spin-Exchange Final FM-States                                    | 166 |
| 5.5 Schematic of the Atomic Collision                                | 169 |
| 5.6 Quantum Trajectories and the Master Equation                     | 172 |
| 5.7 Spin Noise Generation  | 173 |
| 5.8 Dual-Species Quantum Trajectories                                | 174 |
| 5.9 Noise Correlations   | 174 |
| 5.10 Noise Terms   | 176 |
| 6.1 Negativity   | 188 |



---

|     |                                     |     |
|-----|-------------------------------------|-----|
| 6.2 | Negativity vs Correlation . . . . . | 189 |
|-----|-------------------------------------|-----|



# List of Tables



|     |   |     |
|-----|---|-----|
| 4.1 | Laser Beam Waist Measurements. . . . .              | 102 |
| 4.2 | Number Densities Based on Absorption. . . . .       | 109 |
| 4.3 | Experimental Parameters. . . . .                    | 127 |
| 4.4 | Single and Dual Polarimeters: A Comparison. . . . . | 139 |
| 4.5 | Faraday Rotation Measurements. . . . .              | 147 |
| 4.6 | Number Densities Based on Faraday Rotation. . . . . | 148 |

# List of Publications



- K. Mouloudakis and I. K. Kominis, *arXiv:2004.11790* (2020)
- K. Mouloudakis, et.al., *Physical Review Research* **1**, 033017 (2019)

## Side Projects and Previous Papers:

- A. Margaritakis, et.al., *Applied Physics B* **126**, 99 (2020)
- K. Mouloudakis and I. K. Kominis, *Physical Review E* **95**, 022413 (2017)
- K. Mouloudakis and I. K. Kominis, *Biosystems* **147**, 35 (2016)

*Dedicated to Louisa, George, and Bill*

# Chapter 1 Introduction

---

## 1.1 Noise in Quantum Systems

**T**he discovery and the development of the field of quantum noise and the distinction between purely quantum and purely statistical aspects of it that arise in any experimental realization of quantum mechanics [1], gave rise to the expansion of the intriguing field of quantum metrology [2]. During the past decades, high precision measurements accompanied by the growth of laser physics and quantum control have led to a radical evolution of quantum technologies, such as primordial quantum computers, with unprecedented precision [3, 4].

In the field of modern atomic physics and especially at the interface between light and atoms [5, 6], quantum noise sets fundamental limits to the attainable precision of measurements in most of the existing technologies like for example, in atomic magnetometers, atomic clocks, quantum memories or in gravitational wave detectors. Therefore, the study and the deeper understanding of noise appears essential for the further progress and improvement of the aforementioned devices [7] but also for the invention of new.

Moreover, the emerging fields of many-body and open quantum systems seem to play dominant role in the further progress of the field of atomic devices. On the one hand, many-body collective effects are able to enhance the precision and the sensitivities of the quantum measurements, while on the other hand, aside from quantum noises, relaxation processes are always present to set strict limits to the coherence lifetimes of the quantum systems under consideration [8, 9]. The accurate characterization of the interplay between coherence and relaxation in atomic systems are of central interest in the community of atomic devices [10–12].

Since the early days of radio communication the term noise was introduced to describe any unwanted fluctuation disturbing the signal being communicated. These fluctuations are represented more or less as random mixtures of electromagnetic waves with a wide range of frequencies having no essential relation with one another and amplitudes that vary randomly in time. Soon thereafter, the term noise have been applied in many different contexts and its definition varies slightly from context to context.

In physical systems, any quantity to be measured is always accompanied by random and unintentional fluctuations which usually limit the precision of the measurement and as a consequence, the quality of the experimental data is frequently determined by the signal to noise ratio (SNR) [13]. Improving the SNR relies more on using techniques to reduce and control the noise rather than amplifying the signal.

Traditionally, the most common examples of physical systems that exhibit random fluctuations and have been studied in detail are i) voltage fluctuations across the arms of a resistor in electronic circuits, known as Johnson noise [14, 15], ii) current and photon fluctuations due to the discrete character of the energy carriers, known as shot noise or Schottky noise [16, 17] and iii) the Brownian diffusive motion of large particles from the incessant and random bombardment by the surrounding molecules which later led to the derivation of the fluctuation-dissipation theorem and the growth of statistical mechanics [18, 19].

One of the most significant problems that constitute a milestone in the development of the theory of quantum noise and shed light on the advance of the modern aspects of quantum optics and quantum information was the problem of the atomic decay.

Consecutive progress both from a theoretical and an experimental point of view led to the outcome of advanced tools such as quantum Monte-Carlo simulations, stochastic Schrödinger equations [20] but also advanced optical probing techniques such as quantum non-demolition measurements (QND) [21–25], single photon or squeezed light detection [26, 27] that have enabled the study of quantum noise beyond the standard quantum limits [28].

## 1.2 Spin noise and atomic magnetometry

In this thesis we are essentially interested in a particular manifestation of quantum noise, the so called spin noise [29–31]. Spin noise is usually encountered in systems consisting of a large ensemble of mostly uncorrelated and individual spins and is a fundamental noise in the measurement of the spin state of the ensemble. The equilibrium state of a collective system is usually called thermal spin state. Such systems could be for example, a hot or a cold atomic vapor [32–37], electrons in a semiconductor [38–41] or a large ensemble of nuclear spins which is usually encountered in NMR [42–44]. Felix Bloch, in his seminal paper on nuclear induction [45] predicted that in a nuclear spin ensemble consisting of  $N$  independent and undriven nuclear spins, there must be spin fluctuations of the order of  $\sqrt{N}$ , due to insufficient statistical cancellation. Such fluctuations have been observed in [46].



In hot atomic vapors, spin noise has been studied extensively due to its immediate relation to fundamental physics but also because it is directly related to quantum sensing and quantum metrology with the prominent application of atomic magnetometry [47, 48].

The field of atomic magnetometry can be traced back following two separate paths. The first lies on the attempts of Faraday to understand the nature of light which subsequently led to unique discoveries, like for example the rotation of the polarization plane of a linearly polarized light as it transverses a medium placed in a constant magnetic field [49], which nowadays serves as the most sensitive way to probe spin dynamics in an atomic vapor. The second lies on the attempts to understand and measure magnetic fields, with Carl Friedrich Gauss being one of the first representatives of this path, as it is beautifully mentioned in [50].

Modern atomic magnetometers stand on the studies of Dehmelt and Bell and Bloom in 1957 [51, 52] who first demonstrated the design and operation of a magnetometer using alkali atomic vapors and later on, with the subsequent advance of technology and with attention to the detail, Dmitry Budker and Michael Romalis have demonstrated the so far most sensitive optical magnetometers, reaching sub-femtotesla sensitivities [53–55].

There are various types of atomic magnetometers like scalar magnetometers that measure the magnitude of the magnetic field, vector magnetometers that apart from the magnitude provide also information about the direction of the field, radio-frequency (rf) magnetometers where the spin precession is induced by AC radio-frequency magnetic fields and co-magnetometers incorporating more than one atomic species which can also work as very sensitive gradiometers and have been utilized in modern table-top searches of physics beyond the standard model [56–59].

Atomic magnetometry covers a broad range of applications ranging from biomagnetic imaging [60] to geomagnetism [61] and to space applications [62]. Advances have been done in the field of magnetoencephalography (MEG)[63–66] and magnetocardiography (MCG) [67] representing ground-breaking applications of atomic magnetometers in medicine and provide non-invasive ways to measure the magnetic brain and heart activities with high spatial and temporal resolution.

The working principle of atomic magnetometer is based on the measurement of the Larmor precession frequency of the atomic spin in a constant magnetic field. Alkali metal atoms are widely used for magnetometry because they have a single valence electron which is coupled to the nuclear spin of the atom to create the total spin, usually denoted by  $F$ . For a comprehensive discussion about the inner structure of alkali atoms see, [68, 69].



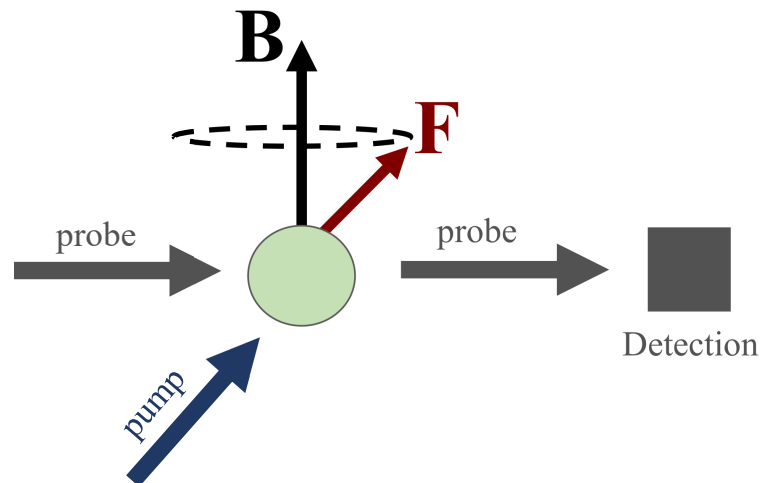


**Figure 1.1:** Adapted from [72]. Working principle of atomic magnetometers. A pump beam polarizes the spins of the vapor, the spins precess in the magnetic field, a weak linearly polarized probe undergoes paramagnetic Faraday rotation and finally the probe beam is detected. The information about the magnetic field is encoded in the properties of the probe field and is captured by the probe measurement.

A strong pump laser, circularly polarized and on resonance with an atomic optical transition is used to polarize the atomic vapor and to generate a collective macroscopic magnetization by transferring angular momentum from the photons to the atoms. This magnetization is then precesses in the magnetic field with frequency  $\omega = \gamma|\mathbf{B}|$  called the Larmor frequency. The constant of proportionality is the gyromagnetic ratio of the atom which expresses the ratio of its magnetic moment to its angular momentum. In many situations the properties of the pump beam are modulated, taking advantage of resonance phenomena to increase the efficiency of optical pumping [70, 71].

As we will discuss later in detail, the spin precession causes modulation of both the dispersive and the absorptive characteristics of the atom, enabling various mechanisms for measuring the spin precession. The most usual is the paramagnetic Faraday effect. A weak off-resonant and linearly polarized probe beam propagates through the atomic vapor and exhibits a rotation of the plane of polarization by an angle proportional to the mean value of the spin along the direction of light propagation. The angle can be measured using a balanced polarimeter. The working principle of atomic magnetometers is schematically described in Fig.1.1.

A typical signal of a spin precession measurement is represented in Fig.1.2. The spin of the initially polarized vapor is precessing in the magnetic field at the Larmor frequency and eventually decays to zero due to various spin relaxation processes that we are going to discuss in detail in the subsequent chapters. In equilibrium, stochastic spin fluctuations directly related to the relaxation processes are omnipresent and they account

for the statistical aspects of the quantum noise. In the case of a polarized vapor, the signal that scales with the number of atoms  $N$ , is much larger than the spin fluctuations, scaling as  $\sqrt{N}$ . In the unpolarized case, all spins of the individual atoms point in random directions in space therefore the mean collective spin signal drops to zero, resulting in uncorrelated fluctuations of the order of  $\sqrt{N}$ .

Additionally, relaxation processes usually drive an initially spin polarized pure state to a mixed equilibrium state revealing statistical uncertainty, while certain spin relaxation processes, like spin exchange collisions, are non-linear and their effect becomes dominant closer to the unpolarized region. In any case, such spin signals are always limited by the fundamental quantum noise which originates from Heisenberg's uncertainty principle and is represented in Fig.1.2 as the variance of the amplitude of the spin evolution of the total collective spin of the atoms.

The variance of the total spin depends on the particular state of the atoms and is different for a polarized vapor (Coherent Spin State) and an unpolarized one (Thermal Spin State). We are mostly interested in probing the transverse spin components with respect to the magnetic field which provide information about the Zeeman and hyperfine resonances. In that case, the lifetime of the spin precession signal is usually called  $T_2$ . That is, roughly the time it takes to a polarized state to become unpolarized. The presence of the magnetic field defines a quantization axis and subsequently a basis relative to which we can distinguish populations from coherences. Absence of the magnetic field, restores the spherical symmetry and populations in one basis are coherences in another and vice versa.

The coherence lifetime of the spin precessing signal is a very important parameter for the sensitivity of the magnetometer and is usually revealed as the broadening of the magnetic resonance when looking at the signal of Fig.1.2 in the frequency domain. Aside from the lifetime, what is also important is the amplitude of the signal which can be increased either by increasing the vapor density or by increasing the length of the glass cell. The fundamental, shot-noise limited error in estimating the magnetic field is [55]:

$$\delta B = \frac{1}{\gamma \sqrt{T_2 N t}} \quad (1.1)$$

Eq.(1.1) can be understood by noting that the error in estimating the center of the Larmor peak in frequency domain is given by  $\delta\omega = \gamma\delta B = \frac{1}{SNR} \frac{1}{T_2}$ . As discussed previously, the SNR in a spin coherent state is proportional to  $\sqrt{N}$  and if we repeat the measurement for time  $t$ , we optimally acquire a statistical gain in precision of the order of  $\sqrt{\frac{t}{T_2}}$ . To give an example, for a  $100 \text{ cm}^3$  Cs vapor cell where  $\gamma = 0.350 \frac{\text{kHz}}{\text{mG}}$  and a coherence



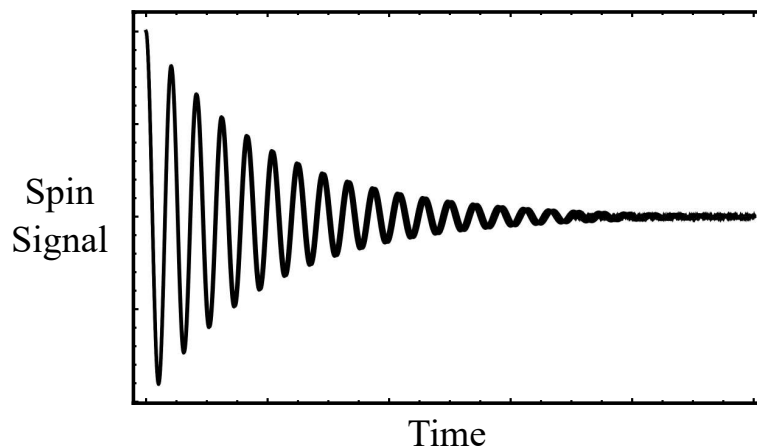


**Figure 1.2:** Typical signal from a spin precession measurement. An initially polarized spin decays to zero due to spin relaxation processes. The relaxation process is accompanied by quantum noise imprinted in the variance of the signal. The variance of the signal is related to the fundamental quantum noise or spin projection noise in the different spin states of the vapor.

lifetime of 10 milliseconds, with a measurement bandwidth of  $1\text{ Hz}$  and a vapor number density of  $n = 10^{12}\text{ cm}^{-3}$ , the sensitivity is approximately  $\delta B = 0.3\text{ fT}/\sqrt{\text{Hz}}$ . For more numerical examples see, [73]. The sensitivity limits of most type of magnetometers and their energy resolution limits have been studied recently in [74–76].

Nowadays, quantum enhanced sensing have become an integral part of spin measurements and constitutes a complete toolbox for sensitivity improvement. It is well-known that using quantum correlated states either for the atoms or the light can enhance the sensitivity of spin measurements and in many situations approach the Heisenberg limit. Moreover, it has been shown that QND measurements can produce spin correlated states like spin squeezed states (SSS) or macroscopic singlet states [77] that are promising candidates for record sensitivities. Quantum resources like entanglement [78–80] and spin squeezing [12, 81, 82] have been applied in magnetometry as well as in spin noise spectroscopy [83, 84] of hot alkali vapors.

Deeper understanding of spin noise and its relation to the collisional relaxation processes [85–87] paves the way towards improving quantum enhanced metrology in hot vapor systems [88–91]. Some of the modern applications of spin noise spectroscopy in hot vapors are: measurement of zero-field spin noise using magnetic pulses [92], measurement of higher order spin noise like alignment noise [93, 94], spin noise measurements with time-dependent magnetic fields [95, 96], demonstration of quantum random number generator using spin noise [97], effects of atomic diffusion on the spin noise spectrum [98, 99] and dual-species spin noise measurements [100–104]. Of particular interest in this thesis is the study of the noise properties in multispecies atomic systems. Similarly, hybrid atomic systems have been traditionally used in spin-exchange

optical pumping of noble gas nuclei [105–109] and subsequently find applications in comagnetometry [110–112] and/or in quantum memories [113–115].

## 1.3 Thesis contents

**Chapter 2** sets the theoretical foundations needed for studying spin physics related to the hot alkali vapors and their interaction with external electromagnetic fields. The chapter begins with a description of the atomic Hilbert space and the density matrix which both constitute the essential tools to describe any atomic effect at the microscopic level.

Afterwards, a complete review of the dynamics of alkali atoms in a magnetic field is given and a complete description of the interaction of the laser light with the alkali atoms is presented, merging the seminal paper of W.Happer and B.S.Mathur [116] with a modern approach [117] presented by P.S.Jessen and I.H.Deutsch. The coupling of light with the atom at the fundamental level leads to the Faraday effect allowing for precise measurements of the spin state of the atom. Finally, the atomic spin evolution is described using semi-classical Bloch equations that have been traditionally used in experiments dominated by spin-exchange and spin-relaxation processes in general.

In **Chapter 3** we describe the spin relaxation processes that affect the spin state of a hot alkali vapor when it is placed in an external and constant magnetic field. Some of the common relaxation processes are: spin-exchange and spin-destructive collisions, diffusion of the atoms in the laser beam, power broadening, relaxation due to wall collisions and relaxation due to magnetic field gradients. The chapter begins with a complete description of spin-exchange collisions and concludes on the relaxation due to magnetic field gradients and diffusion.

**Chapter 4** is devoted to the experimental measurement of spin-noise correlations in dual species alkali vapors of  $^{87}\text{Rb}$  and  $^{133}\text{Cs}$ . At the beginning of the chapter we introduce the balanced polarimeter scheme and we explore the practical limitations set to it, for example by photon shot noise. Subsequently, we analyse the precision at which we can measure a tiny polarization rotation angle and we present different ways that the polarimetric signal can be represented. Afterwards, we describe the experimental setup for measuring spin-noise correlations and a whole range of technical details surrounding it. Absorption and dispersion measurements providing information about the alkali number density are also presented.

We analyse in detail spin-noise correlations between the two species and we find that even in equilibrium the two atomic systems share and exchange spin-noise correlations



that build-up as a result of the spin-exchange interaction. We observe a coherence transfer between the two vapors that is more evident in small magnetic fields and we find that a positive spin-noise correlation at  $\tau = 0$  in agreement with the predictions of [89, 100, 118].

In **Chapter 5** we develop a quantum trajectory picture of the spin-exchange relaxation process in a small dc magnetic field. The motivation is to describe spin-noise generated by the random spin-exchange collisions taking place constantly in the vapor cell. Spin-exchange relaxation is intimately related to spin-noise as a consequence of the fluctuation-dissipation theorem.

The model of quantum trajectories assigns a pure state to each individual atom in the vapor cell which evolves deterministically under the effect of the Hamiltonian and stochastically under the effect of spin-exchange collisions. Averaging over the whole ensemble of atoms we produce a density matrix that evolves in the same way as the master equation of spin-exchange collisions predicts.

The trajectory model allows for an initial assignment of completely random pure states to all of the atoms representing an equilibrium thermal density matrix. Allowing the stochastic evolution of each atom in equilibrium we show how spin-noise is generated out of the collisions and we compare the predictions of the theory with the known characteristics of spin noise measured in the experiment. This is a first-principle demonstration of spin-noise generation due to SE collision.

Finally, we extend the model in dual species vapors where we produce random trajectories in equilibrium between the two vapors and we show that spin-exchange interaction is capable of producing spontaneous correlations between the two species. This is a theoretical demonstration that SE collisions couple the two spin species and produce positive spin-spin correlations.

In **Chapter 6** we study whether spin-correlations that build-up due to spin-exchange collisions could be quantum in nature. We extend the main master equation of spin-exchange collisions to account for binary spin correlations by extending the trace-out process that leads to instant decorrelation of the two colliding partners.

We quantify the amount of entanglement produced by binary spin-exchange collisions using the negativity measure of entanglement and we calculate an analytical upper bound of it independent of the initial colliding states, which applies to any alkali vapor. Moreover, we show that this entanglement is sustained for time at least equal to the spin-exchange time, therefore to the best of our knowledge this is the first theoretical indication that spin-exchange collisions create and sustain bipartite entanglement in hot vapor atomic systems.

**Chapter 7** concludes with a summary of the main results of the thesis and presents possible future perspectives of the current work.



# Chapter 2 Atoms and Light

## 2.1 The Atomic Hilbert Space

**A**lkali atoms are frequently utilized in spin-based measurements and applications due to their single valence electron, which allows the atom, under certain conditions, to be considered as a spin-1/2 particle. The electronic spin of the atom ( $S = 1/2$ ) is coupled to the orbital angular momentum via the spin-orbit interaction resulting in a total angular momentum  $\mathbf{J} = \mathbf{L} + \mathbf{S}$  which takes integer values in the interval  $|L - S| \leq J \leq L + S$  and follows the usual angular momentum rules [119]. The ground state of alkali is an "S"-shell with orbital angular momentum  $L = 0$  and  $J = 1/2$ . In the first excited state, the orbital angular momentum is  $L = 1$ , thus  $J$  can be either  $J = 1/2$  or  $J = 3/2$  and the excited state "P"-shell is fine-splitted into two states.

Transitions from the ground state to the excited  $J = 1/2$  are usually called  $D_1$  transitions, while transitions to  $J = 3/2$  are called  $D_2$  transitions. The same angular momentum rules apply also to the coupling of the total spin  $J$  and the nuclear spin  $I$  of the alkali atom. In that case, the total angular momentum of the atom is  $F = I + J$  and can take integer values in the interval  $|I - J| \leq F \leq I + J$ . In the ground state  $J = S = 1/2$ , thus,  $F$  is restricted in the interval  $|I - \frac{1}{2}| \leq F \leq I + \frac{1}{2}$ . For alkali atoms,  $I$  is always greater or equal to  $S = 1/2$  thus,  $I - \frac{1}{2} \leq F \leq I + \frac{1}{2}$ .

Finally, the above relation implies that  $F$  can take only two possible values, the so called  $a \equiv I + \frac{1}{2}$  and the so called  $b \equiv I - \frac{1}{2}$ . Therefore we find that the ground state of alkali atoms with  $L = 0$  and  $S = 1/2$  splits into two levels (known as hyperfine splitting) where the  $a$  is called upper hyperfine manifold and the  $b$  lower hyperfine manifold. The addition of angular momentum is a consequence of the hyperfine interaction that couples the nuclear spin  $I$  to the total angular momentum  $J$ .

The projections of the total atomic angular momentum on the quantization axis are different for the two hyperfine manifolds. In the upper manifold there are  $2a + 1$  projections taking integer values in the interval  $-a \leq m_F \leq a$  while in the lower there are  $2b + 1$  projections taking integer values in the interval  $-b \leq m_F \leq b$ .

The most common basis of an atom of nuclear spin  $I$  and electron spin  $J = 1/2$  are the  $|F, m_F\rangle$  and the  $|m_I, m_S\rangle$ , defining the so called coupled/uncoupled basis of the atom. Since the angular momentum is  $J = 1/2$ , there are only two projections along

the quantization axis, i.e.  $m_S = \pm \frac{1}{2}$ , while in the most general case, the nuclear spin can be left undefined, hence there are  $[I] = 2I + 1$  projections along the quantization axis. With that said, the ground state Hilbert space where all the atomic spin dynamics take place, can be defined either in the coupled basis or in the uncoupled basis. The dimension of Hilbert space is:  $\dim\{\mathcal{H}\} = \dim\{\mathcal{H}_s \otimes \mathcal{H}_I\} = \dim\{\mathcal{H}_a \oplus \mathcal{H}_b\} = [S][I] = (2S + 1) \times (2I + 1) = 2(2I + 1) = (2a + 1) + (2b + 1)$ . In Fig.2.1 we represent schematically an overview of the previous discussion.

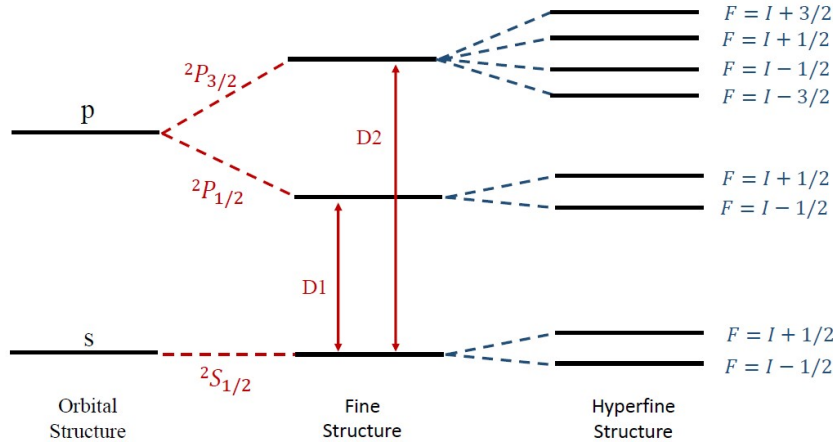


**Figure 2.1:** Adapted from [50, 72]. Atomic energy levels of an alkali atom with nuclear spin  $I$ . The ground "s" and excited "p" orbitals are splitted due to the fine and further due to hyperfine interactions. The energy level spacings are not drawn to scale.

## 2.2 The Density Matrix

An atomic vapor consists of a large amount of spins, each described by a pure wavefunction  $|\psi_j\rangle$  which obeys the Schrödinger equation and evolves under the dynamics of a particular Hamiltonian. The Hamiltonian evolution is interrupted by the random collisions between the atoms that tend to alter the angular momentum of the system.

From an experimental point of view, keeping track of the wavefunction of each atom individually in such a large ensemble, seems to be impossible with the current technology and additionally, the correlations that develop between the atoms through their interactions, their distribution in the cell and their decay times, constitute a tough and ongoing research problem which can be fully resolved only when the complete information of the whole set of such states is available.

From a theoretical point of view, it is always possible to write down a many-body spin wavefunction that in principle contains the aforementioned information, however due to interactions, soon one finds that an exponentially large Hilbert space is needed which saturates the current computational power.

Recent development of advanced techniques in many-body physics, like for example matrix-product-states [120], take advantage of symmetries in order to reduce the dimensions of the problem. Hopefully, the development of quantum computing and quantum simulations might possibly revolutionize the understanding of the correlated spin dynamics in the near future. Such a many-body spin wavefunction is of the form

$$|\Psi\rangle = \prod_{j=1}^N |\psi_j\rangle \quad (2.1)$$

In general, the quantum mechanical state of the  $j_{th}$  particle can be written as a superposition of the available atomic states [121],

$$|\psi_j(t)\rangle = \sum c_n^{(j)}(t)|n\rangle \quad (2.2)$$

where the states  $|n\rangle$  constitute an orthonormal basis for the system. For the alkali metal atoms the most commonly used basis are: (i) the uncoupled basis  $|m_s\rangle|m_l\rangle$  and (ii) the coupled basis  $|F, m_F\rangle$ . As we are going to discuss, in the presence of a small magnetic field, where  $F$  constitutes a "good quantum number", the coupled basis  $|F, m_F\rangle$  is more convenient in the sense that the Hamiltonian is more easily diagonalized in that basis but also in the sense of a better physical perspective where the electronic and nuclear spins are strongly coupled, generating a total angular momentum  $F$  based on the rules of the vector-operator sum.

In the case of uncorrelated, individual atoms, instead of using many-body wavefunctions there is a more convenient way to describe the averaged state of the whole ensemble using the formalism of the density matrix [122, 123]. The expectation value of an observable  $A$  averaged over all of the atomic states in the ensemble can be written as:

$$\begin{aligned} \overline{\langle A \rangle} &= \frac{1}{N} \sum_{j=1}^N \langle \psi_j | A | \psi_j \rangle \\ &= \sum_n \frac{1}{N} \sum_{j=1}^N \langle \psi_j | A | n \rangle \langle n | \psi_j \rangle \\ &= \sum_n \frac{1}{N} \sum_{j=1}^N \langle n | \psi_j \rangle \langle \psi_j | A | n \rangle \\ &= Tr \left( \frac{1}{N} \sum_{j=1}^N |\psi_j\rangle \langle \psi_j | A \right) \\ &= Tr(\rho A) \end{aligned} \quad (2.3)$$

where we have inserted the identity operator  $\mathbb{1} = \sum_n |n\rangle \langle n|$  and defined the density

operator

$$\rho = \frac{1}{N} \sum_{j=1}^N |\psi_j\rangle\langle\psi_j| \quad (2.4)$$

The density operator contains all of the information about the average state of the ensemble and given a particular basis, it can be written in matrix form with matrix elements

$$\rho_{mn} = \langle m|\rho|n\rangle = \frac{1}{N} \sum_{j=1}^N \langle m|\psi_j\rangle\langle\psi_j|n\rangle = \frac{1}{N} \sum_{j=1}^N c_n^{(j)*} c_m^{(j)} \quad (2.5)$$

The density matrix is usually normalized such that  $Tr(\rho) = 1$  and in the case where the whole ensemble can be described by a single wavefunction, the system is said to be in a pure state. For a pure state,  $Tr(\rho^2) = 1$  while for  $Tr(\rho^2) < 1$  the ensemble is said to be in a mixed state. The diagonal matrix elements of the density matrix are called populations and the off-diagonal elements are coherences and furthermore, the density matrix has always positive eigenvalues since they describe populations in the basis in which coherences have been eliminated.

The closed-system time evolution of the density operator is given by the so called von Neumann equation

$$\frac{d\rho}{dt} = -\frac{i}{\hbar}[H, \rho] \quad (2.6)$$

where  $[A, B] = AB - BA$  is the commutator. The von Neumann equation can be derived either by assuming an infinitesimal unitary evolution of the density matrix using the unitary time evolution operator  $U(dt) = \text{Exp}(-iHdt/\hbar)$  and keeping orders up to  $dt$ ,  $U(dt) = \mathbb{1} - \frac{i}{\hbar}Hdt + \mathcal{O}(dt^2)$  thus,  $\rho(t + dt) = U(dt)\rho(t)U^\dagger(dt) = \rho(t) - \frac{i}{\hbar}[H, \rho(t)]dt + \mathcal{O}(dt^2)$  or by directly differentiating Eq.(2.4) and plugging the time dependent Shrödinger equation, as it is usually presented in most of the textbooks.

## 2.3 Irreducible Components of the Density Matrix

It is often useful to expand the density matrix  $\rho$  in terms of a conveniently chosen set of operators which satisfy certain algebraic properties and in many cases can greatly simplify the calculations. For example, when the angular symmetries of the system are important, it is convenient to expand  $\rho$  in terms of a set of irreducible spherical tensor operators. In this way, the consequences of the angular momentum conservation can be used to separate geometrical factors from dynamical ones and moreover, a clear relation between the matrix elements of  $\rho$  and the physical experimental observables can be revealed [122].

Additionally, the transformation properties of irreducible spherical tensor operators under rotations constitute a tool to distinguish the effects of different types of multipole distributions and to characterize its dynamical evolution. The systematic use of tensor operators was first suggested by Fano [124] and since then it has been extensively used in atomic physics [70].

In this section we briefly review spherical tensor operators which are encountered in subsequent chapters, for example when we deconstruct the atom-light interaction into spherical irreducible components. As we are going to discover, light couples to the atomic ensemble only through a second rank spherical tensor allowing only dipole and quadrupole polarizations to sufficiently characterize the interaction.

Consider two atomic multiplets which can be described by the angular momentum basis states  $|Fm\rangle$  and  $|F'm'\rangle$ . Here  $F$  and  $m$  label, respectively, the total and the axial angular momentum of the state. Spherical basis operators for the atom are then defined as

$$T_{LM}(FF') = \sum_m (-1)^{m-M-F'} C(FF'L; m, M-m) |Fm\rangle \langle F'm-M| \quad (2.7)$$

with the inverse relation

$$|Fm\rangle \langle F'm'| = \sum_L (-1)^{m'-F'} C(FF'L; m, -m') T_{L,m-m'}(FF') \quad (2.8)$$

where  $C(FF'L; m, M-m) = \langle LM|Fm; F'M-m\rangle$  is the Clebsch-Gordan (CG) coefficient that vanishes unless the usual angular momentum coupling rules are satisfied  $|F-F'| \leq L \leq F+F'$  and  $-L \leq M \leq L$  and is related to the 3J-Symbols via [119]

$$\langle LM|Fm; F'M-m\rangle = (-1)^{F-F'+M} \sqrt{2L+1} \begin{pmatrix} F & F' & L \\ m & M-m & -M \end{pmatrix} \quad (2.9)$$

The spherical tensor operators form an orthonormal basis, thus one can expand the atomic density matrix in terms of the basis operators

$$\rho = \sum_{L,M,F,F'} (-1)^{F-F'+M} \rho_{LM}(FF') T_{L-M}(F'F) \quad (2.10)$$

The Hermitian conjugate of a basis operator is

$$T_{LM}^\dagger(FF') = (-1)^{F-F'+M} T_{L-M}(F'F) \quad (2.11)$$

For an atomic system of total electronic angular momentum  $J$  and nuclear spin  $I$ , it is often convenient to express the density matrix in terms of the basis operators  $T_{KM}(II)$  and  $T_{LN}(JJ)$ . Therefore, we can write

$$\rho = \sum_{K,L,M,N} (-1)^{M+N} \rho(KM; LN) T_{K-M}(II) T_{L-N}(JJ) \quad (2.12)$$

Relations between the coupled and the uncoupled spherical tensor basis are addressed in



[70].

As a consequence of the spherical tensor expansion, the ground state density matrix of an alkali atom can be written as

$$\rho = \phi + \Theta \cdot \mathbf{S} \quad (2.13)$$

where  $\mathbf{S}$  is the electron spin operator and  $\phi$ ,  $\Theta_x$ ,  $\Theta_y$ ,  $\Theta_z$  are purely nuclear operators. For a spin-1/2 atom we also obtain

$$\phi = \frac{\rho}{4} + \mathbf{S} \cdot \rho \mathbf{S} \quad (2.14)$$

$$\Theta \cdot \mathbf{S} = \frac{3\rho}{4} - \mathbf{S} \cdot \rho \mathbf{S} \quad (2.15)$$

These formulas have been proven useful in studying the relaxation dynamics of the density matrix due to binary collisions since it turns out that each irreducible component relaxes with a different relaxation rate. The above formulas are derived in Appendix A. Higher order multipoles of the atomic density matrix have been studied and experimentally observed in [125].

### 2.3.1 Spin Operators

In many situations it is convenient to express atomic operators, like spin operators, projector operators or higher order quadrupole operators, in the spherical tensor basis. For an alkali atom in the ground state we obtain

$$\mathbf{F} = \sum_{F,M} (-1)^M \hat{\mathbf{e}}_M T_{1,-M}(FF) \sqrt{\frac{F(F+1)(2F+1)}{3}} \quad (2.16)$$

$$\mathbf{S} = \sum_{F,F',M} (-1)^{M-1-1/2-F'-I} \hat{\mathbf{e}}_M T_{1,-M}(FF') \begin{Bmatrix} 1 & \frac{1}{2} & \frac{1}{2} \\ I & F & F' \end{Bmatrix} \sqrt{\frac{(2F+1)(2F'+1)}{2}} \quad (2.17)$$

The projector operator on the upper hyperfine manifold  $a = I + 1/2$  is

$$p(a) = \sqrt{2a+1} T_{00}(aa) = \frac{I+1+2\mathbf{I} \cdot \mathbf{S}}{2I+1} \quad (2.18)$$

and the corresponding projector operator on the lower manifold  $b = I - 1/2$  reads

$$p(b) = \sqrt{2b+1} T_{00}(bb) = \frac{I-2\mathbf{I} \cdot \mathbf{S}}{2I+1} \quad (2.19)$$

Combination of these relations results in a formula for the scalar operator  $\mathbf{I} \cdot \mathbf{S}$  representing the hyperfine interaction

$$\mathbf{I} \cdot \mathbf{S} = \frac{I}{2} p(a) - \frac{I+1}{2} p(b) = \frac{I}{2} \sqrt{2a+1} T_{00}(aa) - \frac{I+1}{2} \sqrt{2b+1} T_{00}(bb) \quad (2.20)$$

Note that  $p(a) + p(b) = \mathbb{1}$ .

The above relations are derived in Appendix A, in combination with a supplementary



and completely equivalent derivation following [50, 126]. Given the spin operators in the spherical basis, one can generate spin operators in Cartesian basis using the basis relations

$$\begin{aligned}\hat{e}_{\pm} &= \mp \frac{1}{\sqrt{2}}(\hat{e}_x \pm i\hat{e}_y) \\ \hat{e}_0 &= \hat{e}_z\end{aligned}\tag{2.21}$$

Instead of Cartesian and spherical basis, an equally useful basis is the angular momentum ladder basis. The ladder basis operators are related to the Cartesian via

$$F_{\pm} = F_x \pm iF_y\tag{2.22}$$

which are often used to describe the creation or the annihilation of an angular momentum excitation

$$F_{\pm}|F, m_F\rangle = \sqrt{F(F+1) - m_F(m_F \pm 1)}|F, m_F \pm 1\rangle\tag{2.23}$$

## 2.4 Alkali Atoms in Magnetic Field

The dynamics in the ground state of an alkali atom placed in an external constant magnetic field  $B$  along the  $\hat{z}$ -direction are governed by the Breit-Rabi Hamiltonian [127]. In general, the Breit-Rabi Hamiltonian describes the coupling of the total angular momentum  $J$  of the atom with the nuclear spin  $I$  and with the external magnetic field  $B$ . In the ground state the orbital angular momentum is zero, therefore the atomic angular momentum is equal to the spin ( $J = S$ ) and the Breit-Rabi Hamiltonian reads

$$\mathcal{H}_0 = \mathcal{H}_{hf} + \mathcal{H}_B = A\mathbf{I} \cdot \mathbf{S} + g_s\mu_B BS_z + g_I\mu_N BI_z\tag{2.24}$$

The first term is the hyperfine interaction resulting from the coupling of the nuclear spin with the electronic spin of the atom. This coupling is a consequence of the electrostatics taking place at the interface between the nucleus and the electron and its derivation takes into account all the effects beyond the point particle electrostatics.

The dominant interactions that mostly contribute to the hyperfine term are in principle nuclear magnetic dipole interactions and Fermi contact interactions [121] accompanied with higher order terms like electric quadrupole interactions which are significantly smaller and can be ignored [128]. The hyperfine constant  $A$ , in terms of frequency, is of the order of hundreds of MHz up to several GHz for all alkali atoms and is related to the hyperfine splitting via  $\hbar\omega_{hf} = 2\pi\frac{A}{2}[I]$ .

The remaining terms, are the Zeeman terms which describe the interaction of the electronic and nuclear spin with the external magnetic field, respectively.  $\mu_B = 9.27 \times 10^{-21}$  erg/G is the Bohr's magneton and  $\mu_N = \frac{m_e}{m_p}\mu_B = 5.05 \times 10^{-24}$  erg/G is the



nuclear magneton, smaller from Bohr's magneton by a factor equal to the electron-proton mass ratio.  $g_s = 2.0023$  is the electron g-factor and  $g_I$  is the nuclear g-factor which will be left unspecified because i) it accounts for the entire complex structure of the nucleus [128] and ii) the upcoming discussion can be applied to any alkali atom. Note that the signs in the Hamiltonian are such that  $g_I$  should have opposite sign than  $g_s$ .

In this thesis, we are mostly interested in small magnetic fields, therefore the hyperfine term is many orders of magnitude larger than the Zeeman terms, thus the later can be assumed as a small perturbation to the hyperfine interaction and perturbation theory can be safely applied [129, 130]. The eigenstates of the total atomic angular momentum  $\mathbf{F}$  are also eigenstates of the hyperfine interaction with eigenvalues given by ( $\hbar = 1$ )

$$\mathbf{A}\mathbf{I} \cdot \mathbf{S}|Fm_F\rangle = \frac{A}{2}(F(F+1) - I(I+1) - S(S+1))|Fm_F\rangle \quad (2.25)$$

resulting in an energy splitting between the two hyperfine manifolds  $\Delta E_{hf} = E_a - E_b = \frac{A}{2}[I]$ . Here  $a = I + 1/2$  is the upper and  $b = I - 1/2$  the lower hyperfine multiplet.  $[I] = 2I + 1$  is the nuclear spin multiplicity.

The Breit-Rabi Hamiltonian can be easily diagonalized either using the coupled angular momentum basis  $|Fm_F\rangle$  or the uncoupled  $|m_I, m_S\rangle$  (always in the case of  $S = 1/2$  atoms). In the following we present the diagonalization process in the coupled basis. For a complete derivation in the uncoupled basis, see [50]. To briefly review the uncoupled basis process, the main idea is to express the Hamiltonian in terms of the ladder operators

$$S_{\pm} = S_x \pm iS_y \quad (2.26)$$

$$S_{\pm}|S, m_S\rangle = \sqrt{S(S+1) - m_S(m_S \pm 1)}|S, m_S \pm 1\rangle \quad (2.27)$$

Therefore the Hamiltonian is written as

$$\mathcal{H}_0 = A \left[ I_z S_z + \frac{1}{2}(I_- S_+ + I_+ S_-) \right] + g_s \mu_B B S_z + g_I \mu_N B I_z \quad (2.28)$$

then, it is easy to calculate the matrix elements  $\langle m_I, m_S | \mathcal{H}_0 | m'_I, m'_S \rangle$  and finally diagonalize a Block Hamiltonian since the ladder operators change the  $m_I$  and  $m_S$  values only by  $\pm 1$ .

In the coupled basis, the goal is to calculate the Hamiltonian matrix elements

$$\langle Fm_F | \mathcal{H}_0 | F'm'_F \rangle = \langle Fm_F | \mathcal{H}_{hf} | F'm'_F \rangle + \langle Fm_F | \mathcal{H}_B | F'm'_F \rangle \quad (2.29)$$

Firstly, the matrix elements of the hyperfine term are easily obtained since  $[\mathbf{I} \cdot \mathbf{S}, \mathbf{F}^2] = 0$ , hence the coupled basis constitutes a common set of eigenstates for both operators

$$\langle Fm_F | \mathcal{H}_{hf} | F'm'_F \rangle = \frac{A}{2}(F(F+1) - I(I+1) - S(S+1))\delta_{F,F'}\delta_{m_F,m'_F} \quad (2.30)$$



Second, regarding the Zeeman matrix elements, it is easy to calculate those for which  $F = F'$  using the Landè projection theorem. The theorem states that the matrix elements of any irreducible spherical tensor operator in a specific angular momentum manifold, are always proportional to the matrix elements of the angular momentum operator, or to put it differently, any irreducible spherical tensor operator in a space spanned by an angular momentum manifold, is always proportional to the angular momentum vector [131]. This theorem is a consequence of the Wigner-Eckart theorem (WET) and in the case of a vector operator like a spin operator, it yields

$$\langle Fm_F | V_q | Fm'_F \rangle = \frac{\langle Fm_F | \mathbf{F} \cdot \mathbf{V} | Fm'_F \rangle}{F(F+1)} \langle Fm_F | F_q | Fm'_F \rangle \quad (2.31)$$

Applying the Landè projection theorem to the electron and nuclear spin operators we obtain

$$\begin{aligned} \langle Fm_F | S_z | Fm'_F \rangle &= \frac{\langle Fm_F | \mathbf{F} \cdot \mathbf{S} | Fm'_F \rangle}{F(F+1)} \langle Fm_F | F_z | Fm'_F \rangle \\ &= \frac{F(F+1) - I(I+1) + S(S+1)}{2F(F+1)} m_F \end{aligned} \quad (2.32)$$

and

$$\begin{aligned} \langle Fm_F | I_z | Fm'_F \rangle &= \frac{\langle Fm_F | \mathbf{F} \cdot \mathbf{I} | Fm'_F \rangle}{F(F+1)} \langle Fm_F | F_z | Fm'_F \rangle \\ &= \frac{F(F+1) + I(I+1) - S(S+1)}{2F(F+1)} m_F \end{aligned} \quad (2.33)$$

Then the diagonal Zeeman matrix elements are

$$\begin{aligned} \langle Fm_F | \mathcal{H}_B | Fm'_F \rangle &= g_s \mu_B B m_F \frac{F(F+1) - I(I+1) + S(S+1)}{2F(F+1)} \\ &+ g_I \mu_N B m_F \frac{F(F+1) + I(I+1) - S(S+1)}{2F(F+1)} \end{aligned} \quad (2.34)$$

One can simplify the notation by defining the Landè g-factor of the total spin

$$g_F = g_s \frac{F(F+1) - I(I+1) + S(S+1)}{2F(F+1)} + g_I \frac{F(F+1) + I(I+1) - S(S+1)}{2F(F+1)} \quad (2.35)$$

obtaining for the two different hyperfine manifolds

$$g_a = \frac{1}{[I]} (g_s + 2I g_I) \quad (2.36)$$

$$g_b = \frac{1}{[I]} (-g_s + (2I + 2)g_I) \quad (2.37)$$

Since  $g_I \ll g_s$  we find that  $g_a \approx -g_b$  which is true in most of the practical situations where the  $g_I$ -terms are usually ignored. By rescaling  $g_I \rightarrow \frac{m_e}{m_p} g_I$ , the diagonal Zeeman matrix elements can be compactly written as

$$\langle am_F | \mathcal{H}_B | am'_F \rangle = g_a \mu_B B m_F \quad (2.38)$$

$$\langle bm_F | \mathcal{H}_B | bm'_F \rangle = g_b \mu_B B m_F \quad (2.39)$$



The off-diagonal matrix elements are calculated using Appendix A and yield

$$\begin{aligned} \langle am_F | \mathcal{H}_B | bm'_F \rangle &= \langle bm_F | \mathcal{H}_B | am'_F \rangle \\ &= \frac{\sqrt{(I+1/2)^2 - m_F^2}}{[I]} (g_s \mu_B B - g_I \mu_N B) \end{aligned} \quad (2.40)$$

Then, for a given value of  $m_F$  the Hamiltonian is block diagonal and can be written in the  $|F, m_F\rangle$  basis as a  $2 \times 2$  matrix that can be easily diagonalized

$$\begin{bmatrix} E_a + g_a \mu_B B m_F & \frac{\sqrt{(I+1/2)^2 - m_F^2}}{[I]} (g_s \mu_B B - g_I \mu_N B) \\ \frac{\sqrt{(I+1/2)^2 - m_F^2}}{[I]} (g_s \mu_B B - g_I \mu_N B) & E_b + g_b \mu_B B m_F \end{bmatrix} \quad (2.41)$$

If we define  $\Delta E_{hf} = E_a - E_b = [I] \frac{A}{2}$  and

$$x = \frac{(g_s \mu_B B - g_I \mu_N B)}{\Delta E_{hf}} \quad (2.42)$$

we arrive at the known Breit-Rabi formula for the eigenvalues of the Hamiltonian (2.24)

$$E(F \pm 1/2, m_F) = -\frac{\Delta E_{hf}}{2[I]} + g_I \mu_N B m_F \pm \frac{\Delta E_{hf}}{2} \sqrt{1 + \frac{4x m_F}{[I]} + x^2} \quad (2.43)$$

In Fig.2.2 we use equation Eq.(2.43) to plot the energy levels of a  $^{87}\text{Rb}$  atom as a function of the magnetic field.

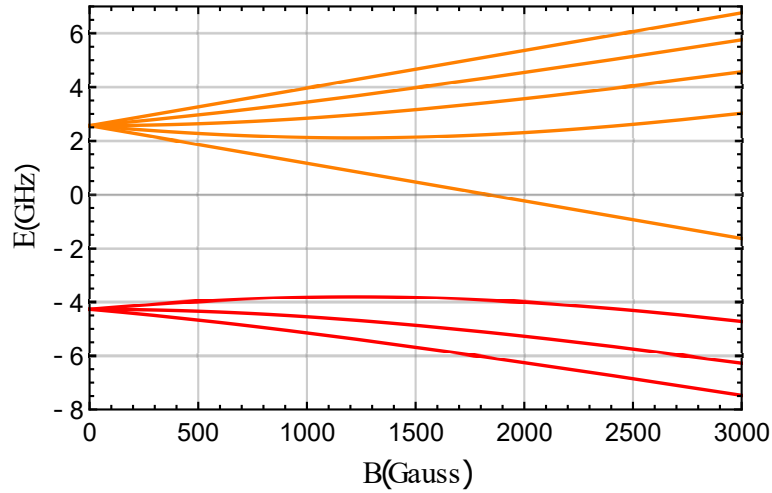


**Figure 2.2:** Energy spectrum of  $^{87}\text{Rb}$  as a function of the magnetic field. For magnetic fields of the order of 50 mG used in this thesis, we are completely in the linear regime. Non-linear Zeeman splittings start to become evident above 500 mG.

For magnetic fields of the order of  $B=50$  mG and smaller, the hyperfine frequency is much larger than the Larmor frequency ( $x \ll 1$ ) therefore we can expand the Breit-Rabi formula around  $x = 0$  ( $\sqrt{1+x} \approx 1 + \frac{1}{2}x - \frac{1}{8}x^2$ )

$$\begin{aligned}
E(F \pm 1/2, m_F) \approx & -\Delta E_{hf} \left( \frac{1}{2[I]} \pm \frac{1}{2} \right) + g_I \mu_N B m_F \pm \frac{(g_s \mu_B - g_I \mu_N) B m_F}{[I]} \\
& \pm \frac{(g_s \mu_B - g_I \mu_N)^2 B^2}{\Delta E_{hf}} \pm \frac{8(g_s \mu_B - g_I \mu_N)^2 B^2 m_F^2}{[I] \Delta E_{hf}} \pm \mathcal{O}\left(\frac{B^3}{\Delta E_{hf}^2}\right)
\end{aligned} \tag{2.44}$$

The Larmor frequency is given by the term proportional to the magnetic field

$$\omega_L = \frac{1}{\hbar} (g_I \mu_N \pm \frac{(g_s \mu_B - g_I \mu_N)}{[I]}) B = g_{F_{\pm}} \mu_B B \tag{2.45}$$

where  $g_{F_{\pm}}$  is the Landè g-factor for the upper and lower manifolds as defined in Eq.(2.35). The expansion above reveals also long term frequencies known as revival and super-revival frequencies being proportional to  $B^2/\Delta E_{hf}$  and  $B^3/\Delta E_{hf}^2$ , respectively. The combination of these frequencies result in the so called quantum beatings. Quantum beatings have been studied extensively in [50, 132, 133] and here are reproduced for reasons of completeness.

### 2.4.1 Time Evolution in the Magnetic Field

The time evolution of the atomic spin due to Breit-Rabi Hamiltonian is governed by the time dependent Schrödinger equation

$$i\hbar \frac{d|\psi(t)\rangle}{dt} = \mathcal{H}_0 |\psi(t)\rangle \tag{2.46}$$

We can calculate the expectation value of any observable, like the transverse spin component  $\langle \psi(t) | F_x | \psi(t) \rangle$  by solving analytically the Schrödinger equation for the state  $\psi(t)$ . As an example, we calculate the time evolution of the transverse spin of a Cesium atom in the upper hyperfine manifold, starting from the maximally polarized, stretched state where  $\langle F_x \rangle = F$ . The state can be found either by calculating the eigenstates of the  $F_x$  operator or by rotating the state  $|F, F\rangle$  by an angle  $\frac{\pi}{2}$  along the y-axis using Wigner's d matrix

$$|\psi\rangle = \sum_{m_F} d_{m_F, F}^F \left( \frac{\pi}{2} \right) |F, F\rangle = \sum_{m_F} \frac{(-1)^{F-m_F}}{2^F} \sqrt{\frac{(2F)!}{(F+m_F)!(F-m_F)!}} |F, m_F\rangle \tag{2.47}$$



The analytical calculation for the  $^{133}\text{Cs}$  atom in a magnetic field of  $B = 0.5$  G yields

$$\begin{aligned} \langle F_x(t) \rangle = & 0.03125 \times [\cos(2\pi \times 175.147 \times 10^3 t) + \cos(2\pi \times 175.081 \times 10^3 t)] \\ & + 0.21875 \times [\cos(2\pi \times 175.041 \times 10^3 t) + \cos(2\pi \times 175.075 \times 10^3 t)] \\ & + 0.65625 \times [\cos(2\pi \times 175.048 \times 10^3 t) + \cos(2\pi \times 175.068 \times 10^3 t)] \\ & + 1.09375 \times [\cos(2\pi \times 175.056 \times 10^3 t) + \cos(2\pi \times 175.062 \times 10^3 t)] \end{aligned} \quad (2.48)$$

The different frequencies correspond to the different transitions between subsequent Breit-Rabi energy levels where the  $m_F$  value changes by  $\pm 1$  in the upper manifold, also known as Zeeman transitions.

As a second example, we plot the analytical value of the transverse spin component along the  $\hat{x}$ -direction, for a  $^{87}\text{Rb}$  atom in a magnetic field of  $B = 0.5$  G,

$$\begin{aligned} \langle F_x(t) \rangle = & 0.25 \times [\cos(2\pi \times 349.851 \times 10^3 t) + \cos(2\pi \times 349.959 \times 10^3 t)] \\ & + 0.75 \times [\cos(2\pi \times 349.888 \times 10^3 t) + \cos(2\pi \times 349.923 \times 10^3 t)] \end{aligned} \quad (2.49)$$

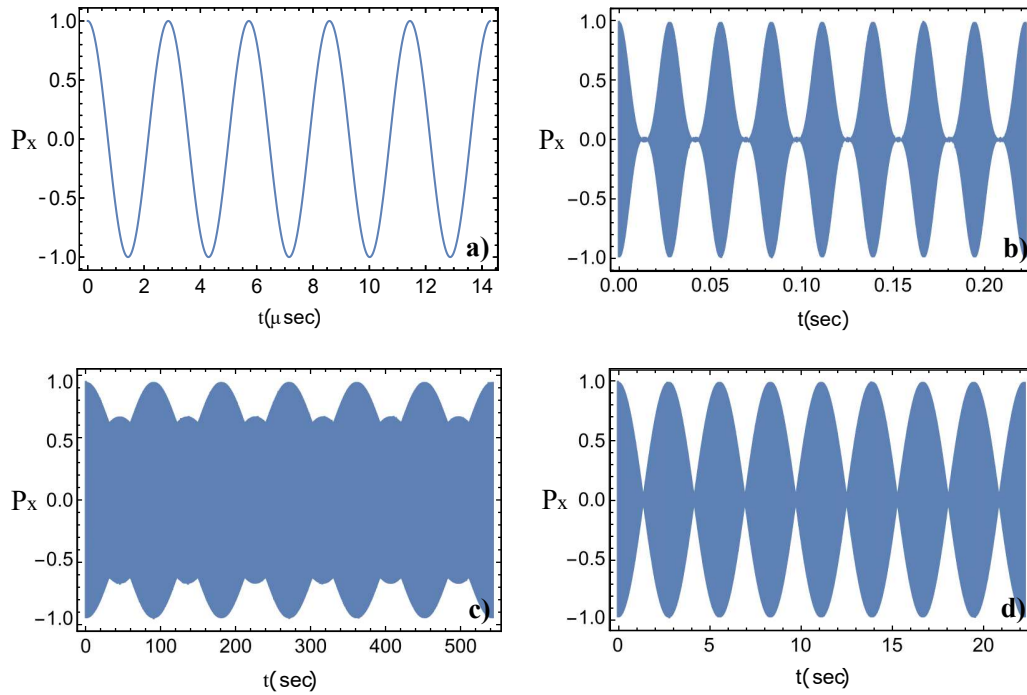


**Figure 2.3:** Plot of the normalized transverse spin polarization along the  $\hat{x}$ - direction in a magnetic field of  $B = 0.5$  G for a  $^{87}\text{Rb}$  atom. **a)** Larmor precession up to time of five Larmor periods. **b)** Quantum revival beats lasting for four revival periods. In each revival period there are two collapses and revivals of the transverse polarization. **c)** Super-revival quantum beats plotted for time up to one super-revival period and **d)** Quantum revival beats starting from the initial state  $|1, 1\rangle_x$  of the lower hyperfine manifold, along the  $\hat{x}$ -direction.

In Fig.2.3 we plot the time evolution of the normalized transverse spin component of a  $^{87}\text{Rb}$  atom in a magnetic field of  $B = 0.5$  G. The mixing of the various frequencies, as indicated above, result in the quantum revival and quantum super-revival beatings.

## 2.5 Atom-Light Interaction

So far we have described the interaction of alkali atoms with a constant external magnetic field generated by the Hamiltonian  $\mathcal{H}_0 = \mathcal{H}_{hf} + \mathcal{H}_B$ . In this section we touch upon a complete and detailed review of the coupling between the atoms and the coherent laser light and we demonstrate how the propagation of the light beam is strongly affected by the atoms in the vapor, and how the atoms of the vapor are strongly affected by the light beam.

A plethora of phenomena associated with light propagation, like linear/circular dichroism or birefringence, are inevitably related to various types of evolution of the atom in the laser beam. For instance, a completely polarized atomic vapor exhibits circular dichroism when a resonant linearly polarized beam is applied to the vapor cell. This dichroic effect is omnipresent because a large amount of atoms is pumped to a particular energy level of the ground state, and could be destroyed for example by an applied resonant rf field that redistributes the populations to the various sublevels, such that right and left circularly polarized components are equally absorbed. It is convenient to think of the vapor as a medium whose optical properties are characterized by a dynamical susceptibility, whose dynamics depend on the atomic dynamics taking place in the ground state of the atom [134].

In this thesis we are mostly dealing with an ensemble of completely unpolarized atoms, therefore we are going to focus mostly on the weak coupling between the atoms and the probe field, which highlights the dispersive and absorptive features of the atom and renders it a medium of either linear or circular birefringence, depending on the type of interaction. The combined effects of the external magnetic field and the light field generate complex dynamics in the atomic state space which in turn affects the properties of the light to be measured. After the interaction, the light carries information about the internal atomic dynamics and there have been developed numerous experimental techniques for optimal read-out of that information.

An example of the light-atom interaction that has been used extensively in spin measurements is the paramagnetic Faraday effect. The paramagnetic Faraday effect is the effect of the rotation of the polarization plane of a linearly polarized light as it transverses a medium exhibiting circular birefringence. In a circularly birefringent medium, the polarization state of a circularly polarized light is unaffected as the light propagates through the medium, whereas the index of refraction differs for the left and right circular polarizations, resulting in the linear polarization plane to be rotated. The difference in the indices of refraction between the two circular polarizations is a result



of the atomic population distributions in the various energy levels and subsequently of the atom-light coupling.

The measurement of the rotation angle of the plane of polarization is used to extract information about the ground state spin dynamics of the atom. The interaction of atoms with light have been extensively studied and there are many remarkable articles containing comprehensive details on the subject [36, 116, 117, 135–141].

In this section we describe the laser light as a weak monochromatic field propagating in free space along the  $\hat{k}$ -direction. We assume that the magnetic field is along the  $\hat{x}$ -direction. We are going to use mostly plane wave description, but for reasons of completeness, we present also the quantized form of the field and a Gaussian beam description is presented in Appendix B. In plane wave form the electric field of the laser light characterized by a wavevector  $\mathbf{k}$  and frequency  $\omega$  is

$$\begin{aligned} \mathbf{E}(\mathbf{r}, t) &= E_0 \hat{\mathbf{e}} \cos(\mathbf{k} \cdot \mathbf{r} - \omega t) = \Re\{E_0 \hat{\mathbf{e}} e^{i(\mathbf{k} \cdot \mathbf{r} - \omega t)}\} \\ &= \frac{\mathbf{E}_0}{2} e^{i(\mathbf{k} \cdot \mathbf{r} - \omega t)} + \frac{\mathbf{E}_0^*}{2} e^{-i(\mathbf{k} \cdot \mathbf{r} - \omega t)} = \mathbf{E}^{(+)} + \mathbf{E}^{(-)} \end{aligned} \quad (2.50)$$

$E_0$  is the field amplitude,  $\hat{\mathbf{e}}$  is the unit vector of polarization and  $\mathbf{E}^{(+)}$  ( $\mathbf{E}^{(-)}$ ) are the positive (negative) frequency components of the field. In quantized form the single mode electric field can be written as [142, 143]

$$E(\mathbf{r}, t) = i \sum_{\lambda} \hat{\mathbf{e}}_{\lambda} \sqrt{\frac{\hbar \omega_{\mathbf{k}, \lambda}}{2 \epsilon_0 V}} \left[ a_{\lambda} e^{i(\mathbf{k} \cdot \mathbf{r} - \omega t)} + a_{\lambda}^{\dagger} e^{-i(\mathbf{k} \cdot \mathbf{r} - \omega t)} \right] \quad (2.51)$$

where the sum is over the polarization basis vectors,  $V$  is the quantization volume and  $a_{\lambda}^{\dagger}$ ,  $a_{\lambda}$  are the photon creation and annihilation operators for the mode  $\mathbf{k}$ . Another formula for the electric field of the quantized radiation that occurs frequently in quantum optics is

$$E(\mathbf{r}, t) = \sum_{\lambda} \hat{\mathbf{e}}_{\lambda} \sqrt{\frac{\hbar \omega_{\mathbf{k}, \lambda}}{2 \epsilon_0 V}} \left[ \hat{X}_{1, \lambda} \sin(\omega t - \mathbf{k} \cdot \mathbf{r}) - \hat{X}_{2, \lambda} \cos(\omega t - \mathbf{k} \cdot \mathbf{r}) \right] \quad (2.52)$$

where  $\hat{X}_{1, \lambda}$  and  $\hat{X}_{2, \lambda}$  are the so-called field quadratures, related to the annihilation and creation operators via

$$\hat{X}_1 = \hat{a} + \hat{a}^{\dagger} \quad (2.53)$$

$$\hat{X}_2 = i(\hat{a}^{\dagger} - \hat{a}) \quad (2.54)$$

The quadrature operators are Hermitian, and thus correspond to an observable. Quadratures are mostly encountered in interferometric experiments like the Mach-Zehnder, the Hong-Ou-Mandel, the Hanbury-Brown and Twiss or other type of interferometers where the field quadratures can be precisely determined. The quadratures



satisfy the following uncertainty relation  $\delta\hat{X}_1\delta\hat{X}_2 \geq 1$  and the commutation relation

$$[\hat{X}_1, \hat{X}_2] = 2i \quad (2.55)$$

### 2.5.1 Light Propagation I

Suppose that the weak monochromatic laser light propagates in free space along the  $\hat{z}$ -direction. We let the light transverse a dilute gas of atoms enclosed in a vapor cell. In the linear regime, the atomic electric dipole induced by the laser field is linearly related to the electric field

$$\langle \mathbf{d} \rangle = a(\omega)\mathbf{E} \quad (2.56)$$

Here  $a(\omega)$  is the polarizability of the atom where in the most general case it could be a tensor indicating that the electric dipole may oscillate in a different direction than the initial polarization direction of the electric field. The brackets denote the expectation value of the quantum mechanical dipole operator for a single atom. The total macroscopic polarization  $P$  is given by

$$\mathbf{P} = n\langle \mathbf{d} \rangle = na(\omega)\mathbf{E} \quad (2.57)$$

where  $n$  is the number density of the atoms in the vapor. The polarization  $P$  is often expressed in terms of the susceptibility  $\chi(\omega) = na(\omega)$ .

Starting from the Maxwell equations in a non-magnetic and polarized medium, where the free charge density  $\rho$  and the free current density  $\mathbf{j}$  are zero, we arrive at the wave equation [123]

$$\nabla^2\mathbf{E} - \frac{1}{c^2}\frac{\partial^2\mathbf{E}}{\partial t^2} = \frac{4\pi}{c^2}\frac{\partial^2\mathbf{P}}{\partial t^2} \quad (2.58)$$

The right hand side is a source term to the free-space wave-equation stemming from the induced polarization in the medium. Plugging the expression for the electric field

$$\mathbf{E}(\mathbf{r}, t) = \text{Re}[\mathbf{E}_0 e^{i(kz - \omega t + \phi_0)}] \quad (2.59)$$

we arrive at a Helmholtz-type partial differential equation

$$(\nabla^2 + \bar{k}^2)\mathbf{E}(\mathbf{r}) = 0 \quad (2.60)$$

where  $\bar{k}^2 = \frac{\omega^2}{c^2}n^2(\omega)$  is an effective complex wavevector  $\bar{k} = \bar{k}_R + i\bar{k}_I$  and  $n(\omega) = \sqrt{1 + 4\pi na(\omega)}$  is the complex index of refraction of the medium  $n(\omega) = n_R + in_I$ .

For a dilute gas we can expand the index of refraction as  $n(\omega) \approx 1 + 2\pi na(\omega)$ . Solutions to the above differential equation are plane waves of the form

$$\mathbf{E}(\mathbf{r}) = \mathbf{E}_0 e^{i\bar{k}z} = \mathbf{E}_0 e^{-\bar{k}_I z} e^{i\bar{k}_R z} \quad (2.61)$$

The real part of the effective wavevector is responsible for the phase change of the



field as it propagates in the atomic medium, while the imaginary part is responsible for the attenuation of the field (provided  $k_I > 0$ ). Using the relations

$$\text{Re}\{n(\omega)\} = 1 + 2\pi n \text{Re}\{a(\omega)\} \quad (2.62)$$

$$\text{Im}\{n(\omega)\} = 2\pi n \text{Im}\{a(\omega)\} \quad (2.63)$$

we can express the electric field as

$$\mathbf{E} = \mathbf{E}_0 e^{i(1+2\pi n \text{Re}\{a(\omega)\})\frac{\omega}{c}z} e^{-2\pi n \text{Im}\{a(\omega)\}\frac{\omega}{c}z} \quad (2.64)$$

The first term is responsible for the dispersion of light while the second for the attenuation in the medium. Upon passing through a vapor cell of length  $l$ , the intensity is proportional to the square of the amplitude of the electric field i.e.,

$$I(\omega) \sim |\mathbf{E}|^2 = I_0 e^{-n\sigma(\omega)l} \quad (2.65)$$

known as the Beer-Lambert law. The optical density of the vapor is defined as  $OD = n\sigma(\omega)l$  and represents a characteristic of the efficiency of the atom-light coupling. At a specific frequency, when  $OD \leq 1$  the vapor is said to be optically thin and the light is partially transmitted, while for  $OD \gg 1$  the vapor is optically thick and the light is completely absorbed. The absorption cross-section is defined as

$$\sigma(\omega) = 4\pi \frac{\omega}{c} \text{Im}\{a(\omega)\} = 4\pi k \text{Im}\{a(\omega)\} \quad (2.66)$$

The integral of  $\sigma(\omega)$  over all frequencies can be expressed in terms of familiar constants and can be used for measuring the number density of the vapor at low temperatures [144]

$$\int \sigma(\nu) d\nu = \frac{1}{nl} \int \ln\left[\frac{I_0}{I(\nu)}\right] d\nu = \pi r_e c f_{\text{osc}} \quad (2.67)$$

where  $r_e = 2.82 \times 10^{-13}$  cm is the classical electron radius and  $f_{\text{osc}}$  is the oscillator strength of either the  $D_1$  or the  $D_2$  transition.

Assuming linearly polarized light along the  $\hat{x}$ -direction and decomposing it into two opposite circular polarizations we obtain [145]

$$\begin{aligned} \mathbf{E} &= E_0 \hat{x} e^{-i\bar{k}l} = E_0 \hat{x} e^{i\frac{\omega}{c}n(\omega)l} \\ &= \frac{E_0}{2} (\hat{x} + i\hat{y}) e^{-i\frac{\omega}{c}n^{(+)}l} + \frac{E_0}{2} (\hat{x} - i\hat{y}) e^{-i\frac{\omega}{c}n^{(-)}l} \\ &= \frac{E_0}{2} (\hat{x} + i\hat{y}) e^{-i\frac{\omega}{c}(n_R^{(+)} + in_I^{(+)})l} + \frac{E_0}{2} (\hat{x} - i\hat{y}) e^{-i\frac{\omega}{c}(n_R^{(-)} + in_I^{(-)})l} \end{aligned} \quad (2.68)$$

In the usual case of equal attenuations for the two polarizations, the imaginary parts of the index of refraction are equal ( $n_I^+ = n_I^- = n_I$ ) [146]. We can also define

$$\bar{n} = \frac{n_R^{(+)} + n_R^{(-)}}{2} \quad (2.69)$$

$$\Delta\bar{n} = \frac{n_R^{(+)} - n_R^{(-)}}{2} \quad (2.70)$$



Thus

$$\begin{aligned}\mathbf{E} &= \frac{E_0}{2} e^{-\frac{\omega}{c} n_I l} e^{i\frac{\omega}{c} \bar{n} l} [(\hat{x} + i\hat{y}) e^{i\frac{\omega}{c} \Delta \bar{n} l} + (\hat{x} - i\hat{y}) e^{-i\frac{\omega}{c} \Delta \bar{n} l}] \\ &= E_0 e^{-\frac{\omega}{c} n_I l} (\cos \theta \hat{x} + i \sin \theta \hat{y})\end{aligned}\quad (2.71)$$

where we have eliminated the common phase factor  $\text{Exp}[i\frac{\omega}{c} \bar{n} l]$  and we have defined the angle of rotation

$$\theta = \frac{\omega}{c} \Delta \bar{n} l = \frac{\omega l}{2c} (n_R^{(+)} - n_R^{(-)}) = \frac{k_0 l}{2} (n_R^{(+)} - n_R^{(-)}) \quad (2.72)$$

where  $k_0$  is the free space propagation wavevector. The above formula gives the angle of rotation of the polarization plane of a birefringent medium and applies equally<sup>1</sup> to linearly and circularly birefringent media. By comparison of the electric field (2.64) with the rotated field (2.71) we find that the polarization rotation depends on the real part of the atomic polarizability and on the number density of the atoms

$$\theta = \frac{4\pi^2 n l}{\lambda} \text{Re}\{a(\omega)\} \quad (2.73)$$

while the Faraday rotation in terms of the medium volume is

$$\theta = \frac{4\pi^2 N l}{\lambda V} \text{Re}\{a(\omega)\} = \frac{4\pi^2 N}{\lambda A} \text{Re}\{a(\omega)\} \quad (2.74)$$

We note that in the following the atomic polarizability is treated as a quantum mechanical operator, therefore the Faraday rotation is frequently encountered to be proportional to the quantum mechanical expectation value of the atomic polarizability operator, namely

$$\theta = \frac{4\pi^2 n l}{\lambda} \text{Re}\{\langle \hat{a}(\omega) \rangle\} \quad (2.75)$$

In the following sections we are going to calculate explicitly the polarizability of alkali atoms and we are going to show how the dispersive and the absorptive characteristics of the atom affect the light and on the other hand, how the light affects the atomic states.

## 2.5.2 The Dipole Interaction

Given the size of alkali atoms and the near infra-red wavelengths of  $D_1$  and  $D_2$  transitions in  $^{133}\text{Cs}$  and  $^{87}\text{Rb}$  we can apply the dipole approximation

$$\mathcal{H}_{int}(t) = -\mathbf{d} \cdot \mathbf{E}(\mathbf{r}, t) \quad (2.76)$$

We are interested in the effects of  $\mathcal{H}_{int}(t)$  on the eigenstates of  $\mathcal{H}_0$  which can be considered as the  $|F, m\rangle$  states since the Zeeman splitting is almost negligible in a magnetic field of the order of a few mG. We define ground and excited state projection

<sup>1</sup>In a linear birefringent medium the circular components of the index of refraction in Eq.(2.72) must be replaced by the corresponding linear indexes of refraction.

operators such as

$$P_F = \sum_m |Fm\rangle\langle Fm| \quad P_{F'} = \sum_{m'} |F'm'\rangle\langle F'm'| \quad (2.77)$$

and

$$P_g = \sum_F P_F \quad P_e = \sum_{F'} P_{F'} \quad P_g + P_e = \mathbb{1} \quad (2.78)$$

Using these definitions, we can express the electric dipole operator in the  $\{|F, m\rangle\}$  basis

$$\mathbf{d} = P_e \mathbf{d} P_g + P_g \mathbf{d} P_e = \mathbf{d}^{(+)} + \mathbf{d}^{(-)} \quad (2.79)$$

The terms  $P_g \mathbf{d} P_g$  and  $P_e \mathbf{d} P_e$  do not contribute since  $\mathbf{d}$  is an odd parity operator. In the rotating wave approximation [147] the dipole interaction is written as

$$\begin{aligned} \mathcal{H}_{int}(t) &= -\mathbf{d} \cdot \mathbf{E}(\mathbf{r}, t) = -(\mathbf{d}^{(+)} + \mathbf{d}^{(-)})(\mathbf{E}^{(+)} + \mathbf{E}^{(-)}) \\ &\approx -(\mathbf{d}^{(+)} \mathbf{E}^{(-)} + \mathbf{d}^{(-)} \mathbf{E}^{(+)}) \\ &= -(P_e \mathbf{d} P_g \cdot \mathbf{E}^{(-)} + P_g \mathbf{d} P_e \cdot \mathbf{E}^{(+)}) \\ &= -\sum_{F, F'} P_{F'} \mathbf{d} P_F \mathbf{E}^{(-)} + P_F \mathbf{d} P_{F'} \mathbf{E}^{(+)} \end{aligned} \quad (2.80)$$

Application of the Wigner-Eckart theorem to the interaction Hamiltonian (See Appendix C) results in [117]:

$$\mathcal{H}_{int}(t) = -\frac{\hbar\Omega}{2} \sum_{F, F'} (e^{-i(\mathbf{k}\cdot\mathbf{r}-\omega t)} \hat{\mathbf{e}}^* \cdot \mathbf{D}_{F'F} + e^{i(\mathbf{k}\cdot\mathbf{r}-\omega t)} \hat{\mathbf{e}} \cdot \mathbf{D}_{FF'}^\dagger) \quad (2.81)$$

where  $\Omega$  is the Rabi frequency and  $\mathbf{D}_{F'F}$  is an effective dipole operator defined in the Appendix C.

To include the Doppler effect, we assume that the center of mass of the atoms is moving with velocity  $\mathbf{v}$ , thus  $\mathbf{r}(t) = \mathbf{r}_0 + \mathbf{v}t$  therefore the interaction takes the form

$$\mathcal{H}_{int}(t) = -\frac{\hbar\Omega}{2} \sum_{F, F'} (e^{-i\mathbf{k}\cdot\mathbf{r}_0} e^{-i(\mathbf{k}\cdot\mathbf{v}-\omega)t} \hat{\mathbf{e}}^* \cdot \mathbf{D}_{F'F} + e^{i\mathbf{k}\cdot\mathbf{r}_0} e^{i(\mathbf{k}\cdot\mathbf{v}-\omega)t} \hat{\mathbf{e}} \cdot \mathbf{D}_{FF'}^\dagger) \quad (2.82)$$

### 2.5.3 Ground State Hamiltonian and Polarizability

Following Appendix D, the next step is to apply adiabatic elimination of the excited state and to arrive at the effective Hamiltonian for the ground state and the polarizability tensor of the multi-level atom [36, 135]. This approximation is possible because the dynamics of the excited state are much faster than the slow-varying ground state amplitudes and effectively the time-averaged excited state dynamics follow the slow dynamics dictated by the ground state. For more information about the adiabatic elimination see [117] where the derivation in the Appendix C is taken from. The effective ground state



Hamiltonian governing the atomic dynamics is compactly written as

$$\mathcal{H}_{\text{eff}} \equiv -\frac{1}{4} \mathbf{E}_0^* \cdot \vec{a} \cdot \mathbf{E}_0 \quad (2.83)$$

where  $\mathbf{E}_0$  is the complex electric field amplitude and  $\vec{a}$  is the polarizability tensor given by:

$$\vec{a} = - \sum_{F, F', F_g} \frac{P_F \mathbf{d}P_{F'} \mathbf{d}P_{F_g}}{\hbar(\Delta_{F'F} - \mathbf{k} \cdot \mathbf{v} + i(\frac{\Gamma}{2} + \gamma_c))} \quad (2.84)$$

$\Gamma$  is the spontaneous emission rate which is of the order of a few MHz and  $\gamma_c$  is the collisionally induced dephasing rate of the optical coherence which depends on the buffer gas pressure in the cell and ranges from several GHz up to hundreds of GHz.  $F$  and  $F_g$  represent in general two different ground state manifolds and  $F'$  represents an excited state manifold. In general, the effective Hamiltonian  $\mathcal{H}_{\text{eff}}$  is not Hermitian since it must describe the disappearance of atoms from the ground state, due to absorption of light. However, we can write  $\mathcal{H}_{\text{eff}}$  as a linear combination of a Hermitian part  $\delta E$  and an anti-Hermitian part  $\delta\Gamma$  [135], then

$$\mathcal{H}_{\text{eff}} = \delta E - \frac{i\hbar}{2} \delta\Gamma \quad (2.85)$$

the real part is called the light-shift operator and is defined as

$$\delta E = \Re[H_{\text{eff}}] = \frac{\mathcal{H}_{\text{eff}} + (\mathcal{H}_{\text{eff}})^\dagger}{2} = -\frac{1}{8} (\mathbf{E}_0^* \cdot \vec{a} \cdot \mathbf{E}_0 + \mathbf{E}_0 \cdot \vec{a}^\dagger \cdot \mathbf{E}_0^*) \quad (2.86)$$

while the imaginary part is called light absorption operator  $\delta\Gamma$  and is defined as:

$$\delta\Gamma = \frac{2}{\hbar} \Im[H_{\text{eff}}] = -\frac{1}{i\hbar} (\mathcal{H}_{\text{eff}} - (\mathcal{H}_{\text{eff}})^\dagger) = -\frac{i}{4\hbar} (\mathbf{E}_0^* \cdot \vec{a} \cdot \mathbf{E}_0 - \mathbf{E}_0 \cdot \vec{a}^\dagger \cdot \mathbf{E}_0^*) \quad (2.87)$$

For an open quantum system description of the effective Hamiltonian dynamics in terms of Lindblad jump operators see the discussion in Chapter 5 or follow [117].

## 2.5.4 Velocity Average

From Maxwell-Boltzmann distribution of velocities at temperature  $T$  we know that the velocities of the various atoms in the gas are normally distributed, thus the probability of occurrence of a particular velocity  $v$  in a phase space volume  $d^3v$  is

$$N(\mathbf{v})d^3v = \left(\frac{M}{2\pi k_B T}\right)^{3/2} e^{-Mv^2/2k_B T} d^3v \quad (2.88)$$

Averaging<sup>2</sup> the atomic polarizability over the velocity distribution of the atoms in the hot vapor cell we obtain [70]:

$$\vec{a} \rightarrow \int a(\mathbf{v})N(\mathbf{v})d^3v \quad (2.89)$$

<sup>2</sup>A similar averaging over the collisional history of the atoms has been taken in order to introduce the collisional width in the polarizability tensor. The interested reader may consult [70].

We simplify the problem by assuming that the beam propagates only in the  $\hat{z}$ -direction, then the probability of finding the atoms within the velocity interval  $u + du$  is

$$N(u)du = \sqrt{\frac{M}{2\pi k_B T}} e^{-\frac{Mu^2}{2k_B T}} du \quad (2.90)$$

which is a Gaussian distribution with width(standard deviation) given by

$$\sigma = \sqrt{\frac{k_B T}{M}} \quad (2.91)$$

On average the atoms move with a root-mean-square velocity  $u_{rms} = \sqrt{\frac{3k_B T}{M}}$ . Due to this motion relative to the beam propagation axis, the laser frequency experienced by an atom is shifted due to the Doppler effect by an amount

$$f' = f\left(1 \pm \frac{u}{c}\right) \quad (2.92)$$

Solving for the velocity and applying the equation into the Maxwell-Boltzmann distribution  $N(v)$  we obtain the known formula for the Gaussian Doppler broadening of optical resonances [50, 148, 149]

$$N(f' - f) = \frac{2\sqrt{\ln 2/\pi}}{\Gamma_G} e^{-\frac{4\ln 2(f'-f)^2}{\Gamma_G^2}} \quad (2.93)$$

with the Doppler width being

$$\Gamma_G = 2\frac{f}{c} \sqrt{\frac{2\ln 2 k_B T}{M}} \quad (2.94)$$

There is an additional correction factor  $2\sqrt{2\ln 2}$  in the width which is described in [150].

The integral of the atomic polarizability of Eq.(2.89) over the velocity distribution is of the form of the so-called plasma-dispersion function defined as

$$Z(\zeta) = \frac{1}{\sqrt{\pi}} \int_{-\infty}^{+\infty} dv \frac{e^{-v^2}}{v - \zeta} \quad (2.95)$$

Thus it is convenient to express the atomic polarizability in terms of the plasma-dispersion function

$$\hat{\vec{a}} = -\frac{1}{\hbar k} \sqrt{\frac{M}{2k_B T}} \sum_{F, F', F_g} P_F \mathbf{d} P_{F'} \mathbf{d} P_{F_g} \times Z(x + iy) \quad (2.96)$$

where

$$x = \frac{1}{k} \sqrt{\frac{M}{2k_B T}} (\omega - \omega_{F'F}^{m'm}) \quad y = \frac{1}{k} \sqrt{\frac{M}{2k_B T}} \left(\frac{\Gamma}{2} + \gamma_c\right) \quad (2.97)$$

We are only concerned in situations where the Zeeman splittings in the two hyperfine manifolds are small with respect to the Doppler and pressure widths of the optical transition, therefore we can neglect the dependence of  $Z(x+iy)$  on the magnetic quantum numbers. Moreover, the excited state hyperfine separations are small compared to the detuning and the collisional broadening used in this thesis, so we can also drop the

dependence of  $Z(x + iy)$  on  $F'$  and write

$$x = \frac{1}{k} \sqrt{\frac{M}{2k_B T}} (\omega - \omega_F) \quad y = \frac{1}{k} \sqrt{\frac{M}{2k_B T}} \left( \frac{\Gamma}{2} + \gamma_c \right) \quad (2.98)$$

It is also convenient to express  $x$  and  $y$  in terms of the Doppler width

$$x = \frac{\sqrt{\ln 2}}{\pi \Gamma_G} (\omega - \omega_F) \quad y = \frac{\sqrt{\ln 2}}{\pi \Gamma_G} \left( \frac{\Gamma}{2} + \gamma_c \right) \quad (2.99)$$

or in terms of frequency

$$x = \frac{2\sqrt{\ln 2}}{\Gamma_G} (f - f_F) \quad y = \frac{2\sqrt{\ln 2}}{\Gamma_G} \left( \frac{\Gamma}{2} + \gamma_c \right) \quad (2.100)$$

Furthermore, we can also express the atomic polarizability tensor in terms of the Doppler width as

$$\vec{a} = -\frac{1}{\hbar} \frac{\sqrt{\ln 2}}{\pi \Gamma_G} \sum_{F, F', F_g} P_F \mathbf{d} P_{F'} \mathbf{d} P_{F_g} \times Z(x + iy) \quad (2.101)$$

Finally, it is also convenient to express the Zeta plasma function in terms of the Voigt profile which is used widely in absorption spectroscopy [151] and incorporates all the convoluted broadening mechanisms. When  $y$  is positive, then there is the following relation between the Zeta function and the complex error function  $W(z)$

$$Z(x + iy) = i\sqrt{\pi} W(x + iy) \quad (2.102)$$

where  $W$  is defined as

$$W(z) = e^{-z^2} (1 - \operatorname{erf}(-iz)) \quad (2.103)$$

The Voigt profile function is also related to the Zeta function via

$$V(x + iy) = \frac{2\sqrt{\ln 2/\pi}}{\Gamma_g} W(x + iy) \quad (2.104)$$

Thus, we can express the atomic polarizability tensor in terms of the Voigt profile

$$\vec{a} = -\frac{i}{2\hbar} \sum_{F, F', F_g} P_F \mathbf{d} P_{F'} \mathbf{d} P_{F_g} \times V(x + iy) \quad (2.105)$$

Finally, we note that the real part of the polarizability is proportional to the imaginary part of the Voigt function  $\operatorname{Re}\{\vec{a}\} \rightarrow \operatorname{Im}\{V\}$  and the imaginary part of polarizability is proportional to the real part of the Voigt function  $\operatorname{Im}\{\vec{a}\} \rightarrow \operatorname{Re}\{V\}$ .

In our experiments, where we probe the spontaneous spin dynamics of a hot atomic vapor, we mostly work far from resonance where the detuning is large compared to the ground state hyperfine splitting and to the pressure broadening of the optical transitions. Most of our cells contain Nitrogen buffer gas ( $N_2$ ) at pressures higher than 100 Torr leading to collisional broadenings of the order of several GHz. Under these conditions ( $|\zeta| \gg 1$ ) the plasma dispersion function and accordingly the Voigt profile can be approximated by [72, 136, 152]:

$$Z(\zeta) = -\frac{1}{\zeta} \quad (2.106)$$

and by substituting the value of  $\zeta$  explicitly we obtain

$$Z(x + iy) = -k \sqrt{\frac{2k_B T}{M}} \frac{1}{(\omega - \omega_F) + i(\frac{\Gamma}{2} + \gamma_c)} \quad (2.107)$$

Therefore we have obtained that the plasma dispersion function, under the conditions of large detuning and large buffer gas pressure can be approached by a complex Lorentzian function which greatly simplifies the calculations.

### 2.5.5 Irreducible Components of the Polarizability Tensor

In the previous section we applied the adiabatic elimination process of the dipole interaction Hamiltonian and we derived i) the velocity averaged polarizability tensor and ii) the effective ground state Hamiltonian that governs the ground state atomic dynamics in the presence of the laser field. The scope of this section is to obtain a deeper understanding of the atomic polarizability and to emphasize the relation of the spin-polarization effects and the absorptive-dispersive light effects that manifest themselves in a broad range of experimental realizations of atomic physics.

We aim in expanding the polarizability Hamiltonian into irreducible spherical components which in turn can be written in terms of the angular momentum operators in the ground state, emphasizing the importance of the Wigner-Eckart theorem. In particular, we will demonstrate an irreducible decomposition of the polarizability tensor into scalar, vector, and tensor components, and we will show that each component, when expressed in angular momentum terms, can be radically simplified and reveal a clear physical picture. The above three terms have a different effect on the atom-light coupling and affect both the atoms and the light [134].

From the atomic point of view, the scalar term is responsible for the state-independent light shift, the vector term is of particular importance in this work and leads to the Faraday effect, to the QND vector Hamiltonian and to the interplay of back-action effects between measurements either on the light or on the atoms. The role of the tensor term is conspicuous only in the case where the detuning is comparable to the excited state hyperfine splitting and in this work its effects can be safely neglected.

From the light point of view, the scalar polarizability defines the frequency response of the atomic vapor in equilibrium, where all the energy levels are almost equally populated. The frequency response is imprinted on the absorption cross section when measuring the transmitted light from a vapor or on the index of refraction when for example measuring the polarization rotation or the phase shift of the light. The vector polarizability can then be interpreted as vector parallel to the net spin-polarization of the



vapor that deforms the equilibrium polarizability and alters the population distribution over the atomic energy space.

The irreducible expansion of the polarizability tensor can be formally presented as

$$\vec{a} = a^{(0)} \oplus a^{(1)} \oplus a^{(2)} \quad (2.108)$$

where  $a^{(0)}$  is the scalar,  $a^{(1)}$  the vector, and  $a^{(2)}$  the tensor polarizabilities. Using Appendix D the direct sum reads

$$\vec{a} = \sum_{L,M} \sum_{F,F_g} \xi^L(F, F_g) (-1)^M Q_{-M}^L T_M^L(F, F_g) Z(x + iy) \quad (2.109)$$

where  $T_M^L(F, F_g)$  are the irreducible components with  $L$  ranging from 0 to 2 as it is evident in Appendix D,  $Z(x + iy)$  contains the frequency response of the vapor and  $\xi^L(F, F_g)$  is a constant given by

$$\begin{aligned} \xi^L(F, F_g) &= 3G(-1)^L \sqrt{(2F+1)(2F_g+1)(2J+1)} \\ &\times (-1)^{-(I+F+J')} \begin{Bmatrix} F & L & F_g \\ J & I & J \end{Bmatrix} \begin{Bmatrix} 1 & L & 1 \\ J & J' & J \end{Bmatrix} \end{aligned} \quad (2.110)$$

### 2.5.6 Scalar Polarizability

The scalar polarizability corresponds to the  $L = 0$  term in Eq.(2.110). The components that only survive out of the summation are  $\xi^0(a, a)$  and  $\xi^0(b, b)$ . To simplify the notation we combine the collisional and the natural broadening into one relaxation rate simply denoted by  $\frac{\Gamma}{2} + \gamma_c \rightarrow \Gamma$ . By making use of (2.18) and (2.19) and the relation (D.15) from Appendix D it is straightforward to show that

$$a^{(0)} = G \sum_F P(F) Z(F) \quad (2.111)$$

In the case of large detuning/large pressure broadening we can replace the plasma dispersion function by the complex Lorentzian (2.107) therefore  $a^{(0)}$  reads

$$a^{(0)} = -\frac{r_e c^2 f_{ge}}{2\omega} \left( \frac{P(a)}{(\omega - \omega_a) + i\Gamma} + \frac{P(b)}{(\omega - \omega_b) + i\Gamma} \right) \quad (2.112)$$

The real and imaginary parts of the scalar polarizability are given by:

$$\text{Re}\{a^{(0)}\} = -\frac{r_e c^2 f_{ge}}{2\omega} \left( \frac{(\omega - \omega_a)}{(\omega - \omega_a)^2 + \Gamma^2} P(a) + \frac{(\omega - \omega_b)}{(\omega - \omega_b)^2 + \Gamma^2} P(b) \right) \quad (2.113)$$

$$\text{Im}\{a^{(0)}\} = -\frac{r_e c^2 f_{ge}}{2\omega} \left( \frac{\Gamma}{(\omega - \omega_a)^2 + \Gamma^2} P(a) + \frac{\Gamma}{(\omega - \omega_b)^2 + \Gamma^2} P(b) \right) \quad (2.114)$$

As mentioned in [72], in the limit where the collisional broadening or the detuning is large compared to the ground state hyperfine separation, i.e. when  $|\omega - (\omega_a + \omega_b)/2| \gg |\omega_a - \omega_b|$ , we can assume that all the hyperfine states have the same profile factor and we can drop the dependence of  $Z(F)$  on  $F$  and use  $\sum_F p(F) = 1$  to write the polarizability



as

$$a^{(0)} = -\frac{r_e c^2 f_{ge}}{2\omega} \left( \frac{(\omega - \omega_0)}{(\omega - \omega_0)^2 + \Gamma^2} - i \frac{\Gamma}{(\omega - \omega_0)^2 + \Gamma^2} \right) \quad (2.115)$$

In that limit the atom responds to the laser beam as a spin-1/2 particle and the polarizability can be derived also using the classical Lorentz model assuming the electron bound to the nucleus via a spring i.e. by solving the differential equation and substituting in the dipole operator  $\mathbf{d} = -e\mathbf{r}$

$$m_e \ddot{\mathbf{r}} = -m_e \omega_0^2 \mathbf{r} - m_e \Gamma \dot{\mathbf{r}} - e\mathbf{E}(z, t) \quad (2.116)$$

Here  $\omega_0$  is the resonance frequency of the spring and  $\Gamma$  is the damping rate. Note that in this limit the Lorentz model and the scalar polarizability differ only by the oscillator strength factor i.e.  $a^{(0)} = f_{ge} a_L$ . In the Fig.2.4 we plot the real and the imaginary parts of the Lorentz model polarizability and we emphasize that in the limit of large detuning the real part drops as  $1/\Delta$  while the imaginary part as  $1/\Delta^2$  allowing for non-invasive dispersive measurements on the atoms [34].

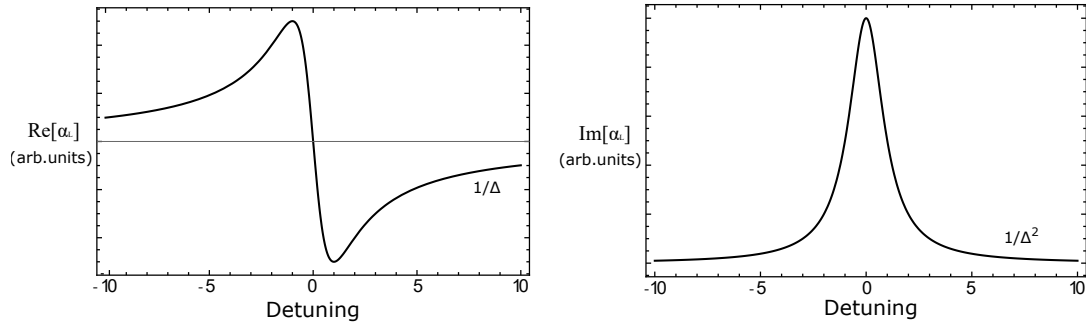


**Figure 2.4:** The real and the imaginary parts of the scalar polarizability in the limit of large detuning. The plots are calculated using the Lorentz model of the electron bound to the nucleus through a spring, driven by the light field. The damping rate is  $\Gamma = 1$  and  $\Delta$  is the detuning in units of  $\Gamma$ . In the limit of large detuning (far away from resonance) the dispersion drops as  $1/\Delta$  while the absorption as  $1/\Delta^2$  indicating that there is a regime where the absorption is negligible, while the dispersion is significantly larger.

Having a relation for the scalar polarizability we can now obtain the scalar part of the effective atomic Hamiltonian which is given by

$$\begin{aligned} \mathcal{H}_{\text{eff}}^{(0)} &= -\frac{1}{4} \mathbf{E}^* \cdot a^{(0)} \cdot \mathbf{E} \\ &= \frac{|E_0|^2 r_e c^2 f_{ge}}{8\omega} \left( \frac{P(a)}{(\omega - \omega_a) + i\Gamma} + \frac{P(b)}{(\omega - \omega_b) + i\Gamma} \right) \end{aligned} \quad (2.117)$$

Using once more (2.18) and (2.19), we can express the operators  $P(a)$  and  $P(b)$  in terms of angular momentum operators which are combined in a way that produce a rank-0

tensor in the ground state of the atom

$$\begin{aligned} \mathcal{H}_{\text{eff}}^{(0)} = & \frac{|E_0|^2 r_e c^2 f_{ge}}{4\omega[I]} \left( \frac{1}{(\omega - \omega_a) + i\Gamma} - \frac{1}{(\omega - \omega_b) + i\Gamma} \right) \mathbf{I} \cdot \mathbf{S} \\ & + \frac{|E_0|^2 r_e c^2 f_{ge}}{8\omega[I]} \left( \frac{I+1}{(\omega - \omega_a) + i\Gamma} + \frac{I}{(\omega - \omega_b) + i\Gamma} \right) \end{aligned} \quad (2.118)$$

It is evident that the scalar effective Hamiltonian can be written as a sum of an effective hyperfine term and a constant term proportional to the identity. By separating the real from the imaginary parts, we can distinguish between shift and broadening terms in the ground state. The scalar part of the light-shift operator is given by the real part of the scalar effective Hamiltonian  $\delta E^{(0)} = \text{Re}\{\mathcal{H}_{\text{eff}}^{(0)}\}$ , which is of the form  $\delta E^{(0)} = \delta E_c + \hbar\delta A \mathbf{I} \cdot \mathbf{J}$ . The constant term  $\delta E_c$  represents an energy shift in the center of gravity of the ground state and is independent of the atomic state. i.e. all energy levels are shifted in the same way, while  $\delta A$  represents an effective energy shift in the hyperfine coupling constant. This term causes the hyperfine transition frequency to be slightly shifted without affecting the Zeeman resonances.

In the same way, the scalar part of the light-absorption operator is given by the imaginary part of the effective Hamiltonian  $\delta\Gamma^{(0)} = -\frac{2\text{Im}\{\mathcal{H}_{\text{eff}}^{(0)}\}}{\hbar}$  and can be accordingly splitted in the same terms.

The rank-0 equilibrium light-absorption operator is equal to the pumping rate of the atom which expresses the rate at which an atom absorb photons of frequency  $\nu$  and is given by

$$R = \int \sigma(\nu) \Phi(\nu) d\nu \quad (2.119)$$

or

$$\delta\Gamma^{(0)} = R = \frac{c|E_0|^2}{2\pi\hbar\nu} r_e f_{ge} c \frac{\Gamma/2\pi}{(\nu - \nu_0)^2 + (\Gamma/2\pi)^2} \quad (2.120)$$

From the above relation we can identify the equilibrium absorption cross-section as

$$\sigma_{\text{abs}}(\nu) = \pi r_e f_{ge} c \frac{\Gamma/2\pi}{(\nu - \nu_0)^2 + (\Gamma/2\pi)^2} \quad (2.121)$$

and

$$\frac{\Phi(\nu)}{A_b} = \frac{c|E_0|^2}{2\pi\hbar\nu} \quad (2.122)$$

where  $\Phi(\nu)$  is the photon flux in units of photons per second and  $A_b$  is the area of the beam profile. For a complete analysis of  $\delta E^{(0)}$  and  $\delta\Gamma^{(0)}$  in the different regimes of detuning and broadening the interested reader may consider [72, 136].

### 2.5.7 Vector Polarizability

The vector polarizability corresponds to the  $L = 1$  term in Eq.(2.109) and as mentioned in the introduction of the section is responsible for the Faraday rotation exhibited to a linearly polarized beam as it transverses the atomic medium.

Faraday rotation of the linearly polarized incident light is a result of circular birefringence in the atomic medium. The circular birefringence results from the different index of refraction between the left ( $\sigma_-$ ) and the right ( $\sigma_+$ ) circularly polarized lights. This anisotropy in the atomic medium stems from the difference of the populations between spin-up and spin-down states.

The anisotropy between these states for circularly polarized light can be mostly understood by thinking of the atom effectively as a spin-1/2 system both in the ground but also in the excited state and looking at the absorption (imaginary part of the polarizability). It is evident from that picture that circularly polarized light is absorbed differently between left ( $\sigma_-$ ) and right ( $\sigma_+$ ). This anisotropy must be also imprinted in the index of refraction, namely the real part of atomic polarizability as a consequence of their interconnection by the Kramer-Kronig relationship [72, 153]

$$\mathbf{a}_R(\omega) = \mathcal{P} \int_{-\infty}^{+\infty} \frac{\mathbf{a}_I(\omega')d\omega'}{\omega' - \omega} \quad (2.123)$$

$$\mathbf{a}_I(\omega) = -\mathcal{P} \int_{-\infty}^{+\infty} \frac{\mathbf{a}_R(\omega')d\omega'}{\omega' - \omega} \quad (2.124)$$

where  $\mathcal{P}$  denotes the principal value of the integral, calculated with the appropriate choice of a contour in the complex plane. Substituting the values of  $J$ ,  $F$  and  $F_g$  in Eq.(2.109), one readily finds that the vector polarizability is comprised of Zeeman and hyperfine terms i.e.  $a^{(1)}(a, a)$ ,  $a^{(1)}(a, b)$ ,  $a^{(1)}(b, a)$  and  $a^{(1)}(b, b)$ .

In our experimental implementation we only observe the Zeeman components of the vector polarizability since the bandwidth of our photodetectors is limited to 1 MHz and higher frequencies were diminished using low pass and anti-aliasing filters. To that end, we are going to focus on the analysis of only the Zeeman terms and exclude the fast hyperfine modulations of the polarizability vector. The interested reader may follow [135] for a complete analysis of the vector term. Direct calculation of the  $\xi^1(F, F_g)$  term in Eq.(2.110) yield

$$\begin{aligned} a^{(1)} &= -\frac{G}{4}[11 - 4J'(J' + 1)] \sum_{F, F_g} \sqrt{(2F + 1)(2F_g + 1)} \\ &\times W\left(\frac{1}{2}FI; \frac{1}{2}F_g\right) \sum_M (-1)^M \mathbf{Q}_M^1 T_{-M}^1(F, F_g) Z(F, F_g) \end{aligned} \quad (2.125)$$

We can express this equation in terms of the spin operator in the ground state by making



explicit use of Eq.(2.17). Then the vector polarizability reads

$$a^{(1)} = -\frac{G\sqrt{2}}{4}[11 - 4J'(J' + 1)] \sum_M \mathbf{Q}_M^1 \sum_F Z(F)S_M \quad (2.126)$$

It is convenient to express Eq.(2.17) in the  $|Fm_F\rangle$  basis and split the operator into diagonal and off-diagonal terms. The off-diagonal terms are of minor importance for this work as we have already discussed, therefore we can safely ignore them

$$\mathbf{S} = \sum_{F,m} \langle Fm|\mathbf{S}|Fm\rangle|Fm\rangle\langle Fm| + \sum_{F \neq F_g, m_g, m} \langle Fm|\mathbf{S}|F_g m_g\rangle|Fm\rangle\langle F_g m_g| \quad (2.127)$$

In the limit of large detuning or large buffer gas pressures we use once more the complex Lorentzian expansion of the Plasma function and the polarizability can be written as

$$\mathbf{a}^{(1)} = \frac{\sqrt{2}r_e c^2 f_{ge}}{8\omega} [11 - 4J'(J' + 1)] \sum_M \mathbf{Q}_M^1 \sum_F \frac{P(F)S_M P(F)}{(\omega - \omega_F) + i\Gamma} \quad (2.128)$$

Finally, in the limit where the detuning or the pressure broadening is larger than the ground state hyperfine splitting [72], as we have already discussed in the case of the scalar polarizability, we can approach the plasma dispersion function with a common complex Lorentzian factor for both ground state transitions and the vector polarizability readily reads

$$\mathbf{a}^{(1)} = \frac{\sqrt{2}r_e c^2 f_{ge}}{8\omega} \frac{[11 - 4J'(J' + 1)]}{(\omega - \omega_0) + i\Gamma} \sum_M \mathbf{Q}_M^1 S_M \quad (2.129)$$

or by making use of the scalar polarizability, in the case of large detuning and large buffer gas pressure (Eq.(2.115)) we obtain

$$\mathbf{a}^{(1)} = \sqrt{2}a^{(0)} \frac{[11 - 4J'(J' + 1)]}{4} \sum_M \mathbf{Q}_M^1 S_M \quad (2.130)$$

where  $a_0$  is the scalar polarizability

$$a^{(0)} = -\frac{r_e c^2 f_{ge}}{2\omega} \frac{1}{(\omega - \omega_0) + i\Gamma} \quad (2.131)$$

## 2.5.8 Vector Interaction Hamiltonian

In the same sense as the scalar component of the effective Hamiltonian that dictates the ground state alkali dynamics, we define the vector effective Hamiltonian, being proportional to the total angular momentum of the atom. The vector part of the Hamiltonian accounts for the coupling of the polarization of light with the spin of the atom in the ground state. The spin is modulated at the hyperfine and the Larmor frequencies, therefore the Hamiltonian coupling is responsible for the transfer of the spin modulation to the polarization of the light crossing the atomic medium.

The vector Hamiltonian is frequently called QND Hamiltonian (Quantum non-

demolition Hamiltonian) because it has been utilized experimentally as well as theoretically for quantum non-demolition measurements where the uncertainty of the measured observable is not increased during the subsequent evolution of the system or to put it differently, the Hamiltonian of the interaction commutes with the Hamiltonian of the system under observation. In the particular case of the atom-light coupling in alkali vapors the system Hamiltonian is the Breit-Rabi Hamiltonian and the interaction Hamiltonian is the effective vector Hamiltonian both being proportional to the total spin of the atom.

Since we have expressed the spin operator in the  $|Fm_F\rangle$  basis and we have kept only the Zeeman components, we can use the Landè projection theorem, defined previously in Chapter 2, in order to write the spin operator  $\mathbf{S}$  in terms of the total spin operator  $\mathbf{F}$  in a given hyperfine multiplet. For the upper and the lower hyperfine manifold we obtain respectively

$$\mathbf{S} = \frac{\mathbf{F}}{2[I]} = \frac{\mathbf{F}}{4F} \quad \mathbf{S} = -\frac{\mathbf{F}}{2[I]} = -\frac{\mathbf{F}}{4F} \quad (2.132)$$

The vector part of the effective polarizability Hamiltonian is then

$$H_{\text{eff}}^{(1)} = -\frac{1}{4}\mathbf{E}^* \cdot a^{(1)} \cdot \mathbf{E} \quad (2.133)$$

We can plug the relation of the vector polarizability Eq.(2.128) into the above equation and then use the relation from Appendix D Eq.(D.16) so that the vector Hamiltonian is written as

$$H_{\text{eff}}^{(1)} = -\frac{1}{4} \frac{r_e c^2 f_{ge}}{8\omega} [11 - 4J'(J' + 1)] \sum_F \frac{P(F)S_M P(F)}{(\omega - \omega_F) + i\Gamma} \frac{\mathbf{E} \times \mathbf{E}^*}{i} \quad (2.134)$$

To calculate the effective Hamiltonian we have also used the property of the dyadic tensor

$$\hat{\mathbf{e}}_q \cdot \mathbf{Q}_M^1 \cdot \hat{\mathbf{e}}_q^* = (-1)^M \hat{\mathbf{e}}_q \cdot \mathbf{Q}_{-M}^1 \cdot \hat{\mathbf{e}}_{q'}^* = \frac{1}{i\sqrt{2}} \epsilon_{qq'M} \hat{\mathbf{e}}_q \cdot \hat{\mathbf{e}}_{q'}^* = \frac{1}{i\sqrt{2}} \hat{\mathbf{e}} \times \hat{\mathbf{e}}^* \quad (2.135)$$

Note that  $\frac{\mathbf{E} \times \mathbf{E}^*}{i} = \mathbf{s} |E_0|^2 = \mathbf{S}_3$ , where  $\mathbf{s}$  is a vector parallel to the light propagation direction and proportional to the degree of circular polarization of the probe light. It is also convenient to express it in terms of the circular polarization Stokes component  $S_3$ .

The Hamiltonian can be compactly written as

$$H_{\text{eff}}^{(1)} = -\frac{1}{2} \sum_F a_F^v(\omega) \frac{\mathbf{F}}{F} \cdot \frac{\mathbf{E} \times \mathbf{E}^*}{i} \quad (2.136)$$

where

$$a_F^v(\omega) = \frac{r_e c^2 f_{ge}}{64\omega} \frac{[11 - 4J'(J' + 1)]}{(\omega - \omega_F) + i\Gamma} \quad (2.137)$$

It is useful to write down the summation explicitly since care must be taken to the sign



of the two hyperfine manifolds

$$H_{\text{eff}}^{(1)} = -\frac{1}{2} \frac{r_e c^2 f_{ge}}{64\omega} [11 - 4J'(J' + 1)] \left( \frac{\mathbf{F}_a/F_a}{(\omega - \omega_a) + i\Gamma} - \frac{\mathbf{F}_b/F_b}{(\omega - \omega_b) + i\Gamma} \right) \cdot \frac{\mathbf{E} \times \mathbf{E}^*}{i} \quad (2.138)$$

Once again in the limit of large detuning or large pressure broadening (larger than the ground state hyperfine separation) the Hamiltonian reduces to [48]

$$H_{\text{eff}}^{(1)} = -\frac{1}{2} a_F^v(\omega) \frac{\mathbf{F}}{F} \cdot \frac{\mathbf{E} \times \mathbf{E}^*}{i} \quad (2.139)$$

The effect of the vector Hamiltonian on the ground state of the atom is to split the magnetic energy sublevels, since the Hamiltonian can be thought as an effective Zeeman term

$$H_{\text{eff}}^{(1)} = -\mathbf{B}_{\text{eff}} \cdot \frac{\mathbf{F}}{F} \quad (2.140)$$

with the effective magnetic field being

$$\mathbf{B}_{\text{eff}} = \frac{1}{2} a_F^v(\omega) \frac{\mathbf{E} \times \mathbf{E}^*}{i} \quad (2.141)$$

It is straightforward in this case to calculate the vector light shift operator and the vector light-absorption operator, namely the real and the imaginary parts of the effective vector Hamiltonian, respectively [72]. For a summary and a compact relationship including both the scalar and the vector components see [72].

## 2.5.9 Light Propagation II

In the section Light Propagation I we have shown that the solution to the Maxwell equations of light propagation in a dielectric medium are given by Eq.(2.64)

$$\mathbf{E} = \mathbf{E}_0 e^{i(1+2\pi n \text{Re}\{\langle \alpha(\omega) \rangle\}) \frac{\omega}{c} z} e^{-2\pi n \text{Im}\{\langle \alpha(\omega) \rangle\} \frac{\omega}{c} z} \quad (2.142)$$

where  $\langle \mathbf{a} \rangle$  is the expectation value of the polarizability tensor. In the most general case of an anisotropically polarized medium, the induced polarization in the medium can be either parallel to the direction of the incident electric field  $\mathbf{E}_0$ , i.e. transverse to the beam propagation axis, whereas, it can also have longitudinal induced components parallel to the direction of beam propagation. The longitudinal components (parallel to the beam propagation axis) are many orders of magnitude smaller than the transverse, and they can be safely ignored. We can project out these components from the polarizability tensor by applying the projector operator [68]

$$\mathbf{T} = \mathbb{1} - \hat{\mathbf{n}}\hat{\mathbf{n}} \quad (2.143)$$

where  $\hat{\mathbf{n}}$  is the unit vector along the light propagation direction. The projector operator satisfies the usual property  $\mathbf{T} \cdot \mathbf{T} = \mathbf{T}$  and can be interpreted as an operator that subtracts out of the spherically symmetric identity operator, a particular direction pointing along

$\hat{\mathbf{n}}$ .

Action of  $\mathbf{T}$  on the polarizability tensor results in a polarizability with only transverse field components, namely a transverse polarizability

$$\langle \alpha_{\perp} \rangle = \mathbf{T} \cdot \langle \alpha \rangle \cdot \mathbf{T} \quad (2.144)$$

or equivalently

$$\hat{\alpha}_{\perp} = \alpha^{(0)} \left( \mathbf{T} + \sqrt{2} \frac{[11 - 4J'(J' + 1)]}{4} \sum_M \mathbf{T} \cdot \mathbf{Q}_M^1 \cdot \mathbf{T} S_M \right) \quad (2.145)$$

which holds in the case of large buffer gas pressure and a detuning larger than the ground state hyperfine separation. Here  $a_0$  is the scalar polarizability given by Eq.(2.115). The projection of the atomic polarizability results in a diagonal form of the polarizability consistent with the axial symmetry of the atomic Hamiltonian and from the assumed axial symmetry of the atomic density matrix<sup>3</sup>. In this case, the atomic polarizability is written as [68, 72] (we assume that the light propagation axis is along the  $\hat{z}$ -direction):

$$\langle \hat{\alpha}_{\perp} \rangle = \alpha^{(0)} (\mathbf{e}_1 \mathbf{e}_1^* + \mathbf{e}_{-1} \mathbf{e}_{-1}^* + \sqrt{2} \frac{[11 - 4J'(J' + 1)] \langle S_z \rangle}{4} \sum_{q=\pm 1} \mathbf{e}_q \mathbf{e}_q^*) \quad (2.146)$$

where the sum extends only on the transverse components. Using the orthonormality condition of the spherical unit vectors, namely  $\mathbf{e}_q \mathbf{e}_q^* = \mathbf{e}_q^* \mathbf{e}_q = \delta_{q,q'}$  it is straightforward to see that the spherical basis components  $\mathbf{e}_{\pm}$  are eigenstates of the polarizability operator, or on a more physical ground an initial circularly polarized beam ( $\sigma_+$  or  $\sigma_-$ ) remains circular after propagating through the medium. This is the definition of a medium exhibiting circular birefringence. Expressing the aforementioned results mathematically we obtain

$$\langle \hat{\alpha}_{\perp} \rangle \cdot \hat{\mathbf{e}}_{\pm 1} = \pm \langle \alpha_{\perp} \rangle \hat{\mathbf{e}}_{\pm 1} \quad (2.147)$$

where

$$\langle \alpha_{\perp} \rangle = \alpha^{(0)} \left( 1 + \sqrt{2} \frac{[11 - 4J'(J' + 1)] \langle S_z \rangle}{4} \right) \quad (2.148)$$

Then the electric field of Eq.(2.142) can be written as

$$\begin{aligned} \mathbf{E} = & |\mathbf{E}_0(0)| \left[ \hat{\mathbf{e}}_1 e^{i(1+2\pi n \text{Re}\{\langle a_{\perp}(\omega) \rangle\}) \frac{\omega}{c} z} e^{-2\pi n \text{Im}\{\langle a_{\perp}(\omega) \rangle\} \frac{\omega}{c} z} \right. \\ & \left. + \hat{\mathbf{e}}_{-1} e^{i(1-2\pi n \text{Re}\{\langle a_{\perp}(\omega) \rangle\}) \frac{\omega}{c} z} e^{2\pi n \text{Im}\{\langle a_{\perp}(\omega) \rangle\} \frac{\omega}{c} z} \right] \end{aligned} \quad (2.149)$$

or equivalently

$$\begin{aligned} \mathbf{E} = & \left[ \hat{\mathbf{e}}_1 (\hat{\mathbf{e}}_1^*) e^{i(1+2\pi n \text{Re}\{\langle a_{\perp}(\omega) \rangle\}) \frac{\omega}{c} z} e^{-2\pi n \text{Im}\{\langle a_{\perp}(\omega) \rangle\} \frac{\omega}{c} z} \right. \\ & \left. + \hat{\mathbf{e}}_{-1} (\hat{\mathbf{e}}_{-1}^*) e^{i(1-2\pi n \text{Re}\{\langle a_{\perp}(\omega) \rangle\}) \frac{\omega}{c} z} e^{2\pi n \text{Im}\{\langle a_{\perp}(\omega) \rangle\} \frac{\omega}{c} z} \right] \cdot \mathbf{E}_0(0) \end{aligned} \quad (2.150)$$

where  $\mathbf{E}_0(0)$  is the electric field of the probe beam at the point where the light enters the

<sup>3</sup>We assume an equilibrium density matrix where the populations are distributed in the various energy levels according to the Boltzmann distribution, or according to the spin-temperature distribution [154].

vapor cell. From the above results and the discussion in the light propagation I section it is straightforward to write a general formula for the Faraday rotation [48, 72]

$$\begin{aligned}\theta_{FR} &= \frac{4\pi^2 nl}{\lambda} \text{Re}\{\langle \alpha_{\perp}(\omega) \rangle\} \\ &= \frac{4\pi^2 nl}{\lambda} \text{Re}\{\alpha^{(0)}\} \sqrt{2} \frac{[11 - 4J'(J' + 1)] \langle S_z \rangle}{4} \\ &= \pi r_e c f_{ge} n l \sqrt{2} \frac{[11 - 4J'(J' + 1)]}{4} \frac{\omega - \omega_0}{(\omega - \omega_0)^2 + \Gamma^2} \langle S_z \rangle\end{aligned}\quad (2.151)$$

where  $r_e$  is the classical electron radius,  $c$  is the speed of light,  $f_{ge}$  the oscillator strength of the optical transition,  $n$  the number density of atoms in the cell,  $l$  the length of the cell,  $\omega_0$  the optical resonance frequency in the case of large detuning either of  $D_1$  or of  $D_2$  transition and  $\langle S_z \rangle = \langle \mathbf{n} \cdot \mathbf{S} \rangle$  is the expectation value of the spin along the beam propagation direction defined by the vector  $\hat{\mathbf{n}}$ . Here we have chosen this direction to be parallel to the z-axis.

Finally we note that the sign of the Faraday rotation is opposite between the  $D_1$  and the  $D_2$  transition. In our experiment both of our lasers probe the  $D_2$ -line of our  $^{87}\text{Rb}$  and  $^{133}\text{Cs}$  alkali vapors.

To conclude we mention that the absorption cross-section related to the imaginary part of the transverse polarizability is given by

$$\sigma_{abs}(\omega) = \pi r_e c f_{ge} \frac{\Gamma}{(\omega - \omega_0)^2 + \Gamma^2} \left(1 - \frac{11 - 4J_e(J_e + 1)}{8} \langle \mathbf{S} \cdot \mathbf{s} \rangle\right) \quad (2.152)$$

## 2.6 Stokes Parameters and Polarimetry

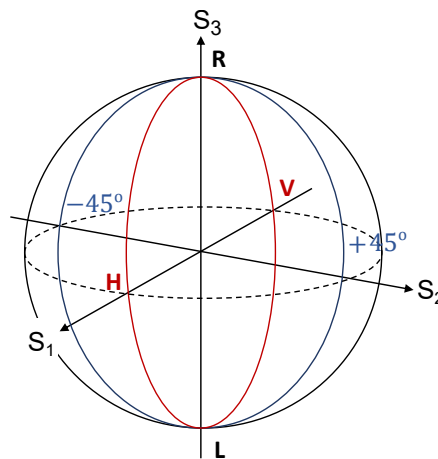


**Figure 2.5:** Poincaré sphere representation of light polarization. The basis vectors are the Stokes components of the electromagnetic field and the set of all "pure" polarization states are mapped to points on the surface.

As indicated in the discussion about the vector polarizability-Hamiltonian the cou-

pling of light with atoms can be expressed in terms of the Stokes parameter  $S_3$ . Stokes parameters are useful in polarization spectroscopy and in polarimetry in general and provide a convenient way to express the polarization of light [155]. Stokes parameters have been traditionally used in experiments where polarization is the main degree of freedom that couples to the atoms [154] and it is extensively used to provide a familiar interpretation of the effects of atoms on the light [117] but also on the effects of the light as it transverses the atomic medium. Assuming the light propagates along the  $\hat{z}$ -direction, the Stokes parameters are defined as [156]

$$S_0 = I_x + I_y \quad (2.153)$$

$$S_1 = I_x - I_y \quad (2.154)$$

$$S_2 = I_{+45} - I_{-45} \quad (2.155)$$

$$S_3 = I_{\text{RCP}} - I_{\text{LCP}} \quad (2.156)$$

where RCP and LCP are the right and left circular polarizations respectively.  $S_0$  is the total intensity of the light,  $S_1$  is the difference between the linear intensities along  $\hat{x}$  and  $\hat{y}$ ,  $S_2$  is the difference between the linear intensities along the direction which is rotated from the  $x - y$  plane by an angle of  $45^\circ$  and  $S_3$  is the difference between right ( $\sigma_+$ ) and left ( $\sigma_-$ ) circularly polarized light. It is common to normalize the Stokes components by dividing with the total intensity  $S_0$  so that  $S_0 = 1$  when normalized. The normalized Stokes parameters satisfy the relation  $S_1^2 + S_2^2 + S_3^2 = 1$  hence we can define the vector  $(S_1, S_2, S_3)$  with magnitude equal to unity.

Such a vector represents a point in the so called Poincare sphere which corresponds to a particular polarization state of light. Poincare sphere is plotted in Fig.2.5. As it is the case for a spin-1/2 particle on the Bloch sphere, a point on the surface of the Poincare sphere represents a pure state of the polarization while points with radius smaller than one, represent mixed states of polarization or partially-polarized states. The point (0,0,0) represents a completely unpolarized mixed polarization state.

In situations where the quantum fluctuations of the polarization are important, it is intuitive to define the Stokes operators as [157]

$$\hat{S}_0 = a_x^\dagger a_x + a_y^\dagger a_y \quad (2.157)$$

$$\hat{S}_1 = a_x^\dagger a_x - a_y^\dagger a_y \quad (2.158)$$

$$\hat{S}_2 = a_{+45^\circ}^\dagger a_{+45^\circ} - a_{-45^\circ}^\dagger a_{-45^\circ} \quad (2.159)$$

$$\hat{S}_3 = a_+^\dagger a_+ - a_-^\dagger a_- \quad (2.160)$$



The Stokes operators satisfy the common SU(2) commutation relations  $[\hat{S}_1, \hat{S}_2] = i\hat{S}_3$  and when there is a large photon-flux polarized along a particular direction then one can use the Holstein-Primakoff approximation [79] and treat the Stokes operator along that direction as a c-number.

Having knowledge about all the Stokes parameters of a light beam is sufficient to completely characterize the polarization state of light. As it is mentioned in [36], it is straightforward to measure all Stokes components in a balanced polarimetric scheme.

A polarizing beam splitter (PBS), two photodetectors and half/quarter-waveplates can be utilized in order to measure the Stokes parameters of a polarized laser beam. For the measurement of  $S_0$  and  $S_1$  only the sum and the difference between the two photodetectors is required when the axis of the PBS are aligned with the x and y axis in the lab frame. For the measurement of  $S_2$  component, a half-waveplate must be placed prior to the PBS with the primary axis at an angle of  $45^\circ$  with respect to the x-y system and the two signals must be subtracted.

Finally, for the circular polarizations  $S_3$ , a quarter-waveplate needs to be placed prior to PBS with the primary axis also at  $45^\circ$  relative to the x-y axis. Again the two signals must be subtracted. Normalizing the Stokes components by the total power  $S_0$ , we can find the direction of the Stokes vector on the Poincare sphere and thus we can characterize completely the polarization state of the light.

## 2.7 Spin-Projection Noise

Spin-projection noise is the fundamental quantum mechanical noise which stems from Heisenberg's uncertainty principle. Spin-projection noise has been studied extensively in [29] in a system of trapped ions and it constitutes a fundamental noise term in spin measurements and in particular, in atomic magnetometry and in spin noise spectroscopy [83] where precise spin measurements are required. Spin-projection noise is state dependent and it has been studied mostly in states of particular importance in quantum sensing like coherent spin states (CSS), thermal spin states (TSS) and squeezed spin states (SSS).

In Fig.2.6, a coherent and a squeezed spin state are represented. In a CSS, orthogonal spin components have equal uncertainty, while in a SSS the noise of a spin component is reduced, in contrast to the noise of an orthogonal component where the noise is increased such that the Heisenberg's uncertainty relation for spin is not violated. In this section we briefly review spin-projection noise following Chapter 2 of [48]. Given a spin polarized stretched state along the x-axis i.e.  $\langle F_x \rangle = F$ , which can be found using Eq.(2.47), we

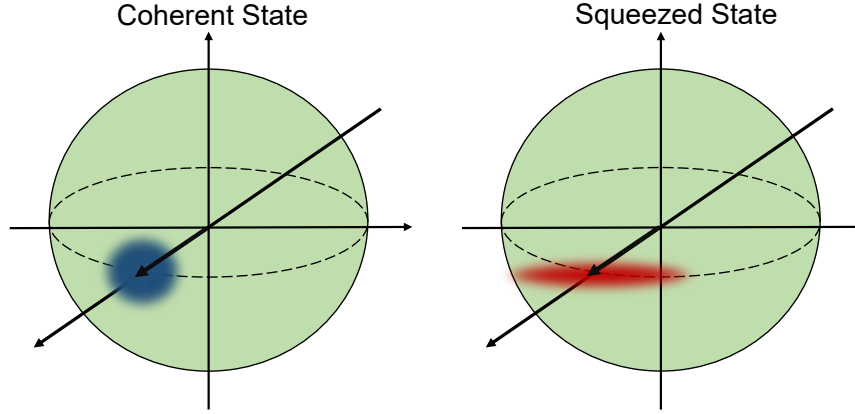


**Figure 2.6:** Schematic representation of the spin polarization in a multi-dimensional Bloch-like sphere. The vector represents a large spin polarization along a given direction, while the painted region represents the uncertainty in the two orthogonal angular momentum components. **a)** Coherent Spin State (CSS); The uncertainties in the two transverse spin components are equal and they satisfy the Heisenberg uncertainty principle (Minimum uncertainty states). **b)** Squeezed Spin State (SSS); The uncertainty in one transverse spin component has been reduced at the expense of the other. The uncertainties also follow Heisenberg’s uncertainty principle.

can obtain the uncertainty in a transverse spin component using the general uncertainty principle which applies between two conjugate operators

$$\Delta A \cdot \Delta B \geq \frac{1}{2} | \langle [A, B] \rangle | \quad (2.161)$$

using the angular momentum commutation relation  $[F_y, F_z] = iF_x$  and assuming that the standard deviations in  $F_y$  and  $F_z$  are the same we obtain the minimum quantum mechanical uncertainty

$$\sigma(F_z) = \sqrt{\frac{F}{2}} \quad (2.162)$$

If we make a measurement of the mean  $\langle F_z \rangle$  for  $N$  atoms, each with the standard deviation given by Eq. (2.162), then the resulting uncertainty will be given by

$$\sigma(\langle F_z \rangle) = \sqrt{\frac{F}{2N}} \quad (2.163)$$

This is known as the atomic spin-projection noise or the standard quantum limit (SQL). For completely unpolarized atoms we obtain  $\langle F_x^2 \rangle + \langle F_y^2 \rangle + \langle F_z^2 \rangle = F(F + 1)$ , and given that the uncertainty is equal in all three spatial directions

$$\sigma(\langle F_z \rangle) = \sqrt{\frac{F(F + 1)}{3N}} \quad (2.164)$$

Moreover, it is worth noting that in the case where the populations are distributed equally among the hyperfine states i.e. the collective state is a maximally mixed state, which is the limit  $\beta \rightarrow 0$  of a spin temperature distribution  $\rho = \frac{e^{\beta F_z}}{\text{Tr}[e^{\beta F_z}]}$ , the variance of the total spin component is

$$\text{Var}(\mathbf{F}) = \text{Var}(F_x) + \text{Var}(F_y) + \text{Var}(F_z) \quad (2.165)$$

The variance of a CSS is given by

$$\text{Var}(\mathbf{F}) = \text{Var}(F_x) + \text{Var}(F_y) = F \quad (2.166)$$

while for a TSS we get

$$\text{Var}(\mathbf{F}) = \text{Var}(F_x) + \text{Var}(F_y) + \text{Var}(F_z) = 3\left(\frac{F(F+1)}{3}\right) = F(F+1) \quad (2.167)$$

Then the above variances have to be weighted by the population fractions in the upper and lower hyperfine manifolds, which then produces the CSS and TSS limits of a maximally mixed state as described in [83]

$$\text{Var}(\mathbf{F})_{\text{CSS}} = (2a+1)F_a + (2b+1)F_b \quad (2.168)$$

$$\text{Var}(\mathbf{F})_{\text{TSS}} = (2a+1)F_a(F_a+1) + (2b+1)F_b(F_b+1) \quad (2.169)$$

Finally, when the uncertainty in a spin component transverse to the mean polarization is smaller than the uncertainty in a coherent spin state, we say that the spin component along this direction is squeezed. Note that a decrease of the uncertainty in this component comes at the expense of an increase in the uncertainty of the orthogonal spin component(also transverse to the mean polarization) so that the Heisenberg uncertainty relation (2.161) is satisfied. The squeezing of the uncertainty in a spin component is characterized by the squeezing parameter  $\xi$ , defined as

$$\xi = \frac{\Delta F_{\perp}}{\sqrt{|\langle \mathbf{F} \rangle|/2}} \quad (2.170)$$

There is a plethora of definitions of the squeezing parameter in literature [158, 159] where all of them are equivalent for a polarized spin state [5, 72]. There are various experimental techniques in order to produce and control spin squeezed states and the most relevant to this thesis are the techniques of QND measurements using the Faraday interaction [12, 160]. Spin squeezing also implies quantum correlations like quantum entanglement between the individual atoms of the vapor and there have been a vast amount of criteria relevant to the entanglement generation via spin squeezing [161]. Spin Squeezing is schematically presented in Fig.2.5 where the macroscopic spin polarization is described by a vector on the Bloch-like sphere and the uncertainty in the transverse spin components is given by the elliptical squeezed shadowed region.

## 2.8 Bloch Equations

Bloch equations, firstly introduced in the seminal paper of F.Bloch [45], is a set of phenomenological differential equations that describe the decaying dynamics of a collection of nuclear spins. Traditionally, Bloch equations have been used for modeling



applications like nuclear magnetic resonance (NMR) or electron spin resonance (ESR), but also in many relevant situations where a macroscopic spin polarization is induced and decays to an equilibrium value.

Bloch equations have been also applied to spin-exchange dynamics [162] to describe relaxation due to spin exchange collisions but also in hybrid atomic systems, or comagnetometers to account for the transfer of polarization from one spin species to another [58, 100, 101].

Given a constant magnetic field along a particular direction, the spin relaxation dynamics is preferably analysed in components parallel and perpendicular to the magnetic field [163]. The relaxation time of the parallel component is known in literature as  $T_1$  while the relaxation of the transverse component is called  $T_2$ .  $T_1$  is associated with the relaxation of populations while  $T_2$  with the relaxation of coherences. Bloch equations can be expressed either using ensemble spin variables, like the ensemble spin  $\mathbf{S} = (1/N_a) \sum_{i=1}^{N_a} \mathbf{S}_i$  or  $\mathbf{F} = (1/N_a) \sum_{i=1}^{N_a} \mathbf{F}_i$ , or in terms of the spin polarization  $\mathbf{P}$ . The ensemble spin is related to the spin polarization  $\mathbf{P}$  via

$$\frac{\mathbf{S}}{S} = \mathbf{P} \quad \frac{\mathbf{F}}{F} = \mathbf{P} \quad (2.171)$$

The coherent evolution of the spin in a constant magnetic field is given by the Heisenberg equation

$$i\hbar \frac{d}{dt} \mathbf{F} = -[H_B, \mathbf{F}] = \gamma \mathbf{B} \times \mathbf{F} \quad (2.172)$$

with the dynamics being governed by the Hamiltonian

$$H_B = -\boldsymbol{\mu} \cdot \mathbf{B} = g_F \mu_B \mathbf{B} \cdot \mathbf{F} \quad (2.173)$$

where  $\gamma = g_F \mu_B / \hbar$  is the gyromagnetic ratio and can be approximated by  $\frac{\gamma_e}{2I+1}$  with  $\gamma_e = g_s \mu_B / \hbar = 2\pi \times 2.8 \text{ MHz/G}$  being the electron's gyromagnetic ratio. In that case the evolution can be written as

$$\frac{d}{dt} \mathbf{F} = \gamma_e \mathbf{S} \quad (2.174)$$

where we use the fact that  $\mathbf{S}_{a,b} = \mathbf{F}_{a,b} / 2I + 1$ . As described in the section *Alkali Atoms in Magnetic Field*, the sign of the gyromagnetic ratio differs between the two hyperfine manifolds and the dynamics can be separated into these two spaces resulting in [48]

$$\frac{d}{dt} \mathbf{F}_a = \gamma \mathbf{B} \times \mathbf{F}_a \quad (2.175)$$

$$\frac{d}{dt} \mathbf{F}_b = -\gamma \mathbf{B} \times \mathbf{F}_b \quad (2.176)$$



Combination of the two equations yield [164]

$$\frac{d}{dt}(\mathbf{F}_a + \mathbf{F}_b) = \gamma \mathbf{B} \times (\mathbf{F}_a - \mathbf{F}_b) \quad (2.177)$$

The same can be equivalently applied to the quantum mechanical expectation values of the ensemble spin. To simplify notation, in the following we assume that the ensemble spin  $\mathbf{F}$  is a complex number following the semiclassical approach to the Bloch equations. The semiclassical model is also applied to Bloch equations regarding the expectation value of the ensemble spin  $\langle \mathbf{F} \rangle$ . On the other hand, one can assume  $\mathbf{F}$  being a quantum mechanical operator and write down a quantum mechanical model in the Heisenberg picture. Both models lead to equivalent results, with basic modifications on the interpretation and on the treatment of the noise [72]. Assuming a magnetic field along the  $\hat{z}$  direction, we can write the Bloch equations for the transverse ensemble spin components

$$\frac{d}{dt}F_x(t) = \gamma B_z F_y(t) - \frac{1}{T_2} F_x(t) \quad (2.178)$$

$$\frac{d}{dt}F_y(t) = -\gamma B_z F_x(t) - \frac{1}{T_2} F_y(t) \quad (2.179)$$

We can simplify further the notation by defining the transverse spin component as  $F_T(t) = F_x(t) + iF_y(t)$ . Combining the previous equations results in a single complex equation

$$\frac{d}{dt}F_T(t) = -i\gamma B_z F_T(t) - \frac{1}{T_2} F_T(t) \quad (2.180)$$

which describes a decaying spin precession in the xy-plane with frequency  $\omega_L = \gamma B_z$  and relaxation time  $T_2$

$$F_T(t) = F_T(t_0) e^{-i\omega_L t} e^{-t/T_2} \quad (2.181)$$

In order to account for noise, it is commonly used to augment the above differential equations with stochastic source terms that produce spin noise related to the spin relaxation processes. The relaxation process and the noise are intimately related as a consequence of the fluctuation-dissipation theorem [165]. As an example, spin noise due to spin-exchange relaxation has been described [48, 100] using zero-mean Gaussian noise terms  $d\xi(t) = \sqrt{2\sigma} d\mathcal{W}$ , where  $\sigma$  is a parameter depending on the total number of spins probed by the laser, on the particular state of the spin system and on the relaxation rate, and  $d\mathcal{W}$  is a Wiener increment  $\mathcal{N}(0, dt)$  with zero mean and variance  $dt$  [166–169]. The properties of the Wiener increment are: i)  $d\mathcal{W}_i d\mathcal{W}_j = \delta_{ij} dt$  ii)  $d\mathcal{W}_i^{N+2} = 0$  and iii)  $d\mathcal{W}_i dt = 0$  where  $i = x, y$ . Therefore, the resulting stochastic equations governing the spin dynamics are

$$dF_x(t) = dt\gamma B_z F_y(t) - \frac{dt}{T_2} F_x(t) + d\xi_x(t) \quad (2.182)$$



$$dF_y(t) = -dt\gamma B_z F_x(t) - \frac{dt}{T_2} F_y(t) + d\xi_y(t) \quad (2.183)$$

replacing the values for  $d\xi_x$  and  $d\xi_y$  we obtain

$$dF_x(t) = dt\gamma B_z F_y(t) - \frac{dt}{T_2} F_x(t) + \sqrt{2\sigma} d\mathcal{W}_x(t) \quad (2.184)$$

$$dF_y(t) = -dt\gamma B_z F_x(t) - \frac{dt}{T_2} F_y(t) + \sqrt{2\sigma} d\mathcal{W}_y(t) \quad (2.185)$$

where the value of  $\sigma$  can be found following the reasoning presented in Chapter 2 of [48], assuming a coherent spin state (CSS). The results can be equally applied to any other spin state of interest.

The standard deviation of the collective ensemble spin of  $N_a$  atoms in a CSS is given by  $\sigma(F_i) = \sqrt{F/2N_a}$  with  $i = x, y$ . In a time interval  $dt$ , assuming that the transverse relaxation time is  $T_2$ , there are  $N_a(dt/T_2)$  atoms that undergo a spin relaxation process. Then, the standard deviation of the collective spin of the atoms that have collided in time  $dt$  is  $\sigma(F_i) = \sqrt{FT_2/(2N_a dt)}$ . The change in  $F_i$  in a time  $dt$  is a random number with a standard deviation  $(dt/T_2)\sqrt{FT_2/(2N_a dt)} = \sqrt{Fdt/(2N_a T_2)}$ . Therefore, we conclude that

$$\sigma = \frac{F}{2N_a T_2} \quad (2.186)$$

The equation for the transverse spin component can be compactly written as:

$$dF_T(t) = -idt\gamma B_z F_T(t) - \frac{dt}{T_2} F_T(t) + \sqrt{2\sigma} d\mathcal{W}_T(t) \quad (2.187)$$

where we applied the properties  $\sqrt{A}d\mathcal{W}_1 + \sqrt{B}d\mathcal{W}_2 = \sqrt{A+B}d\mathcal{W}_3$  and  $(d\mathcal{W}_x + id\mathcal{W}_y)/\sqrt{2} = d\mathcal{W}_T$ . In the language of stochastic calculus, these equations are named Ornstein-Uhlenbeck processes, which describe a random walk with relaxation to the mean [170]. The Ornstein-Uhlenbeck process is equivalently written as a Langevin equation of the form

$$\frac{d}{dt} F_T(t) = -i\omega_L F_T(t) - \frac{1}{T_2} F_T(t) + \xi_T(t) \quad (2.188)$$

where  $\xi_T(t)$ , also known as white noise, stands in for the supposed derivative  $d\mathcal{W}/dt$  of the Wiener process. However,  $d\mathcal{W}/dt$  does not exist because the Wiener process is nowhere differentiable, and so the Langevin equation is, strictly speaking, only heuristic. In physics and engineering disciplines, it is nevertheless a common representation for the Ornstein-Uhlenbeck process and similar stochastic differential equations. The covariance of the noise source is  $\langle \xi_T(t_1)\xi_T(t_2) \rangle = 2\sigma\delta(t_1 - t_2)$ .

Since  $F_T(t)$  is a stochastic process it can be written in terms of an ensemble mean (not to confuse with the quantum mechanical expectation value) and a standard deviation,

$$F_T(t) = \langle F_T(t) \rangle + \Delta F_T(t) \quad (2.189)$$



The general solution of Eq.(2.188) can be found in terms of the Green's function

$$F_T(t) = e^{-i\omega_L(t-t_0)} e^{-(t-t_0)/T_2} F_T(t_0) + \int_{t_0}^t dt' G(t-t') \xi_T(t') \quad (2.190)$$

where the Green's function satisfies the equation

$$\frac{dG}{dt} + (i\omega_L + \frac{1}{T_2})G = \delta(t-t') \quad (2.191)$$

Solving for  $G(t-t')$  we obtain,

$$G(t-t') = e^{-i\omega_L(t-t')} e^{-(t-t')/T_2} \quad (2.192)$$

Therefore, the general solution of the Langevin equation takes the form

$$F_T(t) = e^{-i\omega_L(t-t_0)} e^{-(t-t_0)/T_2} F_T(t_0) + \int_{t_0}^t dt' e^{-i\omega_L(t-t')} e^{-(t-t')/T_2} \xi_T(t') \quad (2.193)$$

Since  $\xi_T(t)$  is a zero-mean noise source, the expectation value of the stochastic transverse spin component and the standard deviation are obtained from

$$\langle F_T(t) \rangle = e^{-i\omega_L(t-t_0)} e^{-(t-t_0)/T_2} F_T(t_0) \quad (2.194)$$

$$\Delta F_T(t) = F_T(t) - \langle F_T(t) \rangle = \int_{t_0}^t dt' e^{-i\omega_L(t-t')} e^{-(t-t')/T_2} \xi_T(t') \quad (2.195)$$

The ensemble averaged variance is given by

$$\begin{aligned} \langle \Delta F_T(t) \Delta F_T^*(t) \rangle &= \int_{t_0}^t \int_{t_0}^t dt' dt'' e^{-i\omega_L(t-t')} e^{-(t-t')/T_2} e^{+i\omega_L(t-t'')} e^{-(t-t'')/T_2} \langle \xi_T(t') \xi_T^*(t'') \rangle \\ &= 2\sigma \int_{t_0}^t dt' e^{-2(t-t')/T_2} = \frac{\sigma}{\frac{1}{T_2}} (1 - e^{-2(t-t_0)/T_2}) \end{aligned} \quad (2.196)$$

For very short timescales  $\frac{(t-t_0)}{T_2} \ll 1$  we can expand the exponential in powers of  $(t-t_0)$ , obtaining

$$\langle \Delta F_T(t) \Delta F_T^*(t) \rangle = \frac{\sigma}{\frac{1}{T_2}} (1 - (1 - 2\frac{(t-t_0)}{T_2})) = 2\sigma(t-t_0) \quad (2.197)$$

we find that the variance is linear with time which is a characteristic of diffusive evolution.

For larger timescales  $\frac{(t-t_0)}{T_2} \gg 1$ , we obtain

$$\langle \Delta F_T(t) \Delta F_T^*(t) \rangle = \frac{\sigma}{\frac{1}{T_2}} = \frac{F}{2N_a} \quad (2.198)$$

that is, the variance is independent of time reflecting the stationary statistics of an ergodic process, consistent with the results of the fluctuation-dissipation theorem. Note that this is the variance of the CSS. To simplify the discussion, without loss of generality, in the following we set  $t_0 = 0$ . To introduce the bandwidth of the measurement we can follow



[50]. The total uncertainty in a continuous measurement is given by [171]

$$\begin{aligned}\Delta F_T(t) &= \sqrt{\frac{\sigma}{1/T_2} \left[ \frac{2}{t} \int_0^t \left(1 - \frac{\tau}{t}\right) e^{-\tau/T_2} d\tau \right]^{1/2}} \\ &= \sqrt{\frac{\sigma}{1/T_2} \left[ \frac{2T_2}{t} + \frac{2T_2^2(e^{-t/T_2} - 1)}{t^2} \right]^{1/2}}\end{aligned}\quad (2.199)$$

Focusing on timescales  $t \gg T_2$  we obtain

$$\Delta F_T(t) = \sqrt{\frac{2FT_2BW}{N_a}} \quad (2.200)$$

where  $BW = 1/(2t)$  is the measurement bandwidth. It is customary to give the noise in units of root-mean-square uncertainty per  $\sqrt{Hz}$  which is given by dividing Eq.(2.200) by  $\sqrt{BW}$ :

$$\Delta F_T(t)_{\text{rms}} = \sqrt{\frac{2FT_2}{N_a}} \quad (2.201)$$

The time correlation for example of the  $F_T(t)$  fluctuations can be expressed by the covariance of  $F_T(t)$  at two different times  $t_1$  and  $t_2$ ,

$$\begin{aligned}\text{Cov}[F_T(t_1), F_T^*(t_2)] &= \langle [\langle F_T(t_1) \rangle + \Delta F_T(t_1)] [\langle F_T^*(t_2) \rangle + \Delta F_T^*(t_2)] \rangle \\ &= \langle \langle F_T(t_1) \rangle \langle F_T^*(t_2) \rangle \rangle + \langle \Delta F_T(t_1) \Delta F_T^*(t_2) \rangle = \langle F_T(0) F_T^*(0) \rangle e^{-(t_1+t_2)/T_2} \\ &+ \int_0^{t_1} \int_0^{t_2} dt' dt'' e^{-i\omega_L(t_1-t')} e^{-(t_1-t')/T_2} e^{+i\omega_L(t_2-t'')} e^{-(t_2-t'')/T_2} \langle \xi_T(t') \xi_T(t'') \rangle \\ &= \langle F_T(0) F_T^*(0) \rangle e^{i\omega_L(t_2-t_1)} e^{-(t_1+t_2)/T_2} + 2\sigma \int_0^{\min(t_1, t_2)} dt' e^{i\omega_L(t_2-t_1)} e^{-(t_1+t_2-2t')/T_2} \\ &= \langle F_T(0) F_T^*(0) \rangle e^{i\omega_L(t_2-t_1)} e^{-(t_1+t_2)/T_2} + \frac{\sigma}{T_2} e^{i\omega_L(t_2-t_1)} (e^{-(t_1+t_2-2\min(t_1, t_2))/T_2} - e^{-(t_1+t_2)/T_2}) \\ &= e^{i\omega_L(t_2-t_1)} \left[ \frac{\sigma}{T_2} e^{-|t_1-t_2|/T_2} + (\langle F_T(0) F_T^*(0) \rangle - \frac{\sigma}{T_2}) e^{-(t_1+t_2)/T_2} \right]\end{aligned}\quad (2.202)$$

In equilibrium, assuming ergodicity and stationary dynamics as dictated by Eq.(2.198) the condition  $\langle F_T(0) F_T^*(0) \rangle = \sigma / (\frac{1}{T_2})$  must be true, leading to the known result for the covariance

$$\text{Cov}[F_T(t_1), F_T^*(t_2)] = \frac{\sigma}{T_2} e^{i\omega_L \tau} e^{-|\tau|/T_2} \quad (2.203)$$

where  $\tau = t_1 - t_2$ . Note that the covariance at equal times  $t_1 = t_2$  is equal to the ensemble averaged variance  $\langle \text{Var}[F_T(t)] \rangle$  in agreement with Eq.(2.198). To bring covariance in a more familiar form we obtain the covariance of the spin along the  $\hat{x}$  direction, being equal to the real part of the right-hand-side of Eq.(2.202)

$$\text{Cov}[F_x(t_1), F_x(t_2)] = \frac{\sigma}{T_2} \cos(\omega_L \tau) e^{-|\tau|/T_2} \quad (2.204)$$



The covariance is related to the correlation function which is defined as

$$\text{Corr}[F_x(t_1), F_x(t_2)] = \frac{\text{Cov}[F_x(t_1), F_x(t_2)]}{\langle \text{Var}[F_x(t)] \rangle} = \cos(\omega_L \tau) e^{-|\tau|/T_2} \quad (2.205)$$

One can also define the symmetrized covariance function as

$$\frac{1}{2}(\text{Cov}[F_x(t_1), F_x(t_2)] + \text{Cov}[F_x(t_2), F_x(t_1)]) \quad (2.206)$$

weighting equally the timings in the two functions. In the particular example, both symmetrized covariance and covariance lead to the same results.

It is also convenient to consider the power spectrum of the atomic spin noise. The power spectral density  $S(\omega)$  is equal to the Fourier transform of the covariance function,

$$S(\omega) = \frac{F}{2N_a} \int_{-\infty}^{+\infty} \cos(\omega_L \tau) e^{-|\tau|/T_2} e^{-i\omega \tau} d\tau \quad (2.207)$$

which results in

$$S(\omega) = \frac{F}{2N_a} \frac{2(T_2 + T_2^3(\omega^2 + \omega_L^2))}{1 + T_2^4(\omega^2 - \omega_L^2)^2 + 2T_2^2(\omega^2 + \omega_L^2)} \quad (2.208)$$

Examining the regime where  $\omega^2 + \omega_L^2 \approx 2\omega_L^2$  i.e. for frequencies close to the resonance frequency and assuming that  $\omega_L \gg \frac{1}{T_2}$ , after some algebra we arrive at the known Lorentzian form

$$S(\omega) = \frac{F}{2N_a} \frac{(1/T_2)}{(\omega - \omega_L)^2 + (\frac{1}{T_2})^2} \quad (2.209)$$

where we have used a coherent spin state. It is more convenient to write the power spectrum in terms of the normalized Lorentzian function in the frequency domain

$$S(\nu) = \frac{d\omega}{d\nu} S(\omega) = \frac{1}{2\pi} S(\omega)$$

$$S(\nu) = \frac{F}{2N_a} \frac{2}{\pi} \frac{\Delta\nu}{(\nu - \nu_L)^2 + \Delta\nu^2} \quad (2.210)$$

where  $\Delta\nu$  is the half-width at half-maximum (HWHM) and it is related to the spin relaxation time through

$$\Delta\nu_{\text{HWHM}} = \frac{1}{2\pi T_2} \quad \Delta\omega_{\text{HWHM}} = \frac{1}{T_2} \quad (2.211)$$

Note that the integral of the power spectrum is equal to the ensemble averaged variance of the spin in the particular state

$$\int_0^{+\infty} S(\nu) d\nu = \frac{F}{2N_a} \quad (2.212)$$

It is generally convenient to express Bloch equations in matrix form

$$\begin{pmatrix} dF_x \\ dF_y \end{pmatrix} = \begin{pmatrix} \frac{dt}{T_2} & -\omega_L dt \\ \omega_L dt & \frac{dt}{T_2} \end{pmatrix} \begin{pmatrix} F_x \\ F_y \end{pmatrix} + \begin{pmatrix} \sqrt{\frac{F}{N_a T_2}} & 0 \\ 0 & \sqrt{\frac{F}{N_a T_2}} \end{pmatrix} \begin{pmatrix} d\mathcal{W}_x \\ d\mathcal{W}_y \end{pmatrix} \quad (2.213)$$

or compactly

$$d\mathbf{X}(t) = -\mathbf{A}\mathbf{X}(t)dt + B d\mathbf{W}(t) \quad (2.214)$$

Since the real part of the eigenvalues of the matrix  $\mathbf{A}$  is positive, then a stationary

solution exists of the form [170]

$$\mathbf{X}(t) = \int_{-\infty}^t \exp[-A(t-t')] B d\mathbf{W}(t) \quad (2.215)$$

the equal time stationary covariance matrix is defined as  $\sigma = \langle \mathbf{X}(t), \mathbf{X}^T(t) \rangle$  and can be found by solving the algebraic equation

$$A\sigma + \sigma A^T = BB^T \quad (2.216)$$

In the case of a  $2 \times 2$  system where A and B are real matrices a general formula for obtaining the covariance matrix exists

$$\sigma = \frac{\text{Det}(A)BB^T + [A - \text{Tr}(A)]BB^T[A - \text{Tr}(A)]^T}{2\text{Tr}(A)\text{Det}(A)} \quad (2.217)$$

The covariance at different times can be easily found from the equal time covariance

$$\langle \mathbf{X}(t_1), \mathbf{X}^T(t_2) \rangle = \begin{cases} \exp[-A(t_1 - t_2)]\sigma & , t_1 > t_2 \\ \sigma \exp[-A^T(t_2 - t_1)] & , t_2 > t_1 \end{cases} \quad (2.218)$$

while the power spectrum is given by

$$S(\omega) = (A + i\omega)^{-1} BB^T (A^T - i\omega)^{-1} \quad (2.219)$$

reproducing the result of Eq.(2.208).

### 2.8.1 Dual Species Spin-Exchange

Bloch Equations can be also used to model the exchange dynamics of electronic spin polarization between two atomic species. In the case of unpolarized vapors, an interesting effect of spin noise exchange between  $^{85}\text{Rb}$  and  $^{87}\text{Rb}$  has been reported in [100] and is revealed as an increase of the spin noise power at low magnetic fields, reflecting a correlation build-up as a consequence of strong cross-exchange. At higher magnetic fields, the fast spin precession averages out the exchange correlations. These effects have been also revealed using a formal quantum-trajectory picture of SE collisions [89] that allows the production of spin-noise from first principles, instead of using the phenomenological Bloch equations. The model is presented in detail in later chapters.

The equilibrium cross-correlations between Cs and Rb in a cell containing  $^{85}\text{Rb}$ ,  $^{87}\text{Rb}$  and  $^{133}\text{Cs}$  has been studied in [101] where the dynamics are mostly governed by diffusion of the atoms in the laser beam. The interesting point that raised in the study of equilibrium spin-exchange dynamics is whether the noise terms in Bloch equations should be anti-correlated (reflecting that spin exchange collisions conserve the total spin) or uncorrelated reflecting that i) the relaxation due to spin-exchange is caused not by the collision itself, but instead, by the combination of the precession in different hyperfine levels and the spin exchange collision, and ii) that the random nature of collisional

dynamics in the vapor cell renders the atoms completely uncorrelated after the collision [172]. The later assumption is an inherent characteristic of the spin-exchange master equation describing relaxation of alkali atoms in the vapor cell.

The spin-exchange interaction in general, tends to transfer the spin *polarization* from ones atomic species to the other, therefore it is convenient to write the Bloch equations in terms of the polarization. The coupled Bloch equations for the spin-components perpendicular to the magnetic field are

$$d\mathbf{P}_1 = dt[\mathbf{P}_1 \times \boldsymbol{\omega}_{L,1} - \gamma_1 \mathbf{P}_1 - \gamma_{11}^{se} \mathbf{P}_1 - \gamma_{12}^{se} \mathbf{P}_1 + \gamma_{12}^{se} \mathbf{P}_2] \\ + \sqrt{\frac{\gamma_1}{N_a}} d\mathbf{W}_1 + \sqrt{\frac{\gamma_{11}^{se}}{N_a}} d\mathbf{W}_{11}^{se} + \sqrt{\frac{\gamma_{12}^{se}}{N_a}} d\mathbf{W}_{12}^{se} \quad (2.220)$$

$$d\mathbf{P}_2 = dt[\mathbf{P}_2 \times \boldsymbol{\omega}_{L,2} - \gamma_2 \mathbf{P}_2 - \gamma_{22}^{se} \mathbf{P}_2 - \gamma_{21}^{se} \mathbf{P}_2 + \gamma_{21}^{se} \mathbf{P}_1] \\ + \sqrt{\frac{\gamma_2}{N_b}} d\mathbf{W}_2 + \sqrt{\frac{\gamma_{22}^{se}}{N_b}} d\mathbf{W}_{22}^{se} + \sqrt{\frac{\gamma_{21}^{se}}{N_b}} d\mathbf{W}_{21}^{se} \quad (2.221)$$

$\mathbf{P}_1$  is the spin polarization of the vapor containing  $N_a$  atoms and  $\mathbf{P}_2$  the polarization of the vapor containing  $N_b$  atoms.  $\gamma^{se}$  represent the spin-exchange collisional rate between the same ( $\gamma_{jj}^{se}$ ) and different ( $\gamma_{ij}^{se}$ ) species. The spin-exchange rate is given by  $\gamma_{ij}^{se} = q_i \sigma_{ij} u_{ij} n_j$ , with  $i, j = 1, 2$ .  $n$  is the vapor number density,  $\sigma$  the spin-exchange cross section,  $u$  the mean thermal velocity and  $q$  the spin-exchange broadening factor which is present when  $|\boldsymbol{\omega}_L| \gg 1/T_2$ .  $\gamma_1$  and  $\gamma_2$  are the relaxation rates due to other relaxation processes. Each relaxation process is associated with the corresponding noise source  $d\mathbf{W}$ . We can define a total decay rate  $\Gamma_j = \gamma_j + \gamma_{jj}^{se}$ , then we can re-write the above equation more compactly as

$$d\mathbf{P}_1 = dt[\mathbf{P}_1 \times \boldsymbol{\omega}_{L,1} - \Gamma_1 \mathbf{P}_1 - \gamma_{12}^{se} (\mathbf{P}_1 - \mathbf{P}_2)] + \sqrt{\frac{\Gamma_1}{N_a}} d\mathbf{W}_1 + \sqrt{\frac{\gamma_{12}^{se}}{N_a}} d\mathbf{W}_{12}^{se} \quad (2.222)$$

$$d\mathbf{P}_2 = dt[\mathbf{P}_2 \times \boldsymbol{\omega}_{L,2} - \Gamma_2 \mathbf{P}_2 - \gamma_{21}^{se} (\mathbf{P}_2 - \mathbf{P}_1)] + \sqrt{\frac{\Gamma_2}{N_b}} d\mathbf{W}_2 + \sqrt{\frac{\gamma_{21}^{se}}{N_b}} d\mathbf{W}_{21}^{se} \quad (2.223)$$

Here  $d\mathbf{W}_1$  and  $d\mathbf{W}_2$  are different than the previous ones. Assuming a magnetic field along the  $\hat{z}$  direction we can expand Bloch equations in spatial components

$$dP_{1,x} = dt[P_{1,y} \omega_{L,1} - \Gamma_1 P_{1,x} - \gamma_{12}^{se} (P_{1,x} - P_{2,x})] + \sqrt{\frac{\Gamma_1}{N_a}} d\mathcal{W}_{1,x} + \sqrt{\frac{\gamma_{12}^{se}}{N_a}} d\mathcal{W}_{12,x}^{se} \quad (2.224)$$

$$dP_{1,y} = dt[-P_{1,x} \omega_{L,1} - \Gamma_1 P_{1,y} - \gamma_{12}^{se} (P_{1,y} - P_{2,y})] + \sqrt{\frac{\Gamma_1}{N_a}} d\mathcal{W}_{1,y} + \sqrt{\frac{\gamma_{12}^{se}}{N_a}} d\mathcal{W}_{12,y}^{se} \quad (2.225)$$

$$dP_{2,x} = dt[P_{2,y} \omega_{L,2} - \Gamma_2 P_{2,x} - \gamma_{21}^{se} (P_{2,x} - P_{1,x})] + \sqrt{\frac{\Gamma_2}{N_b}} d\mathcal{W}_{2,x} + \sqrt{\frac{\gamma_{21}^{se}}{N_b}} d\mathcal{W}_{21,x}^{se} \quad (2.226)$$

$$dP_{2,y} = dt[-P_{2,x} \omega_{L,2} - \Gamma_2 P_{2,y} - \gamma_{21}^{se} (P_{2,y} - P_{1,y})] + \sqrt{\frac{\Gamma_2}{N_b}} d\mathcal{W}_{2,y} + \sqrt{\frac{\gamma_{21}^{se}}{N_b}} d\mathcal{W}_{21,y}^{se} \quad (2.227)$$



This is the case of uncorrelated noise sources. We can simplify the notation by introducing the transverse component of the polarization defined as  $P_{T,j} = P_{x,j} + iP_{y,j}$  with  $j = 1, 2$ . Then we can write the system of differential equations in matrix form

$$d\mathbf{P}_T = -dt\mathbf{A}\mathbf{P}_T + B \cdot d\mathbf{W} \quad (2.228)$$

where the decay matrix is

$$A = \begin{pmatrix} \Gamma_1 + \gamma_{12}^{se} + i\omega_{L,1} & -\gamma_{12}^{se} \\ -\gamma_{21}^{se} & \Gamma_2 + \gamma_{21}^{se} + i\omega_{L,2} \end{pmatrix} \quad (2.229)$$

In the absence of noise, the coupled Bloch equations can be easily solved by diagonalizing the decay matrix  $A$ . The general solution is of the form

$$\mathbf{P}_T = c_1 e^{\lambda_+ t} \hat{\mathbf{v}}_+ + c_2 e^{\lambda_- t} \hat{\mathbf{v}}_- \quad (2.230)$$

where  $\lambda_{1,2}$  are the eigenvalues and  $\hat{\mathbf{v}}_{\pm}$  the eigenvectors of  $A$ . The matrix elements of the tables  $c_{1,2}$  can be specified by the initial conditions for the polarization. For a  $2 \times 2$  system, the eigenvalues and the eigenvectors can be expressed in terms of the determinant and the trace of the matrix  $A$ ,

$$\lambda_{\pm} = \frac{1}{2}(\text{Tr}(A) \pm \sqrt{\text{Tr}(A)^2 - 4\text{Det}(A)}) \quad (2.231)$$

$$\hat{\mathbf{v}}_{\pm} = \begin{pmatrix} -\frac{\text{Tr}(\sigma_z A) \pm \sqrt{\text{Tr}(A)^2 - 4\text{Det}(A)}}{2\gamma_{21}^{se}} \\ 1 \end{pmatrix} \quad (2.232)$$

where  $\sigma_z$  is the  $2 \times 2$  Pauli matrix.

## 2.8.2 Uncorrelated Noise Terms

In the case of uncorrelated noise we have

$$d\mathbf{W} = \begin{pmatrix} d\mathcal{W}_{1,x} \\ d\mathcal{W}_{12,x}^{se} \\ d\mathcal{W}_{1,y} \\ d\mathcal{W}_{12,y}^{se} \\ d\mathcal{W}_{2,x} \\ d\mathcal{W}_{21,x}^{se} \\ d\mathcal{W}_{2,y} \\ d\mathcal{W}_{21,y}^{se} \end{pmatrix} \quad (2.233)$$

and

$$B = \begin{pmatrix} \sqrt{\frac{\Gamma_1}{N_a}} & \sqrt{\frac{\gamma_{12}^{se}}{N_a}} & i\sqrt{\frac{\Gamma_1}{N_a}} & i\sqrt{\frac{\gamma_{12}^{se}}{N_a}} & 0 & 0 & 0 & 0 \\ 0 & 0 & 0 & 0 & \sqrt{\frac{\Gamma_2}{N_b}} & \sqrt{\frac{\gamma_{21}^{se}}{N_b}} & i\sqrt{\frac{\Gamma_2}{N_b}} & i\sqrt{\frac{\gamma_{21}^{se}}{N_b}} \end{pmatrix} \quad (2.234)$$

The equal time covariance matrix  $\sigma$  can be calculated using the complex form of



Eq.(2.216) i.e. as the unique self-adjoint solution to the matrix equation

$$A\sigma + \sigma A^\dagger = BB^\dagger \quad (2.235)$$

resulting in a  $4 \times 4$  system of linear algebraic equations

$$2(\Gamma_1 + \gamma_{12}^{se})\sigma_{11} - \gamma_{se}^{12}\sigma_{12} - \gamma_{se}^{12}\sigma_{21} = 2\left(\frac{\Gamma_1}{N_a} + \frac{\gamma_{12}^{se}}{N_a}\right) \quad (2.236)$$

$$-\gamma_{se}^{21}\sigma_{11} + (\Gamma_1 + \Gamma_2 + \gamma_{12}^{se} + \gamma_{21}^{se} - i(\omega_2 - \omega_1))\sigma_{12} - \gamma_{se}^{12}\sigma_{22} = 0 \quad (2.237)$$

$$-\gamma_{se}^{21}\sigma_{11} + (\Gamma_1 + \Gamma_2 + \gamma_{12}^{se} + \gamma_{21}^{se} + i(\omega_2 - \omega_1))\sigma_{21} - \gamma_{se}^{12}\sigma_{22} = 0 \quad (2.238)$$

$$-\gamma_{se}^{21}\sigma_{12} - \gamma_{se}^{21}\sigma_{21} + 2(\Gamma_2 + \gamma_{21}^{se})\sigma_{22} = 2\left(\frac{\Gamma_2}{N_b} + \frac{\gamma_{21}^{se}}{N_b}\right) \quad (2.239)$$

In order to obtain an analytical solution, we can make the replacements  $\Gamma_1 + \gamma_{12}^{se} \rightarrow \Gamma_1$  and  $\Gamma_2 + \gamma_{21}^{se} \rightarrow \Gamma_2$  and define  $\Delta\omega = \omega_2 - \omega_1$ . Then, the matrix elements of the covariance matrix are given by

$$\sigma_{11} = \frac{\Gamma_2(\gamma_{se}^{12})^2(\Gamma_1 + \Gamma_2)N_a + \Gamma_1 N_b [\Gamma_2(\Gamma_1 + \Gamma_2)^2 \tilde{Q} - (\Gamma_1 + \Gamma_2)\gamma_{se}^{12}\gamma_{se}^{21}]}{N_a N_b [\Gamma_1 \Gamma_2 (\Gamma_1 + \Gamma_2)^2 \tilde{Q} - (\Gamma_1 + \Gamma_2)^2 \gamma_{se}^{12}\gamma_{se}^{21}]} \quad (2.240)$$

$$\sigma_{22} = \frac{\Gamma_1(\gamma_{se}^{21})^2(\Gamma_1 + \Gamma_2)N_b + \Gamma_2 N_a [\Gamma_1(\Gamma_1 + \Gamma_2)^2 \tilde{Q} - (\Gamma_1 + \Gamma_2)\gamma_{se}^{12}\gamma_{se}^{21}]}{N_a N_b [\Gamma_1 \Gamma_2 (\Gamma_1 + \Gamma_2)^2 \tilde{Q} - (\Gamma_1 + \Gamma_2)^2 \gamma_{se}^{12}\gamma_{se}^{21}]} \quad (2.241)$$

$$\sigma_{12} = \sigma_{21}^* = \frac{(\Gamma_1 + \Gamma_2)(1 + i\frac{\Delta\omega}{\Gamma_1 + \Gamma_2})(\Gamma_1 N_a \gamma_{se}^{12} + \Gamma_2 N_b \gamma_{se}^{21})}{N_a N_b [\Gamma_1 \Gamma_2 (\Gamma_1 + \Gamma_2)^2 \tilde{Q} - (\Gamma_1 + \Gamma_2)^2 \gamma_{se}^{12}\gamma_{se}^{21}]} \quad (2.242)$$

where we have defined

$$\tilde{Q} = 1 + \left(\frac{\Delta\omega}{\Gamma_1 + \Gamma_2}\right)^2 \quad (2.243)$$

In the limiting case where cross spin-exchange is not allowed, i.e.  $\gamma_{se}^{12} = \gamma_{se}^{21} = 0$  we obtain  $\sigma_{11} = 1/N_a$ ,  $\sigma_{22} = 1/N_b$  and  $\sigma_{12} = \sigma_{21} = 0$ .

### 2.8.3 Anti-correlated Noise Terms

In the case of anti-correlated noise terms we have

$$d\mathbf{W} = \begin{pmatrix} d\mathcal{W}_{1,x} \\ d\mathcal{W}_{12,x}^{se} \\ d\mathcal{W}_{1,y} \\ d\mathcal{W}_{12,y}^{se} \\ d\mathcal{W}_{2,x} \\ d\mathcal{W}_{2,y} \end{pmatrix} \quad (2.244)$$

and

$$B = \begin{pmatrix} \sqrt{\frac{\Gamma_1}{N_a}} & \sqrt{\frac{\gamma_{12}^{se}}{N_a}} & i\sqrt{\frac{\Gamma_1}{N_a}} & i\sqrt{\frac{\gamma_{12}^{se}}{N_a}} & 0 & 0 \\ 0 & -\sqrt{\frac{\gamma_{12}^{se}}{N_a}} & 0 & -i\sqrt{\frac{\gamma_{12}^{se}}{N_a}} & \sqrt{\frac{\Gamma_2}{N_b}} & i\sqrt{\frac{\Gamma_2}{N_b}} \end{pmatrix} \quad (2.245)$$



The equal time covariance matrix  $\sigma$  can be calculated using the complex form of Eq.(2.216) i.e. as the unique self-adjoint solution to the matrix equation

$$A\sigma + \sigma A^\dagger = BB^\dagger \quad (2.246)$$

resulting in a  $4 \times 4$  system of linear algebraic equations

$$2(\Gamma_1 + \gamma_{12}^{se})\sigma_{11} - \gamma_{se}^{12}\sigma_{12} - \gamma_{se}^{12}\sigma_{21} = 2\left(\frac{\Gamma_1}{N_a} + \frac{\gamma_{12}^{se}}{N_a}\right) \quad (2.247)$$

$$-\gamma_{se}^{21}\sigma_{11} + (\Gamma_1 + \Gamma_2 + \gamma_{12}^{se} + \gamma_{21}^{se} - i(\omega_2 - \omega_1))\sigma_{12} - \gamma_{se}^{12}\sigma_{22} = -2\frac{\gamma_{12}^{se}}{N_a} \quad (2.248)$$

$$-\gamma_{se}^{21}\sigma_{11} + (\Gamma_1 + \Gamma_2 + \gamma_{12}^{se} + \gamma_{21}^{se} + i(\omega_2 - \omega_1))\sigma_{21} - \gamma_{se}^{12}\sigma_{22} = -2\frac{\gamma_{12}^{se}}{N_a} \quad (2.249)$$

$$-\gamma_{se}^{21}\sigma_{12} - \gamma_{se}^{21}\sigma_{21} + 2(\Gamma_2 + \gamma_{21}^{se})\sigma_{22} = 2\left(\frac{\Gamma_2}{N_b} + \frac{\gamma_{21}^{se}}{N_b}\right) \quad (2.250)$$

In order to obtain an analytical solution, we can make the replacements  $\Gamma_1 + \gamma_{12}^{se} \rightarrow \Gamma_1$  and  $\Gamma_2 + \gamma_{21}^{se} \rightarrow \Gamma_2$  and define  $\Delta\omega = \omega_2 - \omega_1$ . Then, the matrix elements of the covariance matrix are given by

$$\sigma_{11} = \frac{\Gamma_2(\gamma_{se}^{12})^2(\Gamma_1 + \Gamma_2)(N_a - 2N_b) + \Gamma_1 N_b [\Gamma_2(\Gamma_1 + \Gamma_2)^2 \tilde{Q} - (\Gamma_1 + \Gamma_2)\gamma_{se}^{12}\gamma_{se}^{21}]}{N_a N_b [\Gamma_1 \Gamma_2 (\Gamma_1 + \Gamma_2)^2 \tilde{Q} - (\Gamma_1 + \Gamma_2)^2 \gamma_{se}^{12}\gamma_{se}^{21}]} \quad (2.251)$$

$$\sigma_{22} = \frac{\Gamma_1(\Gamma_1 + \Gamma_2)N_b((\gamma_{se}^{21})^2 - 2\gamma_{se}^{12}\gamma_{se}^{21}) + \Gamma_2 N_a [\Gamma_1(\Gamma_1 + \Gamma_2)^2 \tilde{Q} - (\Gamma_1 + \Gamma_2)\gamma_{se}^{12}\gamma_{se}^{21}]}{N_a N_b [\Gamma_1 \Gamma_2 (\Gamma_1 + \Gamma_2)^2 \tilde{Q} - (\Gamma_1 + \Gamma_2)^2 \gamma_{se}^{12}\gamma_{se}^{21}]} \quad (2.252)$$

$$\sigma_{12} = \sigma_{21}^* = \frac{\Gamma_1 \Gamma_2 (\Gamma_1 + \Gamma_2) (1 + i\frac{\Delta\omega}{\Gamma_1 + \Gamma_2}) ((N_a - 2N_b)\gamma_{se}^{12} + N_b \gamma_{se}^{21})}{N_a N_b [\Gamma_1 \Gamma_2 (\Gamma_1 + \Gamma_2)^2 \tilde{Q} - (\Gamma_1 + \Gamma_2)^2 \gamma_{se}^{12}\gamma_{se}^{21}]} \quad (2.253)$$

where we have defined

$$\tilde{Q} = 1 + \left(\frac{\Delta\omega}{\Gamma_1 + \Gamma_2}\right)^2 \quad (2.254)$$

In the limiting case where cross spin-exchange is not allowed, i.e.  $\gamma_{se}^{12} = \gamma_{se}^{21} = 0$  we obtain  $\sigma_{11} = 1/N_a$ ,  $\sigma_{22} = 1/N_b$  and  $\sigma_{12} = \sigma_{21} = 0$ .

## 2.9 Quantum Back-action Noise - Light Shift Noise

Back-action is referred as the noise introduced by the quantum probe when interacting with the atoms resulting in a stochastic evolution of the atomic ensemble that may affect back the probe measurement. In Faraday rotation probing, the probe is the quantum light field and in that case the back action noise is also known as AC-Stark Shift or light-shift noise. Although the probe beam is linearly polarized, it will exhibit spontaneous quantum fluctuations on the degree of circular polarization. As described previously, the light-shift can be thought of as an effective magnetic field along the

propagation direction,

$$\mathbf{B}_{\text{eff}} = \frac{1}{2} a_F^v(\omega) \frac{\mathbf{E} \times \mathbf{E}^*}{i} \quad (2.255)$$

hence the quantum fluctuations in the degree of circular polarization are translated into a fluctuating effective magnetic field having a white-noise spectrum [72] which affects the spin polarization via [48]

$$d\langle F_y \rangle = \langle F_x \rangle \text{Re}[a_F^v(\omega)] \frac{4\pi^2 \nu}{cAF} \frac{dN_{ph}}{dt} \frac{1}{\sqrt{dN_{ph}}} \xi(t) dt \quad (2.256)$$

where  $\frac{1}{\sqrt{dN_{ph}}}$  is the photon shot noise fluctuations in the number of photons resulting in the polarization fluctuations, and  $\xi(t)$  is a zero-mean random Gaussian process. Light shift noise is an effect originating from shot noise since in a given time interval  $dt$  in which  $dN_{ph}$  photons have interacted with the atomic ensemble, there are shot noise fluctuations between the right and the left number circularly polarized photons resulting in a fluctuating circular polarization.

Unpolarized vapors, which are relevant to spin noise measurements, are almost insensitive to magnetic field fluctuations, hence the back-action noise is negligible and is usually ignored. On the other hand, polarized vapors relative to magnetometry are highly sensitive to magnetic field fluctuations rendering back-action noise a limitation on the efficiency of the magnetometer.

Although back-action noise is a quantum noise setting limitations on the magnetic field measurements, there have been developed experimental techniques that allow the evasion of it [12, 173–175].

Although the term back-action is referred to the AC-Stark shift, a term produced by a Hamiltonian interaction, there are situations where the term is used in a different context. For example, in [176] the term back-action is used to describe the measurement induced back-action resulting from the acquisition of information about the atomic state at the output of the polarimeter. This back-action term is not described by a Hamiltonian operator, instead it is included in the theory as an additional term in the diffusive master equation describing the atomic evolution [177]

$$d\rho_{tot}(t) = -i[H_c(t), \rho_{tot}(t)]dt + \gamma_{diss} \mathcal{D}[\rho_{tot}(t)]dt + \frac{\kappa}{4} \mathcal{L}[\rho_{tot}(t)]dt + \sqrt{\frac{\kappa}{2}} \mathcal{H}[\rho_{tot}(t)]d\nu(t) \quad (2.257)$$

where  $H_c(t)$  is an externally applied control Hamiltonian <sup>4</sup>,  $\mathcal{D}[\rho_{tot}(t)]$  is a Lindbladian decay channel while the terms  $\mathcal{L}[\rho_{tot}(t)]$  and  $\mathcal{H}[\rho_{tot}(t)]$  are related to the back-action and are defined as

$$\mathcal{L}[\rho_{tot}(t)] = J_z \rho_{tot} J_z - \frac{1}{2} J_z^2 \rho_{tot} - \frac{1}{2} \rho_{tot} J_z^2 \quad (2.258)$$

<sup>4</sup>It could in principle contain also dc terms like an external constant magnetic field.

$$\mathcal{H}[\rho_{tot}(t)] = J_z \rho_{tot} + \rho_{tot} J_z - 2Tr(\rho_{tot}(t) J_z) \rho_{tot} \quad (2.259)$$

The term  $d\nu(t)$  is called innovation process and determines the strength of the measurement back-action in a given time interval, and  $J_z = \sum_{i=1}^N j_z^{(i)}$  is the collective angular momentum operator probed by the laser beam.  $\mathcal{L}[\rho_{tot}(t)]$  is responsible for spin squeezing due to the measurement result and  $\mathcal{H}[\rho_{tot}(t)]$  is the measurement back-action term depending on the mean collective spin ensemble value, the strength of which is determined by  $d\nu(t)$ .



# Chapter 3 Spin-Exchange and Spin Relaxation Processes

---

The spin polarization of alkali-metal atoms, either optically pumped or not, can be strongly affected by a broad range of relaxation mechanisms. Such mechanisms could be for example spin-exchange collisions with other alkali-metal atoms of the same or of different species, electron spin randomization or spin-destruction collisions, collisions with buffer-gas atoms, spatial diffusion between regions with differing spin polarization or spatial diffusion in the laser beam, diffusion in the presence of magnetic field gradients and spin relaxation during adsorption on the walls[70].

In this thesis we are mostly interested in relaxation of ground-state atoms since the lifetime of an alkali-atom in the excited state is small compared to the time-scale of the dynamics studied herein. The depolarization rates of alkali-metal atoms in their ground state are so slow that relatively weak collisional interactions can have a noticeable effect on the relaxation. We suppose that the atoms are uncorrelated with each other and evolve under the influence of a common Breit-Rabi ground state Hamiltonian  $H$  as described in Chapter 2. The collisional spin interaction,  $V$ , which will have a different time history for each atom of the ensemble usually depends on the internuclear separation, and possibly on the collision velocity and the internal state of the perturbing atom or molecule.

For a single collision, the effects of the collisional interaction can be described using partial-wave scattering theory, or by a classical approach assuming that the translational motion of the atom and its collision partner follow well-defined classical paths. The classical-path approximation works well for most collision processes of importance for optical pumping or for spin-noise, with the notable exception of spin-exchange collisions between pairs of alkali-metal atoms, which are best treated with partial-wave scattering theory [68].

## 3.1 Spin-Exchange Collisions

Spin-Exchange (SE) is a dominant relaxation mechanism in optical pumping experiments with polarized and unpolarized alkali atoms. Schematically, SE collisions between atoms A and B which could be of the same or different species, are represented

by



Before the collision the spin of the first atom is up and the spin of the second atom is down. After the collision the spin of atom A is down and the spin of atom B is up. The spin orientations of the two atoms have been exchanged in a way that the total spin is preserved. During a spatial collision of the two atoms, lasting for about a few picoseconds [70], the atoms form instantly a molecule. SE-interaction emerges from the difference between the lowest singlet and the higher triplet potential energy curves of the total spin of the colliding partners, forming the molecular dyad AB. The molecular ST curves are schematically represented in Fig.3.1. The triplet potential is repulsive, while the singlet is attractive. The spin-exchange scattering potential is usually written as  $V_{se} = P_S V_S + P_T V_T$  [68]. Where  $P_S = |S\rangle\langle S|$  is the projector on the singlet state and  $P_T = \sum_j |T_j\rangle\langle T_j|$  with  $j = \pm 1, 0$  is the projector on the triplet state. Introducing the spin-exchange operator

$$P_e = P_T - P_S = \frac{1}{2}\mathbb{1} + 2 \sum_j s_j \otimes s_j \quad (3.2)$$

where  $\mathbb{1}$  is the unit operator, we can write  $V_{se}$  as a sum of a spin-independent and a spin-dependent term,  $V_{se} = V_0 + V_1 P_e$ . The former is immaterial for the spin state evolution, so the unitary operator evolving the initial into the final spin state is  $U = e^{-i \int dt V_1 P_e}$ . The time dependence of  $V_1$  is implicit in its dependence on the internuclear distance, which changes with time along the collision trajectory. Defining the phase  $\phi = \int dt V_1$  and noting that  $P_e$  satisfies the relation  $P_e^2 = \mathbb{1}$ , we find that

$$U_\phi = \cos \phi \mathbb{1} - i \sin \phi P_e \quad (3.3)$$

In the following we are going to call  $U_\phi$  unitary spin-exchange operator.

As it is evident from Fig.3.1, for an inter-nuclear distance of  $r = 6\text{\AA}$  the potential difference  $V$  between singlet and triplet energy curve is about  $V = 0.1$  eV. Therefore, during a collision of  $\tau_c = 1$  psec duration the atoms acquire a relative SE phase shift of the order of 100 rad:

$$\phi = \phi_T - \phi_S = \frac{1}{\hbar} \int_{-\infty}^{+\infty} V dt \approx \frac{1}{\hbar} V \tau_c \approx 100 \quad \text{rad} \quad (3.4)$$

In the original work on spin-exchange scattering by Purcell and Field [178] and by Dicke and Wittke [179] the colliding atoms are assumed to follow classical paths. As it was stated in these papers, the SE cross-section can be obtained by averaging the exchange probability  $\frac{1}{2}(1 - \cos \phi)$  over impact parameters  $R$ . The spins of the two atoms rotate rapidly around the resultant spin,  $\mathbf{S}_A + \mathbf{S}_B$ , which is conserved during the course of the collision [70]. The first quantum mechanical partial-wave analysis of spin-exchange

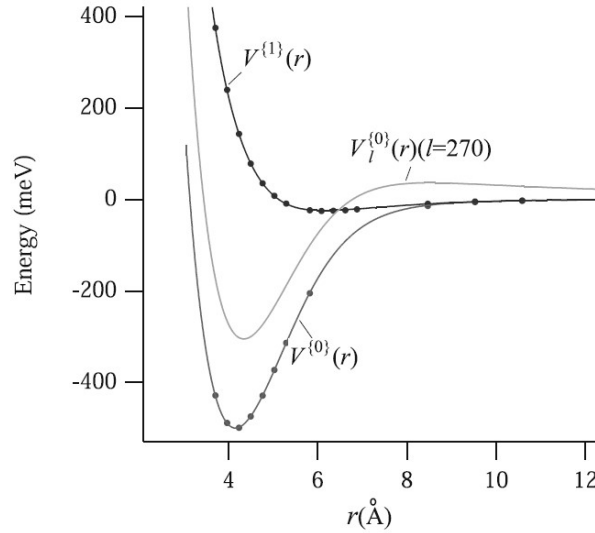


**Figure 3.1:** Taken from [68]. Typical Rb-Rb singlet and triplet potential curves as a function of internuclear distance for an alkali-atom binary collision. The potentials are much too large for a semi-classical analysis of SE interaction. Both the translational and the spin states should be treated quantum mechanically applying partial-wave scattering theory.

scattering was carried out by Dalgarno [180]. He determined the  $l$ -wave phase shifts for scattering from the singlet and triplet potentials. The spin-exchange cross section is shown to be

$$\sigma_{SE} = \frac{\pi}{k^2} \sum_{l=0}^{+\infty} (2l+1) \sin^2(\delta_l^S - \delta_l^T) \quad (3.5)$$

where  $k$  is the propagation wavevector of the incident wave and  $\delta_l^S$  and  $\delta_l^T$  are the singlet and triplet phase shifts. For a complete description of the partial wave analysis of the SE interaction, see [68]. A large amount of literature exists on the subject of SE collisions in alkali atoms including subsequent work using either classical-path theory or partial waves, here we cite a small representative sample of these publications [106–108, 181–184]. For most of the alkali atoms the spin-exchange cross section has been measured to be approximately  $\sigma_{SE} \approx 1.9 - 2.2 \times 10^{-14} \text{ cm}^2$ . Assuming that the radius of the atom is  $r = 0.5 \text{ \AA}$ , the collisional cross-section of the atom is  $\sigma_c = \pi r^2 \approx 8 \times 10^{-16} \text{ cm}^2$ , therefore it is noticed that SE-cross section is even larger than the thermal collisional cross-section, representing the probability of an atom to experience a spatial collision with another atom. We note that the time between subsequent binary collisions is given by  $T = n^{-1/3}u$  where  $u = \sqrt{\frac{8k_B T}{\pi M}}$  is the thermal relative velocity of the atoms and

$$\frac{1}{M} = \frac{1}{M_1} + \frac{1}{M_2} \quad (3.6)$$

is the reduced mass of the binary system.

It is useful to note some properties of the SE operator, like  $P_e = P_e^\dagger = P_e^{-1}$ . Moreover, there are various equivalent ways that the unitary SE operator can be represented,

for example, using the trigonometric identities

$$\sin \phi = \frac{e^{i\phi} - e^{-i\phi}}{2i} \quad (3.7)$$

$$\cos \phi = \frac{e^{i\phi} + e^{-i\phi}}{2} \quad (3.8)$$

we can write

$$U_\phi = e^{i\phi} \frac{1 - P_e}{2} + e^{-i\phi} \frac{1 + P_e}{2} = e^{i\phi} P_S + e^{-i\phi} P_T = e^{2i\phi} P_S + P_T \quad (3.9)$$

where in the last step we multiplied with a global phase  $e^{i\phi}$ .

Before analysing further the SE interaction a small parenthesis regarding notation. The dimension of the operators should be evident from the context. For example, single-atom operators, like  $\mathbf{s}$ , have dimension  $2(2I + 1)$ , where  $I$  is the atom's nuclear spin (we limit this discussion to alkali atoms used in quantum metrology with hot atomic vapors). In the tensor product space used when considering the binary collision, like the operators  $\mathbf{1}$  or  $P_e$  in Eq.(3.3), the relevant dimension is  $2(2I_a + 1)2(2I_b + 1)$ , where  $I_a$  and  $I_b$  are the nuclear spins of the first and second colliding partner, which in general could be of a different species.

### 3.1.1 Spin-1/2 Particles Without Nuclear Spin

We begin the discussion with spin-exchange collisions between spin-1/2 particles without nuclear spin. In this case, the spin operators  $\mathbf{s} = \{s_x, s_y, s_z\}$  are proportional to the  $2 \times 2$  Pauli operators

$$\sigma_x = \begin{pmatrix} 0 & 1 \\ 1 & 0 \end{pmatrix}, \quad \sigma_y = \begin{pmatrix} 0 & -i \\ i & 0 \end{pmatrix}, \quad \sigma_z = \begin{pmatrix} 1 & 0 \\ 0 & -1 \end{pmatrix} \quad (3.10)$$

The commutation relation  $[s_i, s_j] = i\epsilon_{ijk}s_k$  and the anti-commutation  $\{s_i, s_j\} = \frac{1}{2}\delta_{ij}$  when combined yield

$$s_i s_j = \frac{1}{4}\delta_{ij} + \frac{i}{2}\epsilon_{ijk}s_k \quad (3.11)$$

This is a very useful formula that is going to be used frequently in the following discussion and is always revealed in most of the derivations regarding the SE interaction. Some other properties often used are

$$\epsilon_{ijk}\epsilon_{ilm} = \delta_{jl}\delta_{km} - \delta_{jm}\delta_{kl} \quad (3.12)$$

$$\epsilon_{ijk}\epsilon_{ijm} = 2\delta_{km} \quad (3.13)$$

$$\delta_{ik}\delta_{jk} = \delta_{ij} \quad (3.14)$$

Let us examine a simple example of the spin-exchange operation. If we assume that



the state  $|0\rangle$  represents the spin up along the quantization axis and the state  $|1\rangle$  the spin down, then action of the  $P_e$  operator on pairs of such states yield

$$\begin{aligned}
 P_e|0\rangle|0\rangle &= |0\rangle|0\rangle \\
 P_e|0\rangle|1\rangle &= |1\rangle|0\rangle \\
 P_e|1\rangle|0\rangle &= |0\rangle|1\rangle \\
 P_e|1\rangle|1\rangle &= |1\rangle|1\rangle
 \end{aligned} \tag{3.15}$$

We note that  $|0\rangle|0\rangle = |0\rangle \otimes |0\rangle = |00\rangle$ . As the name suggests, spin-exchange operation exchanges the state of the two spins. If the spins are in the same state, then the exchange has no effect. Although this is the case for spin-1/2 particles, when such operation is applied to atoms including nuclear spin, even if the atoms are in the same state, spin exchange has a significant effect. In quantum information literature, the SE operator is usually encountered as the SWAP gate that swaps(exchanges) the qubit states. The unitary spin exchange operator  $U_\phi = \cos \phi \mathbb{1} - i \sin \phi P_e$  is also called partial SWAP operation. This is directly evident since for  $\phi = \pi/2$  we get the SWAP operator while for  $\phi = 0$  we get the identity matrix. For intermediate values of  $\phi$  one can think the effect of the unitary SE operator as part of the state being swapped and part of it being left unchanged. For small values of  $\phi$  the unitary SE operator is called "weak swap" operator [185]. To illustrate the effect of  $U_\phi$  let's see some examples,

$$\begin{aligned}
 U_\phi|0\rangle|0\rangle &= e^{-i\phi}|0\rangle|0\rangle \\
 U_\phi|0\rangle|1\rangle &= \cos \phi|0\rangle|1\rangle - i \sin \phi|1\rangle|0\rangle \\
 U_\phi|1\rangle|0\rangle &= \cos \phi|1\rangle|0\rangle - i \sin \phi|0\rangle|1\rangle \\
 U_\phi|1\rangle|1\rangle &= e^{-i\phi}|1\rangle|1\rangle
 \end{aligned} \tag{3.16}$$

When the two states are identical, then the final state is the same as the initial, multiplied by a global phase which is of no physical significance and can be always omitted. When the initial states are different, then the final state is an entangled state with coefficients defined by the value of  $\phi$ . For  $\phi = \pi/4$  the state is maximally entangled. This example, illustrates the main difference between the two SE operators.  $P_e$  swaps the two spin states, while  $U_\phi$  can in principle generate an entangled state between spin up and spin down. For reasons of completeness, we present also the spin exchange operators in matrix form

$$P_e = \begin{pmatrix} 1 & 0 & 0 & 0 \\ 0 & 0 & 1 & 0 \\ 0 & 1 & 0 & 0 \\ 0 & 0 & 0 & 1 \end{pmatrix} \tag{3.17}$$



$$U_\phi = \begin{pmatrix} e^{-i\phi} & 0 & 0 & 0 \\ 0 & \cos \phi & -i \sin \phi & 0 \\ 0 & -i \sin \phi & \cos \phi & 0 \\ 0 & 0 & 0 & e^{-i\phi} \end{pmatrix} \quad (3.18)$$

The most general spin state of a spin-1/2 particle is written as  $\rho = \frac{1}{2}\mathbb{1} + 2\langle \mathbf{s} \rangle \cdot \mathbf{s}$ . The expectation value ranges between  $0 \leq \langle \mathbf{s} \rangle \leq \frac{1}{2}$ . When  $\langle \mathbf{s} \rangle = \frac{1}{2}$ , the state is said to be pure and can be represented as a point on the surface of the Bloch sphere, whereas when  $\langle \mathbf{s} \rangle = 0$  the state is maximally mixed and can be compactly written as  $\rho = \frac{1}{2}\mathbb{1}$ , represented as a point at the center of the Bloch sphere. In matrix form the state reads

$$\rho = \begin{pmatrix} \frac{1}{2} + \langle s_z \rangle & \langle s_x \rangle - i\langle s_y \rangle \\ \langle s_x \rangle + i\langle s_y \rangle & \frac{1}{2} - \langle s_z \rangle \end{pmatrix} \quad (3.19)$$

We note that throughout the chapter, we will often write the inner product either as a sum of indices like  $\rho = \frac{1}{2}\mathbb{1} + 2\langle \mathbf{s} \rangle \cdot \mathbf{s} = \frac{1}{2}\mathbb{1} + 2\sum_j \langle s_j \rangle s_j$ , where  $j = x, y, z$ , or we will use the Einstein summation notation where the summation of repeated indices is assumed, like for example  $\rho = \frac{1}{2}\mathbb{1} + 2\langle \mathbf{s} \rangle \cdot \mathbf{s} = \frac{1}{2}\mathbb{1} + 2\langle s_j \rangle s_j$ . Let us calculate how these general spin-1/2 states transform under a single spin-exchange collision. Suppose that atom A is in the state  $\rho_A = \frac{1}{2}\mathbb{1} + 2\langle \mathbf{s}_A \rangle \cdot \mathbf{s}_A$  and atom B is in the state  $\rho_B = \frac{1}{2}\mathbb{1} + 2\langle \mathbf{s}_B \rangle \cdot \mathbf{s}_B$ . We first focus in the case where the two atom state is initially separable, (i.e. the two atoms share no quantum correlations). The two atom tensor product state before the SE-operation is then  $\rho_A \otimes \rho_B$  and can be expanded as

$$\begin{aligned} \rho_A \otimes \rho_B &= \left( \frac{1}{2}\mathbb{1} + 2\langle \mathbf{s}_A \rangle \cdot \mathbf{s}_A \right) \otimes \left( \frac{1}{2}\mathbb{1} + 2\langle \mathbf{s}_B \rangle \cdot \mathbf{s}_B \right) \\ &= \left( \frac{1}{2}\mathbb{1} + 2\sum_i \langle s_i^A \rangle s_i^A \right) \otimes \left( \frac{1}{2}\mathbb{1} + 2\sum_j \langle s_j^B \rangle s_j^B \right) \end{aligned} \quad (3.20)$$

Since both particles have  $s = \frac{1}{2}$  and we keep the tensor product notation, we can omit the indices A and B from the spin operators and write  $s^A = s^B = s$ . However, the indices A and B must remain on the expectation values to keep the signature of each state. The above state can then be written as

$$\rho_A \otimes \rho_B = \frac{1}{4}(\mathbb{1} \otimes \mathbb{1}) + \sum_i \langle s_i^A \rangle (s_i \otimes \mathbb{1}) + \sum_j \langle s_j^B \rangle (\mathbb{1} \otimes s_j) + 4 \sum_{i,j} \langle s_i^A \rangle \langle s_j^B \rangle (s_i \otimes s_j) \quad (3.21)$$

Note that this is the most general two-qubit state usually encountered in quantum information literature [186]. The goal is to obtain the way these states transform under SE-operations. The state of the two spins after an SE collision using the SE operator is  $\rho^e = P_e \rho_A \otimes \rho_B P_e$ . In order to make the calculation straightforward we present two

basic properties of the SE-operator

$$P_e(s_i \otimes \mathbb{1})P_e = (\mathbb{1} \otimes s_i) \quad (3.22)$$

$$P_e(s_i \otimes s_j)P_e = (s_j \otimes s_i) \quad (3.23)$$

and since  $P_e^2 = \mathbb{1}$  the opposite relations also hold

$$P_e(\mathbb{1} \otimes s_i)P_e = (s_i \otimes \mathbb{1}) \quad (3.24)$$

$$P_e(s_j \otimes s_i)P_e = (s_i \otimes s_j) \quad (3.25)$$

These relations can be easily proved using Eq.(3.2) for the SE operator and then apply Eq.(3.11). Acting with  $P_e$  on all terms of Eq.(3.21) and using the above properties we find

$$\begin{aligned} \rho^e &= \frac{1}{4}(\mathbb{1} \otimes \mathbb{1}) \\ &+ \sum_i \langle s_i^A \rangle (\mathbb{1} \otimes s_i) + \sum_j \langle s_j^B \rangle (s_j \otimes \mathbb{1}) \\ &+ 4 \sum_{i,j} \langle s_i^A \rangle \langle s_j^B \rangle (s_j \otimes s_i) \\ &= \left( \frac{1}{2} \mathbb{1} + 2 \sum_i \langle s_i^B \rangle s_i \right) \otimes \left( \frac{1}{2} \mathbb{1} + 2 \sum_j \langle s_j^A \rangle s_j \right) \\ &= \rho_B \otimes \rho_A \end{aligned} \quad (3.26)$$

We obtain that the two particles have exchanged their states after the action of the SE operator. Note also that if we trace out either the first or the second partner of the collision we get  $Tr_B\{\rho^e\} = \rho_B$  and  $Tr_A\{\rho^e\} = \rho_A$ . If we denote the total spin as  $\mathbf{s} = \mathbf{s}^A + \mathbf{s}^B$  we see that  $\langle \mathbf{s}^A \rangle + \langle \mathbf{s}^B \rangle$  is preserved before and after the collision. This spin conservation is one of the striking features of SE-collisions and holds also true for particles larger than  $s = \frac{1}{2}$ , including nuclear spin [106].

Correlated states between the two spins [187], for example a maximally entangled Bell state  $|\psi\rangle = \frac{1}{\sqrt{2}}(|01\rangle + |10\rangle)$  remain correlated after the action of  $P_e$ . This is clearly evident from Eq.(3.15). To illustrate this feature, let's start from a general two-body pure state  $|\psi\rangle = a|00\rangle + b|01\rangle + c|10\rangle + d|11\rangle$ , where  $a, b, c$  and  $d$  are complex coefficients with  $|a|^2 + |b|^2 + |c|^2 + |d|^2 = 1$ , and act on the state with  $P_e$ . The final state reads  $|\psi_e\rangle = a|00\rangle + b|10\rangle + c|01\rangle + d|11\rangle$  which is clearly still correlated.

This is a good point to examine the effects of the unitary SE operator on such pure states and then move on to its effect on the most general spin-1/2 states, discussed so far. This example will illuminate the initial statement of the Singlet-Triplet mixing of the spin state of the atoms during the collision. Starting again from the general pure state

$|\psi\rangle$  we use the transformations to the Singlet-Triplet basis given by

$$\begin{aligned} |T_+\rangle &= |00\rangle \\ |T_-\rangle &= |11\rangle \\ |T_0\rangle &= \frac{1}{\sqrt{2}}(|01\rangle + |10\rangle) \\ |S\rangle &= \frac{1}{\sqrt{2}}(|01\rangle - |10\rangle) \end{aligned} \quad (3.27)$$

The initial state can then be written in the ST basis as

$$|\psi\rangle = a|T_+\rangle + \frac{b+c}{\sqrt{2}}|T_0\rangle + \frac{b-c}{\sqrt{2}}|S\rangle + d|T_-\rangle \quad (3.28)$$

Acting with the unitary SE operator in the form  $U_\phi = e^{i\phi}P_S + e^{-i\phi}P_T$  and ignoring a common phase factor we arrive at

$$U_\phi|\psi\rangle = a|T_+\rangle + \frac{b+c}{\sqrt{2}}|T_0\rangle + e^{2i\phi}\frac{b-c}{\sqrt{2}}|S\rangle + d|T_-\rangle \quad (3.29)$$

We find that the singlet state acquired an extra phase after the collision, compared to the triplet states. It is also evident that an initially correlated state remains also correlated after the unitary exchange interaction. This is a first demonstration of the general belief that successive collisions can in principle sustain quantum correlations [83, 118].

To conclude the discussion of spin-1/2 particles and to move to the more realistic case of alkali atoms we examine the unitary SE operation on the most general states  $\rho_A = \frac{1}{2}\mathbb{1} + 2\sum_i\langle s_i^A\rangle s_i^A$  and  $\rho_B = \frac{1}{2}\mathbb{1} + 2\sum_i\langle s_i^B\rangle s_i^B$ .

$$\begin{aligned} U_\phi\rho_A \otimes \rho_B U_\phi^\dagger &= \cos^2\phi\rho_A \otimes \rho_B + \sin^2\phi P_e\rho_A \otimes \rho_B P_e \\ &\quad - \frac{i}{2}\sin 2\phi[P_e, \rho_A \otimes \rho_B] \end{aligned} \quad (3.30)$$

where  $[A, B] = AB - BA$  is the commutator. The second term of Eq.(3.30), namely,  $\sin^2\phi P_e\rho_A \otimes \rho_B P_e = \sin^2\phi\rho_B \otimes \rho_A$  has been already calculated in (3.26) hence we obtain

$$\begin{aligned} U_\phi\rho_A \otimes \rho_B U_\phi^\dagger &= \cos^2\phi\rho_A \otimes \rho_B + \sin^2\phi\rho_B \otimes \rho_A \\ &\quad - \frac{i}{2}\sin 2\phi[P_e, \rho_A \otimes \rho_B] \end{aligned} \quad (3.31)$$

Substituting the relations for  $\rho_A$  and  $\rho_B$ , the most general final state reads

$$\begin{aligned}
\rho_e &= \frac{1}{4}(\mathbf{1} \otimes \mathbf{1}) \\
&+ [\cos^2\phi\langle s_i^A \rangle + \sin^2(\phi)\langle s_i^B \rangle \\
&- \sin(2\phi)(\langle \mathbf{s}^A \rangle \times \langle \mathbf{s}^B \rangle)_i](s_i \otimes \mathbf{1}) \\
&+ [\cos^2(\phi)\langle s_j^B \rangle + \sin^2(\phi)\langle s_j^A \rangle \\
&+ \sin(2\phi)(\langle \mathbf{s}^A \rangle \times \langle \mathbf{s}^B \rangle)_j](\mathbf{1} \otimes s_j) \\
&+ [4\cos^2(\phi)\langle s_i^A \rangle\langle s_j^B \rangle + 4\sin^2(\phi)\langle s_i^B \rangle\langle s_j^A \rangle \\
&+ \epsilon_{kij}\sin(2\phi)(\langle s_k^A \rangle - \langle s_k^B \rangle)](s_i \otimes s_j)
\end{aligned} \tag{3.32}$$

Finally, for same species ( $A = B$ ) the last commutator term of Eq.(3.31) is zero and thus the unitary SE operator has no effect on identical uncorrelated spin-1/2 particles. Note that this is also obvious from Eq.(3.32) where the final state reduces to

$$\rho_e = \frac{1}{4}(\mathbf{1} \otimes \mathbf{1}) + \langle s_i \rangle(s_i \otimes \mathbf{1}) + \langle s_j \rangle(\mathbf{1} \otimes s_j) + 4\langle s_i \rangle\langle s_j \rangle(s_i \otimes s_j) \tag{3.33}$$

### 3.1.2 Spin-Exchange Properties

In this section we present some useful formulas that can greatly simplify the derivations concerning SE collisions in alkali atoms. All relations can be derived using Eq.(3.11).

$$P_e(s_i \otimes \mathbf{1}) = \frac{1}{2}(s_i \otimes \mathbf{1}) + \frac{1}{2}(\mathbf{1} \otimes s_i) + i\epsilon_{ijk}(s_j \otimes s_k) \tag{3.34}$$

$$(s_i \otimes \mathbf{1})P_e = \frac{1}{2}(s_i \otimes \mathbf{1}) + \frac{1}{2}(\mathbf{1} \otimes s_i) - i\epsilon_{ijk}(s_j \otimes s_k) \tag{3.35}$$

$$P_e(\mathbf{1} \otimes s_i) = \frac{1}{2}(s_i \otimes \mathbf{1}) + \frac{1}{2}(\mathbf{1} \otimes s_i) - i\epsilon_{ijk}(s_j \otimes s_k) \tag{3.36}$$

$$(\mathbf{1} \otimes s_i)P_e = \frac{1}{2}(s_i \otimes \mathbf{1}) + \frac{1}{2}(\mathbf{1} \otimes s_i) + i\epsilon_{ijk}(s_j \otimes s_k) \tag{3.37}$$

$$\begin{aligned}
P_e(s_i \otimes s_j) &= \left(\frac{1}{8} - \frac{1}{2} \sum_k (s_k \otimes s_k)\right)\delta_{ij} \\
&+ \frac{1}{2}((s_i \otimes s_j) - (s_j \otimes s_i)) \\
&+ \frac{i}{4}\epsilon_{ijk}(\mathbf{1} \otimes s_k) - \frac{i}{4}\epsilon_{ijk}(s_k \otimes \mathbf{1})
\end{aligned} \tag{3.38}$$

$$\begin{aligned}
(s_i \otimes s_j)P_e &= \left(\frac{1}{8} - \frac{1}{2} \sum_k (s_k \otimes s_k)\right)\delta_{ij} \\
&+ \frac{1}{2}((s_i \otimes s_j) - (s_j \otimes s_i)) \\
&- \frac{i}{4}\epsilon_{ijk}(\mathbf{1} \otimes s_k) + \frac{i}{4}\epsilon_{ijk}(s_k \otimes \mathbf{1})
\end{aligned} \tag{3.39}$$



### 3.1.3 Spin-Exchange in Alkali Atoms

Moving beyond spin-1/2 particles, the next reasonable step is to introduce a nuclear spin as a "spectator", meaning that the total atomic spin state can be written as a tensor product between the electron and the nuclear spin  $|I\rangle \otimes |S\rangle$ . We are going to call these states uncorrelated electron/nucleus states. Given an atomic state for the atom A  $|\psi_A\rangle = |I_A\rangle|S_A\rangle$  and for the atom B  $|\psi_B\rangle = |I_B\rangle|S_B\rangle$ , the SE interaction affects only the electronic spin, producing the final state  $|\psi_A^e\rangle = |I_A\rangle|S_B\rangle$  for atom A and  $|\psi_B^e\rangle = |I_B\rangle|S_A\rangle$  for atom B, respectively. To formally generalize this effect to a global class of such states we are going to touch upon the formalism of irreducible spherical tensor operators that has been extensively used in the field of atomic physics and especially in systems that angular momentum symmetry is conspicuous [70, 122]. For details see Appendix A.

The most general spin density matrix of the atom can be written as  $\rho = \phi + \Theta \cdot \mathbf{s}$ , where  $\Theta$  and  $\phi$  are purely nuclear spin operators and they can be expressed in terms of the density matrix as  $\phi = \frac{\rho}{4} + \mathbf{s} \cdot \rho \mathbf{s}$  and  $\Theta \cdot \mathbf{s} = \frac{3\rho}{4} - \mathbf{s} \cdot \rho \mathbf{s}$ . However, for uncorrelated electron/nucleus states that we are interested for the moment, it can be shown that  $\Theta = 4\phi\langle \mathbf{s} \rangle$  hence the atomic density matrix is  $\rho = \phi(1 + 4\langle \mathbf{s} \rangle \cdot \mathbf{s})$  or  $\rho = 2\phi(\frac{1}{2} + 2\langle \mathbf{s} \rangle \cdot \mathbf{s}) = \rho_I \rho_S$ . In the parenthesis we can identify the most general spin-1/2 state previously discussed. This is the most general uncorrelated state between an electron and a nucleus. In the following we calculate the effect of  $P_e$  and  $U_\phi$  on such uncorrelated states. With the Einstein summation notation the pre-collisional state reads

$$\begin{aligned}
 \rho_A \otimes \rho_B &= (\phi_A + 4\phi_A \langle s_i^A \rangle s_i) \otimes (\phi_B + 4\phi_B \langle s_j^B \rangle s_j) \\
 &= (\phi_A \otimes \phi_B) \\
 &\quad + (\phi_A \otimes 4\phi_B \langle s_j^B \rangle s_j) \\
 &\quad + (4\phi_A \langle s_i^A \rangle s_i \otimes \phi_B) \\
 &\quad + (4\phi_A \langle s_i^A \rangle s_i \otimes 4\phi_B \langle s_j^B \rangle s_j)
 \end{aligned} \tag{3.40}$$

while the post-collisional state reads

$$\begin{aligned}
 P_e \rho_A \otimes \rho_B P_e &= (\phi_A \otimes \phi_B) \\
 &\quad + (\phi_A s_j \otimes 4\phi_B \langle s_j^B \rangle) \\
 &\quad + (4\phi_A \langle s_i^A \rangle \otimes \phi_B s_i) \\
 &\quad + (4\phi_A \langle s_i^A \rangle s_j \otimes 4\phi_B \langle s_j^B \rangle s_i)
 \end{aligned} \tag{3.41}$$

The term  $4\langle s^{A,B} \rangle$  is a constant and can be transferred from one atomic Hilbert space to



the other resulting in

$$\begin{aligned}
P_e \rho_A \otimes \rho_B P_e &= (\phi_A \otimes \phi_B) \\
&+ (4\phi_A \langle s_j^B \rangle s_j \otimes \phi_B) \\
&+ (\phi_A \otimes 4\phi_B \langle s_i^A \rangle s_i) \\
&+ (4\phi_A \langle s_j^B \rangle s_j \otimes 4\phi_B \langle s_i^A \rangle s_i) \\
&= (\phi_A + 4\phi_A \langle s_i^B \rangle s_i) \otimes (\phi_B + 4\phi_B \langle s_j^A \rangle s_j)
\end{aligned} \tag{3.42}$$

It is evident that the electronic parts of the wavefunction have been exchanged while the nuclear remain unaffected. In the case of same species (same atom  $A = B$ ) we obtain

$$P_e \rho_A \otimes \rho_A P_e = \rho_A \otimes \rho_A \tag{3.43}$$

Moving to the case of the unitary SE interaction, we have shown that

$$\begin{aligned}
U_\phi \rho_A \otimes \rho_B U_\phi^\dagger &= \cos^2 \phi \rho_A \otimes \rho_B + \sin^2 \phi P_e \rho_A \otimes \rho_B P_e \\
&- \frac{i}{2} \sin 2\phi [P_e, \rho_A \otimes \rho_B]
\end{aligned} \tag{3.44}$$

Replacing in the above relation the most general density matrix is of no particular interest since the final state written in that way has no significant physical interpretation. However, in the special case of same species  $\rho_B = \rho_A$  following the idea from spin-1/2 particles one can prove that last commutator term of Eq.(3.44) is equal to zero, hence we conclude that uncorrelated electron/nuclear states are also invariant under SE collisions as is exactly the case for spin-1/2 particles. This is expected since in that case the nucleus does not take part in the SE interaction.

The change in the atomic density matrix  $\delta\rho$  due to a SE collision is defined as  $\delta\rho = U_\phi \rho U_\phi^\dagger - \rho$  where  $\rho = \rho_A \otimes \rho_B$  is the initial uncorrelated density matrix [188]. From Eq.(3.44) it is straightforward that

$$\delta\rho = \sin^2 \phi (P_e \rho P_e - \rho) - \frac{i}{2} \sin 2\phi [P_e, \rho] \tag{3.45}$$

Using the SE-operator properties  $P_e^\dagger P_e = P_e^2 = \mathbb{1}$  the change in the density matrix can equivalently be written as

$$\begin{aligned}
\delta\rho &= \sin^2 \phi (P_e \rho P_e - \frac{1}{2} P_e^\dagger P_e \rho - \frac{1}{2} \rho P_e^\dagger P_e) \\
&- \frac{i}{2} \sin 2\phi [P_e, \rho]
\end{aligned} \tag{3.46}$$

which is of the known Lindblad form:

$$\delta\rho = -i[H, \rho] + \sum_j \gamma_j (L_j \rho L_j^\dagger - \frac{1}{2} L_j^\dagger L_j \rho - \frac{1}{2} \rho L_j^\dagger L_j) \tag{3.47}$$

Finally, we can allow also for states where the electronic spin is correlated with the nucleus. The most significant representative of such states are the  $|Fm\rangle$  states that arise naturally in hot/cold atomic vapors due to the hyperfine interaction  $H = A\mathbf{I} \cdot \mathbf{s}$ .

To identify these states as electron/nucleus correlated states one has to expand the state in the so called uncoupled basis [50, 126] and it should be obvious from there that this is an entangled state between the electron and the nucleus. The most general separable, otherwise electron-nucleus correlated two atom state is

$$\begin{aligned}\rho_A \otimes \rho_B &= (\phi_A + \Theta_i^A s_i) \otimes (\phi_B + \Theta_j^B s_j) \\ &= (\phi_A \otimes \phi_B) + (\phi_A \otimes \Theta_j^B s_j) + (\Theta_i^A s_i \otimes \phi_B) + (\Theta_i^A s_i \otimes \Theta_j^B s_j)\end{aligned}\quad (3.48)$$

while the post-collisional state reads

$$P_e \rho_A \otimes \rho_B P_e = (\phi_A \otimes \phi_B) + (\phi_A s_j \otimes \Theta_j^B) + (\Theta_i^A \otimes \phi_B s_i) + (\Theta_i^A s_j \otimes \Theta_j^B s_i) \quad (3.49)$$

For same species the pre-collisional state is

$$\begin{aligned}\rho_A \otimes \rho_A &= (\phi_A + \Theta_i^A s_i) \otimes (\phi_A + \Theta_j^A s_j) \\ &= (\phi_A \otimes \phi_A) + (\phi_A \otimes \Theta_j^A s_j) + (\Theta_i^A s_i \otimes \phi_A) + (\Theta_i^A s_i \otimes \Theta_j^A s_j)\end{aligned}\quad (3.50)$$

and the post-collisional state reads

$$P_e \rho_A \otimes \rho_A P_e = (\phi_A \otimes \phi_A) + (\phi_A s_j \otimes \Theta_j^A) + (\Theta_i^A \otimes \phi_A s_i) + (\Theta_i^A s_j \otimes \Theta_j^A s_i) \quad (3.51)$$

The form of the post-collisional state is clearly different than the one obtained in the case of uncorrelated electron-nucleus or in the case of spin-1/2 atoms. Interestingly, this is a first demonstration so far in the thesis that the coupling of the nucleus with the electron affects the results of the SE. Moving to the master equation of the SE interaction we are going to discover that a hyperfine Hamiltonian creating electron-nucleus correlations and spin-exchange collisions simultaneously lead to spin dephasing and relaxation in alkali atoms[189, 190].

### 3.1.4 Spin-Exchange Master Equation

A formal derivation of SE-master equation for single species and dual species using partial-wave analysis has been described in [68]. Originally the same master equation has been introduced by [188, 191] following a phenomenological treatment. Here we briefly outline the standard derivation of the single-atom density matrix evolution driven by SE collisions. The mean time between two successive spin-exchange collisions is denoted as  $T_{se}$ . The probability of a single atom to experience an SE collision in a time interval  $dt \ll T_{se}$  is  $dt/T_{se}$ . Then, the two-atom density matrix after the collision is described by

$$\rho(t + dt) = \frac{dt}{T_{se}} P_e \rho(t) P_e + \left(1 - \frac{dt}{T_{se}}\right) \rho(t) \quad (3.52)$$

or

$$\frac{d\rho(t)}{dt} = -\frac{1}{T_{se}} (\rho(t) - P_e \rho(t) P_e) \quad (3.53)$$



That is, with probability  $dt/T_{se}$  the two-atom density matrix is  $P_e\rho(t)P_e$  and with probability  $1 - dt/T_{se}$  the density matrix remains in the pre-collisional state. The crucial next step in the standard treatment of SE relaxation from the single-atom perspective is to trace out atom B and using  $\rho'_a = Tr_B\{\rho\}$  we obtain,

$$\frac{d\rho_a(t)}{dt} = -\frac{1}{T_{se}}(\rho_a(t) - Tr_B\{P_e\rho(t)P_e\}) \quad (3.54)$$

This is the master equation for spin-exchange as it was demonstrated for example by [188, 192]. A similar master equation can be written also for the unitary spin exchange operator by replacing  $P_e$  by  $U_\phi$ .

$$\frac{d\rho_a(t)}{dt} = -\frac{1}{T}(\rho_a(t) - Tr_B\{U_\phi\rho(t)U_\phi^\dagger\}) \quad (3.55)$$

The later equation has been introduced in [172, 189]. Both equations are similar regarding the spin-relaxation part<sup>1</sup>, however the second equation contains also a Hermitian Hamiltonian-like term which is frequently encountered as the spin-exchange phase shift [70]. Eq.(3.55) can be found also in the form [189]

$$\frac{d\rho_a(t)}{dt} = -\frac{1}{T_{se}}(\rho_a - \rho_a^e) + \frac{2iK}{T_{se}}[\mathbf{s}^A \cdot \langle \mathbf{s}^B \rangle, \rho_a] \quad (3.56)$$

where  $K$  is a small compared to  $T_{se}$  numerical coefficient and moreover the last term is the effective Hamiltonian term describing the SE-frequency shift. This term can be thought as an effective magnetic field (Zeeman term) whose magnitude is proportional to the mean value of the spin of the second collisional partner. It can be shown that only states with electron/nucleus correlation can exhibit such a frequency shift<sup>2</sup>, therefore the existence of the shift works somehow as an indicator or as a signature of electron-nucleus correlations [118]. The term  $\rho_a^e$  is identified as  $\rho_a^e = Tr_B\{P_e\rho(t)P_e\}$ . Note that using the previous section it is straightforward to calculate the action of  $P_e$  on any possible state. Expanding the spin-exchange operator  $P_e$  in terms of the spin matrices, we obtain another form of the SE master equation

$$\begin{aligned} \frac{d\rho_a(t)}{dt} = & -\frac{1}{T_{se}}\left[-\frac{3}{4}\rho_a + \mathbf{s}^A \cdot \rho_a \mathbf{s}^A + \langle \mathbf{s}^B \rangle \cdot \rho_a \mathbf{s}^A + \rho_a \mathbf{s}^A \cdot \langle \mathbf{s}^B \rangle \right. \\ & \left. - 2i\langle \mathbf{s}^B \rangle \cdot (\mathbf{s}^A \times \rho_a \mathbf{s}^A) - i[\delta\omega \cdot \mathbf{s}^A, \rho_a] \right] \end{aligned} \quad (3.57)$$

If the species B is unpolarized i.e.  $\langle \mathbf{s}^B \rangle = 0$  then the SE master equation becomes identical to the equation for electron spin randomization. This is described in more detail in Chapter 5. The frequency shift can be safely ignored, therefore the time

<sup>1</sup>In fact, spin-relaxation part only exists when at least a hyperfine Hamiltonian is present which is always the case in real experimental conditions.

<sup>2</sup>For example, stretched states being uncorrelated electron-nucleus states cannot exhibit SE-frequency shift.

evolution of the mean value of the spin is given by

$$\frac{d\langle \mathbf{s}^A \rangle}{dt} = \frac{1}{T_{se}} (\langle \mathbf{s}^B \rangle - \langle \mathbf{s}^A \rangle) \quad (3.58)$$

indicating the spin transfer from one species to the other. The steady state of this process is readily shown to be  $\langle \mathbf{s}^A \rangle = \langle \mathbf{s}^B \rangle$ .

### 3.1.5 Spin-Temperature Distribution

In the case where spin-exchange collisions dominate the relaxation dynamics (this is usually the case because the spin-exchange cross-section greatly exceeds the cross-sections of the other relaxation processes, owing to the large mentioned splitting between singlet and triplet molecular states) there are rapid spin-exchange collisions between alkali-alkali atoms, especially when the number density of the vapor is large. In this case, the SE master equation Eq.(3.55) reaches rapidly the steady state solution<sup>3</sup> being the so-called spin-temperature distribution

$$\rho_{ST} = \frac{e^{\beta F_z}}{Z} = \frac{e^{\beta I_z} e^{\beta S_z}}{Z_s Z_t} \quad (3.59)$$

where  $\beta$  is called spin-temperature and is related to the spin-polarization  $P_s$  via

$$\beta = \ln\left(\frac{1 + P_s}{1 - P_s}\right) \quad (3.60)$$

or equivalently [130]

$$P_s = 2\langle S_z \rangle = \tanh \frac{\beta}{2} \quad (3.61)$$

and  $Z = Z_s Z_t$  is the partition function of the distribution. In the above we have assumed that the spin polarization points only along the z-direction. For a spin of integer or half-integer quantum number  $J$  the partition function is written as

$$Z_J = \sum_{m=-J}^J e^{m\beta} = \frac{\sinh(\beta[J]/2)}{\sinh(\beta/2)} \quad (3.62)$$

For spin-1/2 atoms the spin temperature distribution can be also written as [189]

$$\rho_{ST} = \phi(1 + 4\langle S_z \rangle S_z) \quad (3.63)$$

As we have described, the above equation is a steady state solution to the spin-exchange master equation therefore we conclude that this state is invariant under SE-collisions.

## 3.2 Transit-Time Broadening

In the absence of buffer gas, atoms move ballistically inside the vapor cell resulting in a transient effect which lead to the broadening of the magnetic resonance line. This

<sup>3</sup>This is also true in the case of an additional Hamiltonian term in the master equation.



effect is known as transit-time broadening [121]. Assuming that the atoms move with mean velocity  $\vec{u} = u\hat{x}$  and they cross a laser beam propagating along the z axis, with beam diameter  $2w$ , the time an atom stays in the beam is given by  $\Delta t = \frac{2w}{u}$ . In that situation, the spin precession can be monitored only for a limited amount of time, resulting in a loss of information about the spin state, which can be thought as a dephasing mechanism leading to an effective broadening. According to the uncertainty condition this broadening is

$$\Delta\nu\Delta t \approx \frac{1}{2\pi} \quad (3.64)$$

Therefore,

$$\Delta\nu \approx \frac{u}{4\pi w} \quad (3.65)$$

This effect can be of no importance in a vapor cell which is coated with anti-relaxation coating, since atoms are not losing phase coherence as they collide to the walls. For a laser beam diameter of  $2w = 1\text{mm}$  and  $u = 2 \times 10^4 \text{ cm/s}$ , the transit time broadening is  $\Delta\nu \approx 30 \text{ kHz}$ .

### 3.3 Relaxation due to Wall Collisions

Upon striking the wall surface of a glass cell, there is a certain probability that the atom will not rebound but it may stay for a short but otherwise considerable amount of time absorbed in the surface of the wall. In that time the atom will acquire enough energy due to thermal agitation until it shakes loose from the wall. This thermal motion of the atom on the wall surface causes the local electric and magnetic fields produced from the molecules of the surface to fluctuate randomly resulting in complete depolarization of the atom. When the atom breaks loose from the wall, it may fly undisturbed through the cell if no buffer gas is present and if the alkali vapor pressure is low enough. Under these conditions, relaxation occurs only during those periods of time when the atom is stuck to the walls [70]. The average time of flight from wall to wall for a cell with linear dimension  $l = 5 \text{ cm}$  is

$$\tau = l/u \approx 10^{-4} \text{ sec} \quad (3.66)$$

which results in a broadening of the magnetic resonance line of  $\Delta\nu = \frac{1}{2\pi\tau} \approx 1.5 \text{ kHz}$ . The average thermal velocity of an alkali atom of mass  $m$  is

$$u = \sqrt{\frac{8k_B T}{\pi m}} \quad (3.67)$$

Wall relaxation can be suppressed by introducing a buffer gas in the vapor cell. Alkali atoms experience collisions with the buffer gas atoms resulting in an increase



of the wall relaxation time. Usual buffer gas pressures range from 100 up to 1000 Torr. In the presence of buffer gas the wall relaxation time can be found by solving the diffusion equation for the spin polarization along the vapor cell expressed by the function  $P(x, y, z, t)$

$$\frac{\partial P}{\partial t} = D\nabla^2 P \quad (3.68)$$

given the specific geometry of the cell and boundary conditions that destroy the spin polarization on the wall surface [72].  $D = \frac{1}{3}Lu$  is the diffusion constant and  $L$  is the mean free path of alkali atoms due to collisions with the buffer gas. The diffusion constant as a function of the buffer gas pressure is given by [50]

$$D = D_0 \frac{p_0}{p} = D_0 \frac{760 \text{Torr}}{p} \quad (3.69)$$

and  $D_0$  is the value of the diffusion constant calculated at STP conditions. The diffusion constant is usually expressed in units of  $cm^2/s$ . Solving the diffusion equation for a cylindrical or a spherical vapor cell it can be shown that the wall relaxation rates are given by [68]

$$\frac{1}{T_{\text{wall}}} = D \left( \frac{\pi^2}{l^2} + \frac{2.405^2}{r^2} \right) \quad \text{Cylindrical Cell of length } l \text{ and radius } r \quad (3.70)$$

$$\frac{1}{T_{\text{wall}}} = D \left( \frac{\pi}{r} \right)^2 \quad \text{Spherical cell of radius } r \quad (3.71)$$

Although the existence of buffer gas in the cell reduces the wall relaxation, on the other hand it enhances the amount of spin-destructive collisions and an optimization over the to processes is usually required.

A second way to suppress wall relaxation is to make use of anti-relaxation coated cells. The anti-relaxation coating consists of molecules that do not affect the spin-state of alkali atoms and prevent them from reaching the wall surface of the cell. A well-coated cell allows the atom to bounce more than a thousand times without losing its polarization. Although anti-relaxation coating is a well-developed and used method, it can be only applied at low temperatures (lower than  $80^\circ$ ) since molecular coatings like parafin-coating usually melt at higher temperatures. Recent advances in the development of anti-relaxation cells allow the operation at higher temperatures [50].

### 3.4 Relaxation due to Magnetic Field Inhomogeneities

Magnetic field inhomogeneities or magnetic field gradients can be in many situations a main source of decoherence for alkali metal atoms and its analysis can be fairly complicated since it depends on many parameters such as the cell geometry, the gradient strength, the diffusion constant and the boundary conditions at the walls of the cell.



The existence of a magnetic field gradient causes atoms at different parts of the cell to experience different Larmor frequencies leading to an average dephasing of the total spin. The analysis that we are going to follow is a review of the Problem 2.8 of [121] which contains all the physical essence stemming from the seminal theoretical papers such as [193, 194]. For a comprehensive review of the physics behind the gradient relaxation the reader may consult [50].

Suppose a buffer-gas-free spherical cell of radius  $R$ , where the atoms can freely fly around with velocity  $u$ . For simplicity we ignore the wall relaxation, we assume that the polarization is conserved upon many collisions of the atom on the cell walls which is the case of an anti-relaxation coated cell for example. To begin with, suppose that the cell is in a uniform field  $\mathbf{B}_0$  and that the gradients correspond to components of the magnetic field perpendicular to  $\mathbf{B}_0$  with r.m.s value  $\Delta B \ll B_0$ . When the Larmor frequency  $\Omega_L = \gamma B_0$  is much larger than the rate of wall collisions  $\Omega_L \frac{R}{u} \gg 1$  the atomic polarization follows adiabatically the direction of the total magnetic field given by

$$B_{\text{tot}} = \sqrt{B_0^2 + \Delta B^2} \approx B_0 \left(1 + \frac{\Delta B^2}{2B_0^2}\right) \quad (3.72)$$

From the frame moving with the atom whose  $z$ -axis is aligned with the instantaneous field  $\mathbf{B}_{\text{tot}}$ , the field seems to rotate at an angular frequency  $\omega = \theta\tau \approx \frac{\Delta B}{B_0} \frac{u}{R}$ . Thus the atom experiences an instantaneous field  $\mathbf{B}_{\text{tot}} - \mathbf{B}_f$  where  $\mathbf{B}_f = \vec{\omega}/\gamma$  is a fictitious field. Since wall collisions change the velocity of the atom in a stochastic manner, the fictitious field experiences jumps both in magnitude and direction. Then assuming that the spin acquires random phase in each successive wall collision, the phase follows a random walk with step  $(\frac{\Delta B}{\gamma B_0^2} \frac{u}{R})^2$  and the longitudinal spin relaxation is given by

$$\frac{1}{T_1} \approx \left(\frac{\Delta B}{\gamma B_0^2} \frac{u}{R}\right)^2 \frac{u}{R} \approx \frac{\gamma^2 (|\nabla B_x|^2 + |\nabla B_y|^2)}{\Omega_L^4} \left(\frac{u^3}{R}\right) \quad (3.73)$$

On the other hand, when the period of Larmor precession is much larger than the time between collisions, the atom is unable to adiabatically follow the local magnetic field. In that case the atoms fly freely throughout the cell and the field they see is averaged over the volume of the cell leading to a suppression of the gradient effects. In this case the longitudinal relaxation rate is given by

$$\frac{1}{T_1} \approx \frac{R}{u} (\gamma \Delta B)^2 \quad (3.74)$$

In the presence of a dense buffer gas, the atoms collide many times with buffer gas atoms thus their velocity changes are now more frequent and happen on the spatial scale of the mean free path  $l$ . The scale of variation of the transverse magnetic field components for a spatial extent on the order of  $l$  is  $\Delta B l / u \approx \vec{\nabla} \cdot \vec{B} l$ . Similar relations



for the longitudinal relaxation hold in the case of diffusion limited motion

$$\frac{1}{T_1} \approx \frac{\gamma^2(|\nabla B_x|^2 + |\nabla B_y|^2)}{\Omega_L^4} \left(\frac{u^3}{l}\right) \quad \Omega_L l/u \gg 1 \quad (3.75)$$

$$\frac{1}{T_1} \approx \frac{l^3}{u} (\gamma \vec{\nabla} \cdot \vec{B})^2 \quad \Omega_L l/u \ll 1 \quad (3.76)$$

The theory of the transverse spin relaxation due to magnetic field inhomogeneities is much more complicated and can be found in [194]. However for a spherical cell of radius  $R$ , in the high pressure regime the transverse spin relaxation is

$$\frac{1}{T_2} \approx \frac{8R^4 \gamma |\nabla B_z|^2}{175D} \quad (3.77)$$

### 3.5 Radiation Trapping and Quenching

Absorption of light can depolarize the precessing spins in the ground state of alkali atoms because it stochastically interrupts the Larmor precession by exciting the atom [195]. This absorption leads to power broadening of the magnetic resonance line [196] even if the absorption rate or the pumping rate are largely suppressed by a large detuning. Additionally, spontaneous emission from the atoms in the optical excited state can cause relaxation to the ground state precessing spins because they can be resonantly re-absorbed by the vapor in equilibrium. This effect is called radiation trapping and can be a significant source of depolarization, especially in a high density vapor.

Adding a buffer gas in the vapor cell can significantly reduced the spontaneous emission rate by quenching the excited atoms. A molecular buffer gas can absorb the excitation energy of the alkali atom and channel it to the molecular vibrational and rotational degrees of freedom. The photons/phonons produced by these molecular excitations are not resonant with the atomic transition therefore the probability of spontaneous decay is highly suppressed. Values of the quenching cross-sections can be found in [50] with the Nitrogen buffer gas ( $N_2$ ) having the largest quenching efficiency. As discussed in [50] the probability of an excited atom to exhibit quenching decay is given by the quenching rate

$$R_q = n_q \sigma_q \nu \quad (3.78)$$

where  $n_q$  is the density of quenching gas molecules,  $\sigma_q$  is the quenching cross-section, and  $\nu$  is the relative velocity between an alkali atom and a quenching molecule.

The quenching factor  $Q$  expresses the probability that an excited atom decays via spontaneous emission rather than quenching and is given by the ratio of the quenching



rate and the spontaneous emission rate [50]

$$Q = \frac{1}{1 + R_q \tau} \quad (3.79)$$

where  $\tau$  is the natural lifetime of the alkali atom being of the order of a few nanoseconds.

### 3.6 Complete Density Matrix Evolution

For reason of completeness and to get an insight about the whole range of relaxation processes that affect the ground state of alkali atoms we quote the dynamics of the ground state density matrix of an alkali vapor driven by the most important relaxation mechanisms. The interested reader may consult [108].

$$\begin{aligned} \frac{\partial \rho}{\partial t} = & -\frac{i}{\hbar} [A\mathbf{I} \cdot \mathbf{S} + g_s \mu_B \mathbf{S} \cdot \mathbf{B}, \rho] - \frac{i}{\hbar} [\delta E_{op} + \delta E_{SE} + \delta E_{KS}, \rho] \\ & + \frac{1}{T_{SE}} [\phi(1 + 4\langle \mathbf{S} \rangle \cdot \mathbf{S}) - \rho] + \frac{1}{T_{KS}} [\phi(1 + 4\langle \mathbf{K} \rangle \cdot \mathbf{S}) - \rho] \\ & + R[\phi(1 + 2\mathbf{s} \cdot \mathbf{S}) - \rho] + \frac{1}{T_{SD}} (\phi - \rho) - \Gamma_d (\rho - \frac{1}{d} \mathbf{1}) + D \nabla^2 \rho \end{aligned} \quad (3.80)$$

The first line contains unitary evolution due to hyperfine Hamiltonian and an evolution in a longitudinal stationary magnetic field and also frequency shifts due to optical pumping, spin-exchange and collisions with the buffer-gas atoms. The second line describes relaxation due to spin-exchange collisions and relaxation of the alkali atom due to collisions with the buffer-gas atoms and finally the third line contains the effect of optical pumping, the effect of spin-destruction collisions, wall collisions that completely depolarize the state and spatial diffusion of the atoms in the vapor cell.

# Chapter 4 Spin-Noise Cross-Correlations

## Experiment

---

### 4.1 Introduction

Chapter 4 is devoted to the experimental study of dual species spin-noise correlations in a hot vapor cell. In particular, we observe non-zero spin-noise correlations and coherence transfer effects in equilibrium between overlapping  $^{133}\text{Cs}$  and  $^{87}\text{Rb}$  spin ensembles, having naturally different gyromagnetic ratios. Both observations stem from the spontaneous and incessant spin-exchange collisions that tend to couple the two atomic species through the coherent exchange of spin-polarization.

Understanding of spin-noise exchange and spin-noise correlation dynamics in dual-species hot alkali vapors may advance the operation of atomic devices like for example atomic magnetometers and atomic gradiometers and it may also contribute to the development of new quantum protocols and new quantum enhanced devices. The experimental setup for measuring equilibrium spin-noise correlations is illustrated in Fig.4.1.

Two linearly polarized probe beams, blue detuned by  $\Delta_{Cs} = 61$  GHz from the  $^{133}\text{Cs}$   $D_2$  line and  $\Delta_{Rb} = 58$  GHz from the  $^{87}\text{Rb}$   $D_2$  line, respectively, are spatially overlapped by an optical fiber (APC-single mode, polarization maintaining). Both laser beams, after being overlapped using a 50:50 beam splitter, they enter the optical fiber with parallel to each other and parallel with the fast fiber axis, polarization directions. The overlapped beam transverse a cylindrical glass-blown vapor cell containing a mixture of hot  $^{133}\text{Cs}$  -  $^{87}\text{Rb}$  vapors and 329 Torr of  $N_2$  buffer gas, which is housed in a well-insulated oven placed inside a four layer mu-metal magnetic shield. The shield provides a shielding factor of approximately  $10^4$ . The length of the cell is 5 cm and the diameter is half an inch.

The interior of the shield is equipped with cylindrical Helmholtz coils that are penetrated by constant or alternating currents, produced by a low-noise current source. A degaussing process is frequently applied to the shield to eliminate any residual magnetization that might have induced to the shielded ferromagnetic materials.

A static magnetic field along the  $\hat{x}$ -direction causes the randomized spins of both vapors to precess at the Larmor frequency. The two overlapping species have naturally

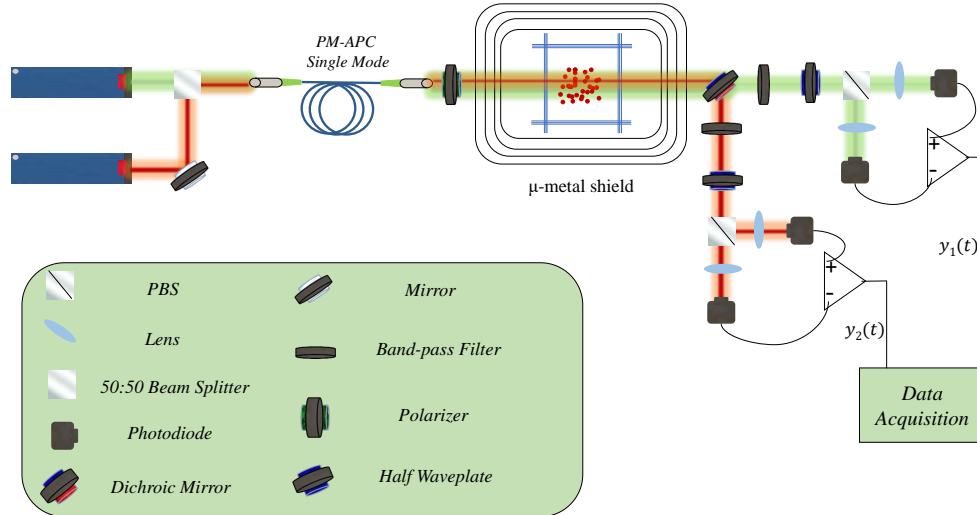


**Figure 4.1:** Experimental Principle. Two linearly polarized probe beams, blue detuned by  $\Delta_{Cs} = 61$  GHz from the  $^{133}\text{Cs}$   $D_2$  line and  $\Delta_{Rb} = 58$  GHz from the  $^{87}\text{Rb}$   $D_2$  line, respectively, are spatially overlapped by an optical fiber (APC-single mode, polarization maintaining). The overlapped beam transverse a glass cell containing a mixture of hot  $^{133}\text{Cs}$  -  $^{87}\text{Rb}$  vapors and 329 Torr of  $N_2$  buffer gas, which is housed in a well-insulated oven placed inside a four layer magnetic shield. A static magnetic field along the  $\hat{x}$ -direction causes the randomized spins to precess at the Larmor frequency. The transmitted light is splitted by a shortpass dichroic mirror with cut-off wavelength at 805 nm and each beam is detected with a shot-noise-limited polarimeter (a Wollaston prism plus a differential photo-detector). The output of each polarimeter indicates  $F_z$ , the projection of the collective spin  $F$  on the probe direction, plus optical photon shot noise. Correlations between the two signals are imprinted on the cross-correlation spectrum, revealing information about random collisional correlated-dynamics of the two atomic species.

different gyromagnetic ratios and the distance of the Larmor peaks in the Zeeman spin-noise spectrum depends on the magnitude of the dc magnetic field. A large overlap of the spin-noise resonances correspond to a large amplitude of the spin noise correlation manifesting itself as an oscillation at the cross-correlation at low magnetic fields.

The transmitted light is splitted again by a shortpass dichroic mirror with cut-off wavelength at 805 nm and each beam is detected with a shot-noise-limited balanced polarimeter consisting of a half-waveplate, a Wollaston PBS prism and a differential photo-detector. The light is focused at the photodetection area using plano-convex lenses. The output of each polarimeter indicates  $F_z$ , the projection of the collective atomic spin  $F$  on the probe direction, plus optical photon shot noise. Correlations between the two signals are imprinted on the cross-correlation spectrum, revealing information about random collisional correlated-dynamics of the two atomic species.

In the following we present a detailed analysis of the performed experiment but also a detailed description of the appropriate equipment used for optimal detection of the spin-exchange driven spontaneous spin-noise correlations.

## 4.2 Photodetectors

The measurements of light intensity in the experiment have been performed using various photodetectors depending on the nature of the measurement. The balanced polarimetry photodetection has been performed using Thorlabs PDB210A/M balanced amplified photodetectors, absorption and Faraday rotation measurements have been performed using Thorlabs PDA36A-Si switchable gain detectors and finally Thorlabs DET110-high speed Si detectors were used in simple generic- purposes quick detection. The modes of operation of the aforementioned photodetectors can be divided into two different categories.

In photovoltaic mode (PV), when light falls on the semiconductor material of the photodiode, it can excite electrons to a higher energy state. Due to this, electrons become mobile and leave behind holes. Next, the electrons move toward the cathode terminal of the photodiode and holes move toward the anode terminal. This charge movement creates voltage between the two terminals. This happens even in the absence of visible light. The tiny amount of current produced without visible light is known as dark current. It is also called zero-bias mode.

In photoconductive mode (PC), when light falls on the photodetection area, it creates pairs of electrons and holes in the semiconductor material. These move toward opposite directions due to an applied bias voltage. As a result small current flows through the photodiode. Photoconductive mode delivers fast response compared to photovoltaic mode. This is due to wider depletion layer and reduction of the capacitance which is a result of the applied reverse bias voltage. Sometimes, it is also called reverse bias mode.

The most simple photodetection scheme is the one that DET110 photodiodes implement. The output voltage is proportional to the incident light power and to the input resistance of the acquisition device, like an oscilloscope for example, a spectrum analyzer or a DAQ board. These devices usually have an input resistance of  $R_{LOAD} \approx 1M\Omega$ . The responsivity  $r(\lambda)$  of the detector has units of [r]= mA/mW and is a linear relation factor between the incident laser power and the photocurrent produced at the output of the photodetector. The responsivity is related to the quantum efficiency  $\eta$  of the detector through the relationship  $r(\lambda) = \eta \frac{qe}{E_{ph}}$ . The quantum efficiency represents the amount of photons that are transformed into electrons

$$V_{out} = r(\lambda)PR_{LOAD} \quad (4.1)$$

The bandwidth  $f_{bw}$  is determined by the diode capacitance  $C_j$  and the load resistance



$R_{LOAD}$  and is given by

$$f_{bw} = 1/(2\pi R_{LOAD} C_j) \quad (4.2)$$

The amplified photodetectors (PDA36A) have a wavelength range from 350 nm to 1100 nm and an output voltage range of 0-10 Volts. For output voltage higher than 10 Volts the photodiode is saturated. These photodetectors contain a transimpedance gain control which amplifies the voltage output from 0 dB up to 70dB with steps of 10 dB. The transimpedance gain (G) has units of resistance, namely  $[G]=V/A$ . Note that increasing the gain, decreases the bandwidth of photodetection.

For maximum performance and in order to avoid reflections of the signal during the transmission in the cable, it is recommended to use coax cable with  $R = 50\Omega$  impedance (short BNC cables RG-58U). At the output of the photodiode, there is a  $R_S = 50\Omega$  series resistor usually called shunt resistor. The resistance  $R_{LOAD}$  of the measurement device when combined with the shunt resistor, form a voltage divider and the voltage output is given by

$$V_{out} = \frac{R_{LOAD}}{R_{LOAD} + R_S} V_{in} \quad (4.3)$$

We see that the scale factor  $\frac{R_{LOAD}}{R_{LOAD} + R_S}$  is very close to unity and contributes in making the voltage output almost independent of  $R_{LOAD}$ , whereas the DET110 photodetectors depend directly on the load resistance.  $V_{in}$  is the voltage produced by the photocurrent and is given by  $V_{in} = G i_{ph} = G r(\lambda) P [mW]$

The output voltage of the photodiode depends on the incident light power, on the responsivity, on the transimpedance gain and on the scaling factor. The relation that converts light power into voltage reads

$$V_{out} = r(\lambda) G d P \quad (4.4)$$

where  $r(\lambda)$  is the responsivity, G is the transimpedance gain, d is the scale factor ( $d \approx 1$ ) and P is the laser power in mW.

Finally, the working principle of the balanced amplified photodetectors (PDB210A/M) used in our balanced polarimetry measurements is the same as the working principle of the amplified photodetectors previously mentioned. The photodetectors have a fixed gain of  $G = 500 \times 10^3$  V/A and a bandwidth of 1 MHz. The wavelength range is from 320 nm to 1060 nm with a maximum responsivity of  $r = 0.6$  at 920 nm. The subtracted signal has a common rejection ratio of 40 dB and the active photodetection area is a square with a size of  $5 \times 5$  mm. The individual photodiodes saturate at 10 Volts corresponding to a laser power below  $P = 1$  mW, however the subtracted signal can be obtained even for laser powers much larger than  $P = 1$  mW. The photodetector has a

noise equivalent power (NEP) of  $2.2 \text{ pW}/\sqrt{\text{Hz}}$  and a damage threshold of 20 mW.

### 4.3 Balanced Polarimeter

For measurements of the paramagnetic Faraday rotation, a balanced polarimeter scheme was utilized as indicated in Fig.4.2. The light beam is initially linearly polarized along the  $\hat{x}$ -direction. In the absence of the atomic medium, the half-waveplate rotates the initial polarization such that the intensities at the outputs of the two photodiodes, after the beam is analysed by the polarizing beamsplitter, are equal.

Although the polarizing beamsplitter conserves the linear polarization of the laser beam, it rotates the plane of it by an angle of  $\pm 45^\circ$  compared to the initial polarization direction <sup>1</sup>. Specifically, the polarization vector at one arm points along the  $+45^\circ$ , while on the other arm, along  $-45^\circ$ .

The light at the outputs of the two photodetectors is transformed into photocurrent which is then subtracted and subsequently amplified. In the presence of an atomic medium, the plane of polarization is affected mostly by circular birefringence exhibited in the medium <sup>2</sup> resulting in a modulation of the polarization plane by an angle  $\phi_0(t)$ , which is then monitored by the balanced polarimeter.

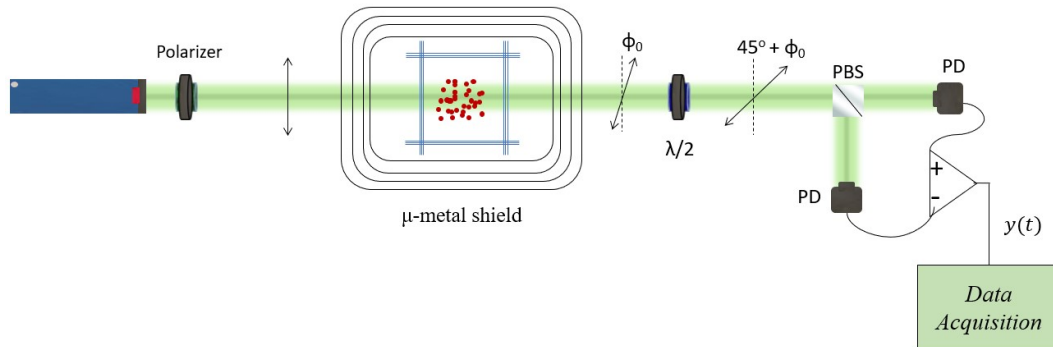


**Figure 4.2:** Optical balanced polarimeter scheme for measuring atomic optical rotation. A linearly polarized probe beam is sent through an atomic vapor. The dispersive atom-light interaction yields a linearly polarized light at a tilted polarization direction, compared to the initial. The rotation angle can be measured using a balanced polarimeter consisting of a half-waveplate, a polarizing beamsplitter and two equivalent photodetectors.

We can model the signal and the noise at each arm of the balanced polarimeter using

<sup>1</sup>We follow the usual notation where the initial linear polarization is along the  $\hat{x}$ -direction.

<sup>2</sup>The paramagnetic Faraday measurement is based on the circular birefringence of the atomic vapor and requires a large detuning from the absorptive atomic resonance and a non-zero spin polarization. Effects of linear birefringence are becoming evident when a non-zero atomic alignment is generated in the vapor [79], requiring a near-resonant detuning in order to be probed. In diamagnetic Faraday rotation measurements, the polarization rotation angle is generated by a dc magnetic field along the beam propagation direction, resulting in a dc rotation angle which is measured using phase sensitive lock-in detection.

some simple classical assumptions. The light intensities arriving at the two photodiodes are given by

$$I_1 = I_0 \cos^2\left(\frac{\pi}{4} - \phi\right) + \delta I_1^{\text{ph}} + \delta I_1 \quad (4.5)$$

$$I_2 = I_0 \sin^2\left(\frac{\pi}{4} - \phi\right) + \delta I_2^{\text{ph}} + \delta I_2 \quad (4.6)$$

when  $\phi = 0$ , the polarimeter is in the balanced position<sup>3</sup>. The photon shot noise is  $\delta I^{\text{ph}}$  and  $\delta I$  represents the excess classical noise that the laser beam carries, arising mostly from classical intensity and phase fluctuations of the laser. Subtracting the two signals and assuming small angle deviations from the balanced condition we arrive at

$$I_1 - I_2 = 2\phi I_0 + \delta I_{\text{ph}} + \delta I \quad (4.7)$$

The appearing photon shot noise is the quadrature sum of the photon shot noises in the two arms  $\delta I_{\text{ph}} = \sqrt{(\delta I_1^{\text{ph}})^2 + (\delta I_2^{\text{ph}})^2}$  while  $\delta I$  is the remaining excess classical noise that arises from the imperfections of the polarimeter and is what really characterizes the optical quality of the polarimeter<sup>4</sup>.

It is practically useful to think  $\delta I_1$  and  $\delta I_2$  consisting of a part that is always cancelled when the two signals are subtracted and a part that is always remnant after subtraction. We can define the extinction ratio<sup>5</sup> of the polarizing beamsplitter as  $R = \frac{I_0}{\delta I}$ . Then the polarimetric output is given by

$$I_1 - I_2 = I_0\left(2\phi + \frac{1}{R}\right) + \delta I_{\text{ph}} \quad (4.8)$$

To perfectly align the polarimeter one can slightly modulate the intensity of the laser beam or the small angle  $\phi$  and then try to reduce the modulated peak height appearing in the power spectrum centered at the modulation frequency.<sup>6</sup>

<sup>3</sup>In the balanced position we obtain  $I_1 = I_2 = \frac{I_0}{2}$ .

<sup>4</sup>Optical imperfections and losses affect the SNR of atomic spin measurements [79]. They effectively result in increasing the photon-shot noise level. The alignment of the optical elements is also very important in the balanced polarimeter scheme. For sensitive measurements of the optical rotation, it is customary to use precision rotation mounts, zero-order waveplates and polarization beam splitters (PBS) with high extinction ratio, that can improve drastically the polarimeter's efficiency and stability. Additionally, one has to make sure that the whole light beam is collected by the photodetector. This can be achieved using anti-reflection coated lenses in front of the photodetection area. The photodetection area must be at least 2-3 times larger than the beam waist, after the light is focused by the lenses. There are situations where the photodetector reflects light back, which is then send back again to detector using additional mirrors [197].

<sup>5</sup>Experimentally, the extinction ratio of a polarizing optical element can be found by applying a very small sinusoidal current modulation in the laser and measuring the power spectrum of the transmitted light with a photodiode. The extinction ratio is given by the ratio of the peak height at the power spectrum between the parallel and the crossed positions of the polarizer.

<sup>6</sup>When such modulation occurs then  $I(t) = I_0 + \delta I(t)$  and  $\phi(t) = \phi_0 + \delta\phi(t)$ . In that case the balanced signal reads

$$I_1 - I_2 = I_0\left(2\phi_0 + \frac{1}{R}\right) + 2I_0\delta\phi(t) + \left(2\phi_0 + \frac{1}{R}\right)\delta I(t) + 2\delta I(t)\delta\phi(t) + \delta I_{\text{ph}} \quad (4.9)$$

### 4.3.1 Standard Quantum Limit

Photon shot noise sets a practical limitation on the precision in which we can measure an angle deviation with the balanced polarimeter scheme. At the balanced position  $I_1 = I_2 = \frac{I_0}{2}$  we have shown that

$$\phi = \frac{I_1 - I_2}{2(I_1 + I_2)} \quad (4.10)$$

Assuming a coherent laser field and the effects of the photon counting statistics based on the Poisson process [198], we know that the light intensity is proportional to the mean photon number  $\langle N_{ph} \rangle = N_{ph}$  and the variance in the photon number is also equal to the mean photon number  $\Delta N_{ph}^2 = \langle N_{ph}^2 \rangle - \langle N_{ph} \rangle^2 = \langle N_{ph} \rangle = N_{ph}$ . Using the error propagation method, the uncertainty in the angle due to the shot noise fluctuations of the coherent laser beam is given by

$$\begin{aligned} \delta\phi &= \sqrt{\left(\frac{\partial\phi}{\partial I_1}\delta I_1\right)^2 + \left(\frac{\partial\phi}{\partial I_2}\delta I_2\right)^2} = \frac{\sqrt{(I_2\delta I_1)^2 + (I_1\delta I_2)^2}}{(I_1 + I_2)^2} \\ &= \frac{\frac{I_0}{2}\sqrt{\delta I_1^2 + \delta I_2^2}}{I_0^2} = \frac{\delta I_0}{2I_0} \approx \frac{\sqrt{N_{ph}}}{2N_{ph}} = \frac{1}{2\sqrt{N_{ph}}} \end{aligned} \quad (4.11)$$

This result can also be interpreted as the minimum angle uncertainty that can be achieved when on average  $N_{ph}$  photons are collected during an acquisition time interval  $T$ . To clarify the notation for subsequent use, we note that in a acquisition time interval  $T$ , the mean value of the number of photons arrived at the photodetector in that time interval is  $N_{ph}$ , and  $\Phi$  is the associated photon flux. Therefore  $N_{ph} = \Phi T$ . We can also express the result of Eq.(4.11) in terms of the photon flux  $\Phi$  yielding  $\delta\phi = 1/(2\sqrt{\Phi T})$ .

The above limit can be also studied in more detail by making use of the characteristics of the photodetector and by translating the incident photon flux into the photocurrent flux. Assuming a photodetector with quantum efficiency  $\eta$  [199, 200]<sup>7</sup> the average photocurrent produced by the arrival of the average  $N_{ph}$  photons in the time interval  $T$  is given by [17]

$$i_{av} = \frac{\eta q_e N_{ph}}{T} = \eta q_e \Phi \quad (4.12)$$

where  $q_e = 1.6 \times 10^{-19}$  C is the electron's charge. The photocurrent at a single arm of the polarimeter is

$$i = \eta q_e \Phi \sin^2\left(\frac{\pi}{4} - \phi\right) \quad (4.13)$$

<sup>7</sup>The quantum efficiency of the photodetector quantifies the amount of photo-electrons generated, given the amount of incident photons. For an ideal detector with  $\eta = 1$ , where each incident photon corresponds to the creation of a single photoelectron. The quantum efficiency  $\eta$  is related to the detector's responsivity via  $\eta = r(\lambda)E_{ph}/q_e$ .

The photocurrent response to a small rotation of the polarization plane by an angle  $\delta\phi$  is

$$\delta i = 2\eta q_e \Phi \sin\left(\frac{\pi}{4} - \phi\right) \cos\left(\frac{\pi}{4} - \phi\right) \delta\phi \quad (4.14)$$

The ratio of the photocurrent response to the photocurrent shot noise fluctuation given by the Schottky's formula [16] ( $\delta i_{\text{ph}} = \sqrt{2q_e i_{\text{av}} BW}$ ) is

$$\frac{\delta i}{\delta i_{\text{ph}}} = \frac{2\eta q_e \Phi \sin\left(\frac{\pi}{4} - \phi\right) \cos\left(\frac{\pi}{4} - \phi\right) \delta\phi}{\sqrt{2\eta q_e^2 \Phi \sin^2\left(\frac{\pi}{4} - \phi\right) BW}} = \sqrt{\frac{2\eta \Phi}{BW}} \cos\left(\frac{\pi}{4} - \phi\right) \delta\phi \quad (4.15)$$

Here  $BW$  is the frequency bandwidth associated with the record time  $T$ . A simple relation holds between the two quantities  $BW = 1/2T$ <sup>8</sup>. Requiring this ratio to be equal to 1 at  $\phi = 45^\circ$ , i.e. we are looking for the minimum angle deviation that can be measured given that the polarimeter is limited by shot noise fluctuations, we find

$$\delta\phi = \sqrt{\frac{BW}{2\eta \Phi}} \quad [\text{rad}] \quad \delta\phi = \frac{1}{\sqrt{2\eta \Phi}} \quad \left[\frac{\text{rad}}{\sqrt{\text{Hz}}}\right] \quad (4.16)$$

For a laser of  $\lambda = 780$  nm and  $P = 1$  mW we obtain  $\delta\phi \approx 8 \frac{\text{nrad}}{\sqrt{\text{Hz}}}$ . Expressing the frequency bandwidth  $BW$  in terms of the time record  $T$  we obtain

$$\delta\phi = \frac{1}{2\sqrt{\eta \Phi T}} = \frac{1}{2\sqrt{\eta N_{\text{ph}}}} \quad (4.17)$$

consistent with the result of Eq.(4.11) for an ideal photodetector with  $\eta = 1$ .

### 4.3.2 Schottky's formula for Shot Noise

Due to Poisson photon statistics of the coherent laser field, the variance in the photon number arriving at the photodetector in a given time interval  $T$  is  $\Delta N_{\text{ph}} = \langle N_{\text{ph}} \rangle = N_{\text{ph}}$ , therefore the variance of the photocurrent  $i = \frac{\eta q_e N_{\text{ph}}}{T}$ <sup>9</sup> is equal to<sup>10</sup>

$$\delta i^2 = \frac{q_e}{T} i_{\text{av}} \quad (4.19)$$

where  $i_{\text{av}}$  is provided by Eq.(4.12). We saw that the auto-correlation of the signal at time  $\tau = 0$ , for a stationary stochastic process like photon shot noise, expresses the total noise power of the signal under consideration and additionally that this power which is

<sup>8</sup>The bandwidth here is referred to the frequency resolution  $\delta f$  that can be achieved in the frequency domain. The longer the measurement time, the smallest the frequency resolution we can achieve. The time and the frequency resolutions are related through the uncertainty relation  $\Delta f \Delta t \geq \frac{1}{2\pi}$ .

<sup>9</sup>Here we use the same notation  $N_{\text{ph}}$  for the stochastic variable of the number of photons and for the mean number of photons in the time interval  $T$ . The distinction between the two should be obvious from the context.

<sup>10</sup>We can arrive directly at this result assuming that the photocurrent is  $i = \eta q_e N_{\text{ph}}/T = q_e N_{\text{el}}/T$  where  $N_{\text{el}} = \eta N_{\text{ph}}$  is the number of photoelectron's produced in the interval  $T$  by the photodetector. Assuming that  $N_{\text{el}}$  follows also Poisson distribution, the variance of the photocurrent is

$$\delta i^2 = \frac{q_e^2}{T^2} (\delta N_{\text{el}})^2 = \frac{q_e^2}{T^2} \langle N_{\text{el}} \rangle = \frac{q_e^2}{T^2} N_{\text{el}} = \frac{q_e}{T} i_{\text{av}} \quad (4.18)$$

also equal to the variance of the stochastic process.

Therefore, the total photon shot noise power is equal to  $\delta i^2 = \frac{q_e}{T} i_{av}$ . Translating in the frequency domain, the total power in the bandwidth  $BW$  is given by

$$\delta i^2 = 2q_e i_{av} BW \quad (4.20)$$

In common experimental situations, utilizing modern commercial photodetectors, the photocurrent is translated into voltage through the relation

$$V(t) = GI(t) \quad (4.21)$$

$G$  is called the transimpedance gain and has units of  $[G] = V/A$ . Then, the measured voltage fluctuations are

$$\delta V^2 = G^2 \delta i^2 = 2G^2 q_e i_{av} BW = 2G^2 q_e^2 \eta \Phi \quad (4.22)$$

In the last step we have replaced the value for the average photocurrent  $i_{av}$ . It is generally convenient to express the voltage fluctuations in terms of the laser power, thus we use the relation between the quantum efficiency and the responsivity  $\eta = \frac{r(\lambda)E_{ph}}{q_e}$  to write

$$\delta V^2 = 2G^2 q_e r(\lambda) E_{ph} \Phi BW = 2G^2 q_e r(\lambda) P BW \quad (4.23)$$

where the laser power is  $P = E_{ph} \Phi$ . The power spectral density of voltage fluctuations in units of  $V^2/Hz$  at the output of the photodetector is

$$\delta V^2 = 2G^2 q_e r(\lambda) P \quad (4.24)$$

This is an important result indicating the known linear scaling of the voltage PSD of the photon shot noise with the laser power  $P$ . From Eq.(4.24) it is also evident that the PSD of photon shot noise is white and independent of the frequency bandwidth<sup>11</sup>. Finally we note that with the use of squeezed light the voltage PSD takes the form [201]

$$\delta V^2 = 2G^2 q_e r(\lambda) P \xi^2 \quad (4.25)$$

where  $\xi^2$  is the light squeezing parameter.

The white power spectral density of photon shot noise as a function of the laser power, for both of our lasers, is plotted in Fig.4.3 having perfect agreement with the expected value given in Eq.(4.24).

<sup>11</sup>As an example, we note that in PSD measurements using the SRS785 we divide the whole frequency span into 800 FFT lines. Keeping the number of FFT lines fixed, a change in the total frequency span will also alter the frequency resolution  $BW$ . However the white photon shot noise background is independent of the measurement bandwidth and therefore not affected. On the other hand, the PSD of a coherent signal depends on the  $BW$  resulting in different output values as the frequency span is altered.

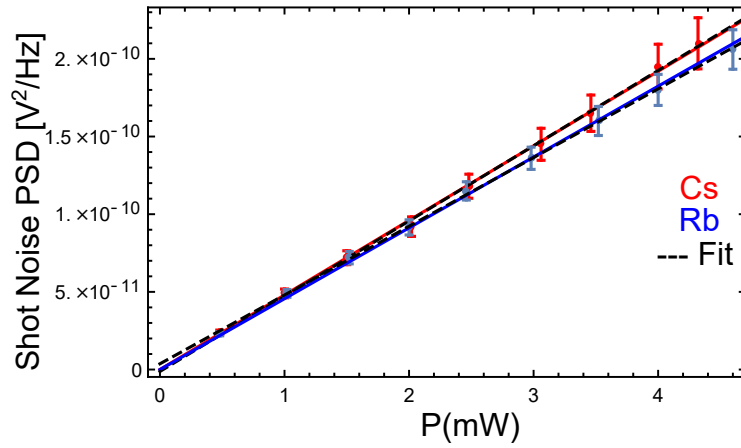


**Figure 4.3:** Shot Noise power spectral density as a function of the laser power reaching the photodetectors. By fitting the data we find  $S_{ph} = -1.20 \times 10^{-12} + 4.84 \times 10^{-11}P$  for the Cs polarimeter and  $S_{ph} = 3.70 \times 10^{-12} + 4.42 \times 10^{-11}P$  for the Rb, consistent with the predictions of Schottky's formula of Eq.(4.24). The error bars are given by the standard deviation of the white spectrum and the fact that they are getting bigger as the laser power increases reflects the fact that the variance of the power spectrum scales with its mean value.

### 4.3.3 Balanced Polarimeter-Stokes Representation

The output of the balanced polarimeter can be conveniently expressed in terms of the light polarization Stokes components [79, 157, 202]

$$\hat{S}_x = \frac{1}{2}(\hat{n}_{ph}(x) - \hat{n}_{ph}(y)) \quad (4.26)$$

$$\hat{S}_y = \frac{1}{2}(\hat{n}_{ph}(+45^\circ) - \hat{n}_{ph}(-45^\circ)) \quad (4.27)$$

$$\hat{S}_z = \frac{1}{2}(\hat{n}_{ph}(\sigma_+) - \hat{n}_{ph}(\sigma_-)) \quad (4.28)$$

The Stokes vector components satisfy the commutation relations

$$[\hat{S}_y, \hat{S}_z] = i\hat{S}_x \quad (4.29)$$

We assume linearly polarized light along the  $\hat{x}$  direction therefore we can replace  $\hat{S}_x \rightarrow S_x = \frac{\Phi}{2}$  and the other two components are zero mean stochastic variables representing the quantum fluctuations of the light polarization. Defining the z-axis as the light propagation axis, a small rotation of the polarization around z, results in the polarimeter response

$$\langle \hat{S}_y \rangle = S_x \sin(2\phi) \approx 2S_x\phi \quad (4.30)$$

also described in the classical scenario. For a small rotation  $\phi$ , the balancing between  $\pm 45^\circ$  components is altered and  $\langle \hat{S}_y \rangle$  results in a non-zero signal. The transverse Stokes

components satisfy

$$\text{Var}(\hat{S}_y) \cdot \text{Var}(\hat{S}_z) \geq \frac{S_x^2}{4} \quad (4.31)$$

where the equality holds for the minimum uncertainty states, like the coherent state of the light field. All of the results are extensively analyzed in the aforementioned references and here are mentioned as a brief introduction to the topic. We can introduce input-output relations for the Stokes components, where  $\mathbf{S}^{in}$  describe the state of light polarization before the interaction with the atoms and  $\mathbf{S}^{out}$  after. Neglecting linear birefringence effects, we know that the vapor is a circularly birefringent medium hence  $\hat{S}_z$  is not affected from the interaction

$$\hat{S}_z^{out}(t) = \hat{S}_z^{in}(t) \quad (4.32)$$

Due to the Faraday rotation effect the  $\hat{S}_y$  component is affected as

$$\hat{S}_y^{out}(t) = \hat{S}_y^{in}(t) + gS_x\hat{J}_z(t) \quad (4.33)$$

i.e. the Stokes vector initially along the  $\hat{x}$  direction is rotated around the z-axis by a small rotation angle  $g|J_z|$ . Here  $g$  is the atom-light coupling constant responsible for the dispersive Faraday interaction as described in Chapter 2. Both  $\hat{S}_y^{in}(t)$  and  $\hat{J}_z(t)$  are stochastic processes, the former describing photon shot noise fluctuations and the later spin noise, the dynamics of which can be either represented using the stochastic Bloch equations or by assuming a fundamental stochastic density matrix model described in Chapter 5.

$\hat{S}_y^{in}(t)$  is a zero mean stochastic variable describing shot noise with covariance function given by

$$\langle \hat{S}_y^{in}(t) \rangle = 0 \quad (4.34)$$

$$\langle \hat{S}_y^{in}(t)\hat{S}_y^{in}(t') \rangle = \frac{S_x}{2}\delta(t-t') \quad (4.35)$$

where  $S_x/2 = \Phi/2$  is the photon flux. The variance of the photon shot noise is

$$\text{Var}(\hat{S}_y^{in}(t)) = \frac{S_x}{2} = \frac{\Phi}{4} \quad (4.36)$$

The acquired signal in a record time  $T$  is assumed to be a timed averaged version of the stochastic variable

$$\hat{S}_y^{in}(t) \rightarrow \frac{1}{T} \int_0^T \hat{S}_y^{in}(t) dt \quad (4.37)$$

Then the variance is given by

$$\begin{aligned}
 \text{Var}(\hat{S}_y^{\text{in}}(t)) &= \text{Var}\left(\frac{1}{T} \int_0^T \hat{S}_y^{\text{in}}(t) dt\right) = \frac{1}{T^2} \left\langle \left( \int_0^T \hat{S}_y^{\text{in}}(t) dt \right)^2 \right\rangle \\
 &= \frac{1}{T^2} \int_0^T \int_0^T \langle \hat{S}_y^{\text{in}}(t) \hat{S}_y^{\text{in}}(t') \rangle dt dt' \\
 &= \frac{1}{T^2} \int_0^T \int_0^T \frac{S_x}{2} \delta(t - t') dt dt' = \frac{1}{T^2} \frac{S_x}{2} T = \frac{S_x}{2T} = \frac{\Phi}{4T}
 \end{aligned} \tag{4.38}$$

The polarization rotation at the polarimeter is  $\phi = \frac{\langle \hat{S}_y^{\text{out}}(t) \rangle}{2S_x}$  and the standard deviation to that angle is

$$\delta\phi = \frac{\delta\langle \hat{S}_y^{\text{out}}(t) \rangle}{2S_x} = \frac{1}{2S_x} \sqrt{\frac{S_x}{2T}} = \frac{1}{2} \frac{1}{\sqrt{2TS_x}} = \frac{1}{2\sqrt{\Phi T}} = \frac{1}{2\sqrt{N_{ph}}} \tag{4.39}$$

consistent with the previous results in this Chapter, as expected.

The photocurrent at the output of the balanced polarimeter is given by [83]

$$I(t) = r(\lambda) \int S_y(x, y, t) dx dy \tag{4.40}$$

where  $r(\lambda) = q_e \eta / E_{ph}$  is the responsivity of the photodetector. The integral is carried over the area of the probe beam at the photodetection region. Using (4.33) we can write the differential photocurrent increment as

$$I(t) dt = \eta \Phi q_e g F_z(t) dt + dw_{sn}(t) \tag{4.41}$$

where  $dw_{sn}(t) = \sqrt{\eta q_e^2 \Phi} dW$  is the stochastic increment due to photon shot noise with  $dW \approx \mathcal{N}(0, dt)$  being a Gaussian differential increment. This can be easily shown using the photo-current variance in Eq.(4.19). In a time interval  $T$  the photon shot noise auto-correlation function is given by

$$\langle dw_{sn}(t) dw_{sn}(t') \rangle = \frac{\eta q_e^2 \Phi}{T} \delta(t - t') \tag{4.42}$$

### 4.3.4 Quantum Description: Homodyne Detection

In this section we review the balanced polarimetry detection scheme using the quantum optical formalism of homodyne detection assuming that the electromagnetic field of light is quantized and hence it is described by the photon creation and annihilation operators [143, 147]. The field operators satisfy the bosonic commutation relation

$$[a, a^\dagger] = 1 \tag{4.43}$$

We start the discussion with some properties of the coherent states. Coherent field states can be written as an infinite superposition of photon number states (Fock states), each state weighted by a fixed coefficients. Coherent states are also eigenstates of the



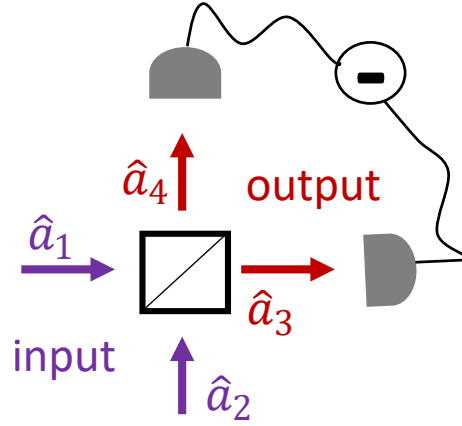


**Figure 4.4:** Quantum Homodyne description of the balanced polarimeter scheme. Input-output relations between the transmitted and the reflected modes of the quantized laser field.

annihilation operator  $\hat{a}$

$$|a\rangle = e^{-|a|^2/2} \sum_{n=0}^{\infty} \frac{a^n}{\sqrt{n!}} |n\rangle \quad (4.44)$$

$$\hat{a}|a\rangle = a|a\rangle \quad (4.45)$$

where  $a$  is a complex eigenvalue usually written in the complex polar form  $a = |a|e^{i\theta}$ .

The photon flux  $\Phi$  is equal to the mean photon number in the coherent state

$$\langle n \rangle = \langle a | \hat{a}^\dagger \hat{a} | a \rangle = |a|^2 \quad (4.46)$$

and the variance

$$\Delta n^2 = \langle n^2 \rangle - \langle n \rangle^2 = |a|^2 + |a|^4 - |a|^4 = |a|^2 = \langle n \rangle \quad (4.47)$$

Assuming that the operator  $\hat{a}_1$  describes the strong local oscillator probe field along the horizontal direction H (p-polarization), then the operator  $\hat{a}_2$  accounts for the quantum polarization fluctuations along the vertical direction V (s-polarization). After the light passes through the polarizing beam splitter, it is separated into the  $\hat{a}_3$  and  $\hat{a}_4$  modes pointing along the  $+45^\circ$  and  $-45^\circ$ , respectively, with respect to the H direction of the incident probe field. The input-output relation of the propagating modes are<sup>12</sup>:

$$\hat{a}_3 = \frac{1}{\sqrt{2}}(\hat{a}_1 + \hat{a}_2) \quad (4.50)$$

$$\hat{a}_4 = \frac{1}{\sqrt{2}}(\hat{a}_1 - \hat{a}_2) \quad (4.51)$$

<sup>12</sup>This is a special case of the more general beam splitter relating the input-output modes though

$$\hat{a}_3 = T\hat{a}_1 + R\hat{a}_2 \quad (4.48)$$

$$\hat{a}_4 = R\hat{a}_1 + T\hat{a}_2 \quad (4.49)$$

where R and T are the reflection and transmission coefficients, respectively.

The mean photon number at the output ports 3 and 4 are therefore given by  $\hat{n}_3 = \langle \hat{a}_3^\dagger \hat{a}_3 \rangle$  and  $\hat{n}_4 = \langle \hat{a}_4^\dagger \hat{a}_4 \rangle$  calculated at the given field state. The mean photocurrent output of the balanced polarimeter is proportional to the difference of the number photons between the two arms [203]

$$\overline{\delta I} \approx \langle \delta \hat{n} \rangle = \langle \hat{n}_3 - \hat{n}_4 \rangle \quad (4.52)$$

using the input-output relations we can write the photon difference  $\delta \hat{n}$  as

$$\delta \hat{n} = \hat{a}_1^\dagger \hat{a}_2 + \hat{a}_2^\dagger \hat{a}_1 \quad (4.53)$$

Assuming that the local oscillator laser field at the input-1 is in a coherent state  $|a\rangle$  and the vacuum field at port-2 in an arbitrary state  $|\psi_2\rangle$  the expectation value yields

$$\langle \delta \hat{n} \rangle = a_1 \langle \hat{a}_2 \rangle + a_1^* \langle \hat{a}_2^\dagger \rangle = |a_1| \langle e^{i\theta} \hat{a}_2 + e^{-i\theta} \hat{a}_2^\dagger \rangle = |a_1| \langle \hat{Q} \rangle = 2|a_1| \text{Re}\{e^{i\theta} \langle \hat{a}_2 \rangle\} \quad (4.54)$$

where we have defined the hermitian operator  $\hat{Q} = e^{i\theta} \hat{a}_2 + e^{-i\theta} \hat{a}_2^\dagger$  usually known as a quadrature of the electromagnetic field at port-2. Similarly, the variance of the differential photocurrent is proportional to the variance of the difference of the photon numbers in the two output ports

$$\begin{aligned} (\hat{n}_3 - \hat{n}_4)^2 &= (\hat{a}_1^\dagger \hat{a}_2 + \hat{a}_2^\dagger \hat{a}_1)^2 \\ &= (\hat{a}_1^\dagger)^2 (\hat{a}_2)^2 + (\hat{a}_2^\dagger)^2 (\hat{a}_1)^2 + \hat{a}_1^\dagger \hat{a}_1 \hat{a}_2 \hat{a}_2^\dagger + \hat{a}_1 \hat{a}_1^\dagger \hat{a}_2^\dagger \hat{a}_2 \\ &= (\hat{a}_1^\dagger)^2 (\hat{a}_2)^2 + (\hat{a}_2^\dagger)^2 (\hat{a}_1)^2 + \hat{a}_1^\dagger \hat{a}_1 \hat{a}_2 \hat{a}_2^\dagger + \hat{a}_1^\dagger \hat{a}_1 \hat{a}_2^\dagger \hat{a}_2 + \hat{a}_2^\dagger \hat{a}_2 \end{aligned} \quad (4.55)$$

where in the last step we have normally ordered the third term with respect to the annihilation operator  $\hat{a}_1$ . The expectation value of Eq.(4.55) over the coherent state of the local oscillator and the arbitrary state of the transverse quantum field  $\hat{a}_2$  yields

$$\langle (\hat{n}_3 - \hat{n}_4)^2 \rangle = (a_1^*)^2 \langle (\hat{a}_2)^2 \rangle + (a_1)^2 \langle (\hat{a}_2^\dagger)^2 \rangle + |a_1|^2 \langle \hat{a}_2 \hat{a}_2^\dagger \rangle + |a_1|^2 \langle \hat{a}_2^\dagger \hat{a}_2 \rangle + \langle \hat{a}_2^\dagger \hat{a}_2 \rangle \quad (4.56)$$

The last term is usually many order of magnitude smaller than the other and can be neglected. Then we obtain

$$\begin{aligned} \langle (\hat{n}_3 - \hat{n}_4)^2 \rangle &= \langle \delta \hat{n}^2 \rangle = (a_1^*)^2 \langle (\hat{a}_2)^2 \rangle + (a_1)^2 \langle (\hat{a}_2^\dagger)^2 \rangle + |a_1|^2 \langle \hat{a}_2 \hat{a}_2^\dagger \rangle + |a_1|^2 \langle \hat{a}_2^\dagger \hat{a}_2 \rangle \\ &= |a_1|^2 \langle \psi_2 | (e^{i\theta} \hat{a}_2 + e^{-i\theta} \hat{a}_2^\dagger)^2 | \psi_2 \rangle = |a_1|^2 \langle \hat{Q}^2 \rangle \end{aligned} \quad (4.57)$$

Then the variance of the observable quantity, namely the photon difference between the ports 3 and 4 is proportional to the variance of the field quadrature  $\hat{Q}$

$$\delta I^2 \approx \langle \delta \hat{n}^2 \rangle - \langle \delta \hat{n} \rangle^2 = |a_1|^2 (\langle \hat{Q}^2 \rangle - \langle \hat{Q} \rangle^2) = |a_1|^2 \Delta \hat{Q}^2 \quad (4.58)$$

The measurement of the differential power of these two modes corresponds to the measurement of the  $S_y$  Stokes operator, whereas with an extra  $\lambda/4$  plate in front of the beam splitter the  $S_z$  Stokes operator is measured [5, 204]

$$S_x(t) = a_x^\dagger a_x - a_y^\dagger a_y \quad (4.59)$$



$$\begin{aligned} S_y(t) &= a_{+45^\circ}^\dagger a_{+45^\circ} - a_{-45^\circ}^\dagger a_{-45^\circ} \\ &= a_x^\dagger a_y + a_y^\dagger a_x \end{aligned} \quad (4.60)$$

$$\begin{aligned} S_z(t) &= a_+^\dagger a_+ - a_-^\dagger a_- \\ &= -i(a_x^\dagger a_y - a_y^\dagger a_x) \end{aligned} \quad (4.61)$$

The first Stokes operator  $\langle S_x(t) \rangle = |a|^2/2$  is equal to the total photon number of the strong field for the case of the strong coherent light  $|a\rangle$  of linear x polarization. Then, a measurement of the Stokes components  $S_y(t)$  and  $S_z(t)$  account for a homodyne detection of the polarization fluctuations along the  $\hat{y}$ -direction [5]

$$\frac{\hat{S}_y(t)}{\sqrt{\langle S_x \rangle}} \approx \frac{1}{\sqrt{2}}(\hat{a}_y + \hat{a}_y^\dagger) = \hat{x}_L(t) \quad (4.62)$$

$$\frac{\hat{S}_z(t)}{\sqrt{\langle S_x \rangle}} \approx -\frac{i}{\sqrt{2}}(\hat{a}_y - \hat{a}_y^\dagger) = \hat{p}_L(t) \quad (4.63)$$

Consistent with the aforementioned description of the homodyne detection.

## 4.4 Stationary Stochastic Processes

Suppose we observe a continuous random and stationary signal described by the real stochastic function  $s(t)$ , where  $t \in (-\infty, +\infty)$ . We denote the Fourier transform of the signal as  $\mathcal{F}[s](\omega)$  and we define it as

$$f(\omega) = \int_{-\infty}^{+\infty} s(t)e^{-i\omega t} dt \quad (4.64)$$

The inverse Fourier transform is

$$s(t) = \frac{1}{2\pi} \int_{-\infty}^{+\infty} f(\omega)e^{i\omega t} d\omega \quad (4.65)$$

Since the Fourier transform is a linear transformation and  $s(t)$  is a stochastic function, we expect that  $f(\omega)$  is also a stochastic function. Suppose we record the stochastic signal for an acquisition time  $T$ . We assume that the signal can be repeated over different realizations and we average over the total number of repetitions to obtain an ensemble averaged form of our stochastic signal. That kind of averaging is expressed using the brackets  $\langle \cdot \rangle$ . We also assume a linear averaging process, weighting equally all the repetitions. From Parseval's theorem the energy in the signal can be calculated either in the time domain or in frequency domain and is given by

$$E = \int_{-\infty}^{+\infty} |s(t)|^2 dt = \frac{1}{2\pi} \int_{-\infty}^{+\infty} |f(\omega)|^2 d\omega \quad (4.66)$$

The energy of the signal at a particular frequency  $\omega$  is given by the power spectrum<sup>13</sup>

$$S_{xx}(\omega) = \langle \{ \mathcal{F}[s](\omega) \}^* \mathcal{F}[s](\omega) \rangle = \langle | \mathcal{F}[s](\omega) |^2 \rangle = \left\langle \left| \int_0^T s(t) e^{-i\omega t} dt \right|^2 \right\rangle \quad (4.67)$$

where the integration extends over the acquisition time.

A commonly used quantity is the average power at a particular frequency  $\omega$  measured for a time interval  $T$ . This is the power spectral density (PSD)<sup>14</sup> and can be calculated by dividing the power spectrum (the average energy at frequency  $\omega$ ) with the total acquisition time  $T$

$$\begin{aligned} PSD[\omega] &= \lim_{T \rightarrow +\infty} \frac{1}{T} S_{xx}(\omega) = \lim_{T \rightarrow +\infty} \frac{1}{T} \langle \{ \mathcal{F}[s](\omega) \}^* \mathcal{F}[s](\omega) \rangle \\ &= \lim_{T \rightarrow +\infty} \frac{1}{T} \int_0^T \int_0^T \langle s(t_1) s(t_2) \rangle e^{-i\omega(t_1 - t_2)} dt_1 dt_2 \end{aligned} \quad (4.68)$$

The quantity  $R_{xx}(t_1, t_2) = \langle s(t_1) s(t_2) \rangle$  is the auto-covariance function<sup>15</sup> of the stochastic signal. Assuming stationary process and ergodicity, the auto-covariance function depends only on the time difference between the two times  $R_{xx}(t_1, t_2) = R_{xx}(t_1 - t_2)$  hence we can write

$$PSD[\omega] = \lim_{T \rightarrow +\infty} \frac{1}{T} \int_0^T \int_0^T R_{xx}(t_1 - t_2) e^{-i\omega(t_1 - t_2)} dt_1 dt_2 \quad (4.69)$$

since the integrand depends only on the variable  $t_1 - t_2$  we can apply one of the standard manipulations in multivariable calculus that frequently occurs [205] and obtain

$$PSD[\omega] = \lim_{T \rightarrow +\infty} \frac{1}{T} \int_{-T}^T R_{xx}(\tau) e^{-i\omega\tau} \left(1 - \frac{|\tau|}{T}\right) d\tau \quad (4.70)$$

This is the so called Wiener-Khinchin theorem that relates the power spectral density of a stationary stochastic process to the auto-covariance function<sup>16</sup>. The auto-covariance function  $R_{xx}(\tau)$  is an even function i.e.  $R_{xx}(\tau) = R_{xx}(-\tau)$  therefore we can simplify the relation

$$\begin{aligned} PSD[\omega] &= \lim_{T \rightarrow +\infty} \int_{-T}^T R_{xx}(\tau) \cos(\omega\tau) d\tau + i \int_{-T}^T R_{xx}(\tau) \sin(\omega\tau) d\tau \\ &= 2 \lim_{T \rightarrow +\infty} \int_0^T R_{xx}(\tau) \cos(\omega\tau) d\tau \end{aligned} \quad (4.72)$$

Applying the inverse Fourier transform to the Wiener-Khinchin relation Eq.(4.70), we

<sup>13</sup>Assuming that the signal is in units of Volts as it is usually the case, the power spectrum is in units of  $V^2$ .

<sup>14</sup>The power spectral density (PSD) has units of  $\frac{V^2}{Hz}$  and is given by dividing the power spectrum with the total acquisition time  $T$ .

<sup>15</sup>The auto-covariance at  $\tau = 0$  is equal to the variance of the signal  $s(t)$ . The auto-correlation function is defined as the auto-covariance divided by the variance of the signal.

<sup>16</sup>This is obvious when we let  $T \rightarrow \infty$

$$PSD[\omega] = \int_{-\infty}^{+\infty} R_{xx}(\tau) e^{-i\omega\tau} d\tau \quad (4.71)$$



can express the auto-covariance function in terms of the PSD

$$R_{xx}(\tau) = \frac{1}{2\pi} \int_{-\infty}^{+\infty} PSD[\omega] e^{i\omega\tau} d\omega \quad (4.73)$$

An interesting relation is obtained when we examine the case of  $\tau = 0$

$$R_{xx}(0) = \frac{1}{2\pi} \int_{-\infty}^{+\infty} PSD[\omega] d\omega \quad (4.74)$$

We obtain that the total integral of the PSD over the whole range of frequencies is equal to the auto-covariance function at  $\tau = 0$ . The auto-covariance function at  $\tau = 0$  is  $R_{xx}(0) = \langle s^*(t)s(t) \rangle = \langle |s(t)|^2 \rangle$  expressing the total power of the signal. In the case of a zero-mean stochastic signal  $R_{xx}(0)$  is equal to the variance of the stochastic variable  $s(t)$ . Even when the mean is not zero, we can frequently redefine a new stochastic function as  $s(t) \rightarrow s(t) - \langle s(t) \rangle$  as a zero-mean stochastic process<sup>17</sup>.

We note that the same analysis is also applicable to the cross-PSD defined as<sup>18</sup>

$$PSD_c[\omega] = \lim_{T \rightarrow +\infty} \frac{1}{T} \langle \{ \mathcal{F}[s_1](\omega) \}^* \mathcal{F}[s_2](\omega) \rangle \quad (4.75)$$

where  $s_1(t)$  and  $s_2(t)$  are two different stochastic signals.

#### 4.4.1 Sampling

In practise, any acquired signal is recorded and digitized as a sampled version of the continuous time signal. Assuming we measure the continuous stochastic signal  $s(t)$  for time  $T_{acq}$ , the sampling process splits the large acquisition time interval into small samples of duration  $\Delta t$ . The number of samples is  $N_s = T_{acq}/\Delta t$ . We define also the sample-rate as  $1/\Delta t$ . Thus, the sampling process maps the signal  $s(t)$  into a discretized form  $s[n]$  where  $n$  is the sample index which takes values from  $n = 0$  up to  $N_s - 1$ . Once the signal is digitized, the transformation in the frequency domain is done using the Fast Fourier Transform (FFT) [206]

$$F[k] = \sum_{n=0}^{N_s-1} s[n] e^{-i2\pi \frac{kn}{N_s}} \quad (4.76)$$

where  $k$  is the sample index in the frequency domain. The frequency resolution is  $\Delta f = 1/T_{acq}$  and the largest frequency limiting the frequency domain is  $1/(2\Delta t) = \text{sample-rate}/2$ . The frequency resolution reflects also the minimum change in frequency that the FFT can detect. Note that the number of samples in the time domain is equal to

<sup>17</sup>Here we have schematically describe the process of deriving the Wiener-Khinchin theorem. In fact the proof is much easier if we follow the opposite direction, i.e. take the Fourier transform of the auto-covariance function and show that is equal to the power spectrum of the stochastic process.

<sup>18</sup>The majority of the spectral measurements in this thesis are performed using the Stanford Research Systems-SRS785 spectrum analyzer, therefore we try to keep the notation as close to the outputs of the SRS as possible.



the number of samples in the frequency domain.

We mentioned that the maximum frequency is given by  $1/(2\Delta t)$ , however, there is also a range of frequencies from  $1/(2\Delta t)$  up to  $1/\Delta t$ . This frequency region is called the "alias" region and is normally hidden<sup>19</sup>.

Sampling a signal of frequency  $\omega$ , the sample-rate must be at least twice large as the frequency  $\omega$ . This is known as the Nyquist theorem. If this is not the case, then the signal is mis-sampled and falsely the original signal is replaced by a different distorted signal at lower frequencies. This artificial effect introduces effectively noise at lower frequencies, and affects the original spectrum. This is exactly the problem with aliasing. Frequencies larger than sample-rate/2 are falsely mirrored in the lower frequency domain of the spectrum. Anti-aliasing filters usually prevent this effect.

Another effect affecting the frequency domain is known as spectrum leakage. This effect is mostly evident when very narrow signals in the frequency domain are utilized. For example a sine-wave in the time domain is almost a delta function in frequency domain, given an acquisition time  $T_{acq}$ . To understand spectral leakage we are going to consider a simple example. Suppose our signal is a sine-wave in the time domain with frequency  $f = 230$  kHz. The sampling rate is chosen to be 1 MHz and the number of samples is  $N_s = 20$ . Then the total acquisition time is  $T_{acq} = 20\mu s$ . The frequency resolution is  $\Delta f = \frac{1}{T_{acq}} = 50$  kHz. Then the frequency bin  $k_f = f/\Delta f = 4.6$ . We obtain that the sine-wave frequency  $f$  is not an exact integer multiple of the frequency resolution  $\Delta f$ . Hence we expect the delta function of the sine-wave in the frequency domain to be between the frequency bin 4 and the frequency bin 5. In fact we expect some power leakage at both bins 4 and 5 resulting in a effective broadening of the measured peak.

Finally, for the FFT to be computed it is assumed that the signal continues infinitely in time. Given a sine-wave as the input signal, if within the acquisition time there is not an integer number of periods (cycles), then as the signal is repeated continuously, there would be phase discontinuities at the interface points where the two signals are joined. These phase discontinuities can lead to artificial broadening when averaged for a long period. To prevent these phase jumps we use time domain windowing functions in convolution with the original signal, with the aim to eliminate the discontinuity at the end of the record. Windows shape the time domain signal and force it to be zero at the

<sup>19</sup>In many situations the alias region causes distortion and affects the spectrum at low frequencies. Commercial spectrum analyzers use anti-aliasing filters to prevent the aliasing effect. However, when the acquisition is performed with DAQ-boards or other analog to digital converters, one has to use different techniques to avoid aliasing such as low pass filters. Especially in noise measurements, aliasing can completely deform the frequency spectrum by introducing excess noise.



end of each record. Windows have a frequency response that is similar to a bandpass filter.

There are various types of windows such as (Hanning, Blackman-Harris, Uniform, Flattop, Kaiser, etc.). In our experiments we use Hanning windowing. The Hanning window is zero at the beginning of the time record and large in the center. This effectively zeroes the signal pulse at the start of the time record leaving nothing in the windowed time record. The amplitude of the windowed time record is not the same as the amplitude of the time record itself. This is because the window functions have gain and attenuation at different parts of the time record. The amplitude of the signal in the windowed time record is twice as large in the case of the Hanning window. The Hanning window is most often used in noise measurements since it has the lowest noise floor. The Hanning window function is

$$w_H = 1 - \cos\left(2\pi \frac{n}{N_s}\right) \quad (4.77)$$

where  $n$  takes values from  $n = 0$  to  $N_s - 1$ .

Regarding the digitization process during acquisition, for a 16-bit DAQ card with an input range of  $\pm 1V$ , the voltage axis is divided into bins of  $\delta V = 2/2^{16} = 30.5\mu V$ . Therefore each sample contains  $\frac{2V}{30.5\mu V} = 65536$  bits of information. It is commonly used to express this number in bytes. Each byte corresponds to 8 bits, therefore each sample contains  $65536/8 = 8.19$  kB of information. For an acquisition time of  $T_{acq} = 60s$  and a sampling rate of 5 kHz, the total amount of information of the whole data acquisition is  $5000 \times 60 \times 32$  in bits. Normally, in the post processing section using Mathematica or Matlab the file size is given in bytes. Given the size of file in bytes, then the number of sample points of the whole acquisition is  $\text{filesize} \times 8/32$ .

## 4.5 Vapor Cells and Oven

### 4.5.1 Vapor Cells

In our experiment we use cylindrical glass-blown vapor cells made from pyrex glass (Manufactured by [Twinleaf](#)) at various buffer gas pressures as shown in Fig.4.5. The cells contain 28% Cesium ( $^{133}\text{Cs}$ ) and 72% Rubidium ( $^{87}\text{Rb}$ ) where the natural isotopic abundance of  $^{85}\text{Rb}$  is negligible. The percentages follow from Raoult's law which states that the partial pressure of each component of an ideal mixture of liquids is equal to the vapor pressure of the pure component multiplied by its mole fraction in the mixture. The vapor pressure of the pure component usually follows the known-Killian formula [207].





**Figure 4.5:** Cylindrical glass-blown vapor cell used in the experiment.

In order to increase the spin coherence lifetime, the cells shown in Fig.4.6 contain 100, 329 and 622 Torr of  $N_2$  buffer gas. The geometric characteristics of the cells are equivalent, the length is  $L = 5$  cm and the diameter  $d = 1.27$  cm. The glass thickness is  $l_g = 1.59$  mm. Although the cell windows are not AR-coated, the oven is manufactured in such a way that the cell fits perfectly between the fused silica oven windows with double-side AR coating at the IR spectrum and with thickness of  $l_w = 1$  mm each, ensuring low optical losses. The transmission after the vapor cell is measured to be  $T = 85\%$  at room temperature and is found to be independent of the wavelength in the IR regime. The measurement is consistent with the expected transmission calculated using Fresnel equations in the case of transverse incidence. The transmission is given by

$$T = \frac{4n_1n_2}{(n_1 + n_2)^2} \approx 96\% \quad R = \left(\frac{n_1 - n_2}{n_1 + n_2}\right)^2 \approx 4\% \quad (4.78)$$

where we must account for all 4 surfaces of the glass that light interacts with during propagation. Here  $n_1 \approx 1$  is the index of refraction of the air and  $n_2 = 1.47$  the index of refraction of the pyrex glass. From each surface there is an amount of 4% optical loss resulting in total to a transmission coefficient of  $T \approx 85\%$ .

### 4.5.2 Oven

To heat the vapor cell up to  $140 - 150^\circ\text{C}$  we use an oven manufactured also by [Twinleaf](#). The oven uses rf radiation uniformly distributed in the central area of the oven, where the cell is placed. The interior part of the oven being in direct contact with

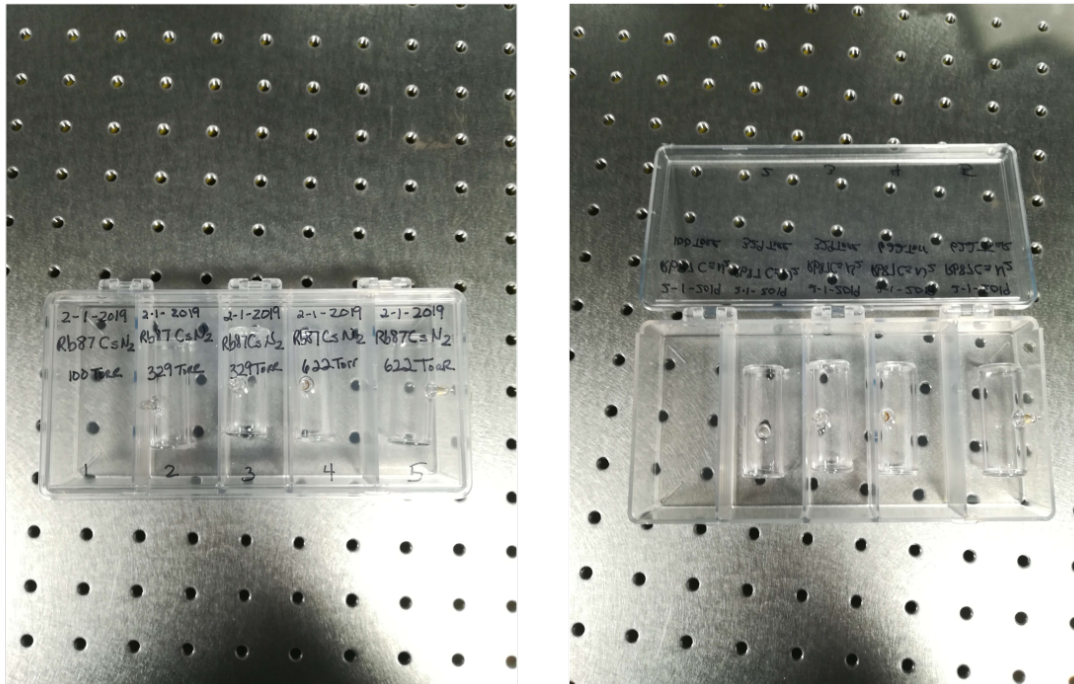


**Figure 4.6:** Glass-blown vapor cells used in our experiment. The cells contain 28% Cs and 72%  $^{87}\text{Rb}$  at various buffer gas pressures of 100 Torr, 329 Torr and 622 Torr. The cells are made from pyrex glass and has a length of 5 cm and a diameter of half an inch. (Manufacturer: Twinleaf).

the vapor cell is made of strong plastic material with high thermal conductivity and the geometry is such that the vapor cell of length 5 cm fits perfectly in the center. The outer part of the oven is made of plastic Teflon material having a large degree of thermal insulation from the environment. Optical access to the oven is provided by a single axis only used to probe the spin dynamics of the vapor via e.g. Faraday rotation.

In each side of the oven there are three windows of 1 mm thickness each, made of fused silica. All windows are double-side AR coated at the IR spectrum and the transmission is measured to be  $T = 84\%$ , being also in agreement with the predictions of Fresnel equations. The windows are separated by a small gap between them. The oven shape is cylindrical and it is comprised of an inner part which holds the cell and an outer part which works as a protective lid to thermally insulate the cell from the environment. As it can be seen in Fig.4.7, the oven is filled with thermally insulating foam material resulting in high thermal isolation. To ensure good thermal stability, the free space inside the Teflon material was insulated using some baffle and the windows are glued and insulated using ceramic silicone-based thermal insulation.

The oven is controlled by a heater controller using rf heating at frequencies ranging from 50 kHz to 1 MHz. At low frequencies the maximum power of the heater is 50 W and it drops as the frequency increases. The temperature is measured with a thermocouple resistive sensor which is embedded in the plastic material close to the cell. The signal

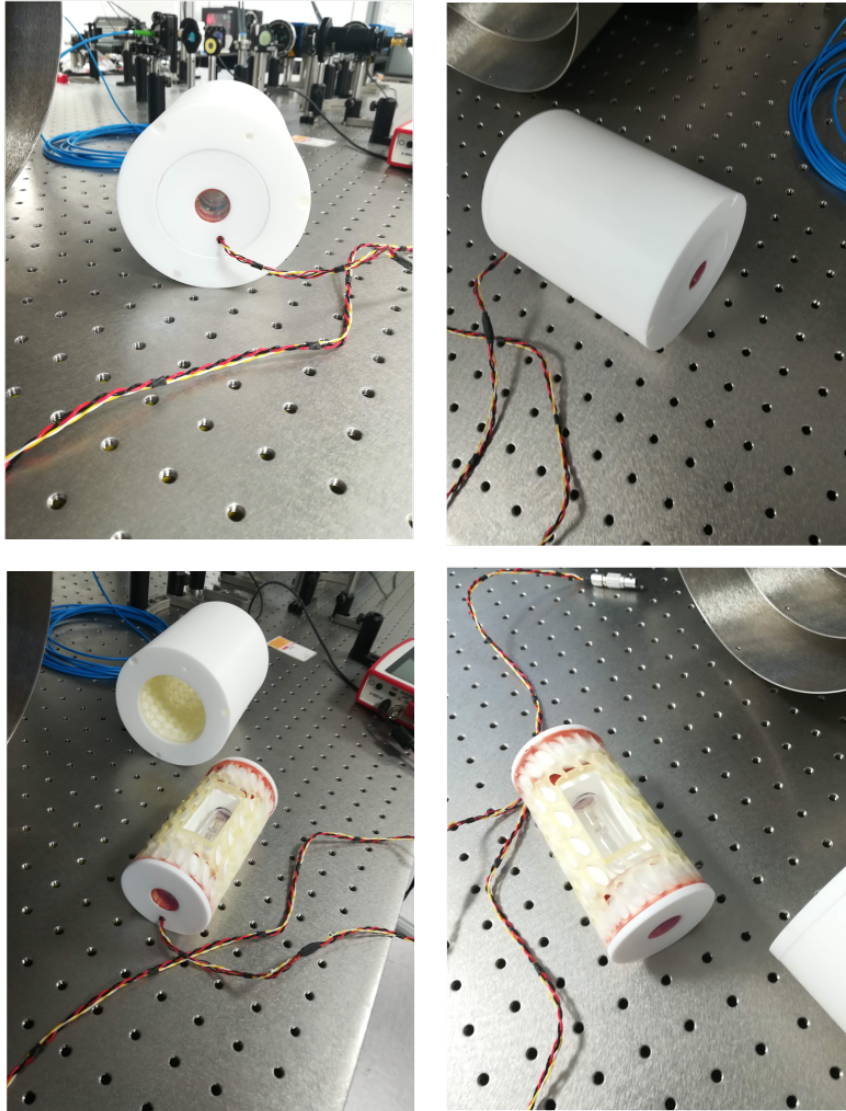


**Figure 4.7:** Different perspectives of the oven used to heat the vapor cell at temperatures up to  $150^{\circ}\text{C}$ . The oven operation is based on rf heating. The internal part is made of a high thermally conducting plastic material being in direct contact with the cell. The outer part of the oven is made of plastic Teflon material having a large degree of thermal insulation from the environment. The temperature close to the cell is measured using an integrated thermocouple sensor in direct contact with the internal material.

from the thermocouple serves as an indicator for a PI circuit which is used to stabilize the temperature at the desired value. The set temperature, the rf frequency, the power of the heater and the PI-circuit parameters are all controlled using a Labview program communicating via usb port with the heater unit. The optimal PI parameters are found to be  $k_P = 25$  and  $k_I = 100$ .

A large integral component damps rapidly the oscillations once the set temperature is reached and a large proportional component increases rapidly the power of the oven reaching the maximum output power value when the heating process begins. The frequency response of the rf oven is a very narrow peak centered at the rf-frequency. There is some pick-up coil detection happening by the dc-coils of the shield, adding an amount of magnetic noise to the system, however the spin vapor in the thermal state is remotely affected by the magnetic noise. The oven usually operates at frequencies higher than 100 kHz such that there is no overlap with the spin signals in small magnetic fields. In Fig.4.8 we plot the time which takes for the temperature to be stabilized at various choices of the set temperature.

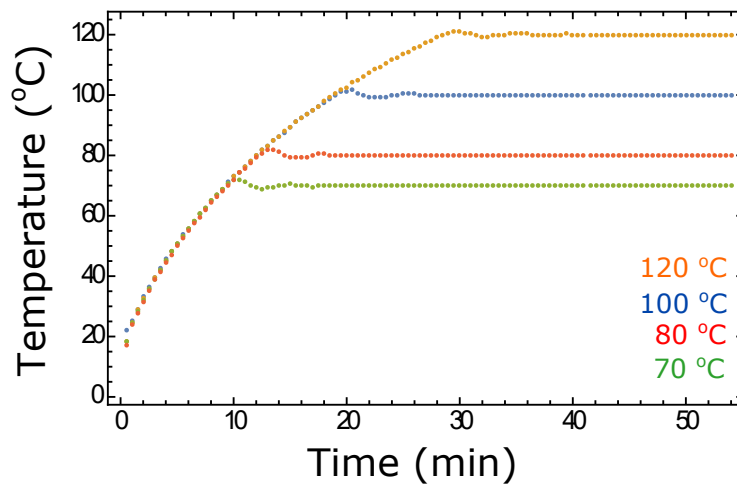


**Figure 4.8:** Oven PI circuit response to four different temperatures. The PI parameters are  $k_P = 25$  and  $k_I = 100$  and the ac heat frequency is 50 kHz. The parameters are such that the oven works at the maximum power at the beginning and it is damped rapidly when the set value is reached. The temperature is stable up to  $\pm 0.1^\circ \text{C}$ .

### 4.5.3 Faraday Rotation from Oven Optical Elements

In each side of the oven there are 3 windows made from fused silica, 1mm thick each separated with some baffle in the middle. Fused Silica is the purest form of  $\text{SiO}_2$ . This glass has large transmission in both the UV and IR spectra, a very low dielectric coefficient and smooth optical properties. Unlike sapphire, fused silica can be shaped

to many forms and sizes. It has excellent resistance to non-fluorinated acids, solvents and plasmas. The Verdet constant of fused silica glass is approximately  $V = 2.9 \times 10^{-6}$  rad/Gm at 700-900 nm [208]. Verdet constant in general is a function of wavelength, typically growing dramatically towards the blue end of the visible spectrum. Becquerel related the Verdet constant also with the dispersion  $dn/d\lambda$  of the material. The Faraday rotation of a material like a glass is given by

$$\phi = VBl \quad (4.79)$$

$V$  is the Verdet constant,  $B$  the magnitude of the magnetic field and  $l$  the thickness of the material.

The total Faraday rotation produced by the six windows of our oven at a field of  $B = 100$  mG is calculated to be  $\phi = 1.7 \times 10^{-9}$  rad, which is close to the shot-noise angle limit at  $P=1$  mW and can be barely observed with the polarimeter of our experimental setup for a measurement time of 1 sec. Note that in paramagnetic Faraday measurements the above effect is negligible, however it must be accounted in diamagnetic Faraday measurements where the magnetic field is parallel to the light propagation axis.

## 4.6 Lasers and Optical Fibers



**Figure 4.9:** Picture of the lasers (Toptica DL-780 pro and DL-850 pro) used to probe the equilibrium spin dynamics via Paramagnetic Faraday rotation in our spin-noise measurements.

In the experiment we use cw semiconductor external cavity diode lasers (ECDL)

provided by Toptica-photonics. More specifically, the models are DL pro 850 and DL pro 780 and both lasers are tuned to probe the  $D_2$  optical lines of  $^{133}\text{Cs}$  and  $^{87}\text{Rb}$ , respectively. ECDLs are appropriate for spin-noise measurements because they provide a large mode-hop free tunability and a very good stability both in the frequency but also in the laser power. They have a very narrow linewidth and they can also be modulated easily using simple electronics. They can be further stabilized using PID feedback circuits that apply directly either to the laser current or the laser piezo, controlling the length of the cavity. The intensity fluctuations at the output of both lasers have been measured to be approximately of the order of 1%.

Each laser is controlled by a separate digital laser controller (Toptica DLC-pro) which provides a plethora of easily applied features. Both lasers come with a collimator lens and an integrated optical isolator to reduce back-reflections in the laser cavity that may cause all sort of instabilities. A broad review of ECDLs and their broad utility in atomic physics can be found in [209].

The DL-780 pro is tuned to  $\lambda_0 = 780.24$  nm and has a coarse tuning ranging in between 765-805 nm. It can provide a maximum output power of 90 mW at 239 mA of current while the lasing threshold of the diode is at 70 mA with a slope efficiency of 0.60 W/A. The geometry of the outgoing beam is rather Gaussian with a polarization ratio of 1:7.

The DL-850 pro is tuned to  $\lambda_0 = 852.36$  nm and has a coarse tuning ranging in between 840-875 nm. It can provide a maximum output power of 77 mW at 138 mA of current while the lasing threshold of the diode is at 38 mA with a slope efficiency of 0.78 W/A. The geometry of the outgoing beam is quite distorted and we use cylindrical lenses to reshape the beam which comes with a polarization ratio of 1:495. A photograph of the lasers in the experimental setup is given in Fig.4.9.

To perform fiber-coupling with high coupling efficiency and in order to have a precise knowledge of the beam waist at various positions along the beam propagation axis, we perform beam-waist measurements using the scanning knife-edge technique [98, 210, 211]. With this technique the beam intensity is modulated using an optical chopper at a frequency  $f_c$  where the light is collected with a photodetector and is presented with an oscilloscope referenced to the chopping frequency. For a demonstration of the technique visit the chopper section in Thorlabs website.

The indication at the oscilloscope is schematically depicted in Fig.4.10. If the beam center is at distance  $R$  from the chopper-wheel center then as the chopper blade crosses the beam, it covers an arc  $s = R\theta = R\omega_c t_r = 2\pi f_c t_r R$ . Here  $t_r$  is the rising time, measured using the oscilloscope. The rise time is measured between the 10% and 90%



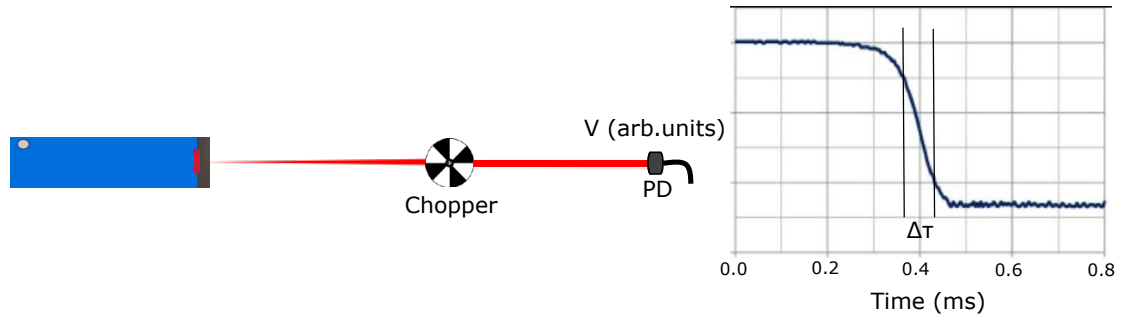


**Figure 4.10:** Scanning knife-edge technique for measuring the beam waist of the Gaussian laser beam. An optical chopper modulates the laser intensity at a frequency  $f_c$  and the intensity is monitored with an oscilloscope referenced to the chopping frequency. The figure indicates a rising intensity as a chopper blade crosses the laser beam.

intensity points. Then the beam diameter is given by  $D = 0.64 \times 2\pi f_c t_r R$ . If the chopper wheel contains  $N$  blades, then the diameter is given by  $D = 2\pi f_c t_r R/N$ . In the following table we present beam-waist measurements for both lasers using the scanning knife-edge technique at the position where the cell is placed. The Gaussian beam profile has been ensured by the use of a single mode optical fiber.

| Distance (cm) | beam-waist Cs laser (mm) | beam-waist Rb laser (mm) |
|---------------|--------------------------|--------------------------|
| –4            | 0.65-0.70                | 0.45-0.50                |
| –2            | 0.65-0.70                | 0.45-0.50                |
| 0             | 0.65-0.70                | 0.45-0.50                |
| +2            | 0.65-0.70                | 0.45-0.50                |
| +4            | 0.65-0.70                | 0.45-0.50                |

**Table 4.1:** Collection of beam waist measurements at the position of the cell. 0 cm correspond to the center of the cell while  $\pm 2$  cm and  $\pm 4$  cm are positions measured from the center of the cell. The measurements have been performed using the scanning knife-edge technique for both Cs and Rb lasers and both laser beams are fiber coupled before entering the cell. The optical fiber ensures the Gaussian beam profile. For the measurement we use a chopper with two large blades with rotation frequency  $f_c = 88.1$  Hz and distance from the center  $R = 3.8$  cm.

Regarding the fiber coupling, both lasers are coupled to a single mode, polarization maintaining (PM) optical fiber (Thorlabs P3-780PM-FC-2) with angled fiber patch (APC) tilted by an angle of  $8^\circ$ . The central wavelength of the fiber is 780 nm, however there is a large transmission also at 850 nm. The fiber length is 2m and the external protective jacket has a diameter of 3 mm. The working principle of the fiber is based on the PANDA technique where two linear polarization axes are formed inside the fiber by two stress rods that push the fiber core symmetrically. These polarization-maintaining fiber optic patch cables are terminated on both ends with narrow key, ceramic-ferrule FC/APC connectors and feature a high-quality polish, which leads to a typical return loss of 60 dB.

The mode field diameter (MFD) of the fiber is  $MFD = 5.3 \pm 1.0 \mu\text{m}$  at 850 nm with a numerical aperture of  $NA = 0.12$ . The mode field diameter is a measure of the width of an irradiance distribution, i.e., the optical power per unit area, across the end face of a single-mode fiber. It is similar to the  $1/e^2$  measure of beam diameter. For a Gaussian distribution, the mode field diameter is twice the standard deviation of the intensity. The MFD is typically slightly larger than the core of an optical fiber extending slightly into the cladding.

The numerical aperture (NA) of an optical system is a measure for its angular acceptance for incoming light. The numerical aperture of an optical fiber is defined as the product of the refractive index of the beam from which the light input is received (air) and the sine of the maximum ray angle against the axis, for which light can be transmitted through the system based on purely geometric considerations (fiber)  $NA = n \sin \theta_{max}$ .

Polarization-maintaining fibers work by intentionally introducing a systematic linear birefringence in the fiber, so that there are two well defined polarization modes which propagate along the fiber with very distinct phase velocities. The beat length  $L_b$  of such a fiber (for a particular wavelength) is the distance (typically a few millimeters) over which the wave in one mode will experience an additional delay of one wavelength compared to the other polarization mode. Thus a length  $L_b/2$  of such fiber is equivalent to a half-wave plate.

For low-noise experiments, APC fibers with AR-coated ports are preferable since flat fibers may behave like an optical cavity where long-lived standing waves are generated at the interior and could propagate in a multi-mode fashion after the fiber. In that case we expect the power spectral density of photon shot noise to drift and fluctuate in a random fashion translated in random explosions of the intensity variance in the time domain.

To efficiently couple the laser light (laser light from both lasers) into the optical fiber we walk the beam with two mirrors in each laser beam and then we combine both with a 50:50 beam splitter. A polarizer before the input of the fiber defines a strong linear polarization (that may have been distorted from the previous optical elements) and a half-waveplate ( $\lambda/2$ ) rotates the linear polarization to be parallel to the fast axis of the fiber. Usually the slow axis is parallel to the narrow key lock of the fiber.

For efficient coupling we need both laser beams to have the approximately equal beam diameter at the input of the fiber-coupler. To achieve this, we measure the diameter of the Rb laser with the scanning knife-edge technique described before and then we use cylindrical lenses and telescope to bring the radius of the Cs laser as close to the measured Rb-diameter as possible.

For a quick reference of the working principle of the optical telescope, if the input



beam diameter is  $w_1$  and we need an output diameter  $w_2$  then we can use two different lenses with focal lengths  $f_1$  and  $f_2$  where the distance between them must be  $d = f_1 + f_2$ , then the output diameter is given by  $\frac{w_2}{w_1} = \frac{f_2}{f_1}$ . By proper choice of  $f_1$  and  $f_2$  we can magnify or shrink the beam radius at the output. Having knowledge of the beam diameter and the MFD of the optical fiber we have to choose the proper focal length of the coupling lens. This is given from the relationship

$$f = \frac{\pi[MFD]d}{4\lambda} \quad (4.80)$$

where  $d$  is the beam diameter and  $\lambda$  the incident wavelength. In our experiment we use Throlabs collimators consisting of lenses with adjustable focal length. The lenses are AR-coated to avoid back-reflections or unwanted propagation in the fiber. If the focal length is not optimum, or the beam diameter has not been measured precisely, then there is a mismatch that costs in coupling efficiency. The losses due to this mismatch are given by

$$L = -10 \log \left[ \frac{4}{\left(\frac{w_2}{w_1} + \frac{w_1}{w_2}\right)^2} \right] \quad (4.81)$$

where  $w_1$  is the measured diameter and  $w_2$  the optimum.

The same lens is used at the output of the fiber in order to collimate the laser beam. Since the two wavelengths are different, one laser beam might be slightly more collimated than the other. Using this scheme we achieve a coupling efficiency of approximately 50 – 60% for both lasers. The formula above can be reversed in order to calculate the output beam diameter  $d$  given a collimator with focal length  $f$ .

## 4.7 Absorption Measurements

The number density of the alkali vapor and the buffer gas pressure in the cell can be measured, at least for small temperatures, by performing absorption measurements as shown schematically in Fig.4.11. For temperatures ranging from 30° C to 80° C, the absorption spectrum can provide a precise indication of the vapor's density either by integrating the whole spectrum or by fitting it using Beer's law for absorption. At higher temperatures, usually the absorption spectrum is saturated and we need other methods to measure the number density of the atoms in the cell. The Beer's law for the transmitted laser power reads

$$P = P_0 e^{-n\sigma_{abs}(\nu)l} \quad (4.82)$$



where  $n$  is the number density of the atoms,  $\sigma_{abs}(\nu)$  the absorption cross-section at the laser frequency  $\nu$  and  $l$  the averaged path length of light in the vapor<sup>20</sup>. The integral of the absorption cross-section over the whole range of frequencies is constant and is given by

$$\int \sigma_{abs} d\nu = \pi r_e c f_{ge} = \frac{1}{nl} \int \ln\left[\frac{P_0}{P(\nu)}\right] d\nu \quad (4.83)$$

The absorption rate expresses *the probability per unit time of a single photon to be absorbed by the whole vapor of number density  $n$* . Therefore, we can think of the absorption cross-section as the probability of a single atom to absorb a single photon from a probe beam of dimensions 1 cm  $\times$  1 cm. If in general the probe beam area is  $A$ , then the aforementioned probability is given by  $\frac{\sigma_{abs}}{A}$ . For a numerical example, the lifetime of a Cs vapor in the  $D2$  line is  $\tau_{nat} \approx 30$  ns. So, every 30 ns an atom absorbs a resonant photon with probability  $\frac{\sigma_{abs}}{A} = 10^{-7}$ , for a beam of  $A = 1$  mm  $\times$  1 mm and a resonant absorption cross-section  $\sigma_{abs} = \frac{\lambda^2}{2\pi} = 10^{-9}$  cm<sup>2</sup>. Equivalently,  $10^7$  atoms absorb a resonant photon with probability 1 every 30 ns or  $10^7$  atoms absorb  $3 \times 10^7$  photons/sec. If the Cs density is  $10^{10}$  cm<sup>-3</sup> in a 1 cm long cell and a probe beam of  $A = 1$  mm  $\times$  1 mm we have  $10^8$  atoms that absorb  $3 \times 10^8$  photons/sec = 300 Mphotons/sec.

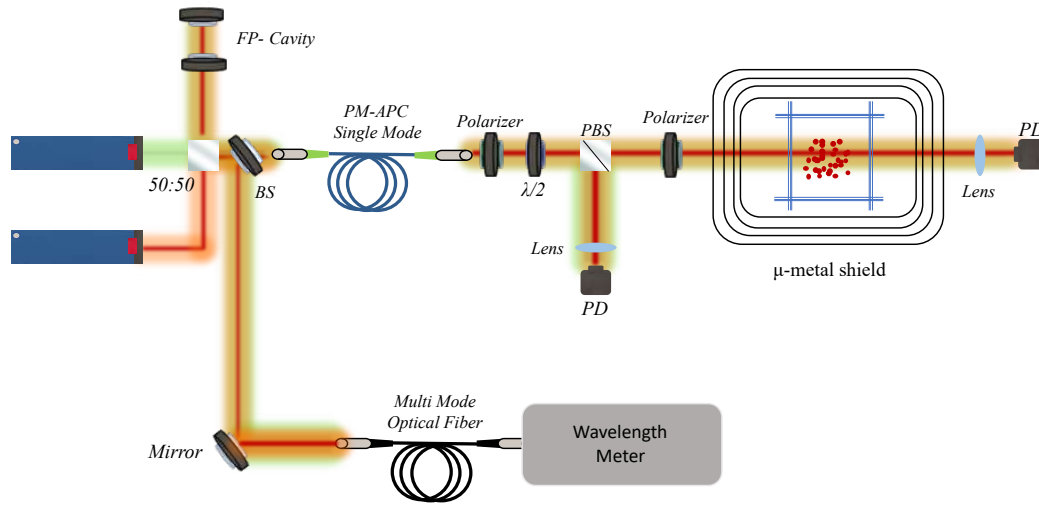


**Figure 4.11:** Experimental setup for measuring absorption. Both lasers are fiber-coupled to a single mode polarization maintaining APC optical fiber. A polarizer after the fiber reshapes the light polarization and then a half-waveplate followed by a PBS control the amount of light that is sent to the cell. Most of the light is sent in a photodiode before the cell to keep track of the incident laser power. After the PBS a final polarizer has been used to drop further the power sent to the cell. A photodiode after the cell measures the transmission. A FP cavity ensures the single mode operation of both lasers and a wavelength-meter reports absolute values of the laser's frequency.

As we can see in the schematic of the experimental setup, both lasers are fiber-

<sup>20</sup>This is given usually by the length of the cell by subtracting the length of the two cell-windows ( $L_{cell} - 2l_g$ ).

coupled in a (single-mode, polarization-maintaining APC with anti-reflection coatings) optical fiber and they are both send through the cell. A polarizer after the fiber is aligned with the polarization axis of the fiber and is placed there to reset the polarization state and to transform any unwanted polarization fluctuation into intensity fluctuation<sup>21</sup>.

A half-waveplate with a PBS are used to send most of the laser power at a photodetector before the vapor cell and finally, an almost crossed-polarizer ensures that the light-power send to the cell is negligible<sup>22</sup>. The wavelength of both lasers is scanned by scanning the cavity length of the laser and the absorption profile is observed in an oscilloscope referenced to the scanning frequency of the wavelength.

A Fabry-Perot confocal cavity ensures the single mode operation of both lasers as they are scanned through the optical resonance and a wavelength-meter reports absolute values of the laser's frequency. The laser wavelength jitter was about 10 MHz, much smaller than the width of the pressure broadened lines, so no instrumental corrections were needed.

In fact, birefringence effects from the glass of the vapor cell can produce a small amount of elliptical polarization that can contribute to the optical pumping process of the atoms. The small amount of optical pumping can produce a small but appreciable amount of spin polarization that may affect the absorption profile through a rank-1 vector cross-section augmented to the rank-0 equilibrium. If the scanning rate of the wavelength is comparable to the optical pumping rate, then the first pass of the scan will polarize the vapor while the second will report a different absorption spectrum than the one observed in the first pass.

In our experiment, in order to eliminate this excess pumping effect, we drop the laser power below  $P = 1\mu\text{W}$ . In this way, the signal arriving at the photodetector after the cell is almost equal to zero and very noisy even when maximum gain is used at the photodetection process. Therefore, we average a lot of spectra ( a lot of scanning cycles) to reduce the noise and observe a nice equilibrium absorption spectrum. The scanning rate of the piezo of the laser cavity was set to  $f_0 = 100$  Hz with a triangle scanning shape and a large scanning amplitude corresponding approximately to 30 GHz mode hop-free scanning of the laser frequency.

To achieve this large mode hop-free range, the feed-forward mode of the laser was used, where the scanning shape of the cavity is also imprinted in the laser's current

<sup>21</sup>This is a consequence of Malus law in the case of a fluctuating incident polarization.

<sup>22</sup>Small amount of laser power is required because (i) the light intensity must be smaller than the saturation intensity ( $I \ll I_{sat}$ ), where  $I_{sat} = \frac{E_{ph}}{\sigma_{abs}\Gamma_{abs}}$  and (ii) we need to decrease the pumping rate  $R_p = \int \sigma_{abs}(\nu)\Phi(\nu)d\nu$  in order to eliminate any effect of optical pumping that could distort the equilibrium absorption profile.



and affects the laser power synchronously with the cavity scan. The feed-forward factor ranging from -1 to 1 controls the amount of triangle modulation passing to the laser current.

This power modulation is clearly evident in both photodetectors during the piezo scan and in order to be removed we divide the transmission signal with the incident signal, using as a final observable the ratio  $P/P_0$ . This signal division is not always optimal, and some remnant signal may completely deform the absorption spectrum. The reason is that as the laser cavity is scanned, there is also a spatial beam modulation in real space (evident also with the bare eye) that sets an obstacle when complete cancellation of the feed-forward effect is required. This effect is magnified when using lenses to focus the light at the input of the photodetector.

To avoid this spatial modulation, we use the optical fiber, so any modulation in free space is transformed into a modulation of the coupling efficiency and subsequently into a fluctuation of the laser intensity after the fiber. This fluctuation is eliminated after taking a few averages of the absorption spectrum.

Finally, to eliminate further any residual pumping effect we apply a very small transverse magnetic field, therefore, any remnant spin polarization will be rapidly depolarized within a few  $\mu s$ , which is fast compared to the wavelength scanning cycle being of the order of 10  $m s$ .

In Fig.4.12 (a) and (b) we plot the absorption spectra of two different reference cells containing  $^{85}\text{Rb}$  and  $^{87}\text{Rb}$  in natural abundance and  $^{133}\text{Cs}$ , respectively. The measurements have been performed in room temperature ( $T = 29^\circ\text{C}$ ). The lines are inhomogeneously broadened due to the Doppler effect and the separations between the hyperfine peaks have been used to calibrate the frequency axis in units of GHz<sup>23</sup>. To ensure that the frequency axis is calibrated properly we compare our measurements with the theoretical predictions given in [50] and we find quite nice agreement.

In Fig.4.12 (c) and (d) we plot the absorption spectra taken at  $T = 60^\circ\text{C}$  from a vapor cell containing 72%  $^{87}\text{Rb}$  and 28%  $^{133}\text{Cs}$ . The cell also contains 329 Torr of  $N_2$  buffer gas. The buffer gas pressure and the number densities of the vapors can be estimated by fitting the data using Beer's law with a cross-section having Lorentzian response as indicated in the figure.

The fitted function is given by Eqs. (4.84) and (4.85). The vapor number density can be estimated using Eq.(2.5.1), since the integral of the cross section over all frequencies is constant and depends only on constant parameters. Although this method is only valid

<sup>23</sup>In the calibration process we assume that the laser scan is linear in frequency which is to a large extent a good approximation



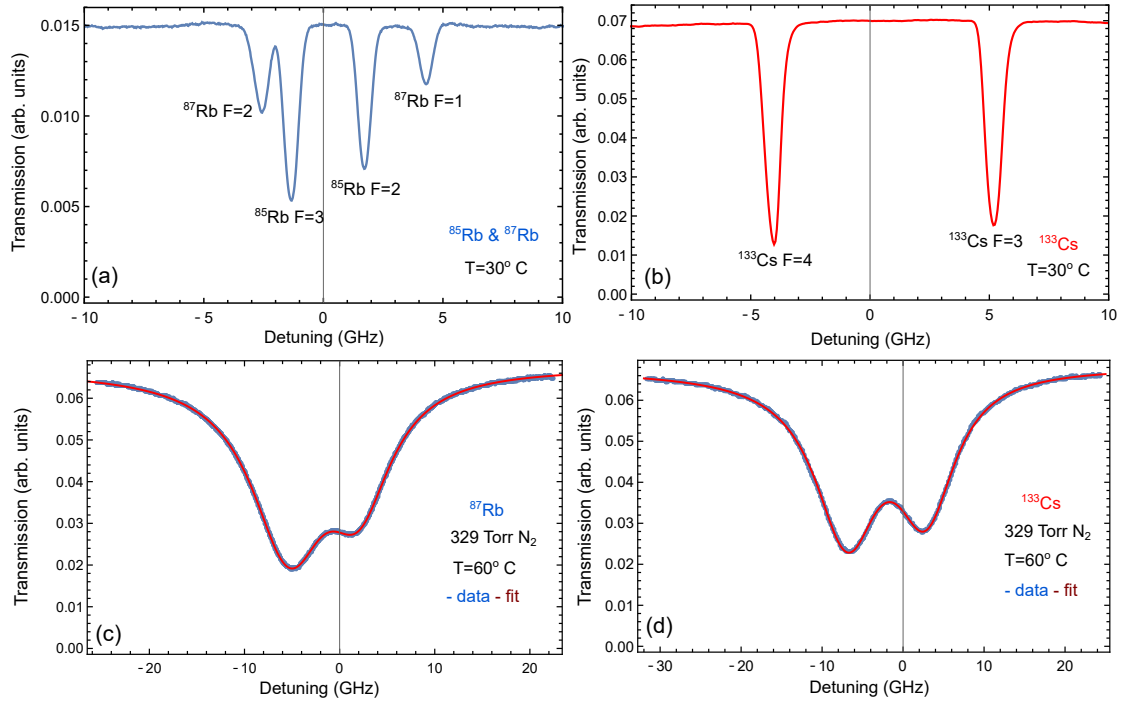


**Figure 4.12:** Absorption Measurements of  $D_2$  optical lines of Rubidium and Cesium. (a) In order to calibrate the frequency axis, we perform absorption measurement of Rb vapor using a reference cell in natural abundance at  $T = 30^\circ\text{C}$ . (b) Cesium absorption measurement using a Doppler broadened reference cell. (c)  $^{87}\text{Rb}$  absorption spectrum at  $T = 60^\circ\text{C}$ . The cell contains 329 Torr of Nitrogen buffer gas and  $^{133}\text{Cs}$ . (d) Absorption spectrum of  $^{133}\text{Cs}$  in the same cell with (c). The spectra are fitted using Beer's law for the transmission with a Lorentzian pressure broadened absorption cross-section. As indicated in the text, a dispersive first order correction in the absorption cross section is applied due to the interactions of the alkali atoms with the Nitrogen buffer gas.

at low temperatures, in the limit of high temperatures the absorption signal is saturated to zero and different ways to calculate the density must be adapted [154].

$$P(\nu) = P_0 \text{Exp} \left( -A \left( \frac{3}{8} \frac{\frac{\Gamma_1}{2}}{(\nu - \nu_1)^2 + (\frac{\Gamma_1}{2})^2} + \frac{5}{8} \frac{\frac{\Gamma_2}{2}}{(\nu - \nu_2)^2 + (\frac{\Gamma_2}{2})^2} \right) - B \frac{\nu - \nu_1}{(\nu - \nu_1)^2 + (\frac{\Gamma_1}{2})^2} - C \frac{\nu - \nu_2}{(\nu - \nu_2)^2 + (\frac{\Gamma_2}{2})^2} \right) \quad (4.84)$$

$$P(\nu) = P_0 \text{Exp} \left( -A \left( \frac{7}{16} \frac{\frac{\Gamma_1}{2}}{(\nu - \nu_1)^2 + (\frac{\Gamma_1}{2})^2} + \frac{9}{16} \frac{\frac{\Gamma_2}{2}}{(\nu - \nu_2)^2 + (\frac{\Gamma_2}{2})^2} \right) - B \frac{\nu - \nu_1}{(\nu - \nu_1)^2 + (\frac{\Gamma_1}{2})^2} - C \frac{\nu - \nu_2}{(\nu - \nu_2)^2 + (\frac{\Gamma_2}{2})^2} \right) \quad (4.85)$$

where the first equation corresponds to the  $^{87}\text{Rb}$  and the second to  $^{133}\text{Cs}$ . In each equation, the first two terms are Lorentzian profiles due to the homogeneous pressure broadening of the absorption line each being weighted by the total transition strength of the particular hyperfine level. The last two dispersive terms are first order corrections

to the Lorentzian absorption profile due to the interaction of the alkali atoms with the atoms of the buffer gas [72, 212].

The parameters  $P_0, A, B, C, \nu_1, \nu_2, \Gamma_1$  and  $\Gamma_2$  are allowed to vary in order to minimize the  $\chi^2$  of the fit. The parameters  $\nu_1, \nu_2$  are the resonant frequencies and  $\Gamma_1, \Gamma_2$  the linewidths (HWHM) corresponding to the optical resonances ( $D_2$ -line). The fit-parameter  $A$  is related to the vapor number density  $n$  through

$$A = n\pi r_e c f_{ge} l \quad (4.86)$$

where  $r_e$  is the classical electron radius,  $c$  the speed of light in vacuum and  $f_{ge}$  the oscillator strength. In the following table, we present the measured density values obtained at various temperatures both using the fitted functions, and the integrated-spectrum method.

| Temperature | $n_{Cs}$              | $n_{Rb}$              | $n_{Cs} - Integral$   | $n_{Rb} - Integral$   |
|-------------|-----------------------|-----------------------|-----------------------|-----------------------|
| 30°C        | $1.15 \times 10^{10}$ | $1.59 \times 10^{10}$ | $1.06 \times 10^{10}$ | $1.56 \times 10^{10}$ |
| 40°C        | $3.15 \times 10^{10}$ | $3.57 \times 10^{10}$ | $2.67 \times 10^{10}$ | $3.82 \times 10^{10}$ |
| 50°C        | $9.19 \times 10^{10}$ | $1.00 \times 10^{11}$ | $7.68 \times 10^{10}$ | $1.04 \times 10^{11}$ |
| 60°C        | $2.23 \times 10^{11}$ | $2.35 \times 10^{11}$ | $1.89 \times 10^{11}$ | $2.60 \times 10^{11}$ |
| 70°C        | $5.19 \times 10^{11}$ | $5.53 \times 10^{11}$ | $4.35 \times 10^{11}$ | $5.94 \times 10^{11}$ |
| 80°C        | $1.13 \times 10^{12}$ | –                     | $9.43 \times 10^{11}$ | –                     |

**Table 4.2:** Collection of density measurements for various temperatures using the absorption spectrum. The cell contains 329 Torr  $N_2$ . All density values are in  $cm^{-3}$ . The first two columns display the densities extracted from the fitted spectra, whereas the next two columns display the densities calculated by the integral of the absorption spectrum over a frequency range around the absorption line.

In the case of large pressure broadening (compared to the Doppler broadening) the absorption cross-section is given by [72]

$$\sigma_{abs}(\nu) = \pi r_e c f_{ge} \frac{\Gamma/2\pi}{(\nu - \nu_0)^2 + (\frac{\Gamma}{2\pi})^2} \left(1 - \frac{11 - 4J_e(J_e + 1)}{4} \langle \mathbf{S} \cdot \mathbf{s} \rangle\right) \quad (4.87)$$

where  $\mathbf{s}$  is the photon spin,  $J_e$  the excited state total orbital angular momentum and  $\Gamma$  the HWHF of the pressure broadened profile. In the case where the atomic polarization  $\langle \mathbf{S} \rangle$  points in the same direction as the photon spin  $\mathbf{s}$  then the absorption cross section can be written as

$$\sigma_{abs}(\nu) = \pi r_e c f_{ge} \frac{\Gamma/2\pi}{(\nu - \nu_0)^2 + (\frac{\Gamma}{2\pi})^2} \left(1 - \frac{11 - 4J_e(J_e + 1)}{8} P_z\right) \quad (4.88)$$

where  $P_z$  is the alkali spin polarization pointing for example along the  $\hat{z}$ -direction. In the case of zero optical pumping, therefore zero polarization, the absorption cross section is related to the imaginary part of the scalar polarizability  $a_0$  and is given by

$$\sigma_{abs}(\nu) = \pi r_e c f_{ge} \frac{\Gamma/2\pi}{(\nu - \nu_0)^2 + (\frac{\Gamma}{2\pi})^2} \quad (4.89)$$



and the resonance absorption cross-section reads

$$\sigma_{abs}(\nu) = \frac{2r_e c f_{ge}}{\Gamma} \quad (4.90)$$

In the most general case, the absorption profile depends on the natural lifetime, the pressure broadening, and the Doppler broadening. The Doppler lineshape stemming from the Maxwell distribution of thermal velocities is described by a Gaussian profile [50]

$$G(\nu - \nu_0) = \frac{2\sqrt{\ln 2/\pi}}{\Gamma_G} \text{Exp}\left(-\frac{4\ln 2(\nu - \nu_0)^2}{\Gamma_G^2}\right) \quad (4.91)$$

where  $\Gamma_G = 2\frac{f}{c}\sqrt{\frac{2\ln 2k_B T}{M}}$  is the Doppler broadening defined in Eq.(2.94). If the Doppler broadening is comparable to the pressure broadening then the atomic response is most effectively described by the Voigt profile [50] being a convolution of the Lorentzian pressure and the Gaussian Doppler broadenings.

$$V(\nu - \nu_0) = \int_0^{+\infty} L(\nu - \nu')G(\nu' - \nu_0)d\nu' \quad (4.92)$$

which can be expressed in complex form as

$$V(\nu - \nu_0) = \frac{2\sqrt{\ln 2/\pi}}{\Gamma_G} w\left(\frac{[2\sqrt{\ln 2}(\nu - \nu_0) + i\Gamma_L/2]}{\Gamma_G}\right) \quad (4.93)$$

where  $w(x)$  is the complex error function given by

$$w(x) = e^{-x^2} \text{erfc}(-ix) \quad (4.94)$$

with  $\text{erfc}(x)$  being the complex complementary error function related to the usual error function via  $\text{erfc}(x) = 1 - \text{erf}(x)$ . In terms of the Voigt profile, the absorption cross-section is given by

$$\sigma_{abs}(\nu) = \pi r_e c f_{ge} \text{Re}[V(\nu - \nu_0)] \quad (4.95)$$

Fitting an absorption signal with the Voigt profile is computationally demanding and difficult. It has been shown [213, 214] that the following numerical approximation can be applied

$$V(\nu - \nu_0) = c_L(d)L(\nu - \nu_0) + c_G(d)G(\nu - \nu_0) \quad (4.96)$$

namely, the Voigt profile is approximated by a weighted sum of the Lorentzian and the Gaussian profiles. Here the dimensionless parameter  $d$  is defined as

$$d = \frac{\Gamma_L - \Gamma_G}{\Gamma_L + \Gamma_G} \quad (4.97)$$

and the coefficients  $c_L$  and  $c_G$  are given by the relations

$$c_L = 0.68188 + 0.61293d - 0.1838d^2 - 0.11568d^3 \quad (4.98)$$

$$c_G = 0.3246 - 0.61825d + 0.17681d^2 + 0.11568d^3 \quad (4.99)$$

The width of the Voigt profile can be approximated to within 0.01% using the Olivero-



Longbothum formula [213, 215] given by

$$\Gamma_V = 0.5346\Gamma_L + \sqrt{0.2166\Gamma_L^2 + \Gamma_G^2} \quad (4.100)$$

## 4.8 Magnetic Shield

In experiments where the coherent spin precession is of central interest, magnetic shields are commonly used in order to reduce or completely eliminate the static or low-frequency environmental magnetic fields, like the Earth’s magnetic field. These external fields may be spatially distributed in a way that they could generate magnetic gradients, which reduce significantly the coherence lifetime of the spin. On the other hand, if these fields are fluctuating they may introduce magnetic noise, which is also an important source of decoherence, especially in the case of spin-polarized atoms. In both cases, a shield from high-permeability ferromagnetic material ( $\mu > 10^5$ ) can empty the magnetic environment in a given region and therefore boost significantly the spin-precession lifetime.

In our experiment we use a four layer cylindrical magnetic shield from mu-metal (Manufacturer: [Twinleaf](#)) as shown in Fig.4.13. Mu-metal is one of the best ferromagnetic materials for shielding low-frequency or dc magnetic fields. It is a mixture of nickel, iron, copper and chromium or molybdenum [216]. The efficiency of the shield is characterized by the shielding ratio i.e. the magnitude of the magnetic field outside the shield compared to that inside,

$$T = \frac{B_{\text{ext}}}{B_{\text{int}}} \quad (4.101)$$

and is measured with a fluxgate magnetometer to be approximately  $10^4$ . An approximate calculation of the shielding factor for a shield of  $n$  layers of diameter  $D$  is given by [48, 217, 218]

$$T_{\text{tot}} \approx T_n \times \prod_{i=1}^{n-1} T_i \left[ 1 - \left( \frac{D_{i+1}}{D_i} \right)^k \right] \quad (4.102)$$

In Eq.(4.102),  $D_i$  is the diameter of the  $i_{th}$  layer and  $T_i$  is the individual layer shield factor given by  $T_i \approx \frac{\mu_i t_i}{D_i}$  and  $k$  is a factor depending on the geometric characteristics of the shield. For a cylindrical shield,  $k = 2$ . Here,  $t_i$  is the thickness of the  $i_{th}$  layer and  $\mu_i$  the magnetic permeability relative to the value in free space.

Inside the shield there are 3 internal magnetic field coils that can hold up to 1 Amp of current. The z-axis coil is larger than the other two and it is designed for high axial Z field uniformity. The coil calibrations provided by Twinleaf are

- Z-coil calibration: 1.05 G/A

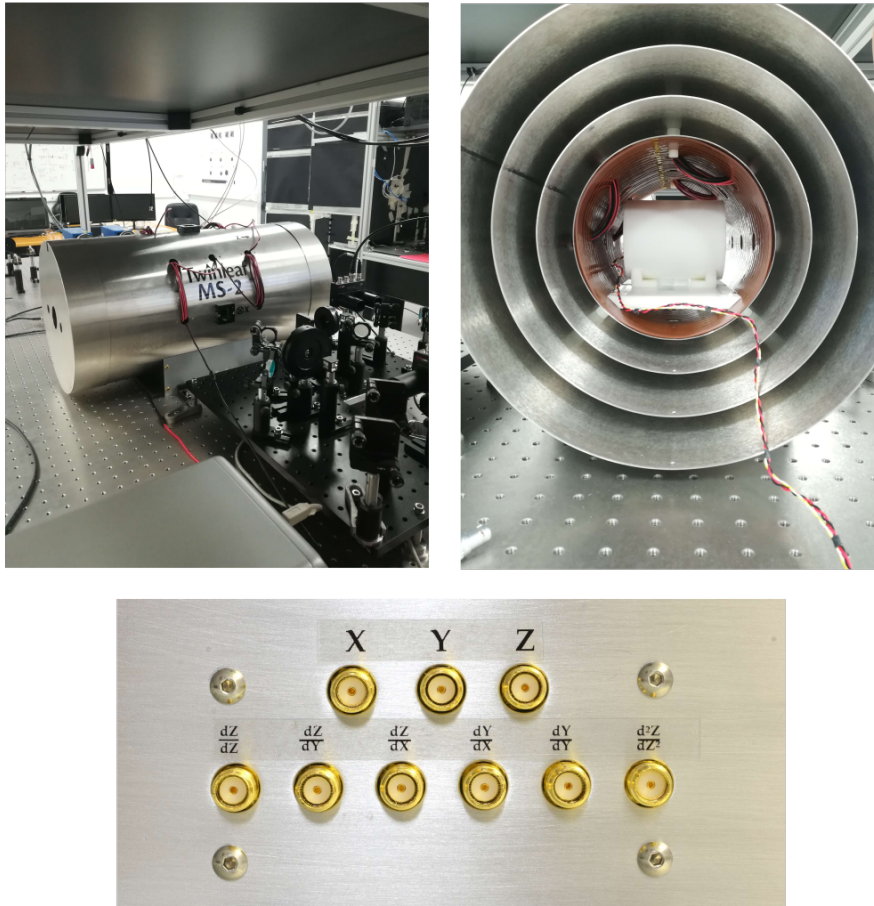


**Figure 4.13:** Front and Side view of the magnetic shield used in our experiment. The bottom picture is taken from [Twinleaf](#) and shows the field and the gradient directions that can be controlled through dc or ac current sources.

- X/Y-coil calibration: 0.576 G/A

To verify the above calibrations and to make sure that our current sources and the magnetometer are calibrated properly we measure the magnetic field for different applied currents as shown in Fig.4.14. The current was applied using two different sources.

For low currents we use the Twinleaf CSBA which provides very low noise current in the range of  $\pm 10$  mA. The main features of this source is that the current drift is  $< 10$  ppm/ $^{\circ}$ C and there is also galvanic isolation of the drivers from the power supply of the current source. For higher currents we used a laser diode current controller (Thorlabs ITC502) which can generate up to 500 mA of stable current. We have verified that for unpolarized atoms, the current fluctuations of the sources do not consist a limitation of the spin precessing signal.

The shield contains also internal stage with breadboard hole pattern made out of teflon with non-magnetic plastic screws in order to fix the oven in the proper position. There is a large axial hole of 46 mm diameter and smaller transverse holes of 18 mm diameter for beam and cable access.

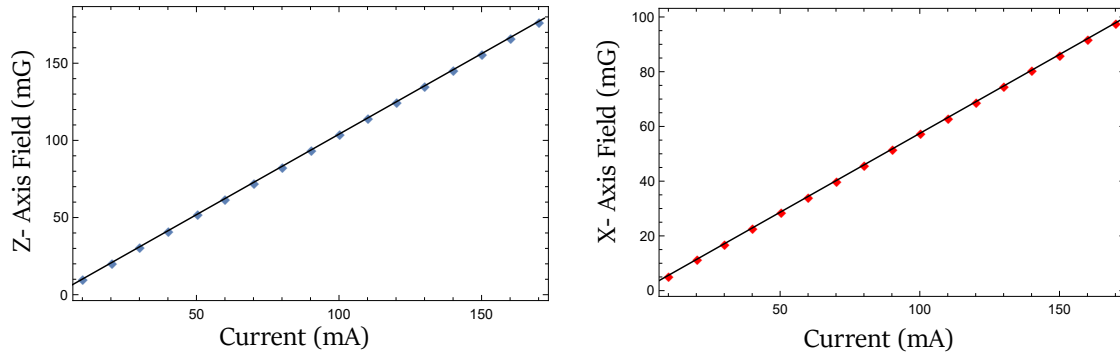


**Figure 4.14:** Z and X coil magnetic fields as a function of the applied current. The black line represents linear fit to the measured data. For the Z coil the fit is  $y = -0.33 + 1.04x$  giving a calibration coefficient of 1.04 G/A while for the X coil the fit is  $y = -0.18 + 0.576x$  with calibration coefficient 0.576 G/A. Note both coefficients are in perfect agreement with the ones given by Twinleaf. The current is produced from Thorlabs ITC502 current source and the magnetic field is measured with a fluxgate magnetometer (Bartington Mag-03MC).

In Fig.4.15 we plot the magnetic field produced from the large z-field coil and measured with the fluxgate magnetometer as a function of the position of the magnetometer along the z-axis. The magnetometer is changed each time by a step of 1cm. The magnetic fields  $B_x$  and  $B_y$  are chosen such that at the center of the shield the field is zero, in that way the figure represents the field  $B_z(0, 0, z)$ . More plots about the field uniformity of the shield can be found at the website of Twinleaf.

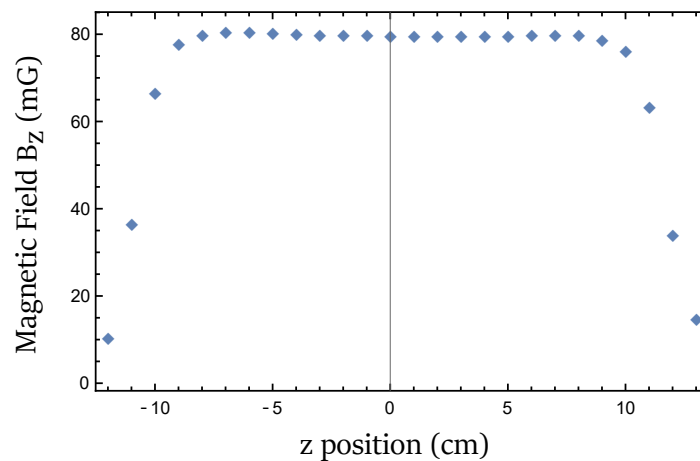


**Figure 4.15:** Plot of  $B_z(0, 0, z)$  as a function of  $z$ , as measured with the fluxgate magnetometer. The applied field along the z-axis is about 80mG and it shows high axial uniformity. For each measurement the magnetometer is moved by approximately 1cm.

The magnetic field noise and the current source noise spectrum are represented in Fig.4.16. Magnetic field noise of the shield is caused by thermal fluctuations of the magnetic domains (magnetization fluctuations) and thermal agitation of conduction electrons in the innermost layer of the shield [48, 219]. The magnetic noise is of the

order of  $1 - 10 \times 10^{-10} \frac{G}{\sqrt{\text{Hz}}}$ . For example in [121] it has been shown that for a large thin metal sheet of resistivity  $\rho$  at finite temperature  $T$ , the rms magnetic fluctuations at a distance  $a$  from the sheet is given by

$$\langle B^2 \rangle = \frac{4k_B T t \Delta f}{c^2 \rho a^2} \quad (4.103)$$

where  $\Delta f$  is the measurement bandwidth and  $t$  is the thickness of the metal sheet. This formula follows from the Johnson noise firstly introduced to describe the voltage fluctuations across a resistor at temperature  $T$

$$\langle V^2 \rangle = 4k_B T R \Delta f \quad (4.104)$$

Note that Eq.(4.103) indicates that magnetic field noise is white noise, namely, independent of frequency. This approximation is true only for low frequencies. In reality, these magnetic field fluctuations produce fluctuating currents (Eddy currents) which in turn consist a new source of magnetic noise. As it is calculated in [121], these induced currents tend to significantly reduce magnetic field fluctuations above a cut-off frequency given by

$$f^* = \frac{c^2 \rho}{2\pi a t} \quad (4.105)$$

This effect is known as self-shielding effect.

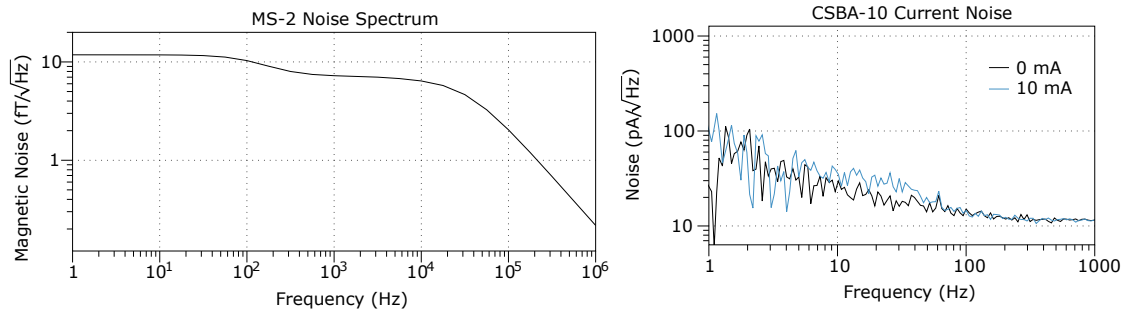


**Figure 4.16:** Taken from: [Twinleaf Website](#). Left plot indicates the magnetic field noise of the magnetic shield used in our experiment as function of frequency. For low frequencies the mean magnetic noise is  $10 \frac{\text{fT}}{\sqrt{\text{Hz}}}$ . Right plot indicates the current noise spectrum produced by the Twinleaf CSBA for two different values of the current. The noise is below  $100 \frac{\text{pA}}{\sqrt{\text{Hz}}}$ .

### 4.8.1 Degaussing

The shield, being a ferromagnetic material, has a residual magnetization which in many cases produces an unwanted magnetic field resulting mostly from the innermost shielding layer. As a result of the magnetic hysteresis, the value of the residual magnetization can be altered due to changes of the applied magnetic field but also due to handling, mounting and loading of the shield [48]. In order to decrease the residual

magnetization and increase the effective permeability a procedure known as degaussing is applied.

Large cables that can handle a lot of amps are wired around the shield (mostly the inner layer) such that an applied ac current generates an alternating magnetic field which is high enough that the material reaches the saturation value in the hysteresis curve. Then the amplitude of the applied ac field is reduced adiabatically to zero and so does the residual magnetization.

For the degaussing process, we wrapped a 20m-long cable around all the layers of the shield as can be seen in Fig.4.13. The total resistance of the cable is  $R = 1.35\Omega$  and the maximum current that it can hold is between 10 – 15 A. In order to produce to ac-current we used a variac whose output is driven though a transformer. The transformer drops the output voltage to the 1/5 of the initial value. Thus, in order to get a current value of  $I = 10A$  we need  $V = IR = 10 \times 1.35 = 13.5$  Volt at the output of the transformer.

Therefore, the maximum value of the voltage output of the variac must be  $5 \times 13.5 \approx 70$  Volt. Since the voltage output must be decreased adiabatically, in practise, there is not enough time for the cable to burn, hence we can work at higher values of voltage but always with precaution.

### 4.8.2 Fluxgate Magnetometer

For precise knowledge of the magnetic field amplitude and direction, we used a flux-gate magnetometer (Bartington Mag-03MC). This sensor, is a three-axis magnetometer providing information about the magnetic fields at three vertical axis simultaneously. Fluxgate magnetometers operate optimally at low magnetic fields in the regime of Earth's magnetic field making them capable for measuring and calibrating magnetic fields for a big family of atomic physics experiments.

Fluxgate consists mainly of three parts, a soft iron core material, a drive coil and a pick-up coil. The drive coil periodically drives the magnetization of the iron core producing the hysteresis curve. During this process the pick-up coil measures the magnetic flux passing through the iron core. At the point where the magnetization is saturated (either positive or negative saturation) the magnetic permeability of the iron core drops significantly and as a result, the magnetic lines of an external magnetic field are pushed away from the iron core, while only the magnetic flux produced by the drive coils remain in the iron. When the core is not saturated, the permeability of the iron core is large allowing the magnetic lines of the external DC field to pass through the metal



and to produce a measurable magnetic flux.

The pick-up coil measures the changes in the magnetic flux through the iron, produced by the external magnetic field as the hysteresis curve is scanned, therefore information for the magnitude of the field can be extracted. Applying this process in three different axis with different iron cores and different coils, provides also information about the directionality of the magnetic field.

There are various geometries used to optimize the signal to noise ratio (SNR), and most of them rely on finding ways to eliminate the magnetic field produced by the drive coil, from the pick-up coil measurement. Of course there are many other details that affect significantly the SNR such as the softness of the iron core, the temperature stability, the isotropy of the sensor and the mechanical stability. Also care must be given to the electronics of the sensor to generate as minimum electronic noises as possible. As it is usually the case in all kind of magnetometers, there is a trade-off between the bandwidth (how fast the hysteresis curve is scanned) and the resolution of the magnetometer that can be optimized based on the application.

Finally, the SNR can be increased using synchronous detection, i.e. synchronizing the pick-up coil with the drive coil in order to measure when for example the flux is maximum and/or minimum [220]. According to the manufacturer the rms noise level of the magnetic sensor is  $8\text{pT}/\sqrt{\text{Hz}}$ . The conversion factor is  $1\text{V} \rightarrow 70\text{mG}$ .

## 4.9 Data Acquisition

Data acquisition is performed either in the time or in the frequency domain depending on the nature of the measurement. For spectral measurements, we use the vintage and precise Stanford Research Systems (SRS-785) dynamic signal analyzer whereas for time-domain measurements we use low noise analog to digital converters ( National Instruments DAQmx cards) and Labview.

The SRS spectrum analyzer provides a frequency span from DC to 128 kHz using a 8 ms time record. Because the signal passes through an anti-aliasing filter at the input, the entire frequency span is not useable. The flat response of the filter is from DC to 100 kHz and then rolls off steeply. The SRS provides a broad range of measurements like single and dual channel acquisition, FFT spectrum, power spectrum and power spectral density, cross-correlation spectrum, correlation, phase, coherence, etc. It provides also a lot of different choices of windows and a broad set of averaging choices.

In our measurements we use AC coupling, with a Hanning window, a span of 102.4 kHz divided into 800 FFT lines and a linear averaging. The acquisition time of each



repetition is  $T_{acq} = 7.81$  ms. Data from the SRS are communicated via a GPIB-to-USB cable to the computer and are decoded and saved using a Labview program which is also capable to control the operation of the SRS. Finally, after the required averages are completed, the data are saved in a .txt or in a .dat file.

In cases of a spectral measurement where a higher sample rate or a larger acquisition time are required, we have developed a pc-based spectrum analyzer using Labview. Special care has been given in the development of the spectrum analyzer to produce as similar results to the ones that SRS produces as possible. For the acquisition we use a low noise National Instruments DAQmx board (NI usb-6361) with maximum sampling rate of 2 Msamples/sec (for a single channel).

Comparison of shot noise measurements between the DAQ and the SRS, show that the DAQ-board introduces excess noise. This additional noise is a result of the aliasing effect and has been eliminated (i) by using a large sampling rate (500 kSamples/sec) (ii) by applying an analog low pass filter at the input of the record channel and (iii) by making use of short BNC cables<sup>24</sup>. The low pass analog filter consists of a resistor of  $R = 6.8$  k $\Omega$  and a capacitor of  $C = 100$  pF resulting in a cut-off frequency of  $f_c = 1/(2\pi RC) = 234$  kHz. The response and the phase of the filter are plotted in Fig.4.17.

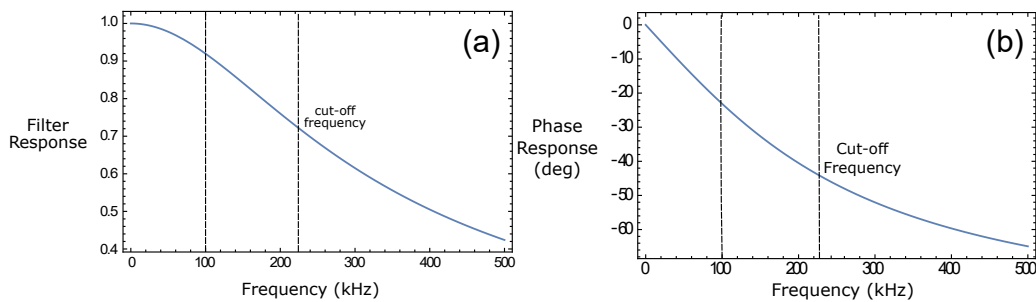


**Figure 4.17:** (a) Frequency response of the analog low pass filter placed at the output of the photodetector. The filter consists of a resistor of  $R = 6.8$  k $\Omega$  and a capacitor of  $C = 100$  pF resulting in a cut-off frequency at  $f_c = \frac{1}{2\pi RC} = 234$  kHz. (b) Calculated phase response of the filter as function of frequency.

In reality, the combination of the analog filter with the photodetector's bandwidth and the effective low-pass of the transmission cable produce a more complicated response but still good enough to avoid aliasing and to approach the SRS absolute values. For the power spectral density, we use a Hanning window and a linear RMS averaging.

Similarly, for time-domain measurements we use DAQmx and Labview. We record

<sup>24</sup>We use BNC-58U cables having a resistance of  $R = 50\Omega$  and a capacitance density of  $= 80$  pF/meter. Large BNC cables act as low pass filters (LPF). As an example, a  $L = 1$  meter cable is effectively a LPF with cut-off frequency  $f_c = 1/(2\pi \times 50\Omega \times 80\text{pF}) \approx 40$  MHz. The interested reader may consult the lecture notes of the undergraduate lab course Physics 77 of Caltech, namely "Transmission Lines and Electronic Signal Handling", May 2019.

the signals for an acquisition time  $T_{acq} = 1$  ms approximately 10 times larger than the  $T_2$  relaxation rate. (The rate has been estimated by the decay of the auto-correlation function of spin noise). After a single acquisition time is completed, the data are saved in a binary file (.bin) and were decoded in the post-processing session using Mathematica.

Measuring noise correlations with a single DAQmx board is not recommended mainly due to a cross-talk that exists between different channels. This is known as ghosting effect and is a result of a capacitive coupling of all channels of the board to a single common output.

To avoid the ghosting effect which impacts on the correlations and the photon-shot noise measurements, we use two different DAQ cards (NI usb-6361 and NI usb-6363) with their sample and start clocks being synchronized by exchanging fast digital pulses. Each board acquires data from a single photodetector and correlations are calculated in the post-processing section.

The input range was set to 1 Volt and since both boards have a resolution of 16-bit, the voltage resolution is  $\delta V = 30.5\mu V$ . The sampling rate and the record time is common to both DAQs and it was set to 500 kSamples/s and  $t_{max} = 1$  ms, respectively. The acquisition was repeated until all the  $N_{avg}$  are completed, where  $N_{avg}$  is the pre-determined number of averages. If the acquisition requires long runs of the order of a few hours, then the time traces were automatically saved and distributed among various files, each keeping a fraction of the total amount of averages. The amount of averages in each file and the amount of total files were selected based on the amount of data in bytes before the beginning of the acquisition.

### 4.9.1 Cross-Talk

Before measuring spin-noise correlations, in the absence of the atomic vapor, we perform a series of consistency checks to ensure that there is no cross-talk (or excess cross-correlations) between the two polarimeters generated from other than atomic sources of noise like for example electronic correlations or photon shot noise correlations.

Initially, we examine whether there is electronic cross-correlation between the two photodetectors, that might cause a bias correlation, positive or negative. In Fig.4.18 we present a set of measurements regarding the electronic noise.

In Fig.4.18 (a) we plot the time traces of the electronic noises for both photodetectors for an acquisition time of 1 ms. We find that they are both centered around zero. In (b) we plot the PSD of both electronic signals showing a technical noise peak centered around 6 kHz. In (c) we plot the time domain of electronic cross-correlation and we find a small



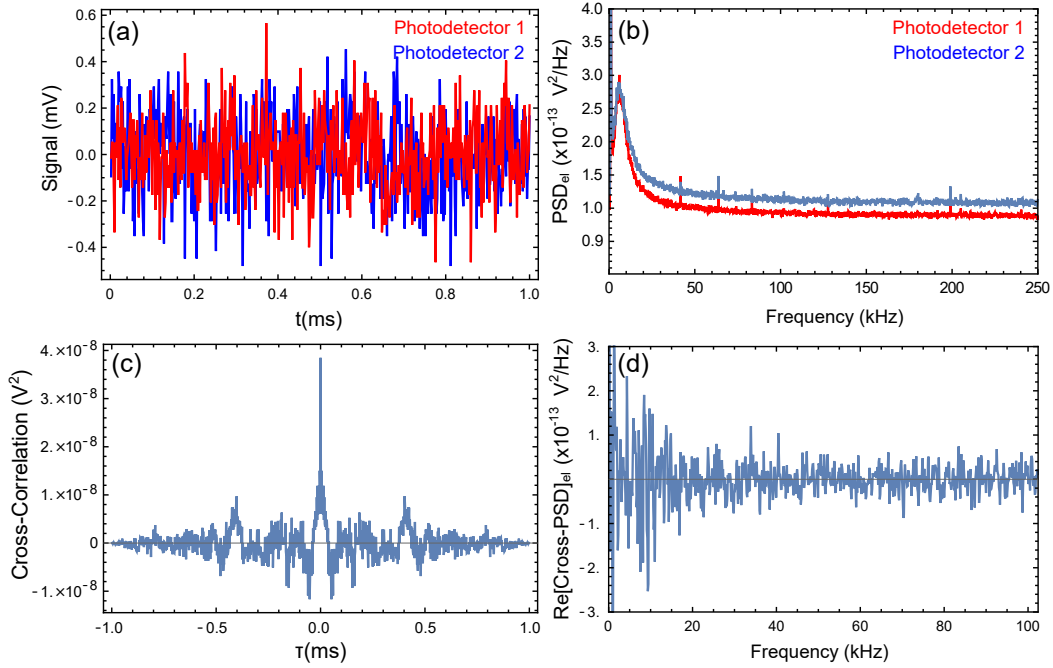


**Figure 4.18:** Set of electronic noise measurements for both photodetectors. (a) Time traces, (b) Power spectral density shows a large peak around 6 kHz for both detectors. (c) Cross-correlation in time domain of electronic noise indicates a very small bias correlation. This correlation is related to the peak shown in the PSD of fig. (c), and (d) Power spectral density of the cross-correlation spectrum of electronic noise. Again at low frequencies there is a noisy activity due to technical noise around 6 kHz.

correlation oscillating at about 6 kHz in agreement with the PSD spectrum and finally, in Fig.(d) we show the power spectral density of the cross-correlation function indicating a small noisy activity at small frequencies also consistent with the PSD spectrum in (b). The above plots quantify the electronic cross-correlation and ensure that the electronic cross-correlations are at least two orders of magnitude smaller than the atomic spin noise cross-correlations. This will be evident in the following discussion.

In order to test whether there is leakage of the one laser light into the opposite polarimeter we measure the cross-correlation when only a single laser is in operation. If there is no leakage we expect a zero cross-correlation whereas a small amount of leakage would result in a small Lorentzian peak in the power spectrum of the cross-correlation as a consequence of the single-species spin noise modulation. The time trace of the cross-correlations and the PSD spectra are shown in Fig.4.19.

All figures indicate a zero cross talk between the two polarimeters. We note that the noise in the cross-correlation spectrum of Fig.4.19(c) and (d) seems smaller than the electronic PSD in Fig.4.18, however this is an artificial effect due to different averaging conditions during the two measurements.

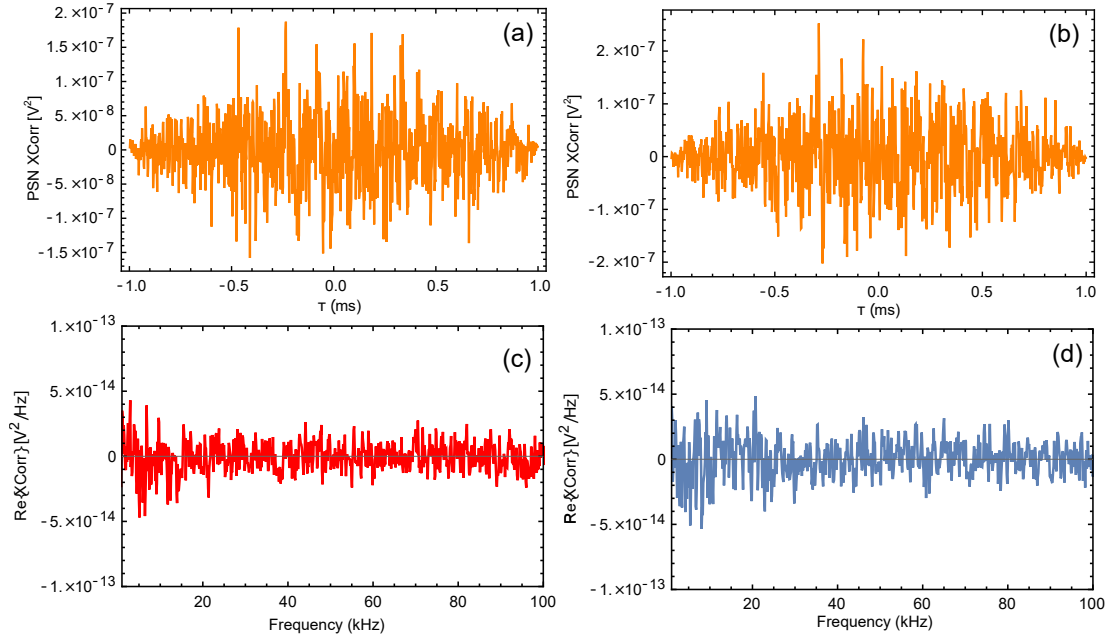


**Figure 4.19:** Cross-talk between the two polarimeters. (a) Cross-Correlation at the output of the two photodetectors when only the Rb laser is operating. (b) similar when Cs laser is operating. (c) and (d) represent the PSD of the real part of the cross-correlation also when one laser is operating at a time. All figures indicate zero cross talk between the two channels.

## 4.10 Spin-noise Spectrum and Spin-noise Broadening

The experimental setup for measuring spin-noise from dual species alkali vapors is presented in Fig.4.1 and has been already discussed at the beginning of Chapter 4. Here we recall its main features.

Two linearly polarized and far off-resonant laser beams are overlapped by a 50:50 beam splitter and subsequently fiber-coupled in a polarization maintaining single mode optical fiber. The spatially overlapped laser beam is sent through the vapor cell which is placed in a well-insulated oven, housed in a four layer mu-metal magnetic shield. The beam propagates along the  $\hat{z}$ -direction and an applied dc magnetic field along the  $\hat{x}$ -direction makes the two species to precess at their natural Larmor frequencies. We note that the gyromagnetic ratio of  $^{133}\text{Cs}$  is  $\gamma_{\text{Cs}} = 0.70 \text{ kHz/mG}$  and the gyromagnetic ratio of  $^{87}\text{Rb}$  is  $\gamma_{\text{Rb}} = 0.35 \text{ kHz/mG}$ . Therefore Cs atoms precess twice as fast as the Rb atoms.

Spontaneous spin-exchange collisions contribute i) to the relaxation of the spontaneous spin polarization generated in a random particular direction and ii) to the coherent exchange of spin-polarization between the two alkali species in as they precess in the magnetic field. The overlapped laser beam monitors the projection  $F_z$  of the collective spin  $\mathbf{F}$  along the beam direction for both alkali vapors.

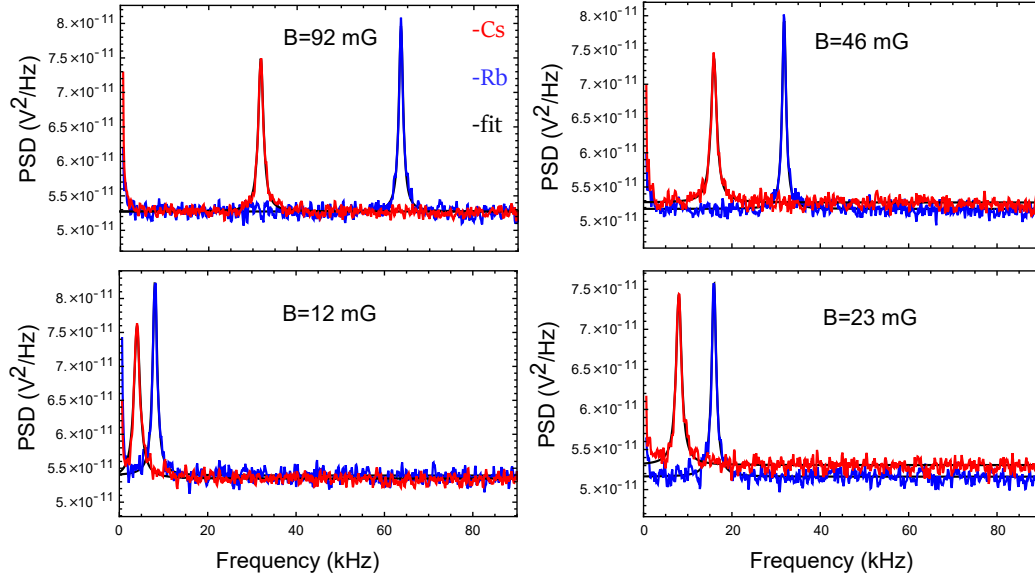


**Figure 4.20:** Spin-noise Spectrum as a function of the magnetic field  $B$ . Spin noise spectrum for both  $^{133}\text{Cs}$  and  $^{87}\text{Rb}$  at  $T = 373^\circ \text{K}$ . At small magnetic fields the two spin-noise resonances overlap whereas at large they are completely separated. The laser powers are  $P_{Cs} = 5.12 \text{ mW}$  and  $P_{Rb} = 5.88 \text{ mW}$  and the detunings  $\Delta_{Cs} = 27 \text{ GHz}$  and  $\Delta_{Rb} = 26 \text{ GHz}$  from the  $D_2$  line, respectively. The record time for these measurements is  $t_{\max} = 8 \text{ ms}$  and the frequency span  $102.4 \text{ kHz}$ . The spectrum is fitted using a Lorentzian and a constant shot noise background. The laser beam diameter has been expanded enough so that power broadening and diffusion effects consist a negligible amount of the total broadening.

After the cell, a dichroic mirror separates the two wavelengths into two different balanced polarimeters consisting of a half-waveplate, a polarizing beam splitter and a balanced photodetector. The output signal consists of the photon shot noise plus the  $F_z$  projection of the random spin projection noise as it precesses at the Larmor frequency of each individual species.

In Fig.4.20 we present spin-noise spectra for both Cs and Rb species at  $T = 100^\circ \text{C}$  for various values of the magnetic field. The individually observed power spectral densities of the two species can be fitted by the following function

$$S(\nu) = S_{el} + S_{ph} + S_{at} \frac{\Delta\nu/2}{(\nu - \nu_0)^2 + (\frac{\Delta\nu}{2})^2} \quad (4.106)$$

where  $S_{el}$  is the electronic noise of the photodetector which is at least 2 orders of magnitude smaller than the other noise sources in the experiment and can be safely ignored,  $S_{ph}$  is the white spectrum of photon shot noise and  $S_{at}$  is the atomic spin noise having a Lorentzian response, centered at the Larmor frequency of each species. We note that in small magnetic fields, close to the dc frequency there is a small deviation from the Lorentzian profile as it has been described in Chapter 2. The Lorentzian response is a consequence of the Wiener-Khinchin theorem resulting from the Fourier transform of the auto-correlation function of the spin signal.

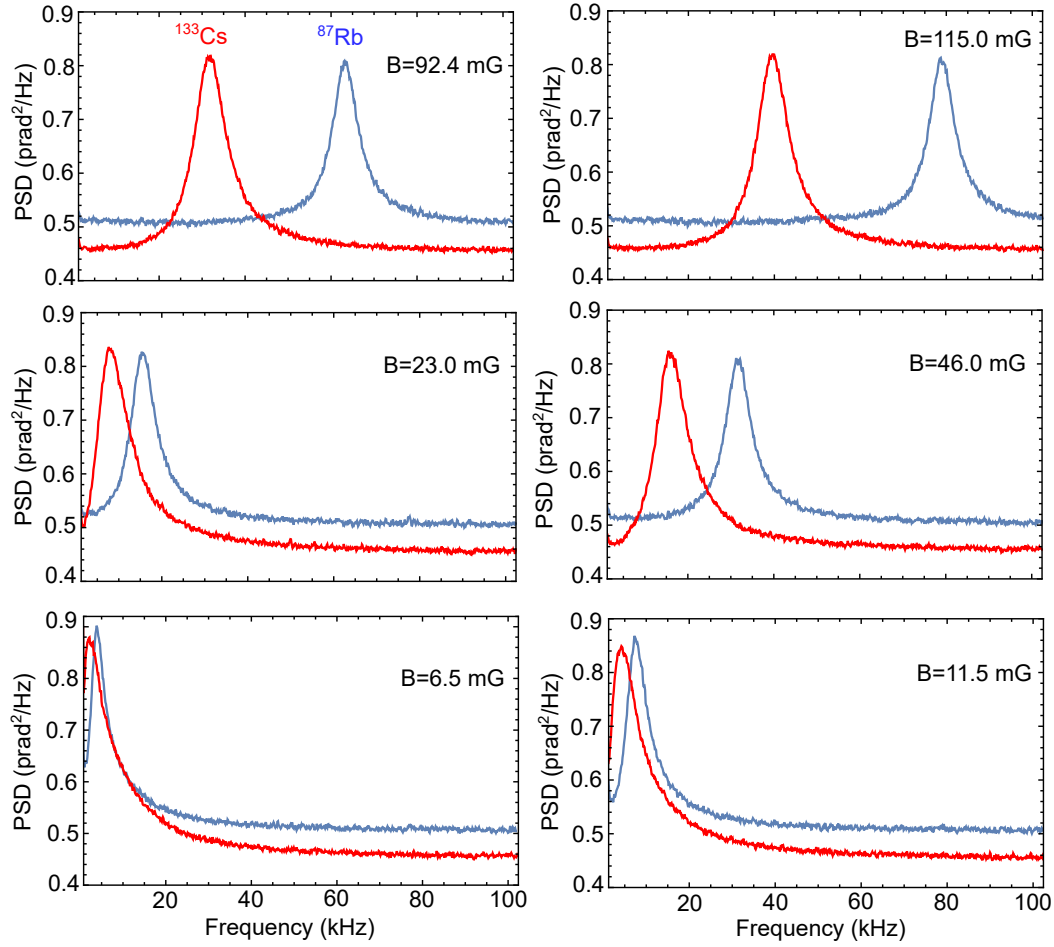


**Figure 4.21:** Spin-noise Spectrum as a function of the magnetic field  $B$ . Spin noise spectrum for both  $^{133}\text{Cs}$  and  $^{87}\text{Rb}$  at  $T = 413^\circ\text{K}$ . At small magnetic fields the two spin-noise resonances overlap whereas at large they are completely separated. The laser powers are  $P_{Cs} = 5.00\text{ mW}$  and  $P_{Rb} = 5.00\text{ mW}$  and the detunings  $\Delta_{Cs} = 61\text{ GHz}$  and  $\Delta_{Rb} = 58\text{ GHz}$  both blue detuned from the  $D_2$  line. The record time for these measurements is  $t_{\text{max}} = 8\text{ ms}$  and the frequency span  $102.4\text{ kHz}$ . The beam diameter is approximately  $1\text{ mm}$  for both lasers. Red solid line:  $^{133}\text{Cs}$  spin-noise. Blue solid line:  $^{87}\text{Rb}$  spin-noise.

In Fig.4.21 we show spin-noise spectra for various magnetic fields at  $T = 140^\circ\text{C}$ . At small magnetic fields the spin-noise resonances overlap while at higher fields the two spin-noise resonances start to separate. The spin-noise Lorentzian peaks are broader than the resonances at  $T = 100^\circ\text{C}$  as a result of the increase in the number density of the atoms and consequently of the spin-exchange relaxation rate. A broader resonance allows for an appreciable overlap of the lines even at higher magnetic fields resulting in a strong coupling between the two species due to spin-exchange collisions which tend to create spin-noise correlations. In this thesis, spin noise correlations have been measured at  $T = 140^\circ\text{C}$ .

The broadening(HWHM) of the spin noise signal observed in the experiment is

related to the one predicted by the theory via

$$\Delta\nu_{\text{HWHM}} = \frac{1}{2\pi T_2} \quad (4.107)$$

$1/T_2$  is the transverse spin relaxation rate given by [50]

$$\frac{1}{T_2} = \Gamma_{\text{rel}} = \frac{1}{T_1} + \frac{1}{q_{se}} R_{se} + \gamma_{\nabla B} \quad (4.108)$$

where  $\gamma_{\nabla B}$  is the transverse relaxation due to magnetic gradients.  $\frac{1}{T_1}$  is the longitudinal spin relaxation rate given by

$$\frac{1}{T_1} = \frac{1}{q} (R_{sd} + R_{pr} + R_D) + \gamma_{\text{wall}} \quad (4.109)$$

where  $\gamma_{\text{wall}}$  is the relaxation due to wall collisions,  $R_{sd} = R_{sd}^{\text{self}} + R_{sd}^{\text{buffer}}$  the relaxation due to spin destruction collisions between alkali-alkali collisions and alkali-buffer gas, and  $R_{pr}$  is the relaxation due to the absorption of the probe beam (power broadening) and  $R_D$  is the relaxation due to diffusion of the alkali atoms in the area of the laser beam. The factor  $q$  is the nuclear slowing down factor which depends on the spin polarization [50]. In the zero polarization regime, we obtain the values  $q_{Rb} = 6$  and  $q_{Cs} = 22$  [189]. The term  $\frac{1}{q_{se}} R_{se}$  describes relaxation due to spin exchange collisions and  $q_{se}$  is the spin-exchange broadening factor and at high magnetic fields such that  $\omega \gg R_{se}$ , takes the value

$$q_{se} = \frac{3(2I + 1)^2}{2I(2I - 1)} \quad (4.110)$$

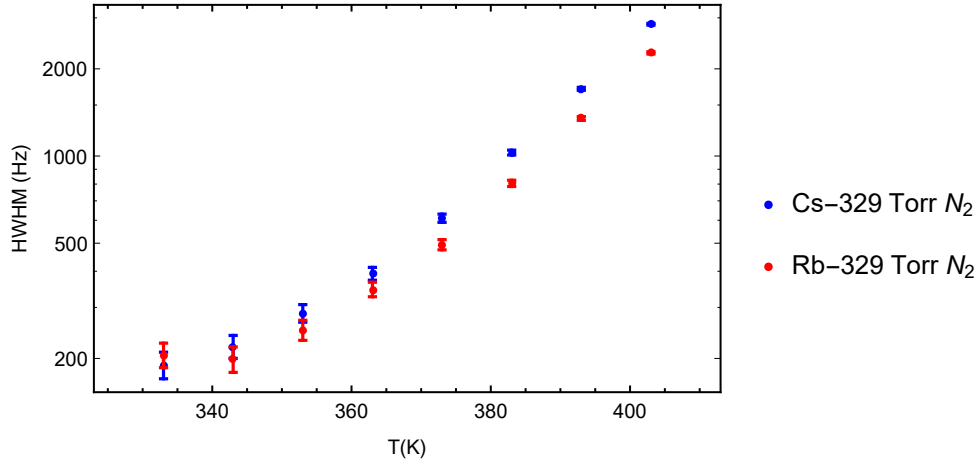


**Figure 4.22:** Spin-noise broadening as a function of temperature. The measurements have been performed with laser beams of large beam diameter in order to eliminate as much as possible power broadening and diffusion effects. Error bars correspond to statistics from two different measurements. The cell contains overlapping  $^{133}\text{Cs}$  and  $^{87}\text{Rb}$  alkali ensembles and 329 Torr of  $\text{N}_2$  buffer gas.

For  $^{87}\text{Rb}$  and  $^{133}\text{Cs}$  we obtain the values  $q_{se}^{\text{Rb}} = 8$  and  $q_{se}^{\text{Cs}} = 32/7$ . As the magnetic field approaches zero,  $1/q_{se} \rightarrow 0$ , and spin-exchange no longer affects the polarization

lifetime. The spin exchange rate is given by

$$R_{se}^i = n_i \sigma_{se}^{i,i} u_{i,i} + n_j \sigma_{se}^{i,j} u_{i,j} \quad (4.111)$$

where  $i=Rb, Cs$  and  $j \neq i$ . Here  $n_i$  is the number density of the  $i_{th}$  species,  $\sigma_{se}$  is the spin exchange cross-section and  $u_{i,j}$  is the relative thermal velocity of the atoms. In transverse spin-noise measurements, spin-exchange is a dominant relaxation mechanism. In our experiment, the number densities at high temperatures have been measured using the diamagnetic Faraday effect and are presented in Fig.4.41. The relative thermal velocity is given by

$$u = \sqrt{\frac{8k_B T}{\pi} \frac{1}{M}} \quad (4.112)$$

where  $M$  is the reduced mass, namely

$$\frac{1}{M} = \frac{1}{m_1} + \frac{1}{m_2} \quad (4.113)$$

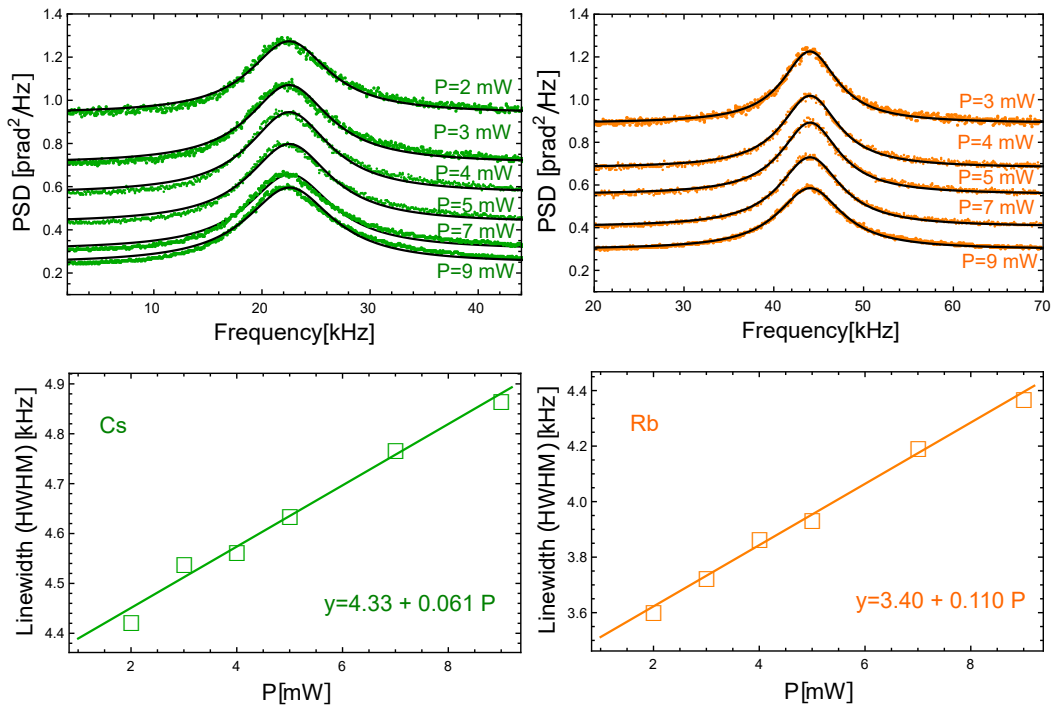


**Figure 4.23:** Magnetic resonance power broadening for various laser powers. The spin noise spectra have been acquired at  $T = 140^\circ\text{C}$  with the usual vapor cell containing  $^{87}\text{Rb}$ ,  $^{133}\text{Cs}$  and 329 Torr of Nitrogen buffer gas. The upper green (Cs) and orange (Rb) spectra are fitted spin noise data as a function of the laser power. The lower plots show that the broadening scales linearly with the power, as expected, resulting in a power broadening of 61 Hz/mW for  $^{133}\text{Cs}$  and 110 Hz/mW for  $^{87}\text{Rb}$ . The measurements have been performed with with detunings of  $\Delta_{Rb} = 58$  GHz and  $\Delta_{Cs} = 61$  GHz above the  $D_2$  optical resonance.

In the same sense as the spin-exchange relaxation rate, the spin-destruction collisional rate is given by

$$R_{sd}^i = n_i \sigma_{sd}^{i,i} u_{i,i} + n_j \sigma_{sd}^{i,j} u_{i,j} \quad (4.114)$$

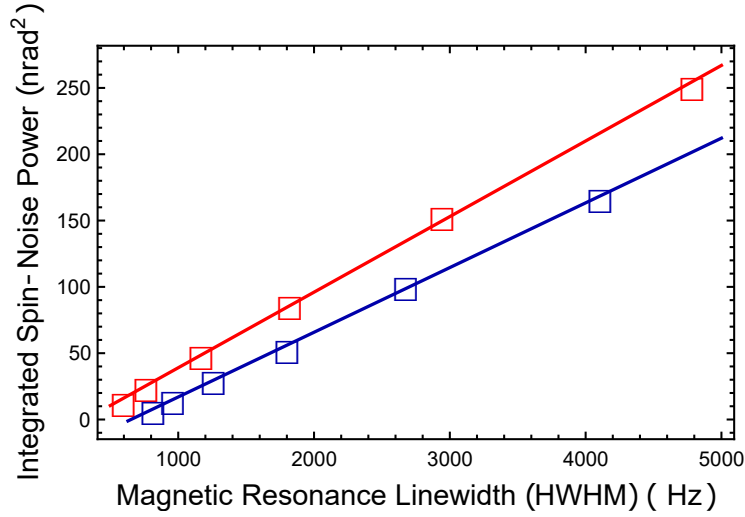


**Figure 4.24:** Linear scaling of the integrated spin-noise power as a function of the number density. Due to lack of a precise knowledge of the number density we plot the integrated spin-noise power vs the spin noise broadening (HWHM). The linear scaling indicates that the spin-noise is a fundamental noise process that scales with the square root of the number of atoms. The measurements have been performed with  $P = 4$  mW of laser power at detunings of  $\Delta_{Rb} = 58$  GHz and  $\Delta_{Cs} = 61$  GHz above the  $D_2$  optical resonance.

where here the indices extend also to collisions of both alkali atoms with the  $N_2$  buffer gas atoms. Spin-destruction collisions contribute usually a negligible amount in spin-noise relaxation due to their small cross-section being of the order of  $10^{-18}$  cm<sup>2</sup> for most of the alkali-metal vapors.

The power broadening, resulting from the interruption of the spin-precession in the ground state by the absorption of a near-resonant photon from the probe beam is equal to the pumping rate

$$R_{pr} = \int \Phi(\nu)\sigma_{abs}(\nu)d\nu \quad (4.115)$$

The photon flux  $\Phi(\nu)$  is distributed in frequencies following the laser linewidth which usually very narrow and can be approximated by a delta function, compared to the frequency profile of the absorption cross-section, centered at the frequency of the laser. The laser being a monochromatic source of radiation generates photons of energy  $E_{ph} = h\nu$ . In that case, the power broadening can be approximated by

$$R_{pr} = \Phi(\nu)\sigma_{abs}(\nu) \quad (4.116)$$

where the photon flux is given by  $\Phi = \frac{P}{h\nu} \frac{1}{\pi R_{beam}^2}$ . The measured power broadening for both vapors is presented in Fig.4.23. We find a power broadening of 61 Hz/mW for <sup>133</sup>Cs and 110 Hz/mW for <sup>87</sup>Rb.

The relaxation due to diffusion of the atoms in the probe beam is given by [33, 54]

$$R_D = 5.8 \frac{D}{R_{\text{beam}}^2} \quad (4.117)$$

where  $D$  is the diffusion constant defined as

$$D = D_0 \frac{P_0}{P} \left( \frac{T}{T_0} \right)^{3/2} \quad (4.118)$$

For a cylindrical cell of length  $L$  and radius  $R$  containing buffer gas, the wall relaxation rate is

$$\gamma_{\text{wall}} = D \left( \frac{\pi^2}{L^2} + \frac{2.405^2}{R^2} \right) \quad (4.119)$$

Finally, the presence of  $N_2$  buffer gas serves also as a quenching gas. The quenching factor is defined as:

$$Q = \frac{1}{1 + R_Q \tau_{\text{nat}}} \quad (4.120)$$

and describes the probability that an excited atom decays via spontaneous emission rather than quenching. The quenching rate is given by  $R_Q = n_{N_2} \sigma_Q u_{Rb, N_2}$ .

In Fig.4.24 we plot the total integrated spin-noise power at different temperatures. For the integral we used both the  $^{87}\text{Rb}$  and the  $^{133}\text{Cs}$  spin-noise resonances at high magnetic field. The resonance linewidth is proportional to the atom number probed by the laser being equal to  $N = nAL$  with  $A$  being the beam area and  $L$  the length of the cell. We have normalized each measurement with the laser power in voltage, to avoid the effects of the absorption on the spin-noise spectrum and to transform the voltage units into radian. Spin-noise signals scale as the square root of the atom number, hence spin-noise power scales linearly with the linewidth being proportional to the atom number in the case of spin-exchange dominated relaxation.

In the following table we present a set of experimental parameters utilized to perform spin-noise and spin-noise correlation measurements at a temperature of  $T = 120^\circ\text{C}$ .

| Parameters  | Value                   |
|---|-------------------------|
| Temperature [K]( $^{\circ}C$ )                                | 393 (120 $^{\circ}C$ )  |
| Measured density $n_{Rb}$ [ $cm^{-3}$ ]                       | $2.90 \times 10^{13}$   |
| Measured density $n_{Cs}$ [ $cm^{-3}$ ]                       | $2.34 \times 10^{13}$   |
| Measured Rb HWHM [kHz]  | 1.348                   |
| Measured Cs HWHM [kHz]  | 1.706                   |
| Mass $^{87}Rb$ [Kg]   | $1.443 \times 10^{-25}$ |
| Mass $^{133}Cs$ [Kg]  | $2.207 \times 10^{-25}$ |
| Mass $N_2$ [Kg]   | $4.653 \times 10^{-26}$ |
| $N_2$ Buffer gas Pressure $P$ (Torr)                          | 329                     |
| Nuclear slowing down factor $q_{Rb}$                          | 6                       |
| Nuclear slowing down factor $q_{Cs}$                          | 22                      |
| SE broadening factor $q_{se}^{Rb}$                            | 8                       |
| SE broadening factor $q_{se}^{Cs}$                            | 32/7                    |
| Diffusion constant in $N_2$ , $D_0^{Rb}$ [ $cm^2/s$ ]         | 0.19                    |
| Diffusion constant in $N_2$ , $D_0^{Cs}$ [ $cm^2/s$ ]         | 0.10                    |
| Diffusion constant in $N_2$ , $D_{Rb}$ [ $cm^2/s$ ]           | 0.48                    |
| Diffusion constant in $N_2$ , $D_{Cs}$ [ $cm^2/s$ ]           | 0.25                    |
| Buffer gas number density $n_{N_2}$ [ $cm^{-3}$ ]             | $8.06 \times 10^{18}$   |
| $D_2$ Optical Line Buffer gas Broadening Rb [GHz]             | 5.43                    |
| $D_2$ Optical Line Buffer gas Broadening Cs [GHz]             | 5.17                    |
| $D_2$ Optical Line Buffer gas frequency shift Rb [GHz]        | -1.77                   |
| $D_2$ Optical Line Buffer gas frequency shift Cs [GHz]        | -1.53                   |
| SE cross section Rb-Rb [ $cm^2$ ]                             | $1.9 \times 10^{-14}$   |
| SE cross section Cs-Cs [ $cm^2$ ]                             | $2.1 \times 10^{-14}$   |
| SE cross section Rb-Cs [ $cm^2$ ]                             | $2.3 \times 10^{-14}$   |
| SD cross section Rb-Rb [ $cm^2$ ]                             | $1.6 \times 10^{-17}$   |
| SD cross section Cs-Cs [ $cm^2$ ]                             | $2.0 \times 10^{-16}$   |
| SD cross section Rb-Cs [ $cm^2$ ] [221]                       | $9.8 \times 10^{-17}$   |
| SD cross section Rb- $N_2$ [ $cm^2$ ]                         | $1.0 \times 10^{-22}$   |
| SD cross section Cs- $N_2$ [ $cm^2$ ]                         | $5.5 \times 10^{-22}$   |
| Mean thermal velocity Rb-Rb [cm/s]                            | 437.5                   |
| Mean thermal velocity Cs-Cs [cm/s]                            | 353.8                   |
| Mean thermal velocity Rb-Cs [cm/s]                            | 397.9                   |
| Photon Energy Rb [J]  | $2.54 \times 10^{-19}$  |
| Photon Energy Cs [J]  | $2.32 \times 10^{-19}$  |
| Quenching cross section of $D_2$ line for $N_2$ Rb [ $cm^2$ ] | $4.3 \times 10^{-15}$   |
| Quenching cross section of $D_2$ line for $N_2$ Cs [ $cm^2$ ] | $6.4 \times 10^{-15}$   |

**Table 4.3:** Collection of various parameters of the experiment calculated at  $T = 120^{\circ}C$  and at a buffer gas pressure of 329 Torr of  $N_2$ . All values are with respect to calculations presented in [50].

## 4.11 Spin-noise Correlations

The measurement procedure of spin-noise correlations has been already discussed at the introduction of Chapter 4. In this section we investigate spin-noise correlations



between  $^{133}\text{Cs}$  and  $^{87}\text{Rb}$  overlapping spin ensembles in a vapor cell containing also 329 Torr of  $N_2$  buffer gas at  $T = 140^\circ\text{C}$ . We study the cross-correlations between the two species, having naturally different gyromagnetic ratios, as a function of the magnetic field, the laser power for both lasers and the detuning.

We find that even in equilibrium there are non-zero spin-noise correlations as a consequence of the dual-species spin-exchange collisions that transfer spin-noise polarization and spin-spin correlations between the colliding partners in a coherent fashion.

The interesting aspect of the spin-noise correlations observed in [100, 101] is that without in any way perturbing the atoms, significant spin-noise correlations build up when the spin-exchange rate is similar to or larger than the difference of the Larmor frequencies of the two atomic species. This finding could potentially have interesting applications in precision spin measurements with multispecies atomic vapors [111].

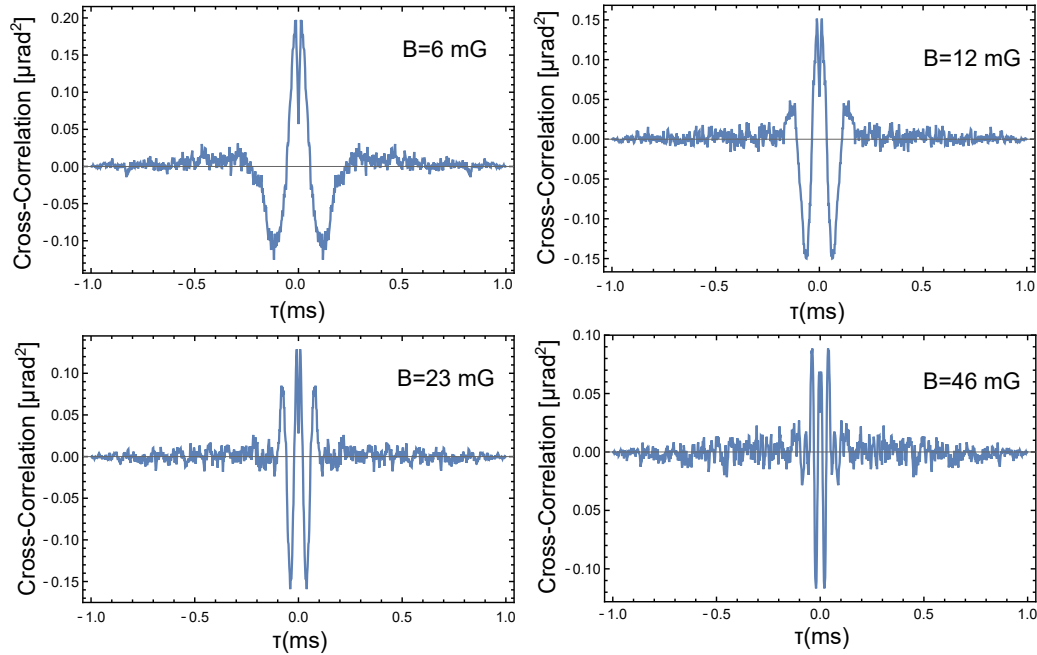


**Figure 4.25:** Plot of the spin-noise cross-correlation between  $^{87}\text{Rb}$  and  $^{133}\text{Cs}$  in the time-domain for various values of the magnetic field. Oscillations indicate coherence transfer between the two species and a non-zero value value at  $\tau = 0$  indicates a total positive amount of correlation even in the equilibrium spin state. The laser power is  $P = 5$  mW for both lasers which are blue detuned by  $\Delta_{Rb} = 58$  GHz and  $\Delta_{Cs} = 61$  GHz above the  $D_2$  optical transition.

In Fig.4.25 and 4.26 we present spin-noise correlations in the time and in the frequency domain, respectively as a function of the magnetic field. In time domain we observe a coherence transfer effect of spin-noise correlations between the two species even in equilibrium, manifesting itself as coherent oscillations at the difference of the Larmor frequencies of the two species. Interestingly, a deep at  $\tau = 0$  is currently under investigation with a lot of potential explanations depending on the choice of the noise

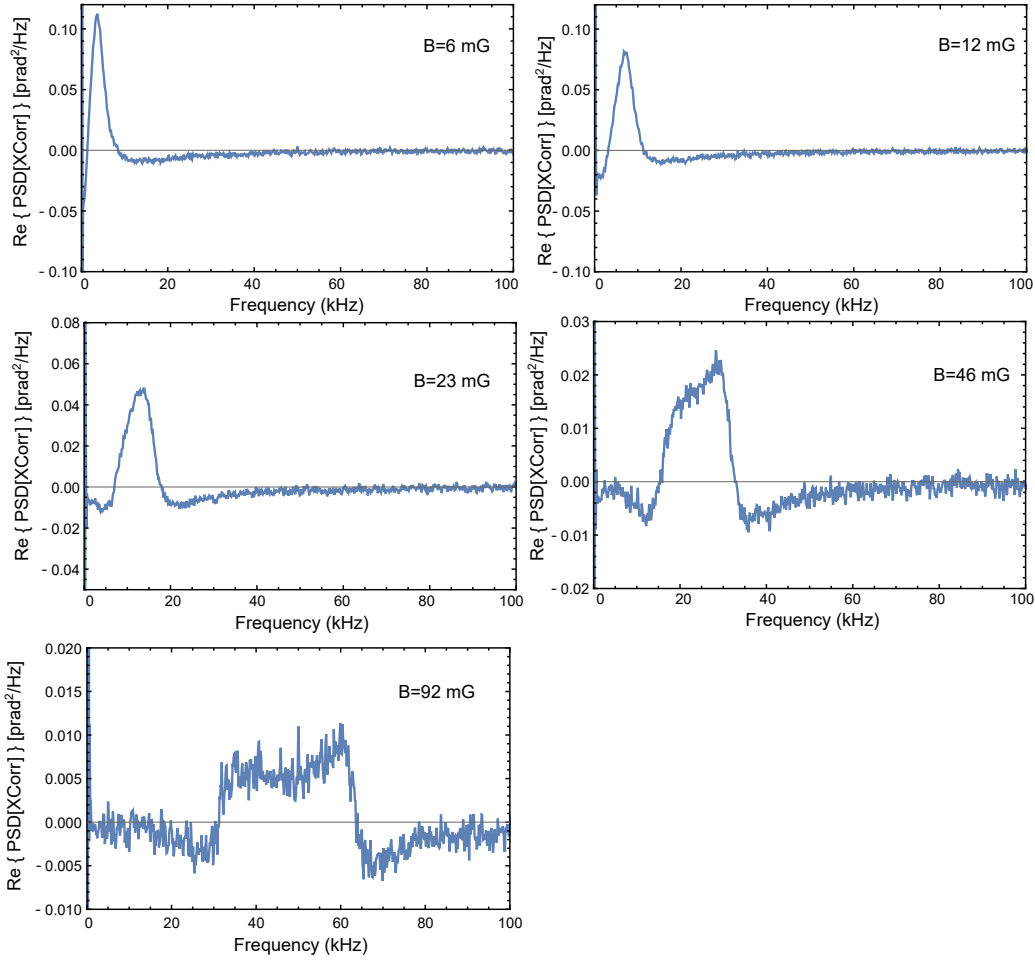


**Figure 4.26:** Plot of the real part of the power spectral density of the spin-noise cross-correlation between  $^{87}\text{Rb}$  and  $^{133}\text{Cs}$  in the frequency-domain for various values of the magnetic field. The spectra can be nicely approached by two opposite dispersive curves overlapping at the center. The integrated cross-correlation power over the whole range of frequencies is related to the value of the correlation in the time domain at  $\tau = 0$ . The laser power is  $P = 5$  mW for both lasers which are blue detuned by  $\Delta_{Rb} = 58$  GHz and  $\Delta_{Cs} = 61$  GHz above the  $D_2$  optical transition.

terms inserted in the coupled Bloch equations described in Chapter 2.

The measurement of a non-zero correlation at  $\tau = 0$  reflects that there are in total non-zero spin-noise correlations in an ensemble of dual alkali species in equilibrium. This is an interesting observation that may lead to new quantum protocols and a modern understanding of spin-spin correlations in overlapping alkali ensembles.

Both in the time and in the frequency domain we observe a decrease of the corresponding signal of the cross-correlation as the magnetic field increases. This effect was also observed in [100, 101] and can be understood by the physical interpretation provided in [100]. In the rotating frame of atom  $i$  the transverse spin of atom  $j$  precesses at the frequency  $\delta\omega = |\omega_2 - \omega_1|$ . If  $\delta\omega \gg \Gamma_{se}$ , in other words if the two spin-noise resonances are far apart, the spin polarization of atom  $j$  seen in the rotating frame of atom  $i$  averages out to zero within the spin-exchange time of  $1/\Gamma_{se}$ . If, however,  $\delta\omega \leq \Gamma_{se}$ ,

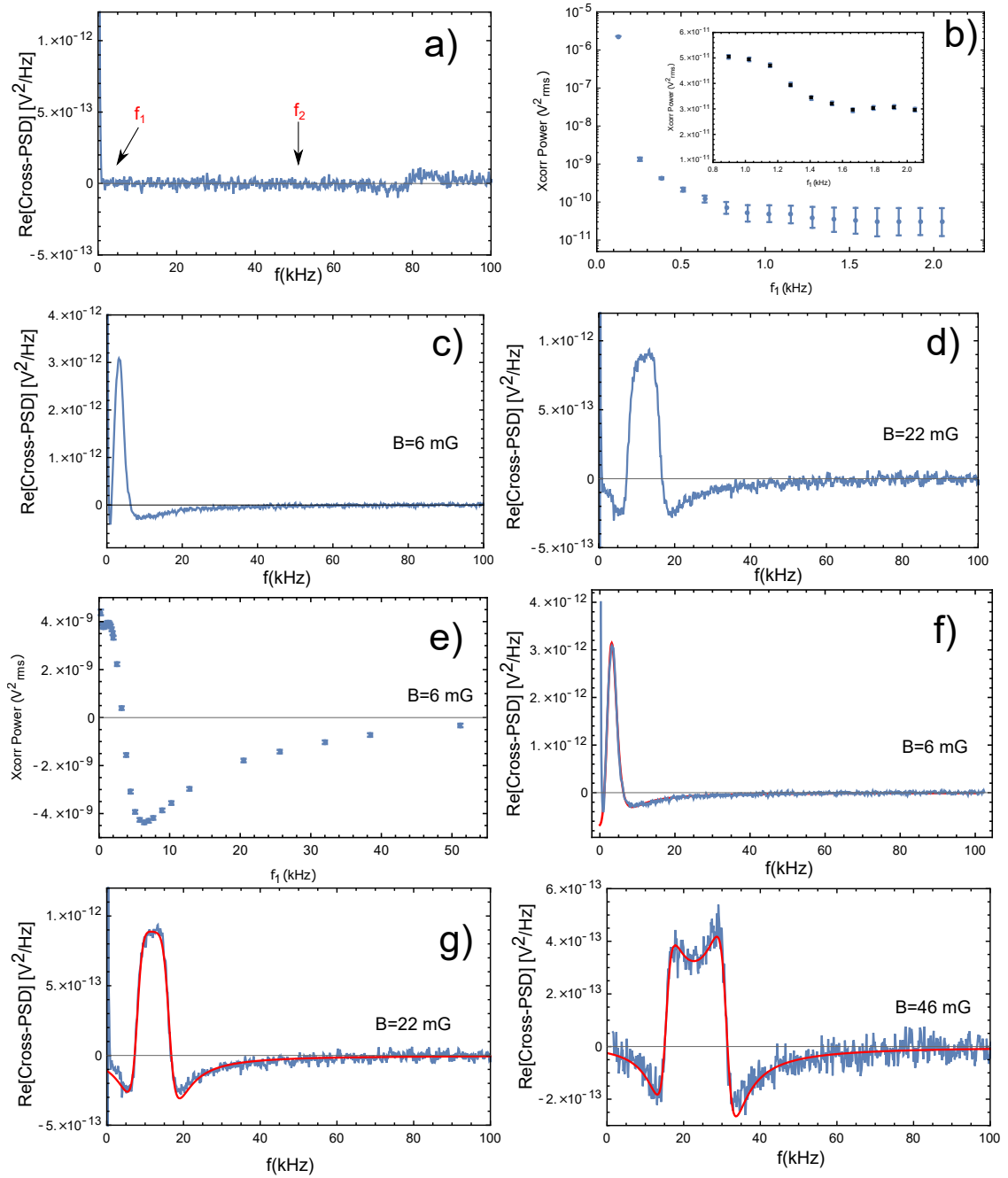


**Figure 4.27:** Effect of the low-frequency noise on the cross-correlation PSD.

then the noise polarization of atom  $j$  transferred to  $i$  adds up, to some extent coherently due to the nonzero correlations, to the noise polarization of  $i$ . This is due to the strong polarization-noise correlations produced by spin exchange.

Note that this decreasing oscillating amplitude as the magnetic field becomes larger than the spin-exchange rate is a general characteristic of the single-species SE master equation as can be seen from Fig.5.1 and 5.2 of Chapter 5.

The above data correspond to measurements with a 329 Torr  $N_2$  buffer gas vapor cell, at a laser power of  $P \approx 5mW$  for both lasers and cell temperature  $T = 120^\circ C$ . The detunings are 28 GHz for Cs and 27 GHz for Rb, both being blue-detuned from the  $D_2$  optical resonances. The beam radius is approximately 0.5-0.7 mm for both lasers.

In Fig.4.27 (a) and (b) we quantify the noise power of the  $1/f$  noise. To do so, we integrate the cross-correlation spectrum (in the absence of the atomic signal) within a frequency range  $\Delta f = f_2 - f_1$  where  $f_1$  and  $f_2$  are low and high cut-off frequencies, respectively and we perform a "moving-integration" while moving the frequency interval towards higher frequencies using a constant frequency step. We expect that at low frequencies the integral will be dominated by the  $1/f$  noise whereas at higher frequencies it will saturate to a constant value.

The transition frequency between these two regions serves as an indicator of whether the  $1/f$  noise stops to affect the spectrum. In order to remove the spin resonances away from the integration region, we apply a large dc field so that the spin correlations have been moved to frequencies above 70 kHz. This is evident in Fig.(a). To perform the integration we choose a frequency span of  $\Delta f = f_2 - f_1 = 49.92$  kHz. In Fig.(b) we plot the integrated noise power in logarithmic scale as a function of the cut-off frequency  $f_1$ .

To produce this plot we move simultaneously the cut-off frequencies  $f_1$  and  $f_2$  towards higher frequencies by a step of 128 Hz each time. In this way, the frequency span is kept constant. From the logarithmic plot it is evident that  $1/f$  noise stops to affect the integrated noise power at  $f_1 = 0.9$  kHz. However, a closer look in this region using a linear plot (inset of Fig.(b)) indicates that the  $1/f$  noise is eliminated above  $f_1 \approx 1.5$  kHz.

In Fig.(c) and (d) we plot the atomic cross-correlation spectrum for magnetic fields of  $B=6$  mG and  $B=22$  mG, respectively. Regarding averaging, each spectrum corresponds to 100 repetitions of 5000 averages each. The total noise power of the background from  $f_1 = 1.536$  to  $f_2 = 51.456$  kHz is  $P_{sn} = (3.21 \pm 9.12) \times 10^{-11} V^2$  while the total cross-correlation powers in Fig.(c) and (d) are  $P_6 = (3.88 \times 10^{-9} \pm 7.50 \times 10^{-11}) V^2$  and  $P_{22} = (2.29 \times 10^{-9} \pm 1.00 \times 10^{-10}) V^2$ , respectively.



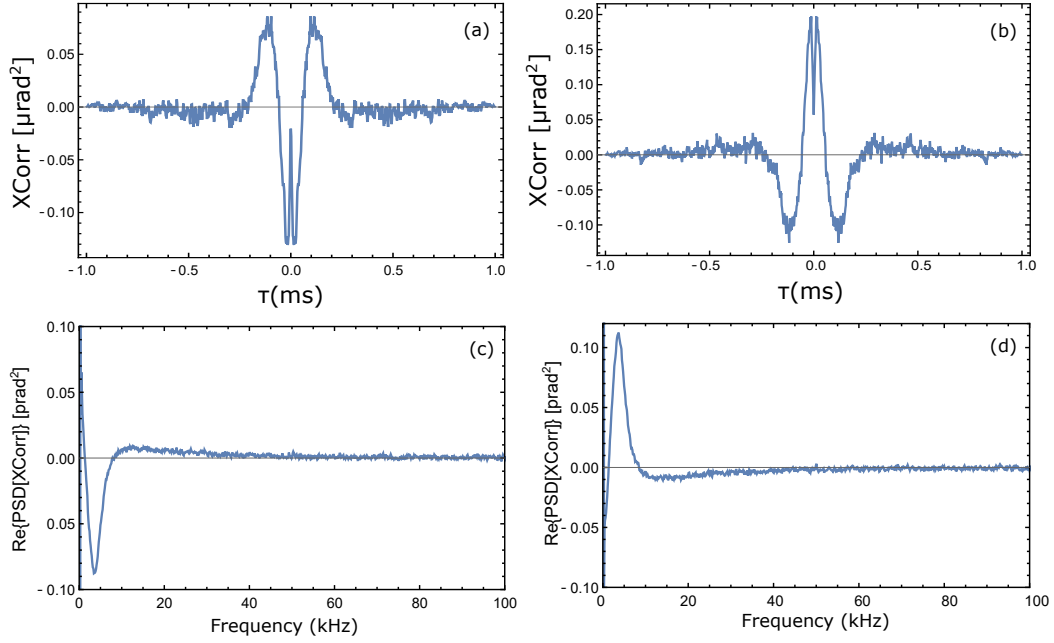


**Figure 4.28:** Dependence of the spin-noise cross-correlation on the detuning. The laser power is  $P = 5$  mW for both lasers while the Rb laser is blue detuned by  $\Delta_{Rb} = 58$  GHz and the Cs laser is red detuned by  $\Delta_{Cs} = 84$  GHz above and below the  $D_2$  optical transition, respectively. The magnetic field is  $B = 6$  mG. The upper plots indicate the difference in the time domain between blue-red detunings (left plot) and blue-blue detunings (right plot). The lower plots represent the frequency domain measurements of the above. The detunings are chosen such that the absorption is the equal in both sides of the line. The cell temperature is  $T = 140^\circ\text{C}$ .

The value of the cross-correlation power is given by the mean of the  $N=100$  measurements and the error bar is calculated from the standard deviation of the previous measurements. In Fig.(e) we plot the total power of the atomic cross correlation as shown in Fig.(c) as a function of the cut-off frequency  $f_1$ . Finally to correctly account for the amount of spectrum that is lost or covered by the  $1/f$  noise in the frequency range below the frequency cut-off  $f_1 = 1.536$  kHz, we fit the cross-correlation spectrum with the difference of two dispersive curves of the form

$$f(\nu) = A(B \frac{(\nu - \nu_1)}{(\nu - \nu_1)^2 + \Gamma_1^2} + C \frac{(\nu - \nu_2)}{(\nu - \nu_2)^2 + \Gamma_2^2}) \quad (4.121)$$

Integrating the fitted function from  $f_0 = 0$  to  $f_1 = 1.536$  kHz we find that the cross-correlation power in this frequency regime is  $-4.38 \times 10^{-10} V^2$  at  $B=6\text{mG}$  and  $-1.93 \times 10^{-10} V^2$  at  $B=22\text{mG}$ . The fitted spectra are shown in Fig.(f) and Fig.(g). Correcting the total integrated power by these amounts we obtain:  $P_6 = (3.44 \times 10^{-9} \pm 7.50 \times 10^{-11}) V^2$  and  $P_{22} = (2.10 \times 10^{-9} \pm 1.00 \times 10^{-10}) V^2$ . At  $B = 6$  mG the power below  $f_1 = 1.536$  kHz is 11% of the total power in the frequency range  $\Delta f = f_2 - f_1$  and respectively 8% at  $B = 22$  mG.

In Fig.4.28 we compare a measurement of spin-noise correlations with blue-blue detunings  $\Delta_{Rb} = +58$  GHz and  $\Delta_{Cs} = +61$  GHz, with a measurement of blue-red

detunings  $\Delta_{Rb} = +58$  GHz and  $\Delta_{Cs} = -84$  GHz. The measurement is performed in a magnetic field of  $B = 5$  mG, at  $T = 140^\circ\text{C}$  with laser power  $P = 5$  mW for both lasers. We chose these detunings in order to have the same absorption from both sides of the  $D_2$  optical transition.

Since the dispersive paramagnetic Faraday rotation measured with the balanced polarimeter scales with the detuning as  $1/\Delta$ , we expect the change of the sign in the cross-correlation as the detuning changes sign. A small asymmetry in the cross-correlations in the two cases is due to the non-symmetric detuning and due to the fact that the pressure shift of the optical transition contributes also in that asymmetry.

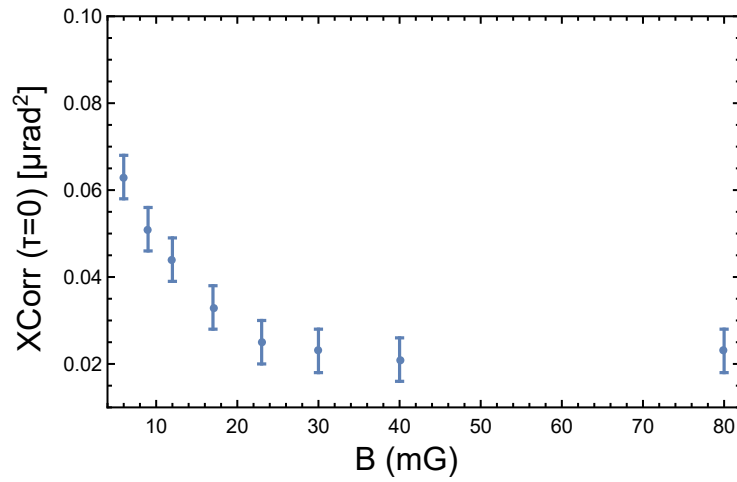


**Figure 4.29:** Cross-Correlation at  $\tau = 0$  as a function of the magnetic field. The laser power is  $P = 5$  mW for both lasers while both lasers are blue detuned from  $D_2$  fine transition by  $\Delta_{Rb} = 58$  GHz and  $\Delta_{Cs} = 61$  GHz, respectively. Each point represents the mean estimated by the cross-correlation at  $\tau = 0$  of 20.000 time-traces of duration 1 ms each. The error bar represents the uncertainty in estimating the mean value out of all the 20.000 values. The measurement has been performed at  $T = 140^\circ\text{C}$ .

In order to obtain an intuition of the measured correlations we describe the balanced polarimeter signals using the input-output relations for the Stokes components

$$S_{y,1}^{\text{out}}(t) = S_{y,1}^{\text{in}}(t) + a_1 S_{x,1} J_{z,1}(t) \quad (4.122)$$

$$S_{y,2}^{\text{out}}(t) = S_{y,2}^{\text{in}}(t) + a_2 S_{x,2} J_{z,2}(t) \quad (4.123)$$

where  $S_{y,1}^{\text{out}}(t)$  is the signal at the output of the first polarimeter and respectively  $S_{y,2}^{\text{out}}(t)$ . Here  $J_{z,i}$  with  $i = 1, 2$  is the spin component along the beam direction, evolving under the stochastic Bloch equations presented in Chapter 2,  $a$ 's are the coupling constants of the spin-light interaction [83] and  $S_{x,1}, S_{x,2}$  are the Stokes components of the initial linear polarization being proportional to the photon flux of the initial  $\hat{x}$ -polarized photons i.e.  $S_{x,j} = \frac{\Phi_j}{2}$ .

The cross-correlation is given by

$$\begin{aligned}
\langle S_{y,1}^{\text{out}}(t)S_{y,2}^{\text{out}}(t') \rangle &= \langle (S_{y,1}^{\text{in}}(t) + a_1\Phi_1J_{z,1}(t))(S_{y,2}^{\text{in}}(t') + a_2\Phi_2J_{z,2}(t')) \rangle \\
&= \langle S_{y,1}^{\text{in}}(t)S_{y,2}^{\text{in}}(t') \rangle + a_2\Phi_2\langle S_{y,1}^{\text{in}}(t) \rangle \langle J_{z,2}(t') \rangle \\
&\quad + a_1\Phi_1\langle S_{y,2}^{\text{in}}(t') \rangle \langle J_{z,1}(t) \rangle + a_1\Phi_1a_2\Phi_2\langle J_{z,1}(t)J_{z,2}(t') \rangle \\
&= a_1\Phi_1a_2\Phi_2\langle J_{z,1}(t)J_{z,2}(t') \rangle
\end{aligned} \tag{4.124}$$

where we have absorbed a factor of 1/2 in the the coupling constants  $a_1$  and  $a_2$  and the expectation value denotes ensemble average over different realizations of the experiment in equilibrium. Sometimes it is customary to normalize the cross-correlation by dividing by

$$\sqrt{\text{Var}\{S_{y,1}^{\text{out}}(t)\}\text{Var}\{S_{y,2}^{\text{out}}(t')\}} \tag{4.125}$$

where

$$\begin{aligned}
\text{Var}\{S_y^{\text{out}}(t)\} &= \text{Var}\{S_y^{\text{in}}(t)\} + a_1\phi_1\text{Var}\{J_z(t)\} \\
&= \text{PSN} + a_1\phi_1\text{Var}\{J_z(t)\}
\end{aligned} \tag{4.126}$$

Hence, when the signal is dominated by photon shot noise, the correlations are highly diminished. It is often convenient to define the symmetrized cross-correlation as

$$C(1, 2) = \frac{1}{2}(\langle S_{y,1}^{\text{out}}(t)S_{y,2}^{\text{out}}(t') \rangle + \langle S_{y,2}^{\text{out}}(t)S_{y,1}^{\text{out}}(t') \rangle) \tag{4.127}$$

In equilibrium, assuming ergodicity, the symmetrized cross-correlation takes the form[101]

$$C(1, 2) = \frac{1}{2}(\langle S_{y,1}^{\text{out}}(0)S_{y,2}^{\text{out}}(t) \rangle + \langle S_{y,2}^{\text{out}}(t)S_{y,1}^{\text{out}}(0) \rangle) \tag{4.128}$$

The Fourier transform of the cross-correlation is

$$P_{cr}(\omega) = \frac{1}{2} \int_{-\infty}^{+\infty} dt e^{i\omega t} [\langle S_{y,1}^{\text{out}}(0)S_{y,2}^{\text{out}}(t) \rangle + \langle S_{y,2}^{\text{out}}(t)S_{y,1}^{\text{out}}(0) \rangle] \tag{4.129}$$

The integral over all frequencies of the above relation is then

$$\int_{-\infty}^{+\infty} P_{cr}(\omega) d\omega = 2\pi \langle \{S_{y,1}^{\text{out}}(0)S_{y,2}^{\text{out}}(0)\} \rangle \tag{4.130}$$

Therefore, the total power of the cross-correlation in the frequency domain, expressed by the integral over the whole range of frequencies is equal to the value of the cross-correlation at  $\tau = 0$  in the time-domain. This is only applicable in equilibrium where the ergodicity condition is satisfied.

Finally, in Fig.4.30 we plot a distribution of the cross-correlation values at  $\tau = 0$  as a function of the laser power for 100.000 time traces of duration 1 ms each. The mean value is estimated by an uncertainty given by the standard deviation of these histograms divided by  $\sqrt{100.000}$ . Then mean values and the estimated error bars are presented in Fig.4.31 indicating i) non-zero spin noise correlations as it was also evident in Fig.4.29 and ii) an almost flat response with the power concluding that there is any conspicuous optical pumping effect that could offset the measured correlations.

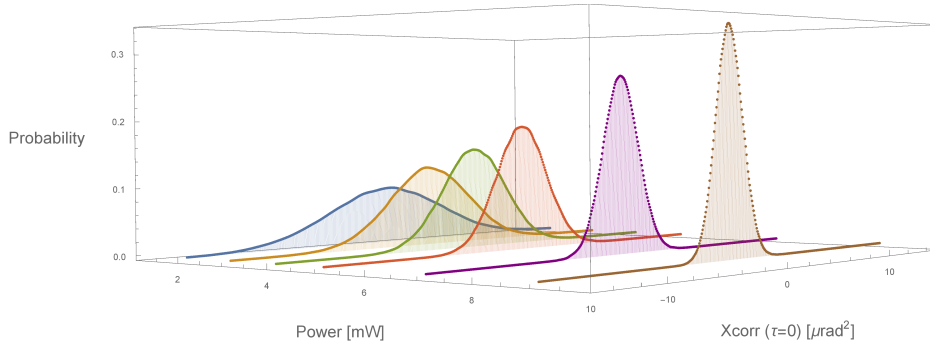


**Figure 4.30:** Histograms of Cross-Correlation at  $\tau = 0$  values as a function of the laser power for both lasers for various laser powers. Both lasers are blue detuned from  $D_2$  optical transition by  $\Delta_{Rb} = 58$  GHz and  $\Delta_{Cs} = 61$  GHz, respectively. Each Histogram represents the distribution of the cross-correlation values at  $\tau = 0$  of 100.000 time-traces of duration 1 ms each. The measurement has been performed at  $T = 140^\circ\text{C}$  at a magnetic field of  $B = 6$  mG.

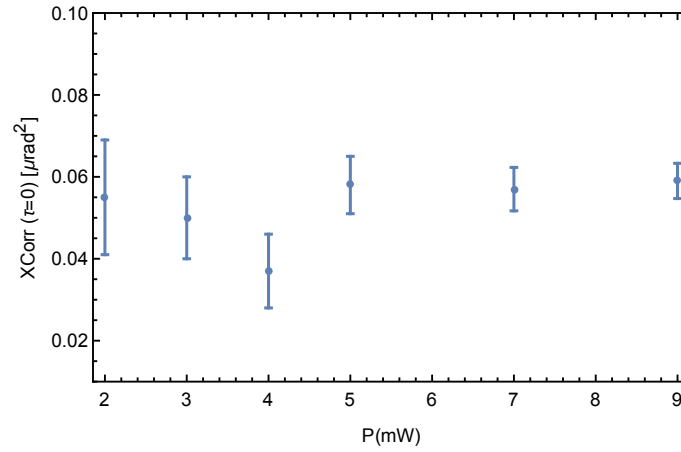


**Figure 4.31:** Cross-Correlation at  $\tau = 0$  as a function of the laser power for both lasers. Both lasers are blue detuned from  $D_2$  optical transition by  $\Delta_{Rb} = 58$  GHz and  $\Delta_{Cs} = 61$  GHz, respectively. Each point represents the mean estimated by the cross-correlation at  $\tau = 0$  of 100.000 time-traces of duration 1 ms each. The error bar represents the uncertainty in estimating the mean value out of all the 100.000 values. The measurement has been performed at  $T = 140^\circ\text{C}$  at a magnetic field of  $B = 6$  mG.

To conclude, as a final systematic check we have also measured spin-noise correlations when we slightly optically pump both vapors and we conclude that no-optical pumping effect that could be produced by the birefringence of the cell glass or the oven windows could affect the featured spin-noise correlations.

## 4.12 Dual Balanced Polarimeter Scheme

In this section we present a measurement of spin-noise with the usual single polarimeter scheme and we compare it with a measurement using a dual polarimeter scheme. The later is schematically presented in Fig.4.32.

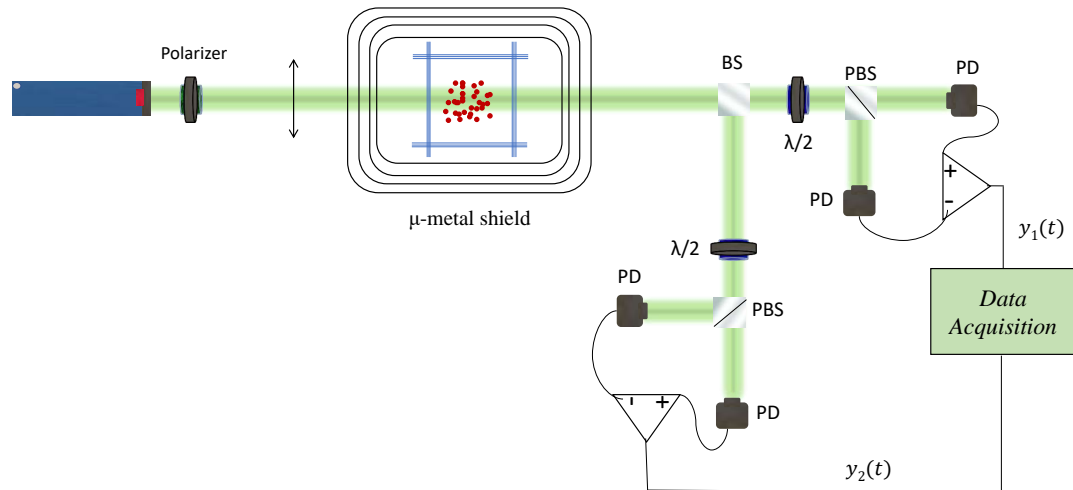


**Figure 4.32:** Experimental setup for spin-noise measurement using a single laser and a single vapor while measuring with two polarimeters simultaneously. The measurement is performed in a cell containing both  $^{87}\text{Rb}$  and  $^{133}\text{Cs}$  vapors. Measurement of the cross-correlation between the outputs of the two polarimeters reveal an amplified spin-noise spectrum increasing the spin-noise signal-to-noise-ratio (SNR) by approximately a factor of 80.

The probe Cs laser, linearly polarized and blue-detuned by  $\Delta = 34$  GHz from the  $D_2$  resonance, transverses the vapor cell containing 28%  $^{133}\text{Cs}$ , 72%  $^{87}\text{Rb}$  and 329 Torr of  $N_2$  buffer gas. The laser probes only the Cs atoms. A transverse magnetic field of  $B = 42.74$  mG enables the signal to be modulated at the Larmor frequency  $f_L = g_F \mu_B B / (2\pi) = 29.9$  kHz.

The cell is heated at  $T = 120^\circ\text{C}$  and after the interaction the light is i) driven to a single polarimeter or ii) is splitted into two arms by a 50:50 beam splitter and is driven towards two different polarimeters. In both cases, the spin noise signal is extracted by measuring i) the PSD of a single polarimetric output and ii) the cross-PSD between the two polarimetric signals. In Fig.4.33 we present the measured spin-noise spectra in both cases. Both spectra correspond to approximately 4 minutes of real-time averaging.

To understand the dual polarimeter signal it is convenient to express the polarimetric outputs in terms of the Stokes parameters. For a single polarimeter we have seen that

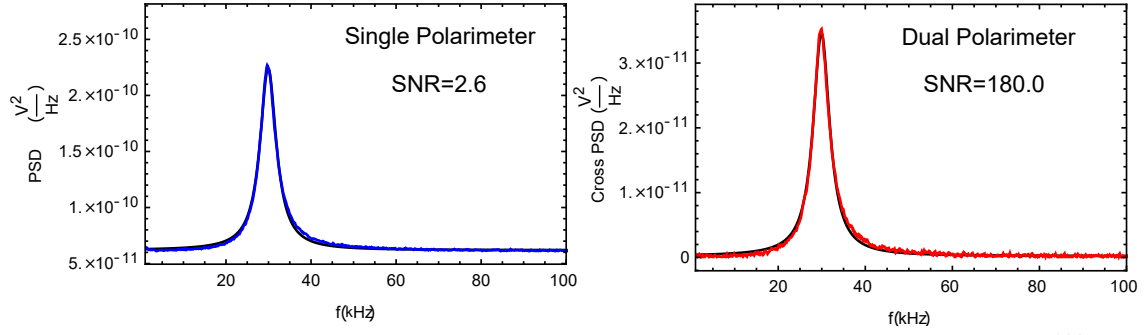


**Figure 4.33:** Left Plot: Power spectral density (PSD) of a spin-noise measurement of  $^{133}\text{Cs}$  vapor in a vapor cell containing 28%  $^{133}\text{Cs}$ , 72%  $^{87}\text{Rb}$  and 329 Torr of  $N_2$  buffer gas. Right plot: Cross-power spectral density of the same spin noise measurement using the balanced polarimeter detection shown in Fig.4.32. The probe laser power of the measurement is  $P = 4.9$  mW and the detuning from the center of the  $D_2$  resonance line  $\Delta = 34$  GHz towards blue. In the dual polarimeter scheme, the shot noise background has been shrunk resulting in a signal to noise ratio (SNR) of 180 compared to the single polarimeter where  $\text{SNR}=2.6$ . Both spectra have been fitted by a normalized Lorentzian profile and a constant background  $f(\nu - \nu_0) = S_{ph} + S_{at} \frac{1}{\pi} \frac{\Delta\nu/2}{(\nu - \nu_0)^2 + (\Delta\nu/2)^2}$ .

the balance output reads as

$$\hat{S}_y^{out}(t) = \hat{S}_y^{in}(t) + gS_x \hat{J}_z(t) \quad (4.131)$$

The power spectrum is proportional to the Fourier transform of the auto-correlation function which is given by

$$\begin{aligned} \langle \hat{S}_y^{out}(t) \hat{S}_y^{out}(t') \rangle &= \langle \hat{S}_y^{in}(t) \hat{S}_y^{in}(t') \rangle + g^2 S_x^2 \langle \hat{J}_z(t) \hat{J}_z(t') \rangle \\ &\approx \delta(t - t') + g^2 S_x^2 \langle \hat{J}_z(t) \hat{J}_z(t') \rangle \end{aligned} \quad (4.132)$$

The first term represents the delta correlated photon shot noise and the second the atomic spin noise or the atomic auto-correlation function. In the case of dual polarimetry, the information of the atomic auto-correlation can be extracted by looking at the cross-correlation of the dual polarimeter outputs as indicated in Fig.4.32. Assuming that the dual polarimetric signals are given by

$$\hat{S}_{y,1}^{out}(t) = \hat{S}_{y,1}^{in}(t) + gS_x \hat{J}_z(t) \quad (4.133)$$

$$S_{y,2}^{out}(t) = \hat{S}_{y,2}^{in}(t) + gS_x \hat{J}_z(t) \quad (4.134)$$

The photon-shot noises at the two polarimetric arms are different, while the atomic signal imprinted on the laser beam is equivalent in both polarimeters. The cross-correlation between the two polarimetric output is

$$\langle \hat{S}_{y,1}^{out}(t) \hat{S}_{y,2}^{out}(t') \rangle = g^2 S_x^2 \langle \hat{J}_z(t) \hat{J}_z(t') \rangle \quad (4.135)$$

Interestingly, we obtain that the photon shot noises has been eliminated since it is uncorrelated noise in the two arms of the polarimeters. It is therefore evident that the power spectrum of the cross-correlation between the two polarimeters results in the

atomic spin noise without the photon shot noise background. One may ask whether this might be also useful in magnetometry. Assuming that the signal that carries the magnetic information is the cross-correlation function given by Eq.(4.135), the noise of this signal, expressed by its variance, depends on the photon shot noise. A comparison between the single and the dual polarimeter scheme for magnetometry has shown that a single polarimeter scheme is more efficient.

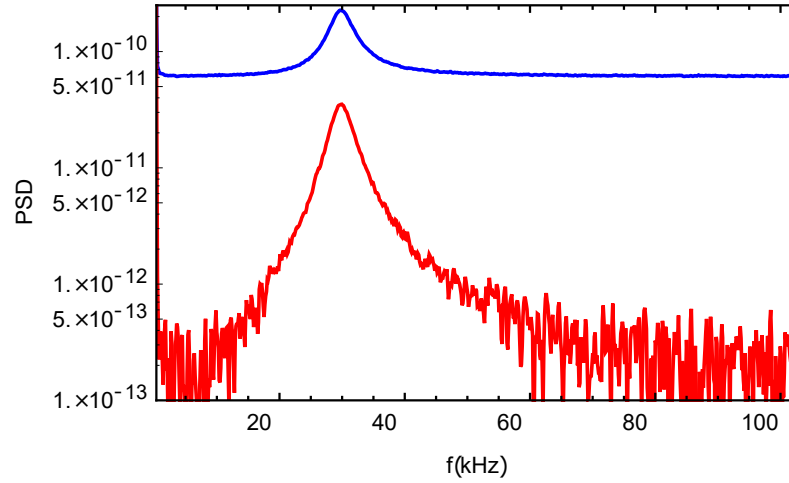


**Figure 4.34:** Comparison of the power spectral densities of the single polarimeter scheme (Blue solid line) with the dual polarimeter scheme (red solid line) in Log-scale.

Both spectra are fitted using a normalized Lorentzian function with a constant background given by the formula

$$S(\nu - \nu_0) = S_{ph} + S_{at} \frac{1}{\pi} \frac{\Delta\nu/2}{(\nu - \nu_0)^2 + (\frac{\Delta\nu}{2})^2} = S_{ph} + S_{at} \mathcal{L}(\nu) \quad (4.136)$$

The fitted spectra are shown in Fig.4.33 and a log-plot comparison is given in Fig.4.34.

Both spin-noise spectra are centered at the same resonance frequency  $\nu_0 = 29.92$  kHz in the Zeeman spectrum and have the same broadening (FWHM) of  $\Delta\nu = 4.6$  kHz. The broadening is dominated by spin-exchange, power broadening and diffusion relaxation processes. Regarding the single polarimeter we find  $S_{ph} = 6.18 \times 10^{-11} V^2/\text{Hz}$  and  $S_{at} = 1.19 \times 10^{-6} V^2$  while for the dual polarimeter we obtain  $S_{ph} = 1.90 \times 10^{-13} V^2/\text{Hz}$  and  $S_{at} = 2.50 \times 10^{-7} V^2$ . Integrating the whole spectrum up to  $\nu = 101.8$  kHz we find for the single polarimeter the photon shot noise power  $P_{sn} = 6.29 \times 10^{-6} V^2$  and the total atomic noise power  $P_{at} = 1.14 \times 10^{-6} V^2$ .

The ratio of the atomic spin noise power to the photon shot noise power is  $R = 0.18$ . For the dual polarimeter we obtain  $P_{sn} = 1.94 \times 10^{-8} V^2$ ,  $P_{at} = 2.41 \times 10^{-7} V^2$  and a ratio of the power equal to  $R = 12.41$ . We find that the power ratio of the single polarimeter is amplified by a factor of approximately 70 times. The spin-noise signal to noise ratio (SNR) is defined as the ratio of the peak height at the center of the Lorentzian

to the mean value of the photon shot noise background

$$\text{SNR} = \frac{S_{at}}{S_{ph}} \mathcal{L}(\nu_0) \quad (4.137)$$

For the single polarimeter we get  $\text{SNR} = 2.6$  while for the second  $\text{SNR} = 180.0$ . We find that the SNR of the single polarimeter is magnified by a factor of approximately 80 when using a dual polarimeter scheme. Finally, the precision of the spectral parameter estimation<sup>25</sup> defined as the Lorentzian peak height over the fluctuations of the photon shot noise background are defined as  $S_{at}\mathcal{L}(\nu_0)/\text{STD}[\text{PSD}]$  where  $\text{STD}[\text{PSD}]$  is the standard deviation of the photon shot noise background in the power spectral density plot.

For the single polarimeter we find a standard deviation of  $\text{STD}[\text{PSD}] = 3.30 \times 10^{-13} \text{V}^2/\text{Hz}$  and a precision of spectral parameter estimation of 490.74 while for the dual polarimeter  $\text{STD}[\text{PSD}] = 1.13 \times 10^{-13} \text{V}^2/\text{Hz}$  and precision of spectral parameter estimation equal to 302.52 quite smaller than the single polarimeter. We find that the single polarimeter scheme is more reliable is the precision of spectral parameter estimation. In table **Table 4.4** we summarize the presented results and we quote a straightforward comparison between the two polarimetric schemes.

| Parameter                          | Single Polarimeter     | Dual Polarimeter       |
|------------------------------------|------------------------|------------------------|
| Resonance Frequency (kHz)          | 29.91                  | 29.92                  |
| Broadening FWHM (kHz)              | 4.67                   | 4.63                   |
| Spin-noise SNR                     | 2.6                    | 180.0                  |
| Prec. of spec. par. est.           | 490.7                  | 302.5                  |
| PSN STD ( $\text{V}^2/\text{Hz}$ ) | $3.30 \times 10^{-13}$ | $1.13 \times 10^{-13}$ |
| Spin-noise Power ( $\text{V}^2$ )  | $1.14 \times 10^{-6}$  | $2.41 \times 10^{-7}$  |
| Shot-noise Power ( $\text{V}^2$ )  | $6.29 \times 10^{-6}$  | $1.94 \times 10^{-8}$  |
| Power ratio                        | 0.18                   | 12.41                  |

**Table 4.4:** Comparison of the single with the dual polarimeter schemes. In general The dual polarimeter scheme is advantageous in spin noise SNR and in the power ratio of spin-noise to the photon shot-noise rendering it preferable to applications where a strong spin signal in the time domain is required. For spectral parameter estimation the single polarimeter is preferable.

A thing to notice about the discussion in this section is that it is observed that the noisiness of the power spectrum  $\text{Var}[S(\nu)]$  increases with increasing the mean value of the spectrum  $\overline{S(\nu)}$ . In other words the smaller the mean value of the spectrum the smaller the error in estimating the noise of the mean PSD. This is also related to the fact that in a single acquisition run from  $t = 0$  to  $t = T_{acq}$  the error in estimating the PSD is approximately equal to the mean value of the PSD. The error drops with subsequent

<sup>25</sup>The precision of spectral parameter estimation indicates the accuracy in which we can extract spectroscopic parameters by fitting the spectrum. In other words how precise are the obtained fitting parameters when minimizing the  $\chi^2$  of the fit.

averages. For more information the interested reader may consult [84].

## 4.13 Diamagnetic Faraday Rotation

At high temperatures (above 100° C) we use the diamagnetic Faraday rotation effect to measure the number density of the vapor in the cell. In this temperature regime, the absorption profile is saturated and can no longer serve as a reliable and easy method to find the number density.

The method of the diamagnetic Faraday effect as described in [154] is based on the linear Zeeman splitting which produces a difference in the index of refraction for the  $\sigma_+$  and the  $\sigma_-$  circularly polarized lights as they transverse the vapor. The difference in the index of refraction is caused by the different detunings that the two circular polarizations experience. In the far wing, where the absorption is negligible the diamagnetic Faraday rotation is given by

$$\theta(\lambda) = \frac{nr_e\lambda_0^4 f_{ge} l}{2c} \frac{k\mu_B B/h}{(\lambda - \lambda_0)^2} + \frac{2d}{(\lambda - \lambda_0)^4} \quad (4.138)$$

where  $n$  is the number density of the vapor,  $f_{ge}$  the oscillator strength of the  $D_2$  line,  $c$  the speed of light in vacuum,  $l$  the averaged path length of light in the vapor,  $k = 7/6$  a factor for the  $D_2$  line coming from angular momentum analysis in the theory and  $\lambda_0$  the resonance wavelength of the  $D_2$  optical transition. A complete description of the theory of the diamagnetic Faraday rotation can be found in [154].

In Fig.4.35 we describe schematically the experimental setup. Both laser beams are fiber-coupled and they are send through the cell. A Fabry-Perot cavity ensures the single mode operation of the laser while a wavelength-meter reports the absolute value of the wavelength. The linear light polarization is modulated as it passes through a Faraday rotator placed in an AC magnetic field, produced by a small solenoid coil. The modulation frequency is given as a reference to a lock-in amplifier. Then, the beam passes through the vapor cell which is placed in a large solenoid producing a large dc magnetic field along the beam direction.

Finally a polarization measurement is performed using a crossed polarizer and a photodetector. The output of the photodetector is demodulated with the lock-in amplifier and the Faraday rotation signal is extracted from the output of the lock-in.

A longitudinal magnetic field  $B$  is generated by a large solenoid coil as shown in Fig.4.36. The wire diameter is  $d_w = 1.2$  mm and the total resistance of the coil is  $R = 6\Omega$ . Two layers of  $N = 400$  turns each, in total  $N = 800$  turns are wrapped around a PVC tube of length 65 cm and diameter 12.5 cm.



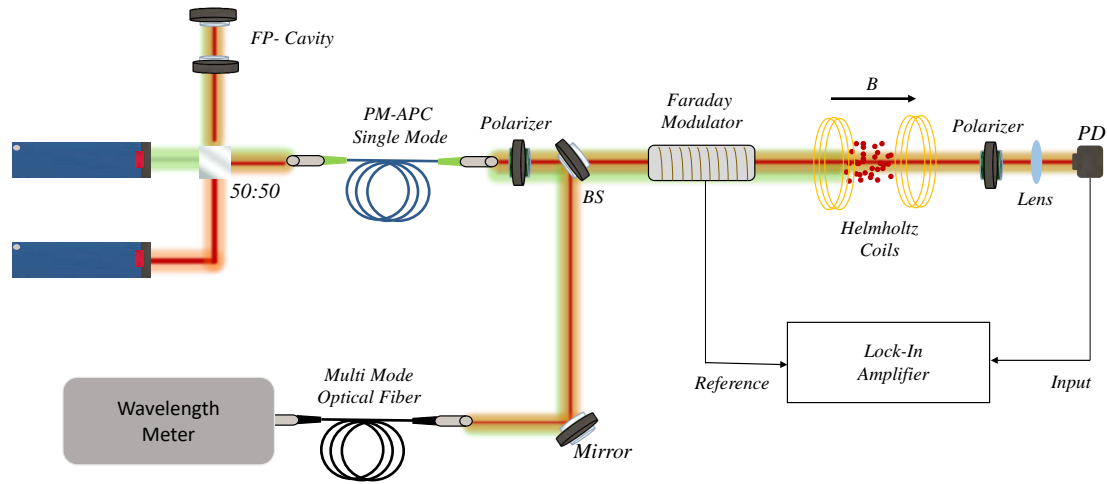


**Figure 4.35:** Experimental setup for density measurement in a cell containing both  $^{87}\text{Rb}$  and Cs vapors. Both lasers are driven through the cell via a single mode polarization maintaining optical fiber. The cell is placed in a Solenoid coil producing a large dc magnetic field along the beam direction. After the cell there is a cross-polarizer. Before the cell, the probe beams pass through a Faraday modulator whose modulation frequency is given as reference to the lock-in amplifier. As we scan the line, the wavelength is monitored with a wavemeter and a FP cavity ensures the single-mode operation of the laser.

The radius of the coil is approximately  $r = 7.5$  cm and the length  $L = 48.5$  cm. The diameter of the tube is chosen such that the oven fits inside easily and the length of the tube is quite large in order for the field to be homogeneous at the center. The field homogeneity is calculated using the relation

$$B = \frac{\mu_0 N I}{2} \left( \frac{L/2 - z}{L \sqrt{R^2 + (L/2 - z)^2}} + \frac{L/2 + z}{L \sqrt{R^2 + (L/2 + z)^2}} \right) \quad (4.139)$$

and far away from the ends the field to a very good extent is given by

$$B = \frac{\mu_0 N I}{L} \quad (4.140)$$

where  $L$  is the length of the solenoid,  $R$  the radius,  $I$  the current,  $N$  the number of turns and  $\mu_0 = 4\pi \times 10^{-7}$  H/m is the magnetic permeability of the vacuum.

The current through the coil is supplied by a digital voltage source (switching mode-working principle) which is current limited, with a maximum voltage supply of  $V_{\max} = 40$  Volts, resulting in a maximum current of  $I_{\max} = V_{\max}/R \approx 6.6$  A. The maximum field at the center produced by such current is  $B_{\max} \approx 137$  G.

In order to calibrate the current with the measured magnetic field as can be seen in Fig.4.36, we place the solenoid inside a magnetic shield to reduce Earth's magnetic field and we measure the field using a semiconductor fluxgate magnetometer at low currents.

A remnant offset Earth's field is subtracted from the measurements. We find that the measurements are within 1% to the theoretically expected value given by Eq.(4.140). In Fig.4.37 we provide these measurements.

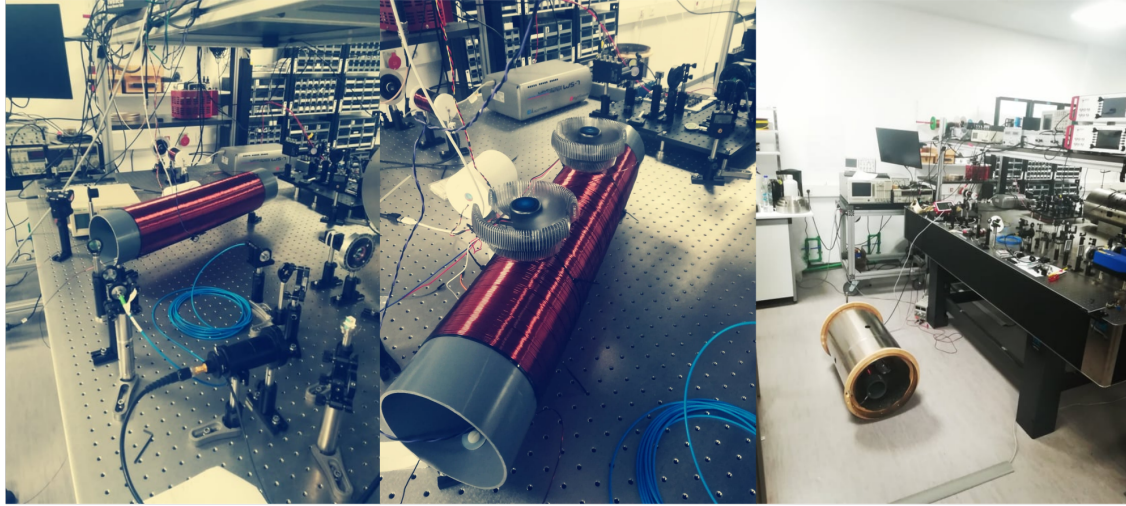


Figure 4.36

The field homogeneity is also found to be consistent to a very good extent with the one provided by Eq.(4.139).

The coil is cooled using two CPU fans placed at the top of the coil and water-cooling was also installed although not used. The heat is directly related to the electric power supplied to the coil  $P = I^2R$ . Since the power depends on the square of the current it is more efficient to apply small current and large R, thus, regarding the heat, it is better to have more turns than larger current. Both the number of turns and the current are linear in B therefore a decrease of the current let's say by a factor of 2 can be compensated by an increase in the number of turns (or R) by a factor of 2. Finally, note that it is crucial to measure the magnetic field with precision since the density measurement depends directly on the knowledge of the magnetic field.

After exiting the fiber, the light is linearly polarized using a polarizer and the power is always monitored using a power-meter. The error in the power is mostly due to the fiber-induced intensity noise and due to the intrinsic intensity fluctuations of the laser. In order to avoid saturation effects or a small amount of optical pumping (the glass of the oven and the cell may turn a small amount of linear to elliptical polarization), we make sure that the power entering the cell is kept always at the level of a few  $\mu\text{W}$ .

A pumping effect will be evident in the measurement if we change the direction of the dc magnetic field and we observe a different indication at the lock-in. In our measurements a small amount of pumping was evident but it was removed by signal

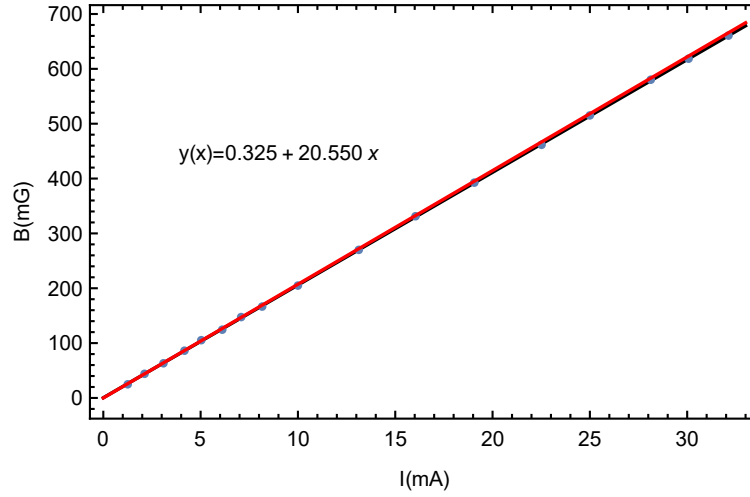


**Figure 4.37:** Magnetic Field measured with a fluxgate magnetometer as a function of the current applied to the solenoid. The black line is a linear fit, yielding  $B = 0.325 + 20.550I$ . The red line is the theory given by Eq (4.140).

reversals<sup>26</sup> when alternating the direction of the applied dc magnetic field.

After the polarizer, the light pass through the vapor cell and finally through a Faraday rotator of length  $l_{FR} = 2$  cm which is placed inside a small solenoid coil of length 12 cm and total coil resistance  $R = 3.3\Omega$ . The verdet constant of the crystal depends on the wavelength and it is given by the manufacturer to be  $V = 90 \frac{\text{rad}}{Tm}$  at  $\lambda = 780$  nm and  $V = 72.5 \frac{\text{rad}}{Tm}$  at  $\lambda = 850$  nm.

The light polarization is modulated at a frequency of  $f = 1$  kHz, by applying an AC-current through the solenoid. The current is produced by a sine function generator with amplitude  $V_{rms} = 0.7$  Volt. In order to amplify further the signal from the coil we change the resonance frequency by applying a capacitor of  $C = 2\mu\text{F}$  in series with the coil. This method is based on an enhancement of the signal by resonance. The coil inductance is  $L = 14.2$  mH. The schematic circuit of the coil in series with the capacitor is presented in Fig.4.38.

The total resistance of the circuit is  $R_{tot} = R + Z_L + Z_C = R + jL\omega + \frac{1}{j\omega C} = R + j(L\omega - \frac{1}{\omega C})$  where  $Z_L = jL\omega$  and  $Z_C = \frac{1}{j\omega C}$  are the inductor and capacitor impedances, respectively. Applying Ohm's law in the circuit we obtain

$$V(t) = I(t)R_{tot} \Leftrightarrow I(t) = \frac{V_0 e^{j\omega t}}{R_{tot}} = \frac{V_0 e^{j\omega t}}{R + j(L\omega - \frac{1}{\omega C})} \quad (4.141)$$

where the current I is a complex function having an in-phase and an out of phase

<sup>26</sup>Since the rotation angle is linear in B, changing the direction of the dc magnetic field the sign of the rotation angle also changes. A pumping effect along the beam direction deforms the equilibrium index of refraction of the vapor and is not affected by the field reversal. Therefore by subtracting the two signal S(B)-S(-B) we get rid of the pumping effect.

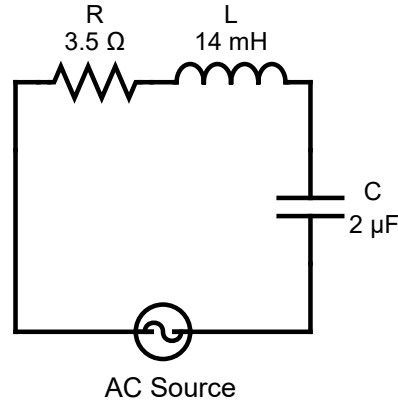


**Figure 4.38:** Equivalent circuit of the solenoid coil used to modulate the light polarization. The coil's ohmic resistance is  $R = 3.3\Omega$ , the coil inductance is  $L = 14 \text{ mH}$  and the capacitor placed in series has a capacitance of  $C = 2\mu\text{F}$ . The corresponding impedances are: Coil impedance  $Z_L = jL\omega$  and Capacitor impedance  $Z_C = \frac{1}{j\omega C}$ . The total impedance of the circuit is  $R_{tot} = R + Z_L + Z_C$ .

component. The magnitude of the complex current is given by

$$|I|^2 = \left( \frac{V_0 e^{j\omega t}}{R + j(L\omega - \frac{1}{\omega C})} \right)^* \left( \frac{V_0 e^{j\omega t}}{R + j(L\omega - \frac{1}{\omega C})} \right) = \frac{|V_0|^2}{|R + j(L\omega - \frac{1}{\omega C})|^2} \quad (4.142)$$

or

$$|I| = \frac{|V_0|}{\sqrt{R^2 + (L\omega - \frac{1}{\omega C})^2}} \quad (4.143)$$

It is evident from the above relationship that in order to amplify the current we need to choose  $C$  such that  $L\omega = \frac{1}{\omega C}$  for a given  $\omega$ . This is the method of signal enhancement due to resonance. Finally, the sine-wave is further amplified using a sound-amplifier with adjustable gain, making sure that the output resistance ( $4\Omega$ ) matches the coil resistance.

The amplitude of the magnetic field at the center of the solenoid is measured using a pick-up coil. The pick-up coil is designed by an extremely thin wire of diameter  $0.14 \pm 0.02 \text{ mm}$ . We construct a coil of  $N = 30$  turns and diameter  $d_{pc} = 5.00 \pm 0.05 \text{ mm}$ . The voltage across the pick-up is measured with a lock-in amplifier referenced at the modulation frequency.

The magnetic field produced by the small solenoid along the beam direction is

$$B(t) = B_0 \sin \omega_{mod} t \quad (4.144)$$

where  $\omega_{mod} = 2\pi \times 1 \text{ kHz}$  is the modulation frequency. The voltage across the pick-up coil is equal to the magnetic flux through the surface of the coil given by  $V = -\frac{d\Phi(t)}{dt}$ .

The magnetic flux through the pick-up coil is

$$\Phi(t) = \int B(t) dA = B_0 \sin \omega_{mod} t \times \pi r^2 \times N \quad (4.145)$$



where  $r$  is the radius and  $N$  the number of turns of the pick-up coil, respectively. The time derivative of the magnetic flux through the pick-up coil is then

$$\frac{d\Phi(t)}{dt} = B_0\pi r^2 N\omega_{mod} \cos \omega_{mod}t \quad (4.146)$$

Therefore, the output of the lock-in at the reference frequency is (R-component of the lock-in )

$$V_R = B_0\pi r^2 N\omega_{mod} = B_0\pi r^2 N2\pi f \quad (4.147)$$

Solving for the magnetic field we obtain

$$B_0 = \frac{\sqrt{2}V_R}{\pi r^2 N2\pi f} \quad (4.148)$$

where the factor of  $\sqrt{2}$  results from the rms indication of the lock-in amplifier.

We place the pick-up coil at the center of the solenoid and we slightly move around the central position in order to measure an average of  $V_R = 44.63 \pm 0.05$  mV. The error is given by the total standard deviation of the measured values assuming that each measurement has the same uncertainty with the others. Given the above measured value and the corresponding uncertainty the magnitude of the magnetic field is found to be:

$$B_0 = (170.5 \pm 2.4)\text{G} \quad (4.149)$$

The error bar is calculated by the error propagation method since the errors in the individual measured parameters are uncorrelated. The error in the magnetic field is found to be 1.4%. Now we can calculate the amplitude of the modulation angle of the polarization as it passes through the Faraday rotator. It is given by

$$\phi_0 = V(\lambda)l_{FR}B_0 \quad (4.150)$$

$$\phi_0^{Cs} = (24.72 \pm 0.35)\text{mrad} \quad (4.151)$$

$$\phi_0^{Rb} = (30.69 \pm 0.43)\text{mrad} \quad (4.152)$$

The error is calculated again by error propagation , given the uncertainty in the measurement of the magnetic field  $B_0$ . Note the error is still 1.4%.

We can independently measure the value of  $\phi_0$  using polarizers and the Faraday modulator. We remove the vapor-cell and the large solenoid coil completely from the experimental setup and we place a polarizer at the crossed position relative to the initial polarization using a high precision rotational mount. We monitor the intensity of the light after the second polarizer using a photodiode with a gain at 70dB, corresponding to a voltage multiplication factor of  $4.75 \times 10^6$  V/A.

The output of the photodetector is connected to the lock-in which is referred to the Faraday modulation frequency. If we add a small relative angle  $\theta$  between the two



polarizers by manually rotating one of them the output of the photodiode is

$$V(t) = V_0 \sin^2(\theta + \phi_0 \sin \omega_{mod} t) \quad (4.153)$$

For small  $\theta$  and  $\phi_0$  we can expand the sine function

$$\begin{aligned} V(t) &= V_0(\theta + \phi_0 \sin \omega_{mod} t)^2 \\ &= V_0(\theta^2 + 2\theta\phi_0 \sin \omega_{mod} t + \phi_0^2 \sin^2 \omega_{mod} t) \\ &= V_0\theta^2 + 2V_0\theta\phi_0 \sin \omega_{mod} t + V_0\phi_0^2 \left( \frac{1 + \cos(2\omega_{mod} t)}{2} \right) \end{aligned} \quad (4.154)$$

The output of the lock-in at the first harmonic is

$$V_1 = 2V_0\theta\phi_0 \quad (4.155)$$

while the output at the 2nd harmonic is

$$V_2 = \frac{V_0\phi_0^2}{2} \quad (4.156)$$

and the ratio of the two harmonics is given by

$$\frac{V_1}{V_2} = \frac{4\theta}{\phi_0} \quad (4.157)$$

Measuring the first and the second harmonics we find a value for  $\phi_0$ . Note  $\theta$  is measured in degrees and it should be transformed into radians and  $V_1$  and  $V_2$  are the rms voltage values. First we set the polarizers at the crossed position (The second polarizer at  $90^\circ$  relative to the first) and we measure the second harmonic. For a laser power of  $P = 0.11.7 \mu\text{W}$  we find  $V_0^{Cs} = (30.01 \pm 0.02) \text{ V}$  and  $V_0^{Rb} = (26.12 \pm 0.02) \text{ V}$ . For the second harmonic measurement we obtain  $V_2^{Rb} = (7.00 \pm 0.01) \text{ mV}$  and  $V_2^{Cs} = (5.00 \pm 0.01) \text{ mV}$ , respectively. These measurements correspond to a modulation angle of

$$\phi_0^{Cs} = (21.70 \pm 0.10) \text{ mrad} \quad (4.158)$$

$$\phi_0^{Rb} = (27.53 \pm 0.09) \text{ mrad} \quad (4.159)$$

Next we rotate the second polarizer by known angles  $\{1^\circ, 2^\circ, 3^\circ, 4^\circ, 5^\circ\}$  and we measure the first harmonic  $V_1$ . We plot  $V_1$  as a function of  $\theta$  and then we fit to find  $\phi_0$ . In Fig.5 and Fig.6 we plot the measured first harmonic as a function of the angle  $\theta$  for  $^{87}\text{Rb}$  and  $^{133}\text{Cs}$ , respectively. Each value is the mean out of 10 lock-in indications. Based on the fits, the resulting values for  $\phi_0$  are:

$$\phi_0^{Cs} = (19.18 \pm 0.19) \text{ mrad} \quad (4.160)$$

$$\phi_0^{Rb} = (25.63 \pm 0.18) \text{ mrad} \quad (4.161)$$

In the following table we present the measured values for the modulation angle using the different techniques described so far. The average value and the error bar have



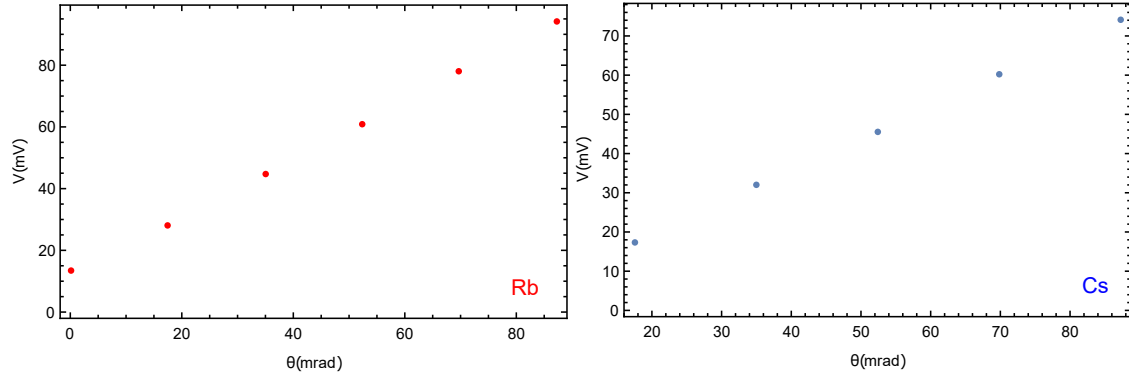


**Figure 4.39:** Left figure: first harmonic for  $^{87}\text{Rb}$  as a function of the angle  $\theta$  in mrad. The linear fit is  $V_1 = a_0\theta + b_0 = 0.93\theta + 12.59$ . Right figure: First harmonic for Cs as a function of the angle  $\theta$  in mrad. The linear fit  $V_1 = a_0\theta + b_0 = 0.81\theta + 3.35$ .

| Measurement Type         | $\phi_0^{Cs}$ | $\delta\phi_0^{Cs}$ | $\phi_0^{Rb}$ | $\delta\phi_0^{Rb}$ |
|--------------------------|---------------|---------------------|---------------|---------------------|
| pick-up & Verdet         | 24.72         | 0.35                | 30.69         | 0.43                |
| 1 <sup>st</sup> Harmonic | 19.18         | 0.19                | 25.63         | 0.18                |
| 2 <sup>nd</sup> Harmonic | 21.70         | 0.11                | 27.53         | 0.10                |
| <b>Average</b>           | 22.25         | 0.09                | 27.95         | 0.09                |

**Table 4.5:** Collection of  $\phi_0$ -measurements. All values are in mrad.

been calculated by the usual method for combining different measurements of the same quantity. The average is given from the weighted average based on the error-bars:

$$\bar{\phi}_0 = \frac{\phi_0^1 \left(\frac{1}{\delta\phi_0^1}\right)^2 + \phi_0^2 \left(\frac{1}{\delta\phi_0^2}\right)^2 + \phi_0^3 \left(\frac{1}{\delta\phi_0^3}\right)^2}{\left(\frac{1}{\delta\phi_0^1}\right)^2 + \left(\frac{1}{\delta\phi_0^2}\right)^2 + \left(\frac{1}{\delta\phi_0^3}\right)^2} \quad (4.162)$$

and the error

$$\delta\bar{\phi}_0 = \sqrt{\frac{1}{\left(\frac{1}{\delta\phi_0^1}\right)^2 + \left(\frac{1}{\delta\phi_0^2}\right)^2 + \left(\frac{1}{\delta\phi_0^3}\right)^2}} \quad (4.163)$$

We place again the vapor cell back in position and we set the current of the large solenoid coil at  $I = 4.86$  A, corresponding to a magnetic field of  $B = 100.7$  G. The field is calculated using the fit of Fig.4.37. We scan the wavelength manually, making sure that the laser is always in single mode operation and the power right before the analyzer is a few  $\mu\text{W}$ . We also measure for both directions of the field, since there is a small pumping and then we subtract the two measurements. In the following figures we plot the atomic responses (optical rotation) for various temperatures.

In order to fit the measured data we use a function [154]

$$\theta(\lambda) = A_0 + \frac{A_2}{(\lambda - \lambda_0)^2} + \frac{A_4}{(\lambda - \lambda_0)^4} \quad (4.164)$$

where  $A_0$ ,  $A_2$  and  $A_4$  are fitting parameters optimized to minimize the  $\chi^2$  of the fit.

The constant term  $A_0$  is a dc offset rotation angle that is related mainly to the birefringence effects of the light by the glass of the cell or the window elements of the

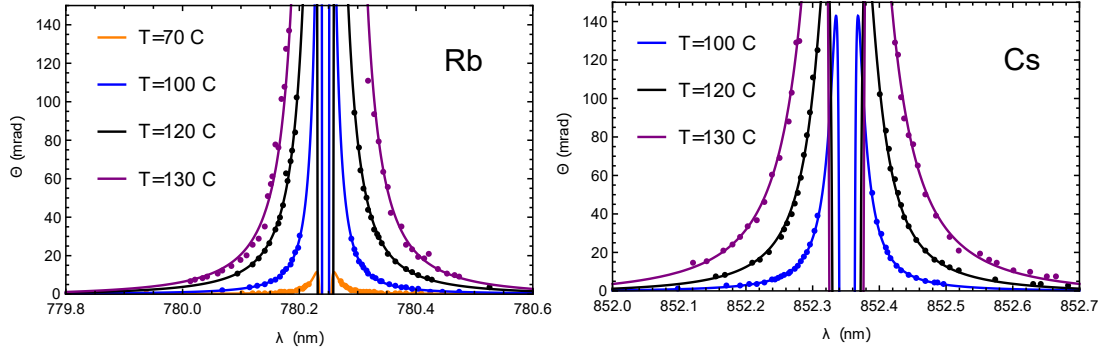


**Figure 4.40:** Lock-in detection output. Dispersive rotation curves due to the diamagnetic Faraday effect. Left figure corresponds to  $^{87}\text{Rb}$  measurements and the right to  $^{133}\text{Cs}$  measurements. The measurements are for various temperatures in a cell with 329 Torr of  $N_2$  buffer gas. The solid lines are dispersive fits described by Eq.(4.164).

| Temperature             | $n_{Cs}$              | $n_{Rb}$              |
|-------------------------|-----------------------|-----------------------|
| $T = 70^\circ\text{C}$  | –                     | $5.49 \times 10^{11}$ |
| $T = 100^\circ\text{C}$ | $5.64 \times 10^{12}$ | $6.48 \times 10^{12}$ |
| $T = 120^\circ\text{C}$ | $2.34 \times 10^{13}$ | $2.90 \times 10^{13}$ |
| $T = 130^\circ\text{C}$ | $5.91 \times 10^{13}$ | $5.20 \times 10^{13}$ |

**Table 4.6:** Collection of density measurements for various temperatures. The cell contains 329 Torr  $N_2$ . All values are in  $\text{cm}^{-3}$ .

oven when placed in the large dc solenoid field. At the far wings the dominant term is the one proportional to  $A_2$ , however for detunings closer to the resonance the  $A_4$  term dominates. The number density of the vapor is given by

$$n = \frac{2cA_2h}{r_e\lambda_0^4 f_{ge} l k \mu_B B} \quad (4.165)$$

where  $c = 299792458$  m/s is the light speed in vacuum,  $h = 6.62 \times 10^{-34}$  J s is the Planck's constant,  $r_e = 2.81 \times 10^{-15}$  m is the classical electron radius,  $k = 7/6$  for the D2 line that both lasers are tuned to. This is a factor regarding angular momentum calculations of the Faraday rotation and can be found in Eq.(A28) and Eq.(3) of [154]. The length  $l = L_{\text{cell}} - 2l_g = (50.06 - 2 \times 1.599) \times 10^{-3}$  m, is the averaged path length of the light inside the vapor, equal to the length of the cell minus two times the thickness of the glass of the cell. The resonance wavelengths (vacuum) are  $\lambda_0^{Rb} = 780.241209$  nm and  $\lambda_0^{Cs} = 852.347275$  nm while the oscillator strengths  $f_{ge}^{Rb} = 0.6956$  and  $f_{ge}^{Cs} = 0.7148$ . Finally,  $\mu_B = 9.274 \times 10^{-24}$  J/T is the Bohr's magneton.

In **Table 4.6** we present the various measured densities for the different temperatures for both alkali vapors in the cell.

In **Fig.4.41** we show the number density of both alkali vapors in the vapor cell containing 329 Torr  $N_2$  buffer gas as a function of the temperature. The dependence of

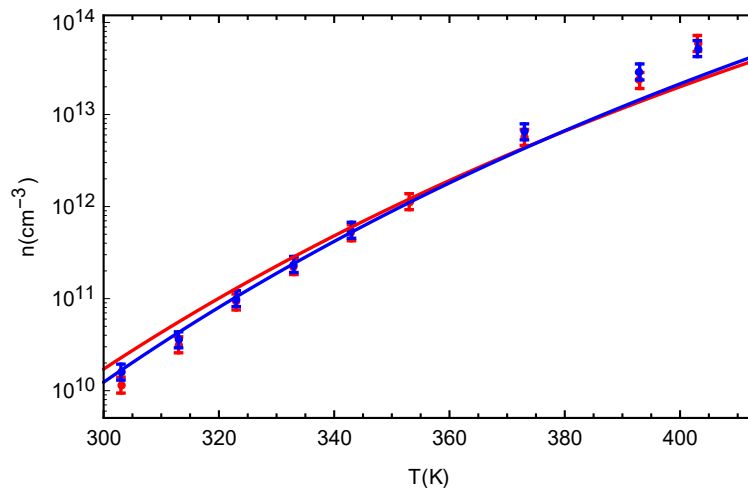


**Figure 4.41:** Comparison of the measured vapor densities with the ones proposed by the cell manufacturer for both vapors in the cell. The cell contains 329 Torr of  $N_2$  buffer gas. The theoretical  $^{87}\text{Rb}$  number density (red solid line) is given by  $\frac{0.72}{T} \times 10^{21.866+4.312-4040/T}$  while the  $^{133}\text{Cs}$  number density (blue solid line) is given by  $\frac{0.28}{T} \times 10^{21.866+4.165-3830/T}$ . Low temperature measurements are performed using the optical absorption method whereas at higher temperatures where the absorption profile is saturated we use the method of the diamagnetic Faraday effect.

the number density on the temperature is approximately given by the Killian formula.

## 4.14 Wavelength Measurement

An amount of the laser power is used to monitor the wavelength of both lasers using a high precision wavelength meter (High-Finesse WS7). The wavemeter shown in Fig.4.42 has a measurement resolution of 10 MHz and a measurement speed up to 500Hz. It works for either pulsed or cw laser sources and its construction is based on non-moving part mechanical technology and on temperature compensated technology.

The light is coupled into the device via a multimode optical fiber and then collimated by a lens, before entering the solid-state Fizeau-interferometers. The interference pattern is imaged by a cylindrical lens onto arrays of CCD photodiodes. The recorded pattern is transferred to the computer via a high-speed USB connection which allows data acquisition rates of up to 76 kHz. The software fits and compares the pattern to a previously recorded calibration to calculate the wavelength. For more information about the wavelength-meter visit [High-Finesse](#). The optical setup is shown also in Fig.4.42.

Fizeau interferometers are commonly used for measuring the shape of an optical surface. Typically, a fabricated lens or a mirror is compared to a reference piece having the desired shape. A precisely figured reference optical element is placed on top of the optical element being tested, separated by narrow spacers. The reference element is

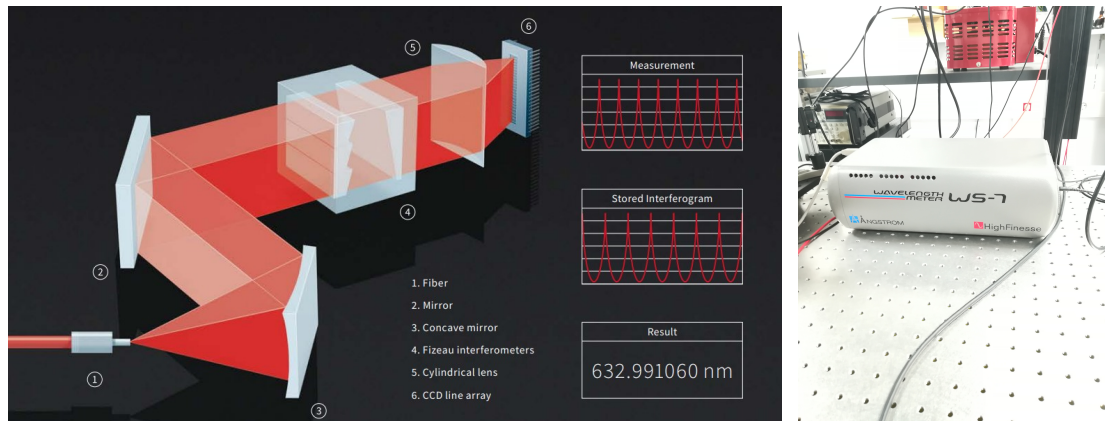


**Figure 4.42:** Left Figure: Light path into the wavelength meter. The light exiting the fiber is collimated via two mirrors and it is driven into a setup of solid state Fizeau inteferometers. The output of the interferometer is re-shaped and focused onto an array of CCD photodiodes using a cylindrical lens. Taken from [High-Finesse](#). Right Figure: External view of the wavelength-meter.

slightly beveled to prevent the rear surface of the element from producing interference fringes. A collimated beam of monochromatic light illuminates the two optical elements, and the transmitted interference fringes are collected to a CCD photodiode array [222].

In our experimental setup, the wavelength meter was used in order to measure the stability of the largely detuned ECDL lasers. In order to monitor both wavelengths with a single wavelength-meter, each beam passes through an AOM and the  $1_s t$  order diffracted beam enters the optical fiber leading to the wavemeter. The AOM causes a frequency shift of approximately 60 MHz for both wavelengths which is an negligible offset compared to the order of 100 GHz detuning that the lasers where operated. Moreover, this frequency shift is not important when the wavelength stability is of interest. The two AOMs were driven by two different rf drivers which were in turn controlled by a TTL pulse produced by a computer via Labview. The TTL pulse enables the operation of the rf driver.

A NOT-gate applied between the two TTL pulses is used to send either the Cs or the Rb laser into the wavelength-meter but never both simultaneously. A train pulse with pulse duration of 20 sec was produced in Labview, enabling each laser to be measured for 20 seconds before the other laser takes place. The experimental setup for measuring simultaneously the wavelength of the two lasers is schematically described in [Fig.4.43](#)

Although the wavelength stability is very crucial in most of the experimental situations, especially for experiments that require resonant conditions, in the case of our experiment where the lasers are detuned approximately 100 GHz away from the  $D_2$  line of  $^{133}\text{Cs}$  and  $^{87}\text{Rb}$ , the laser frequency drifts are negligible and cannot directly affect the measured spin noise signals. As we can see in [Fig.4.44](#), the measured wavelength is drifting slowly by n amount of approximately half a GHz in a period of roughly 1.5

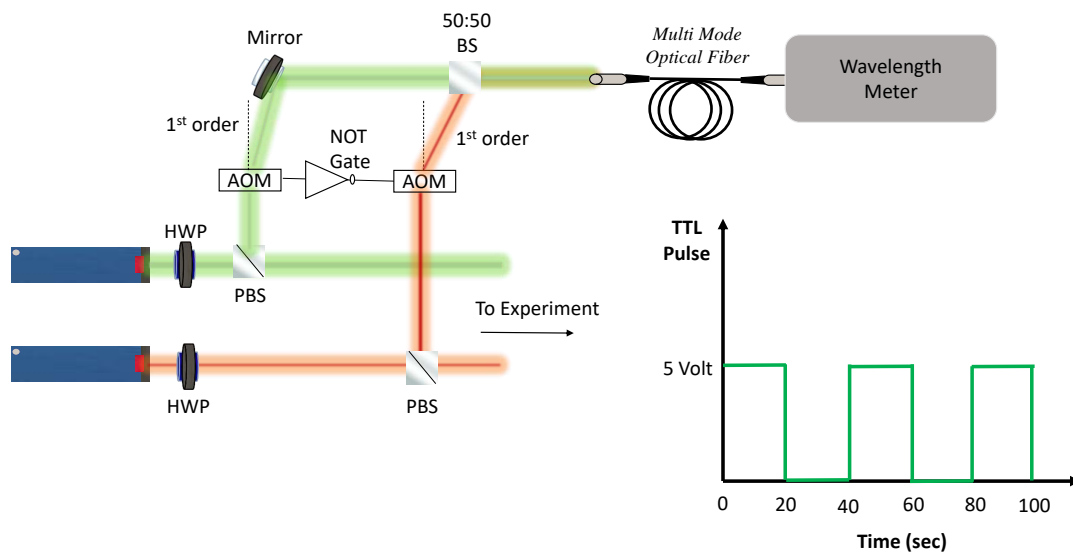


**Figure 4.43:** Experimental setup for measuring two wavelengths with a single wavelength meter. Both lasers pass through an AOM and the 1<sup>st</sup> order diffracted beam is sent to the wavelength-meter. The operation of AOMs is controlled with a TTL pulse generated with labview. A NOT-gate between the TTL pulses of the two AOMs is alternatively switching the operation of the AOMs, ensuring that only one laser beam reaches the wavemeter at a time. The plot shows the TTL train pulse enabling the measurement of each wavelength for time 20 sec, every 20 sec. The amount of power reaching the wavemeter is controlled by a half-waveplate (HWP) and a polarizing beam splitter (PBS) placed in front of the laser and it is chosen such that the wavemeter output is equal for both lasers.

hours. This drift is negligible compared to the detuning and causes low frequency noise very close to zero frequency.

As can be seen from the same plot, the slow frequency drift is accompanied by quite faster frequency fluctuations. Again for the case of our experimental conditions these fluctuations are very slow (compared for example to the Larmor frequencies of the atoms) and cause almost zero frequency drifts in the power spectrum. These frequency drifts measured with the wavemeter are mostly generated from the laser, with a small amount coming from the AOM operation and a smaller amount coming from changes of the index of refraction of the multi-mode fiber that couples the light into the wavemeter. For the timescales of this experiment, i.e. 1000-5000 averages of spin precession data each of duration 1 ms, the wavelength is to a very good approximation constant.

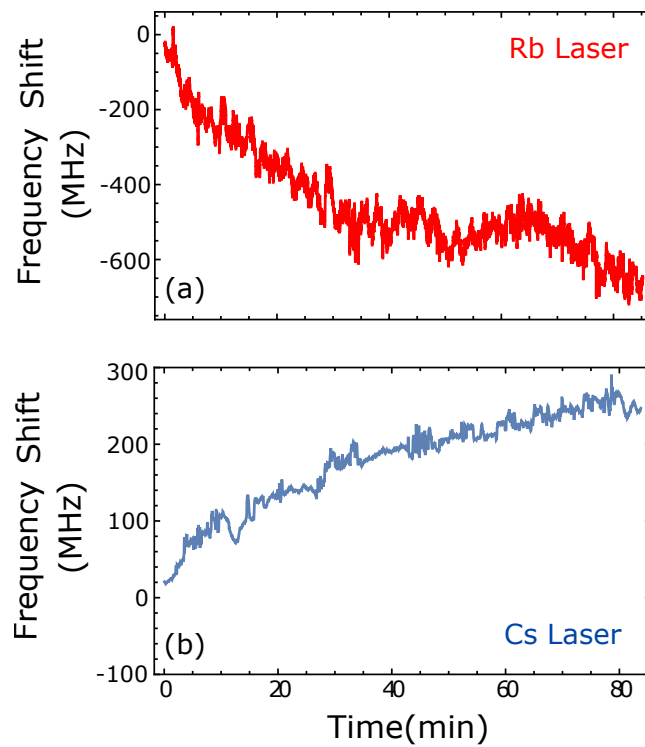


**Figure 4.44:** Frequency drifts of the laser frequency as a function of time for **a)** the Rb laser and **b)** the Cs laser. The measurements are recorded with the wavemeter. The shift is measured from the initial indication of the wavemeter at the beginning of the measurement. The absolute values of the frequencies of the two lasers are 384.26090 THz and 351.32082 THz, respectively.

# Chapter 5 Quantum Trajectory Theory in Spin-Exchange Collisions

---

In this chapter we introduce a quantum trajectory model of the spin-exchange relaxation process, that reproduces the well-known results of the spin-exchange master equation and it might stand as a possible candidate for a first-principle model that could in principle account for the production of spin-polarization noise due to spin-exchange collisions. It is well-known that under normal conditions spin-exchange collisions comprise the dominant relaxation mechanism of the spin polarization in a hot vapor cell [70]. As the fluctuation-dissipation theorem dictates, equilibrium fluctuations are intimately related to the dissipation process of the system under consideration, hence here we aim on a dynamical model of spin noise consistent with the aforementioned reasoning. The results of the fluctuation dissipation theorem are commonly studied in experiments of spin-noise spectroscopy.

Relaxation due to spin-exchange collisions as developed by F.Grossetête [188, 191] and W.Happer [189] results in the master equation for spin-exchange collisions, describing the way a polarized vapor initially in a pure quantum state after the effect of spin-exchange collisions eventually decays to an equilibrium unpolarized state corresponding to a mixed state. This process has been traditionally described by the following master equation

$$\frac{d\rho_A}{dt} = -\frac{i}{\hbar}[H, \rho_A] + \frac{1}{T_{se}}(\rho_{Aex} - \rho_A) + \frac{2iK}{T_{se}}[\mathbf{s}_A \cdot \langle \mathbf{s}_B \rangle, \rho_A] \quad (5.1)$$

where  $1/T_{se}$  is the spin-exchange rate,  $2K/T_{se}$  is a frequency shift due to spin-exchange,  $H$  is the Breit-Rabi Hamiltonian analysed in chapter 2 and

$$\rho_{Aex} = Tr_B(P_e \rho_A \otimes \rho_B P_e^\dagger) \quad (5.2)$$

with  $P_e$  being the spin-exchange operator,

$$P_e = \frac{1}{2} + 2\mathbf{s}_A \cdot \mathbf{s}_B \quad (5.3)$$

This master equation describes the state evolution of a quantum system  $A$ , (like an atom or a vapor) after exhibiting exchange collisions with a quantum system  $B$ . Note that relaxation of the system  $A$  due to collisions with itself can be described by setting  $A = B$  in (5.1). Although we focus on spin polarization precessing at the Larmor frequency, it is clear that a master equation provide information about the state of the

system and hence about any kind of observables.

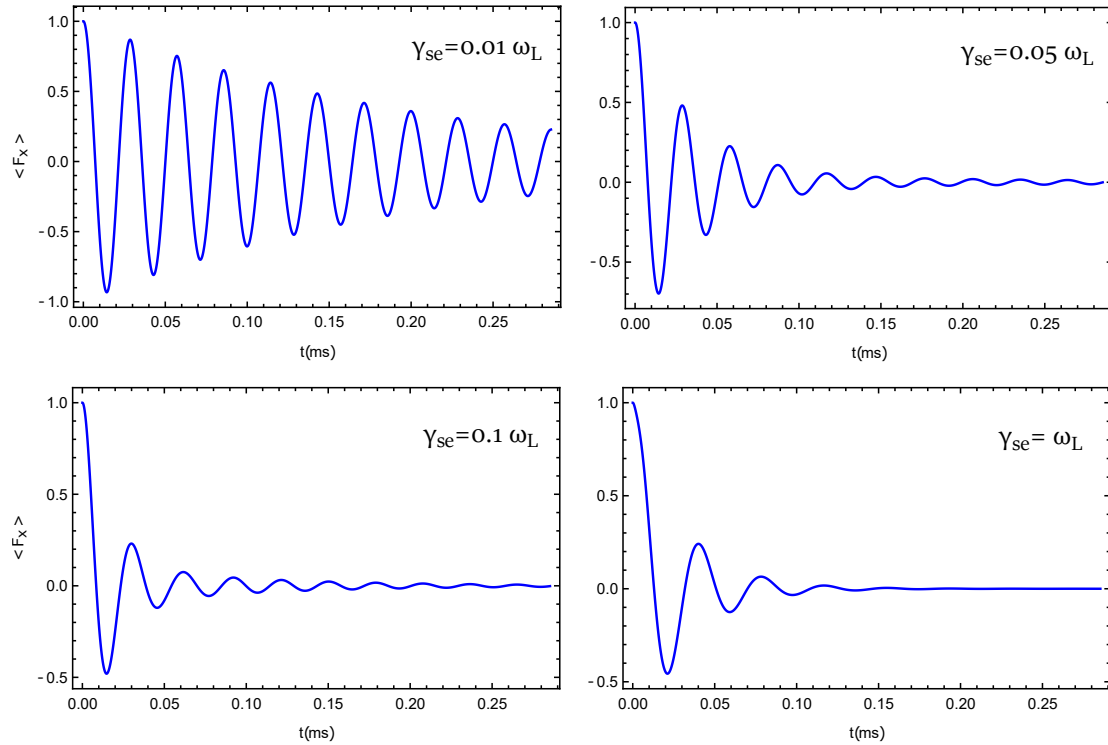


**Figure 5.1:** Real Parameter-numerical simulations of  $^{87}\text{Rb}$  spin precession in a magnetic field of  $B = 50$  mG along the  $\hat{z}$  direction. The initial state is the  $|Fm_F\rangle = |11\rangle_x$  state along  $\hat{x}$  direction. The different plots show relaxation for various values of the SE rate  $\gamma_{se} = 1/T_{se}$  in the case where  $\gamma_{se} \leq \omega_L$ . As expected, increasing the relaxation rate results in faster decay of the spin-precession. The total running time is  $10\tau_L$  where  $\tau_L = 2\pi/\omega_L$  is the Larmor period with  $\omega_L = \frac{g_s\mu_B}{\hbar[I]}B$ .

In Figs. 5.1 and 5.2 we perform realistic numerical simulations of the SE dynamics as described by the master equation (5.1). For the simulation we use a  $^{87}\text{Rb}$  atom with  $I = 3/2$  at a magnetic field of  $B = 50$  mG along the  $\hat{z}$  direction and we examine the cases where the spin exchange rate  $1/T_{se}$  is smaller, comparable or greater from the Larmor frequency. In order to perform the simulation we make use the numerical trick described in [48, 164]. In a small magnetic field, electronic and nuclear spin are strongly coupled hence  $F$  is a "good" quantum number. It is then convenient to expand the density matrix  $\rho$  in a complete basis of coupled hyperfine states  $|i\rangle = |Fm_F\rangle$ ,

$$\rho = \sum_{i,j} \rho_{ij} |i\rangle\langle j| \quad (5.4)$$

The off-diagonal elements in this basis correspond to fast oscillations at the hyperfine frequency. Since we are interested in Zeeman coherences in a small magnetic field, these fast hyperfine oscillations average out at the timescales of the Larmor frequency. It is then convenient to exclude these off-diagonal elements from the density

matrix by projecting-out these elements using the projector operators  $P(a)$  and  $P(b)$  at the upper and lower hyperfine manifolds, respectively. In other words we let  $\rho$  go to  $\rho \rightarrow P(a)\rho P(a) + P(b)\rho P(b)$  where the projector operators are defined as

$$P(a) = \sum_{m_F=-a}^a |am_F\rangle\langle am_F| \quad (5.5)$$

$$P(b) = \sum_{m_F=-b}^b |bm_F\rangle\langle bm_F| \quad (5.6)$$

In matrix form this process is described as

$$\Pi\left\{\begin{bmatrix} \rho_a & * \\ * & \rho_b \end{bmatrix}\right\} = \begin{bmatrix} \rho_a & 0 \\ 0 & \rho_b \end{bmatrix} \quad (5.7)$$

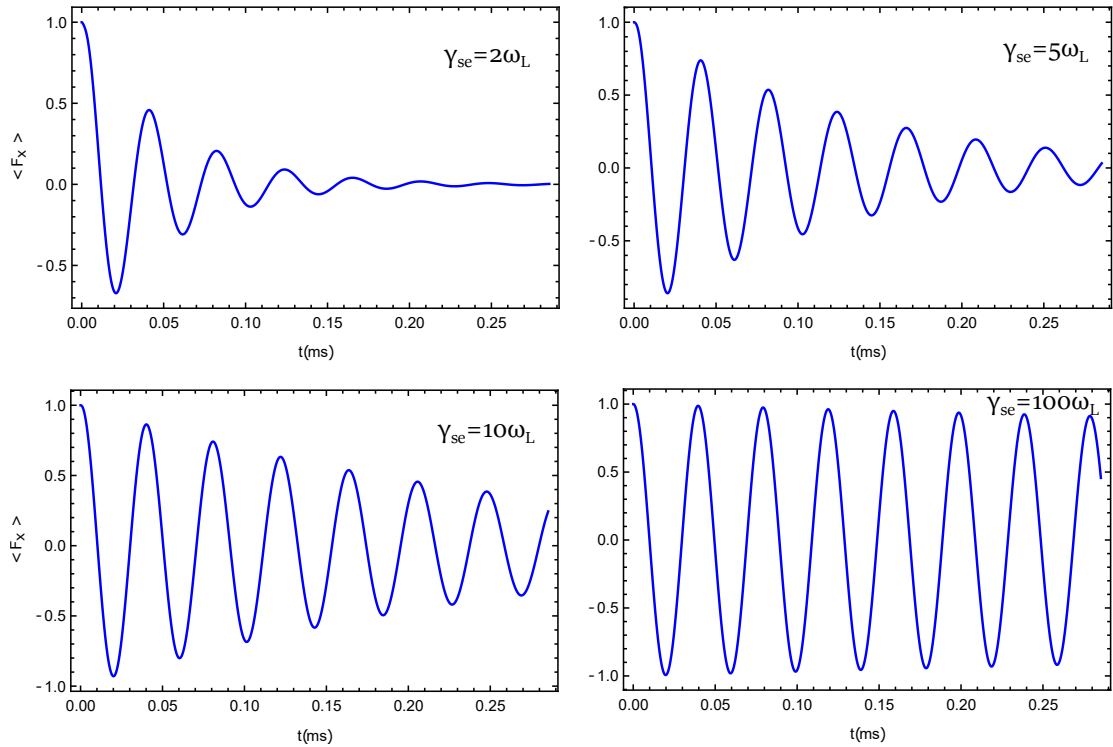


**Figure 5.2:** Real Parameter-numerical simulations of  $^{87}\text{Rb}$  spin precession in a magnetic field of  $B = 50$  mG along the  $\hat{z}$  direction. The initial state is the  $|Fm_F\rangle = |11\rangle_x$  state along  $\hat{x}$  direction. The different plots show relaxation for various values of the SE rate  $\gamma_{se} = 1/T_{se}$  in the case where  $\gamma_{se} \geq \omega_L$ . Increasing the relaxation rate higher above the Larmor frequency result in the so called SERF effect where the spin-exchange relaxation is almost completely suppressed. Note there is also a frequency change consistent with [189]. The total running time is  $10\tau_L$  where  $\tau_L = 2\pi/\omega_L$  is the Larmor period with  $\omega_L = \frac{g_s\mu_B}{\hbar[I]} B$ .

Note that the projection of the hyperfine coherences can be only applied when the hyperfine frequency greatly exceeds the Zeeman and the spin-exchange rate. Care must be taken also in quite higher magnetic fields where the non-linear Zeeman splittings are becoming evident. In these cases the full hyperfine term must be retained. In the

mentioned studies it has been shown that the complete solution with the hyperfine term included agrees closely with the projected solution at the proper parameter regime. In the limit of low polarization, we can ignore the non-linear term of the SE master equation proportional to  $\langle s \rangle$ , then there are analytical relations for the frequency shift and the relaxation rates [189]

$$\frac{\kappa}{\omega_L} = -\frac{[I]^2 + 2}{3T_{se}[I]^2\omega_L} \pm \sqrt{-1 - \frac{2i}{T_{se}\omega_L[I]} + \left(\frac{[I]^2 + 2}{3T_{se}\omega_L[I]^2}\right)^2} \quad (5.8)$$

where the real part of  $\kappa$  is related to the relaxation rate and the imaginary part to the frequency shift. In the case of low polarization, for slow spin-exchange ( $\omega_L T_{se} \gg 1$ ) we obtain

$$\gamma_{se} = \frac{1}{q_{se}} \frac{1}{T_{se}} \quad (5.9)$$

where the so-called spin exchange broadening factor is given by

$$\frac{1}{q_{se}} = \frac{2I(2I - 1)}{3(2I + 1)^2} \quad (5.10)$$

The relaxation of spin polarization due to spin-exchange can be understood as a kind of a dephasing mechanism. The spins in the two different hyperfine manifolds precess with opposite frequencies. If the spin of an atom is localized in a particular hyperfine subset, a spin-exchange collision can alter this subset, resulting in a precession with the opposite frequency. Hence, it is understood that SE relaxation is a combined process between collisions and Hamiltonian evolution in the magnetic field. The sudden collision results in a quantum phase-jump, when averaged over the whole ensemble of atoms leads to the decay of spin polarization.

The phase jumps are schematically described in Fig.5.3. For slow SE rate  $\gamma_{se} \ll \omega_L$ , an SE collision is a rare event, happening within a few cycles resulting in a decay described in the aforementioned numerical simulations. For intermediate values of SE rate  $\gamma_{se} \approx \omega_L$  the decay is large resulting in broadened FFT lines. Finally, for fast SE rate  $\gamma_{se} \gg \omega_L$ , SE is sudden compared to the larmor frequency yielding a coherent sawtoothed sine wave with diminished SE relaxation. This phase jump model initiated our interest about a quantum trajectory picture of SE collisions and laid the foundations towards a dynamical picture of spin-noise production yielding from SE interactions.

## 5.1 Phase-Jump Toy Model

In the present section we review a phase diffusion model applied to spin-1/2 atoms [26]. Although alkali atoms are multilevel atoms with complex collisional dynamics, this toy model embodies the main physical scenario behind the SE phase jumps that

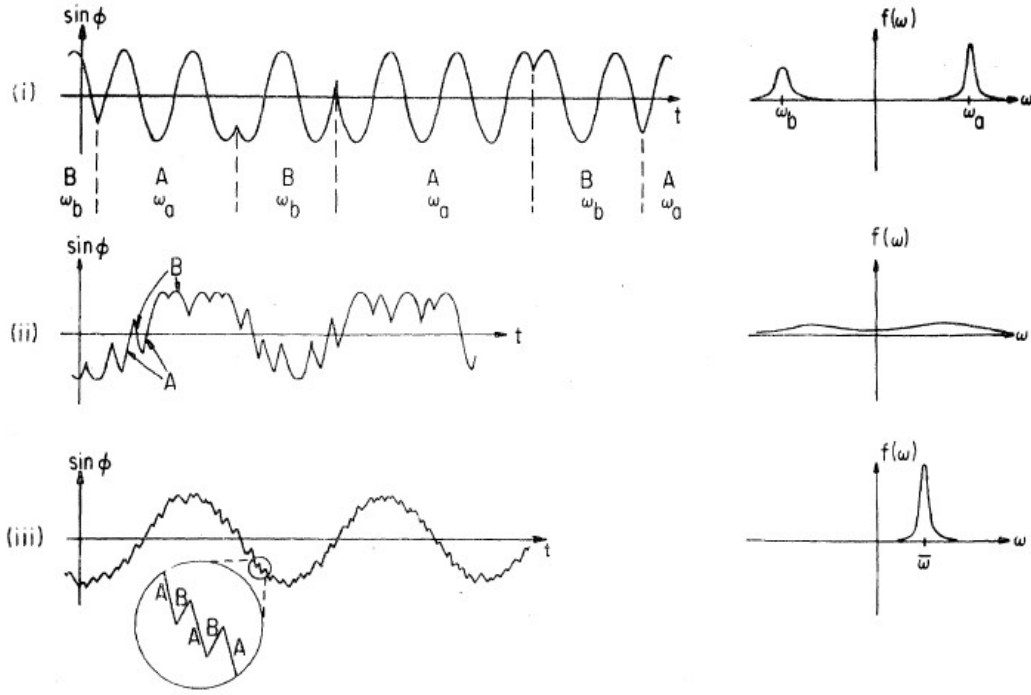


**Figure 5.3:** Taken from [189]. Precession phase angle SE jumps and Fourier spectrum  $f(\omega)$  for various SE rates. i) Slow SE rate  $\gamma_{se} \ll \omega_L$ , ii) intermediate SE rate  $\gamma_{se} \approx \omega_L$  and iii) fast SE rate  $\gamma_{se} \gg \omega_L$ .

drive spin-noise dynamics and when averaged, result in the relaxation of the collective spin component. Suppose we have a collection of  $N$  independent two level spin-1/2 atoms enclosed in a vapor cell.

In the absence of any relaxation process, spins precess coherently in a constant magnetic field along the  $z$ -axis. The precession of transverse spin component of the  $i_{th}$  atom is given by

$$s_T^i(t) = s_x^i(t) + i s_y^i(t) = s_T^i(0) e^{-i(\omega_i t - \phi_i(t))} \quad (5.11)$$

where  $\omega_i$  is the Larmor frequency and  $\phi_i(t)$  is the phase of the oscillation of the  $i_{th}$  atom. We assume that the atoms are distinguishable and independent, hence the total collective transverse spin component is the sum of all transverse spin components of all atoms, all precessing at the Larmor frequency  $\omega$ ,

$$S_T(t) = \sum_{i=1}^N s_T^i(t) = s_T(0) e^{-i\omega t} \sum_{i=1}^N e^{i\phi_i(t)} \quad (5.12)$$

Collisions between different atoms in the vapor cell destroy the coherent oscillation of the spins. As we have discussed, they disturb the phase of the oscillation and reset it in a random way. Thus the coherent spin precession receives random phase kicks at random points in time. These collisions depend on the density of the atoms in the gas, on the velocity and on the cross-section of the collisional interaction. Therefore, the

covariance function of the total transverse spin component at two different points in time is

$$\langle S_T^*(t_A)S_T(t_B) \rangle = \langle s_T^*(0)s_T(0) \rangle e^{-i\omega(t_B-t_A)} \left\langle \sum_{i,j}^N e^{i(\phi_i(t_B)-\phi_j(t_A))} \right\rangle \quad (5.13)$$

where the brackets  $\langle \cdot \rangle$  denote the ensemble average over different realizations of the random variable  $\phi(t)$ . We find convenient to split the sum into terms  $i = j$  and  $i \neq j$ , therefore

$$\langle S_T^*(t_A)S_T(t_B) \rangle = \langle s_T^*(0)s_T(0) \rangle e^{-i\omega(t_B-t_A)} \left\langle \sum_{i=j}^N e^{i(\phi_i(t_B)-\phi_j(t_A))} + \sum_{i \neq j}^N e^{i(\phi_i(t_B)-\phi_j(t_A))} \right\rangle \quad (5.14)$$

The equal time covariance is given for  $t_A = t_B$ . Assuming that there is no correlation between atoms  $i$  and  $j$  and since  $\phi(t)$  is a random variable, the spin  $i$  will acquire a completely random phase with respect to the spin  $j$  at the same time instant  $t_A$ . Hence, the average value over all particles and over all realizations is zero resulting in

$$\langle S_T^*(t_A)S_T(t_A) \rangle = N \langle s_T^*(0)s_T(0) \rangle \quad (5.15)$$

which is proportional to the variance of the collective transverse spin component in agreement with the results presented in the *Bloch Equations* section. For different times  $t_A \neq t_B$ , different atoms share no-correlation similar to the equal time case. However, for same spins  $i = j$  there is a timescale in between collisions that there exists some coherence. Thus, for the spin within a time interval  $\tau$  there is "memory" of the oscillation whereas for timescales larger than  $\tau$  the correlation is lost. In that case the covariance function is given by

$$\langle S_T^*(t_A)S_T(t_B) \rangle = \langle s_T^*(0)s_T(0) \rangle e^{-i\omega(t_B-t_A)} \left\langle \sum_{i=1}^N e^{i(\phi_i(t_B)-\phi_i(t_A))} \right\rangle \quad (5.16)$$

in equilibrium, assuming ergodicity, that is the phase difference depends only on the time interval  $t_B - t_A$ , not on the origin  $t = 0$  we obtain a phase coherence in the case where  $t_B - t_A \approx \tau$

$$\langle S_T^*(t_A)S_T(t_B) \rangle = \langle s_T^*(0)s_T(0) \rangle e^{-i\omega\tau} \left\langle \sum_{i=1}^N e^{i(\phi_i(\tau)-\phi_i(0))} \right\rangle \quad (5.17)$$

where we can arbitrarily chose  $\phi_i(0) = 0$ . Assuming further that  $\phi(t)$  is a zero-mean Gaussian process, that is, its values are spanned from a Gaussian probability distribution [121], we obtain the familiar formula for the covariance function

$$\langle S_x(t_A)S_x(t_B) \rangle = \text{Re}[\langle s_T^*(0)s_T(0) \rangle e^{-i\omega\tau} e^{-\gamma\tau}] = \langle s_x^2(0) \rangle \cos(\omega\tau) e^{-\gamma\tau} \quad (5.18)$$



## 5.2 Overview of Quantum Trajectory Theory

Quantum trajectory theory is a theoretical formalism developed in 1980's and 1990's to describe the relaxation dynamics of open quantum systems subjected to continuous monitoring [177]. In quantum optics, quantum trajectories gained a lot of attention since a lot of known results could be reproduced by the theory, providing a new interpretation founded on more statistical grounds [147]. The theory is also known as quantum Monte-Carlo wavefunction or quantum jump method or quantum state diffusion.

In the theory of open quantum systems, the decoherence and the energy dissipation of the system results from a system-environment interaction leaving the former in a mixed quantum state. The environment is assumed to be a large ensemble of quantum systems usually in a thermal equilibrium state with infinitely many degrees of freedom such that reversible behaviour is eliminated, at least for all practical timescales. However, there are situations where the environment contains a small number of degrees of freedom, like for example in the case where an atomic spin is embedded in an environment of a few nuclear spins, where there have been developed techniques like dynamic decoupling that aim to increase the coherent lifetime using coherent rf or microwave pulses by decoupling the system from the nuclear spin environment [223–225].

The relaxation of a quantum system, especially in the case of the spin, is understood either as the decay of the spin polarization to zero or as decoherence, i.e. the loss of the ability of a quantum system to exhibit interference (or quantum coherence) between different alternatives [226]. Both effects are intimately related and in most of the cases, loss of the one implies directly loss of the other.

The main idea of open quantum systems can be summarized in the following scenario<sup>1</sup>. Suppose we track the dynamics of two quantum systems in a common Hilbert space, spanned by the tensor product of the individual Hilbert spaces of each subsystem. We call the one "system" of interest and the other "environment" or "bath" or "reservoir". The two-system state at time  $t = 0$  is described by  $\hat{\rho}_{SE}(0)$  and the combined state evolves in time according to a unitary evolution described by the unitary operator  $\hat{U}_{SE}(t)$ . For simplicity we omit the hat ^ symbol from operators and we recover it when there could be potential confusion. The state of the combined system at time  $t$  is then

$$\rho_{SE}(t) = U_{SE}(t)\rho_{SE}(0)U_{SE}^\dagger(t).$$

If we want to know the state of the system alone at time  $t$ , we have to trace-out the environment's state, resulting in  $\rho_S(t) = Tr_E(\rho_{SE}(t)) = Tr_E(U_{SE}(t)\rho_{SE}(0)U_{SE}^\dagger(t))$ .

<sup>1</sup>The following discussion is a brief review of the online video lectures of Prof. Ivan Deutsch for the course "Quantum Optics II -Fall 2014".



The usual starting assumption is that at time  $t = 0$  the system and the environment can be written in separable form reflecting that the two quantum systems have not interacted in the past. Therefore the initial state can be written as  $\rho_{SE}(0) = \rho_S(0) \otimes \rho_E(0)$ . Furthermore we can assume that initially both the system and the bath are described by pure quantum states. Let's denote the system state as  $\rho_S(0) = |s\rangle\langle s|$  and the reservoir state as  $\rho_E(0) = |r\rangle\langle r|$ . In that case, the state of the system at time  $t$  is given by  $\rho_S(t) = Tr_E(\rho_{SE}(t)) = Tr_E(U_{SE}(t)\rho_{SE}(0)U_{SE}^\dagger(t)) = Tr_E(U_{SE}(t)\rho_S(0) \otimes \rho_E(0)U_{SE}^\dagger(t)) = Tr_E(U_{SE}(t)\rho_S(0) \otimes |r\rangle\langle r|U_{SE}^\dagger(t))$ . We assume that there is an orthonormal basis  $\{|j\rangle_E\}$  for the environment hence we can evaluate the trace, resulting in the state of the system at time  $t$  to be written as

$$\rho_S(t) = \sum_j \langle j|_E U_{SE}(t)|r\rangle \rho_S(0) \langle r|U_{SE}^\dagger(t)|j\rangle_E \quad (5.19)$$

The quantity  $\langle j|_E U_{SE}(t)|r\rangle$  is called partial matrix element because  $U_{SE}(t)$  is an operator that acts both on system and environment whereas the matrix-element refers only on the environment's states. We define the so-called Kraus operators as  $\mathcal{K}_j(t) = \langle j|_E U_{SE}(t)|r\rangle$  acting only on the system's state, therefore we obtain

$$\rho_S(t) = \sum_j \mathcal{K}_j(t)\rho_S(0)\mathcal{K}_j^\dagger(t) \quad (5.20)$$

The above formula describes the Kraus-representation of the system's density matrix which relates the state of the system at time  $t$  with the state at time  $t = 0$  after the interaction with the environment. The process  $\rho_S(t) = a(t)[\rho_S(0)]$  sometimes is called a completely positive quantum map or a quantum operation [186]. Given that the state of the system at time  $t = 0$  is a pure quantum state  $\rho_S(0) = |s\rangle\langle s|$  the state at time  $t$  can be simplified to

$$\rho_S(t) = \sum_j \mathcal{K}_j(t)|s\rangle\langle s|\mathcal{K}_j^\dagger(t) = \sum_j P_j(t)|\psi_j(t)\rangle\langle\psi_j(t)| \quad (5.21)$$

where  $|\psi_j(t)\rangle$  is a normalized pure state and  $P_j(t)$  is the probability to find the system at the state  $|\psi_j(t)\rangle$ . The normalized state and the probability are defined as

$$|\psi_j(t)\rangle = \frac{\mathcal{K}_j(t)|s\rangle}{\|\mathcal{K}_j(t)|s\rangle\|} \quad (5.22)$$

$$P_j(t) = \|\mathcal{K}_j(t)|s\rangle\|^2 = \langle s|\mathcal{K}_j^\dagger(t)\mathcal{K}_j(t)|s\rangle \quad (5.23)$$

We obtain that generally the state of the system at time  $t$  is a quantum mixed state, whereas the initial state was pure. Note that the final state is a physical state, meaning that it has always positive eigenvalues and it is a Hermitian operator. This is a pure state decomposition of the open quantum system dynamics where  $P_j(t)$  is the probability associated with the particular pure state decomposition  $|\psi_j(t)\rangle$ . We note that there is



not a unique pure state decomposition of the open evolution and that  $|\psi_j(t)\rangle\langle\psi_j(t)|$  is not necessary a diagonal representation.

By diagonalizing we obtain the so-called Schmidt decomposition of the state. The fact that this decomposition is not unique is obvious since the trace-out process can be applied using different sets of complete basis. The fact that the final state is a mixed whereas the initial was a pure state, reflects an entropy growth due to the interaction with the environment, since the initial pure state by definition has zero entropy. This phenomenon i) reflects that information is leaking out from the system to the environment and ii) serves as an indicator of quantum correlations <sup>2</sup> built-up between the system and the environment <sup>3</sup>. The Kraus operators satisfy the following relation

$$\sum_j \mathcal{K}_j^\dagger(t) \mathcal{K}_j(t) = \sum_j \langle r | U_{SE}^\dagger(t) | j \rangle_E \langle j |_E U_{SE}(t) | r \rangle = \mathbb{1}^4 \quad (5.24)$$

reflecting that the total probability is conserved  $\sum_j P_j(t) = 1$  and that  $\text{Tr}_s(\rho_s(t)) = 1$ . In the proof above we used the completeness relation of the environmental basis states  $\sum_j |j\rangle_E \langle j|_E = \mathbb{1}$  and the property  $U_{SE}^\dagger(t) U_{SE}(t) = \mathbb{1}$  of the unitary operators. In that case the quantum map is said to be trace-preserving and completely positive quantum map <sup>5</sup>, denoted as CP-map.

Searching for a connection of the quantum map at time  $t + dt$  to that at time  $t$  and using only the characteristics of the map we defined previously and the Markovian approximation <sup>6</sup>, one can arrive at known Lindblad master equation [227]. The state of the system at time  $t + dt$  is related to the one at time  $t$  via  $\rho_s(t + dt) = \mathcal{K}_0 \rho_s(t) \mathcal{K}_0^\dagger + \sum_{j>0} \mathcal{K}_j \rho_s(t) \mathcal{K}_j^\dagger$  where  $\mathcal{K}_0 = \mathbb{1} - \frac{i}{\hbar} H_{eff} dt$  and  $\mathcal{K}_j = L_j \sqrt{dt}$ , with  $H_{eff} = H - \frac{i\hbar}{2} \sum_j L_j^\dagger L_j$  <sup>7</sup> being an effective non-Hermitian Hamiltonian. Replacing the formulas for

<sup>2</sup>There is a plethora of quantum correlations depending on the interaction and the particular states of interest, the interested reader may consult [187]. The most studied and simple to interpret representative of quantum correlations is the quantum entanglement.

<sup>3</sup>For more information and for formal derivations of the discussed effects, see for example [8].

<sup>4</sup>The dimension of the identity matrix  $\mathbb{1}$  should be obvious from the context. The same notation is used either for the identity matrix of the combined system-environment space or for the system space alone.

<sup>5</sup>Note that the complete positivity is a more strict criterion than the simple positivity we have shown above. Although it is out of the scope of this thesis to get into that kind of technical details, most of the physical systems of interest here satisfy the CP criterion.

<sup>6</sup>The Markovian approximation refers to the bath correlation function, rendering it a delta correlation function in the time-domain. Physically, the delta correlation describes a "memoryless" bath meaning that the information leaking from the system to the environment is instantly lost or in other words the state of the bath is not affected by the interaction, therefore the system eventually interacts with the same bath-state at each moment, regardless the coarse-graining time interval  $dt$ . In practise, there is always a correlation time  $\tau_c$ , however we assume  $dt \gg \tau_c$ .

<sup>7</sup> $H_{eff}$  is the effective non-Hermitian Hamiltonian comprised of a usual Hermitian-Hamiltonian part and a non-Hermitian one. Note that this open quantum system formalism can be applied to the atom-light interaction's non-Hermitian Hamiltonian introduced in chapter 2, exploring Happer's seminal paper [135] using the modern tools of quantum optics. Actually, this has been done in [117], extending the theory also

the Kraus operators, we find the equation for the time-evolution of state of the system

$$\begin{aligned} \frac{d\rho_s(t)}{dt} &= -\frac{i}{\hbar}(H_{eff}\rho_s(t) - \rho_s(t)H_{eff}^\dagger) + \sum_j L_j\rho_s(t)L_j^\dagger \\ &= -\frac{i}{\hbar}[H, \rho_s(t)] + \sum_j \left(-\frac{1}{2}L_j^\dagger L_j\rho_s(t) - \frac{1}{2}\rho_s(t)L_j^\dagger L_j + L_j\rho_s(t)L_j^\dagger\right) \end{aligned} \quad (5.25)$$

The set  $\{L_j\}$  is the set of the so-called Lindblad operators, sometimes also known as jump operators. Given that the system is in a state  $|\psi_i\rangle$ , the total decay rate to all possible final states  $|\psi_f\rangle$  via the process  $L_j$  is given by  $\gamma_{i\rightarrow f} = \sum_f |\langle\psi_f|L_j|\psi_i\rangle|^2 = \sum_f \langle\psi_i|L_j^\dagger L_j|\psi_i\rangle$  that is, the expectation value of the decay part of the effective Hamiltonian in the state of the system  $|\psi_i\rangle$ .

So far the above description applies to the case where we trace-out the environmental degrees of freedom and we arrive at a dynamical equation for the quantum system of interest. Suppose now that we have access to the environment and instead of tracing-out over all possible states, we can perform projective measurements on the environmental states using a particular set of basis states, in order to extract information about specific outcomes of the system-bath interaction on that particular states. Suppose we measure the environment and we find it in the state  $|j\rangle_E$ . As we have discussed, the normalized post measurement state of the system is

$$|\psi_j(t)\rangle = \frac{\mathcal{K}_j(t)|s\rangle}{\|\mathcal{K}_j(t)|s\rangle\|} \quad (5.26)$$

and the probability with which we obtain the  $j_{th}$  outcome of the measurement, corresponding to the eigenvector  $|j\rangle_E$  and subsequently to the state of the system  $|\psi_j(t)\rangle$  is

$$P_j(t) = \|\mathcal{K}_j(t)|s\rangle\|^2 = \langle s|\mathcal{K}_j^\dagger(t)\mathcal{K}_j(t)|s\rangle \quad (5.27)$$

This is a generalized measurement on the system, by letting it interact with a quantum probe and then perform measurements on the probe. These generalized measurements are usually encountered with the acronym *POVM* measurements (Positive Operator Value Measure). In general, if we want to perform a measurement of a quantum state  $|\psi\rangle$ , the probability of obtaining the  $j_{th}$  outcome is given by  $P_j = \langle\psi|\hat{E}_j|\psi\rangle$ , where  $\hat{E}_j$  are positive operators that sum up to unity  $\sum_j \hat{E}_j = \mathbb{1}$ . In the particular case that we can write down the interaction of system-environment in terms of Kraus operators, the POVM elements are  $\hat{E}_j = K_j^\dagger K_j$ . Therefore, we can interpret the open quantum system dynamics as the environment performing POVM measurements on the system, where these generalized measurements are described by a set of Kraus operators

---

in the case where spontaneous emission is included. Spontaneous emission is introduced in the theory by the Lindblad operator-part not included in  $H_{eff}$ . This term is usually called refeeding term, while the effective Hamiltonian contains a Hamiltonian and a decay term.



$\{\hat{K}_j\}$ . If we don't have access to the measurement outcomes of the POVM, then we have to average over all the possible measurement outcomes, resulting in an equivalent way of describing the trace-out process discussed previously. Then the final state is  $\rho = \sum_j P_j |\psi_j\rangle\langle\psi_j|$  which is a complex combination of all the possible pure state outcomes that could occur weighted by the associated probabilities. Going back to the Lindblad case we saw that the state of the system can be decomposed as

$$\begin{aligned}\rho_s(t + dt) &= \mathcal{K}_0(dt)\rho_s(t)\mathcal{K}_0^\dagger(dt) + \sum_j \mathcal{K}_j(dt)\rho_s(t)\mathcal{K}_j^\dagger(dt) \\ &= P_0|\psi_0(t)\rangle\langle\psi_0(t)| + \sum_j P_j|\psi_j(t)\rangle\langle\psi_j(t)|\end{aligned}\quad (5.28)$$

where  $\rho_s(t) = |\psi(t)\rangle\langle\psi(t)|$ . This formula can be interpreted as a complex combination of different potential pure evolutions that are random and occur with some certain probability that depends on the given state of the system at time  $t$  and on the particular measurement outcome. The pure state of the system  $|\psi(t + dt)\rangle$  corresponding to a particular measurement is

$$|\psi_j(t + dt)\rangle = \frac{\mathcal{K}_j(t)|\psi(t)\rangle}{\|\mathcal{K}_j(t)|\psi(t)\rangle\|} = \frac{L_j(t)|\psi(t)\rangle}{\|L_j(t)|\psi(t)\rangle\|}\quad (5.29)$$

while the probability is given by

$$P_j(t + dt) = \langle\psi(t)|\mathcal{K}_j^\dagger(t)\mathcal{K}_j(t)|\psi(t)\rangle = |\psi(t)\rangle L_j^\dagger(t)L_j(t)|\psi(t)\rangle dt\quad (5.30)$$

Moreover, the quantities  $\hat{K}_0$  and  $P_0 = \langle\psi(t)|\mathcal{K}_0^\dagger(t)\mathcal{K}_0(t)|\psi(t)\rangle = 1 - \sum_j P_j$  can be directly calculated using the formulas introduced previously

$$|\psi_0(t + dt)\rangle = \frac{\mathcal{K}_0(t)|\psi(t)\rangle}{\|\mathcal{K}_0(t)|\psi(t)\rangle\|} = \frac{e^{-\frac{i}{\hbar}\hat{H}_{eff}dt}|\psi(t)\rangle}{\left\|e^{-\frac{i}{\hbar}\hat{H}_{eff}dt}|\psi(t)\rangle\right\|}\quad (5.31)$$

Hence, the dynamics of the system has been unravelled into a pure state decomposition where with probability  $P_j$  the Lindblad jump operator  $L_j$  acts on the state of the system, while with probability  $1 - P_j$  the system evolves under the non-Hermitian effective Hamiltonian  $H_{eff}$ . Then the post-measurement states are evolved accordingly.

The idea of quantum trajectories is based on this pure state unravelling of the open quantum system dynamics. In each time interval  $dt$  we let a random number generator to produce a random number  $x$  in the interval  $x \in [0, 1]$ . This number is a realization of the probabilities  $P_0$  and  $P_j$  and determines in each  $dt$  whether a jump with  $L_j$  or an evolution with  $H_{eff}$  is going to occur. Then the state is updated based on this particular random outcome. In the subsequent time steps  $dt$  we repeat the same process again and again until a final time  $T$ . Note that in each time interval the state remains pure. If we repeat the same process many times, different pure state realizations of the open quantum system dynamics will occur. An ensemble average of all these dynamics will reproduce



the Lindblad master equation dynamics that drives the system towards a final mixed state. Note that since the pure trajectory unravelling of the dynamics is a stochastic process, the mean ensemble average will follow the predictions of the master equation while there will be also stochastic fluctuations around this mean, that are quantum in nature and stem from the random state choice, with the probability being defined based on the particular interaction.

## 5.3 Quantum Trajectories and Spin-Exchange Dynamics

In this section we examine and apply the formalism of quantum trajectories to the case of an alkali vapor enclosed in a vapor cell and we interpret the stochastic spin dynamics in equilibrium as different manifestations of the pure state decomposition of the open quantum system dynamics. Initially, we will introduce some useful concepts of the spin-exchange interaction and then we are going to apply the theory of quantum trajectories to an example system of a vapor with  $\langle \mathbf{s} \rangle = 0$ . It can be shown that in that case, the spin-dynamics are governed by a Lindblad master equation and the collisions that drive randomly the spin state are known as spin-randomization collisions. In the beginning of the chapter we introduced the SE operator as  $P_e = \frac{1}{2}\mathbb{1} + 2\mathbf{s}_1 \cdot \mathbf{s}_2$ . This operator is responsible for the electron spin-spin interaction of the two vapors<sup>8</sup>. In small magnetic fields, the commonly used basis for an atom is the coupled  $|Fm\rangle$  basis. The action of the spin exchange operator on two such uncorrelated  $|Fm\rangle$  states of two different atoms result in

---

<sup>8</sup>Since we follow the general assumption that the atoms in the vapor cell are completely uncorrelated, then the same physics applies whether we talk about single atoms or about the density matrix of the whole vapor.



$$\begin{aligned}
|\psi_f\rangle = P_e|F_1m_1\rangle|F_2m_2\rangle = & \\
& q_1^A(m_1)q_1^B(m_2)c_1^A(m_1)c_1^B(m_2)|a_1m_1\rangle|a_2m_2\rangle \\
& - q_1^A(m_1)q_1^B(m_2)c_1^A(m_1)c_2^B(m_2)|a_1m_1\rangle|b_2m_2\rangle \\
& - q_1^A(m_1)q_1^B(m_2)c_2^A(m_1)c_1^B(m_2)|b_1m_1\rangle|a_2m_2\rangle \\
& + c_1^A(m_1)c_1^B(m_2)c_2^A(m_1)c_2^B(m_2)|b_1m_1\rangle|b_2m_2\rangle \\
& + q_2^A(m_1)q_2^B(m_2)c_2^A(m_1)c_2^B(m_2)|a_1m_1\rangle|a_2m_2\rangle \\
& + q_2^A(m_1)q_2^B(m_2)c_2^A(m_1)c_1^B(m_2)|a_1m_1\rangle|b_2m_2\rangle \\
& + q_2^A(m_1)q_2^B(m_2)c_1^A(m_1)c_2^B(m_2)|b_1m_1\rangle|a_2m_2\rangle \\
& + q_2^A(m_1)q_2^B(m_2)c_1^A(m_1)c_1^B(m_2)|b_1m_1\rangle|b_2m_2\rangle \\
& + q_1^A(m_1)q_2^B(m_2)c_2^A(m_1+1)c_1^B(m_2-1)|a_1m_1+1\rangle|a_2m_2-1\rangle \\
& - q_1^A(m_1)q_2^B(m_2)c_2^A(m_1+1)c_2^B(m_2-1)|a_1m_1+1\rangle|b_2m_2-1\rangle \\
& + q_1^A(m_1)q_2^B(m_2)c_1^A(m_1+1)c_1^B(m_2-1)|b_1m_1+1\rangle|a_2m_2-1\rangle \\
& - q_1^A(m_1)q_2^B(m_2)c_1^A(m_1+1)c_2^B(m_2-1)|b_1m_1+1\rangle|b_2m_2-1\rangle \\
& + q_2^A(m_1)q_1^B(m_2)c_1^A(m_1-1)c_2^B(m_2+1)|a_1m_1-1\rangle|a_2m_2+1\rangle \\
& + q_2^A(m_1)q_1^B(m_2)c_1^A(m_1-1)c_1^B(m_2+1)|a_1m_1-1\rangle|b_2m_2+1\rangle \\
& - q_2^A(m_1)q_1^B(m_2)c_2^A(m_1-1)c_2^B(m_2+1)|b_1m_1-1\rangle|a_2m_2+1\rangle \\
& - q_2^A(m_1)q_1^B(m_2)c_2^A(m_1-1)c_1^B(m_2+1)|b_1m_1-1\rangle|b_2m_2+1\rangle
\end{aligned} \tag{5.32}$$

To obtain the result above one needs to start from two general pure  $|F_1m_1\rangle$  and  $|F_2m_2\rangle$  states, express them in the uncoupled basis, then act with the SE operator  $P_e$  and finally move again back to the coupled basis. This is achieved by making use of the general Clebsch-Gordan coefficients defined in [50]

$$c_1 = \sqrt{\frac{a+m_F}{[I]}} \quad c_2 = \sqrt{\frac{a-m_F}{[I]}} \tag{5.33}$$

we note that the states between the coupled and the uncoupled basis are related via:

$$|am_F\rangle = c_2|m_F + \frac{1}{2}, -\frac{1}{2}\rangle + c_1|m_F - \frac{1}{2}, \frac{1}{2}\rangle \tag{5.34}$$

$$|bm_F\rangle = -c_1|m_F + \frac{1}{2}, -\frac{1}{2}\rangle + c_2|m_F - \frac{1}{2}, \frac{1}{2}\rangle \tag{5.35}$$

$$|m_I, \frac{1}{2}\rangle = c_1|a, m_I + \frac{1}{2}\rangle + c_2|b, m_I + \frac{1}{2}\rangle \tag{5.36}$$

$$|m_I, -\frac{1}{2}\rangle = c_2|a, m_I - \frac{1}{2}\rangle - c_1|b, m_I - \frac{1}{2}\rangle \tag{5.37}$$

The coefficients  $q_1^A$ ,  $q_2^A$ ,  $q_1^B$  and  $q_2^B$  are equal to  $c_1$  or  $c_2$  depending on the initial state. For example, for  $|F_1m_1\rangle = |a_1m_1\rangle$  and  $|F_2m_2\rangle = |b_2m_2\rangle$  the coefficients  $q$  take the



following values

$$q_1^A = c_2 \quad q_2^A = c_1 \quad q_1^B = -c_1 \quad q_2^B = c_2 \quad (5.38)$$

defined by equations (5.34) and (5.35). This result applies to all alkali atoms, being in any pure  $|Fm\rangle$  state and can be generalized easily to mixed states when expanded in the  $\{|Fm\rangle\}$  basis. Although the result looks complicated, it turns out it can be easily interpreted in terms of spin conservation. It is a well-known characteristic of SE collisions that they conserve the total spin of the interaction. This is expressed by the relation  $m_1 + m_2 = m'_1 + m'_2$  where  $m_1$  and  $m_2$  are the spin projections along the quantization axis before the collision while the prime denotes the projections after the collision. Based on this conservation law, the states participating in this large superposition are all the possible states that satisfy this conservation law. Given that the second atom is found in a particular state  $|F'_2 m'_2\rangle$  after the collision, then atom one should be found to the corresponding state  $|F'_1 m'_1\rangle$  that satisfies the angular momentum conservation law. A useful formula for calculating the probability of a particular jump-

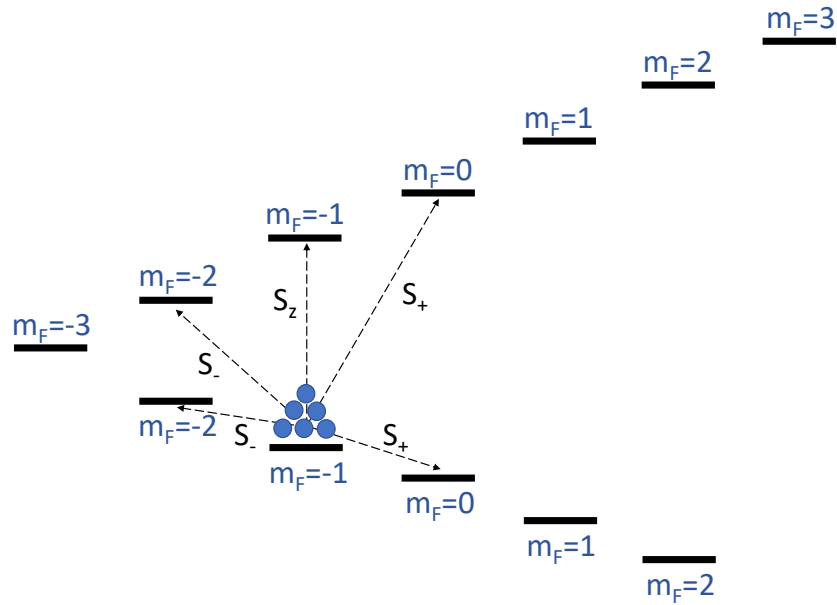


**Figure 5.4:** Schematic representation of all possible final states of a  $^{85}\text{Rb}$  atom initially in the state  $|Fm\rangle = |2 - 1\rangle$ , when the second atom is projected to a particular state out of all the possible states of the superposition.

transition to happen due to SE is given by [184, 228, 229]

$$\begin{aligned} \langle F'_1 m'_1 F'_2 m'_2 | \mathbf{s}_1 \cdot \mathbf{s}_2 | F_1 m_1 F_2 m_2 \rangle &= \sum_q (-1)^{q+F'_1+F'_2-m'_1-m'_2} \\ &\times \begin{pmatrix} F'_1 & 1 & F_1 \\ -m'_1 & q & m_1 \end{pmatrix} \begin{pmatrix} F'_2 & 1 & F_2 \\ -m'_2 & -q & m_2 \end{pmatrix} \langle F'_1 || S_1 | F_1 \rangle \langle F'_2 || S_2 | F_2 \rangle \end{aligned} \quad (5.39)$$

where the parenthesis denote 3J-symbols, spin operators are rank-1 tensors written in the spherical basis as  $\mathbf{s}_1 \cdot \mathbf{s}_2 = \sum_q (-1)^q s_q^1 s_{-q}^2$  and the reduced matrix elements are given by

$$\langle F' || S || F \rangle = \sqrt{\frac{3}{2}} (-1)^{F+I+1+S} \sqrt{(2F'+1)(2F+1)} \begin{Bmatrix} 1/2 & F' & I \\ F & 1/2 & 1 \end{Bmatrix} \quad (5.40)$$

Based on the formulas above it is straightforward to define also jump operators for example for the first atom when the second is projected in a particular  $|F'_2 m'_2\rangle$  state. These operators (let's call them L) must be proportional to the spin operators  $S_+$ ,  $S_-$  and  $S_z$  as indicated by the Fig.5.4 and can be written as

$$\hat{L}_q = (-1)^q \hat{s}_q^1 \langle F'_2 m'_2 | s_{-q}^2 | F_2 m_2 \rangle = (-1)^{q+F'_2-m'_2} \hat{s}_q^1 \begin{pmatrix} F'_2 & 1 & F_2 \\ -m'_2 & -q & m_2 \end{pmatrix} \langle F'_2 || S_2 || F_2 \rangle \quad (5.41)$$

Since we completed the description of the tools needed to understand the effects of SE interaction on the atomic energy sublevels we are going to apply the quantum trajectory theory to the case where the expectation value of the ensemble spin is kept to zero. This is the case described in [33] ( $\hbar = 1$ )

$$\frac{d\rho_s}{dt} = -i[H_g, \rho_s] + \frac{1}{T_2} (s_z \rho_s s_z - \frac{3}{4} \rho_s + \frac{1}{2} s_+ \rho_s s_- + \frac{1}{2} s_- \rho_s s_+) \quad (5.42)$$

using the identity

$$\frac{3}{4} = s^2 = s_x^2 + s_y^2 + s_z^2 = \frac{1}{2} (s_+ s_- + s_- s_+) + s_z^2 \quad (5.43)$$

we can write (5.42) in Lindblad form,

$$\frac{d\rho_s}{dt} = -i[H_g, \rho_s] + \sum_j \left( -\frac{1}{2} L_j^\dagger L_j \rho_s - \frac{1}{2} \rho_s L_j^\dagger L_j + L_j \rho_s L_j^\dagger \right) \quad (5.44)$$

where the Lindblad operators are

$$\hat{L}_1 = \frac{1}{\sqrt{2T_2}} s_+ \quad \hat{L}_2 = \frac{1}{\sqrt{2T_2}} s_- \quad \hat{L}_3 = \frac{1}{\sqrt{T_2}} s_z \quad (5.45)$$

The Lindblad operators can be understood when a pure state decomposition of the density matrix in the  $\{|Fm\rangle\}$  basis is considered. In matching with Fig.5.4,  $\hat{L}_1$  and  $\hat{L}_2$  are responsible for the change of  $m_F$  value by  $\pm 1$ , while  $\hat{L}_3$  is responsible for the jumps that do not affect the total projection of the spin along the quantization axis. Note also that the three Lindblad operators being proportional to the spin matrices can in principle allow for hyperfine but also for Zeeman transitions within the state space of the atom. Using the Landè projection theorem we can distinguish between the two [72], since Zeeman transitions happen within the same hyperfine manifold. Therefore, regarding Zeeman jumps due to spin-exchange, we observe that  $\hat{L}_1$  and  $\hat{L}_2$  could produced a transverse measurable effect in the Zeeman resonances, while the action of  $\hat{L}_3$  renders the state unaffected by the collision.

The state of the system being always pure, as the theory of quantum trajectories implies, can be always expanded in the familiar  $\{|Fm\rangle\}$  basis, thus  $|\psi_s(t)\rangle = \sum_{F,m} c_{Fm}(t)|Fm\rangle$  and therefore the action of the Lindblad operators on this state is simplified to the action of the spin operators on the general  $|Fm\rangle$  states which have been calculated in [50]. The effective Hamiltonian of this system is given by

$$H_{eff} = H_g - \frac{i}{2} \sum_j L_j^\dagger L_j = H_g - \frac{i}{4T_2} (s_- s_+ + s_+ s_- + \frac{1}{2} \mathbb{1}) \quad (5.46)$$

Defining the Lindblad operators, and the effective Hamiltonian it is straightforward to calculate the post-collisional states and the probabilities of a jump to occur at a particular time interval  $dt$ . One could run numerical simulations to ensure the agreement with the Lindblad master equation after averaging over  $N$  trajectories. Note that after such averaging there is a remnant statistical uncertainty of the order of  $\sqrt{N}$  around the mean density matrix evolution that can be considered as the measured spin noise in spin-noise spectroscopy experiments. One could use different approaches to encounter the production of spin-noise from SE collisions like for example the picture described in [33] based on the state-diffusion equation, producing equivalent results with the quantum trajectory formalism

$$\begin{aligned} d|\psi\rangle = & -idtH_g|\psi\rangle + \sum_j (\langle L_j^\dagger \rangle L_j - \frac{1}{2} \langle L_j^\dagger \rangle \langle L_j \rangle - \frac{1}{2} L_j^\dagger L_j) |\psi\rangle dt \\ & + \sum_j (L_j - \langle L_j \rangle) |\psi\rangle d\xi_j \end{aligned} \quad (5.47)$$

where  $d\xi_j$  are zero-mean, normally distributed stochastic differential increments with standard deviation  $\sqrt{dt}$ . Another approach is to use the quantum regression theorem to study the quantum correlations of the spin in the spin-temperature distribution being a steady state of the collisional evolution. This approach has been considered in Chapter 6 of [72] producing spin variances in good agreement with the measured values.

In the following we apply formally the quantum trajectory picture to the full case of spin-exchange interaction in a dc magnetic field and we demonstrate the consistency of our unraveling with the well-established density matrix master equation [68]. Quantum trajectories in such systems can be used to understand, at the single-atom level, alkali-metal–alkali-metal or even alkali-metal–noble-gas collisions. We demonstrate how quantum trajectories can seamlessly produce spin noise from first principles and then moving to dual-species vapors, we use quantum trajectories to reveal the nature of spin-noise correlations that spontaneously build up by the SE interaction. As a by-product of the above, we present an approach to the stochastic terms augmenting the density matrix master equation describing spin-exchange collisions. The quantum trajectory approach

is schematically described in the following figure.

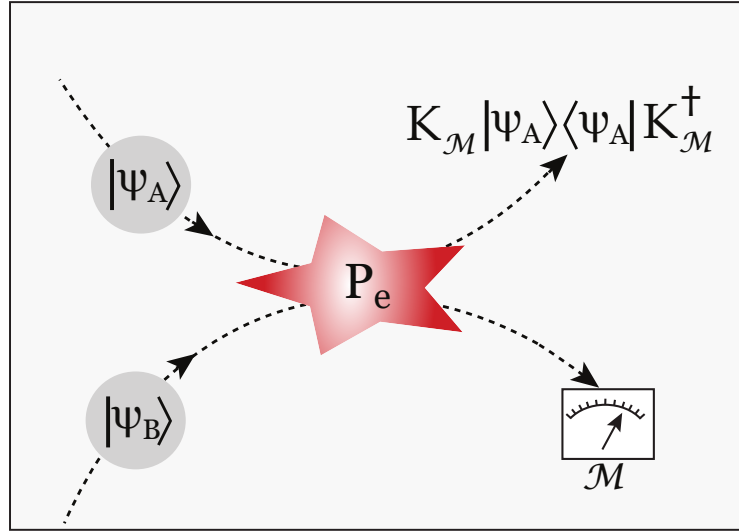


**Figure 5.5:** Quantum measurement picture of a binary spin-exchange collision. One atom is assumed to be the quantum system of interest while the second acts as a probe, where its post-collisional state after projected to a measurement basis, defines the state of the quantum system.

Spin-exchange collisions between two atoms A and B, of the same or different species, result from the different interaction potentials  $V_S$  and  $V_T$  for the singlet and triplet total spin of the colliding partners, respectively. If  $s_a$  and  $s_b$  are the electron spins of the colliding atoms, the singlet and triplet projectors are  $P_S = \frac{1}{4}\mathbb{1} - \mathbf{s}_a \cdot \mathbf{s}_b$  and  $P_T = \frac{3}{4}\mathbb{1} + \mathbf{s}_a \cdot \mathbf{s}_b$ . Introducing the exchange operator  $P_e = P_T - P_S$ , the SE interaction potential  $V_{SE} = P_S V_S + P_T V_T$  is written as a sum of a spin-independent and a spin-dependent term  $V_{SE} = V_0 \mathbb{1} + V_1 P_e$ . Only the latter is of interest for the unitary operator evolving the initial into the final spin state,  $U = \exp(-i \int dt V_1 P_e)$ <sup>9</sup>. Defining  $\phi = \int dt V_1$  and noting that  $P_e^2 = 1$ , we get  $U = \cos \phi \mathbb{1} - i \sin \phi P_e$ .

For a single-species vapor of atoms A with number density  $[A]$  the ensemble description of SE collisions follows either [188] by using  $P_e$  and considering the SE rate  $1/T_{SE} = [A]\nu\sigma_{SE}$  or by using  $U$  [68] and identifying  $\overline{\sin^2 \phi}/T$  with  $1/T_{SE}$ , where  $T$  the time between collisions and  $\overline{\sin^2 \phi}$  the collisional average of  $\sin^2 \phi$ . Here  $\sigma_{SE}$  is the SE cross section and  $\nu$  the mean relative velocity of the colliding atoms. Neglecting the SE frequency shift [68], both approaches result in the same master equation. For following use, we here briefly reiterate the first approach.

Let two atoms A and B collide, initially assuming they are of different species, with their (uncorrelated) pre-collision states being  $\rho_a$  and  $\rho_b$ . Hence the combined two-atom

<sup>9</sup>The time dependence of  $V_1$  is implicit in its dependence on the internuclear distance, which changes with time along the collision trajectory.

initial state is  $\rho_a \otimes \rho_b$ . The state of atom A after the collision is  $\rho_a^e = Tr_B(P_e \rho_a \otimes \rho_b P_e^\dagger)$

$$\rho_a^e = \frac{1}{4} \rho_a + \mathbf{s}_a \cdot \rho_a \mathbf{s}_a + (\rho_a \mathbf{s}_a + \mathbf{s}_a \rho_a) \cdot \langle \mathbf{s}_b \rangle - 2i \langle \mathbf{s}_b \rangle \cdot (\mathbf{s}_a \times \rho_a \mathbf{s}_a) \quad (5.48)$$

For treating a single-species vapor, one substitutes  $b \rightarrow a$  and arrives at the master equation describing both Hamiltonian evolution and SE collisions

$$\frac{d\rho_a}{dt} = -i[H_a, \rho_a] - \frac{1}{T_{SE}}(\rho_a - \rho_a^e) \quad (5.49)$$

where  $H_a = \omega s_{az} + A \mathbf{s}_a \cdot \mathbf{I}_a$  is the alkali-metal ground-state Hamiltonian in the presence of a z-axis magnetic field  $\omega$  and  $A$  is the hyperfine coupling with the nuclear spin  $\mathbf{I}_a$ . The second term in Eq (5.49) is responsible for transverse spin relaxation [164]. The above are well-known results, comprehensively presented in Ref. [68] and discussed also in previous chapters.

We will now develop the quantum-trajectory approach, that is consistent with the above ensemble description. We start with two, initially uncorrelated, atoms 1 and 2 in the pure states  $|\psi_1\rangle$  and  $|\psi_2\rangle$ . The combined two-atom pre-collision and post-collision states are  $|\psi_1\rangle \otimes |\psi_2\rangle$  and  $P_e |\psi_1\rangle \otimes |\psi_2\rangle$ , respectively. We now consider atom 1 as the system and atom 2 as the probe, from which we can extract information about the system. To do so, we perform a projective measurement on the probe. For this we here use the  $|FM\rangle$  basis (zero-field eigenstates of  $\mathbf{I} \cdot \mathbf{s}$  and  $F_z$ ), but any other complete basis would do equally well. Atom 2 is projected in some state  $|FM\rangle$  with probability,  $p_{FM}$ , given by the norm of the state  $\Pi_{FM} P_e |\psi_1\rangle \otimes |\psi_2\rangle$ , where  $\Pi_{FM} = \mathbb{1} \otimes |FM\rangle\langle FM|$ . Defining the Kraus operator corresponding to the particular measurement outcome on atom 2 as  $K_{FM} = \langle FM | P_e | \psi_2 \rangle$ , we find that  $p_{FM} = \langle \psi_1 | K_{FM}^\dagger K_{FM} | \psi_1 \rangle$ . Therefore, atom 1 is projected to

$$|\psi_1^e\rangle_{FM} = \frac{K_{FM} |\psi_1\rangle}{\sqrt{p_{FM}}} \quad (5.50)$$

The Kraus operators satisfy the completeness relation  $\sum_{FM} K_{FM}^\dagger K_{FM} = \mathbb{1}$ , which readily follows from the completeness of the  $|FM\rangle$  basis states and the property  $P_e^2 = \mathbb{1}$ <sup>10</sup>. Hence it is also  $\sum_{FM} p_{FM} = \mathbb{1}$ , as it should be. Finally, the state  $|\psi_1^e\rangle_{FM}$  is properly normalized.

For the numerical production of quantum trajectories, we consider  $N$  atoms, each in any desired pure initial state. We split time into intervals  $dt$ <sup>11</sup>, and in every  $dt$  we evolve each atom unitarily with the Hamiltonian. Moreover, in each  $dt$  there is a

<sup>10</sup>Here the unit operator refers to the single-atom Hilbert space, because  $K_{FM}$  are single-atom operators.

<sup>11</sup>The value of  $dt$  is chosen so that oscillating observables are numerically well represented. Since realistic values of  $\omega$  and  $A$  in the Hamiltonian  $H$  would require such a small value of  $dt$  that the simulation would not run in realistic times, we here choose unrealistically small hyperfine couplings, which in any case do not affect the physical considerations herein.

probability  $dt/T_{SE}$  that an atom suffers an SE collision. A random number drawn for each atom determines whether this probability is realized. For those atoms (system atom 1) undergoing an SE collision during  $dt$ , the collision partner (probe atom 2) is randomly chosen from the same list of  $N$  atoms. Finally, given  $p_{FM}$ , we let another random number determine what the projective measurement outcome  $|FM\rangle$  of atom 2 is. Then atom 1 is projected to  $|\psi_1^e\rangle_{FM}$  given by Eq. (5.50).

Crucially, although the particular projection of the probe atom to a state  $|FM\rangle$  determines the projection of the system atom to  $|\psi_1^e\rangle_{FM}$ , after the collision we leave atom 2 in its initial pre-collision state. This has imprinted a Markovian interpretation, i.e., all probe atoms instantly lose memory of the collisions taking place during  $dt$  and reconstitute the ensemble pre-collision state. We here do not investigate whether the above picture is physically precise, but only care to lay out the single-atom physics behind the SE master equation, which has been impressively successful in accounting for a broad set of experimental data.

Having access to  $N$  quantum trajectories, we can evaluate the time evolution of any observable  $Q$  either for the particular  $j$ th trajectory, as  $\langle Q \rangle_t^{(j)} = \langle \psi_j(t) | Q | \psi_j(t) \rangle$ , or for the trajectory average used to compare with the master equation, as  $\langle Q \rangle_t = \frac{1}{N} \sum_{j=1}^N \langle Q \rangle_t^{(j)}$ .

In Fig.5.6(a) we choose for  $Q$  the transverse spin  $F_x$  and show an example of a single trajectory depicting the discontinuities due to SE collisions. In Fig.5.6(a) we show how the average of many such trajectories accounts for spin relaxation at the ensemble level and compare the trajectory average with (5.50), both for  $F_x$  and for a second observable  $\mathbf{I} \cdot \mathbf{s}$ . The perfect agreement demonstrates the consistency of our quantum-trajectory approach.

We next show how the trajectory picture produces spin noise. We choose for each of the  $N$  atoms a random initial state among all eigenstates of  $F_x$ . In Fig.5.7(a) we plot the resulting fluctuations of  $\langle F_x \rangle$  and in Fig.5.7(b) a fast Fourier transform (FFT) power spectrum that is typically observed in spin-noise spectroscopy. We note that the spin noise in Fig.5.7(a) is not due to an imbalance of the initial states in a finite number of  $N$  trajectories. Similar spin-noise traces can be produced even by exactly balancing the initial states so that at  $t = 0$  it is  $\langle F_x \rangle = 0$  and even by using as initial states eigenstates of  $F_z$ . Hence spin noise produced by SE collisions is a genuine quantum effect originating from the quantum randomness of the post-collision states.

We now move to the case of a dual-species vapor of atoms A and B with relative abundances  $\eta_a$  and  $\eta_b$  ( $\eta_a + \eta_b = 1$ ). This is treated similarly, using  $N$  atoms with ground-state Hamiltonian  $H_a$  and another  $N$  atoms with ground-state Hamiltonian  $H_b$ . Now we



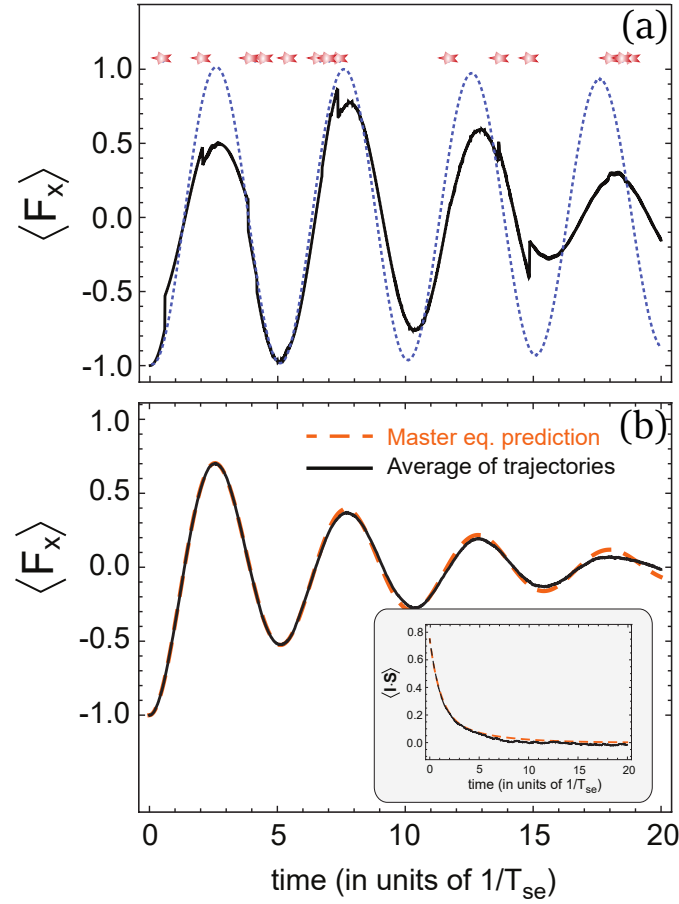


**Figure 5.6:** (a) Single-atom trajectory expectation value of the transverse spin component  $\langle F_x \rangle$ . Red stars depict the random occurrences of SE collisions. The chosen parameters were  $I = 3/2$  and in units of  $1/T_{SE}$ ,  $\omega = 5$  and  $A = 100$ , while time from  $t = 0$  to  $t = 20$  was split into 6M steps. The initial state was the  $|FM\rangle = |2, -1\rangle_x$  eigenstate of  $\hat{F}_x$ . The blue dotted line is just the Hamiltonian evolution. (b) Average (black solid line) of 4000 trajectories like in (a), compared with the predictions of Eq.(5.50) (orange dashed line). The inset is similar but for the observable  $\langle \mathbf{I} \cdot \mathbf{s} \rangle$ .

need to introduce four kinds of collisions, i.e., A-A, A-B, B-A, and B-B collisions, with the respective relaxations rates  $\gamma_{\alpha\beta}$  and SE collision probabilities  $dP_{\alpha\beta} = \gamma_{\alpha\beta}dt$ . The rates  $\gamma_{\alpha\beta}$  are proportional to the mean relative  $\alpha - \beta$  velocity and to the abundance  $\eta_\beta$ , i.e.,  $\gamma_{\alpha\beta} \propto \nu_{\alpha\beta}\eta_\beta$ , since the SE relaxation rate of the first collision partner is proportional to the atom number density of the second collision partner. Given  $dP_{\alpha\beta}$ , we let random numbers determine whether each of the  $2N$  atoms will perform a self and/or a cross-exchange collision and we again randomly choose the collision partner. Extending Eq.(5.49) to a dual-species vapor, we arrive at the two coupled master equations (derived in Ref. [68]).

$$\frac{d\rho_a}{dt} = -i[H_a, \rho_a] - \gamma_{aa}(\rho_a - \rho_{aa}^e) - \gamma_{ab}(\rho_a - \rho_{ab}^e) \quad (5.51)$$

$$\frac{d\rho_b}{dt} = -i[H_b, \rho_b] - \gamma_{bb}(\rho_b - \rho_{bb}^e) - \gamma_{ba}(\rho_b - \rho_{ba}^e) \quad (5.52)$$

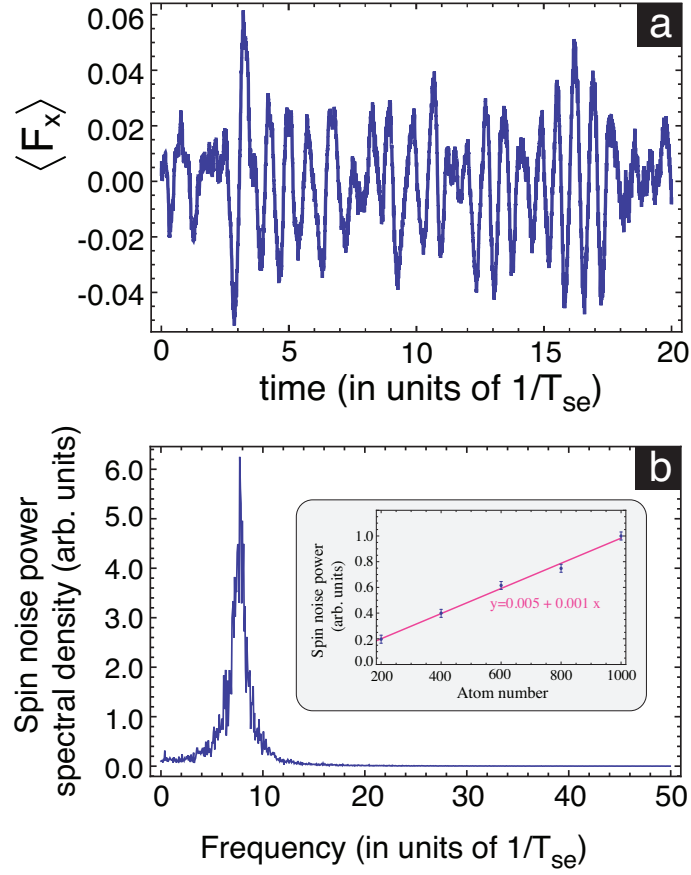


**Figure 5.7:** (a) Spin noise produced by randomly choosing one of the eigenstates of  $F_x$  as the initial state for each of 400 trajectories. Here  $I = 3/2$ ,  $\omega = 32$ , and  $A = 100$ . (b) Spin noise spectrum resulting from the average of 50 FFT power spectra derived from 50 time traces like (a). The inset shows the linear dependence of the total spin noise power of a single FFT power spectrum as a function of atom number. Error bars were estimated from two different FFT power spectra.

where  $\rho_{ba}^e$  and  $\rho_{bb}^e$  follow from  $\rho_{ab}^e$  in Eq.(5.49) by exchanging  $a \leftrightarrow b$  and by substituting  $a \rightarrow b$ , respectively. We provide two examples of the consistency between Eqs. (4) and (5) and the trajectory average. In Fig.5.8 we demonstrate the transfer of spin polarization from type-B atoms to type-A atoms. This is described by the simple equation  $d\langle s_{za} \rangle / dt = (\langle s_{zb} \rangle - \langle s_{za} \rangle) / T_{SE}$  [172] and can be experimentally realized by optically pumping with circularly polarized light atoms B and measuring the spin polarization building up in atoms A. To translate these dynamics into the trajectory picture we use a  $+1/2$  eigenstate of  $s_z$  as the initial state of atoms B and an equal mixture of eigenstates of  $s_z$  for atoms A. Atoms B are always kept in their initial state, and we consider only A-B collisions. Next we consider coherent dynamics, by setting the initial spin polarization of atoms B transversely to the magnetic field and by again having atoms A unpolarized. We now observe simultaneously (i) the precession, (ii) the cross transfer, and (iii) the decay of the transverse polarizations, as shown in the inset of Fig.5.8. Perfect

agreement is again observed for both cases.

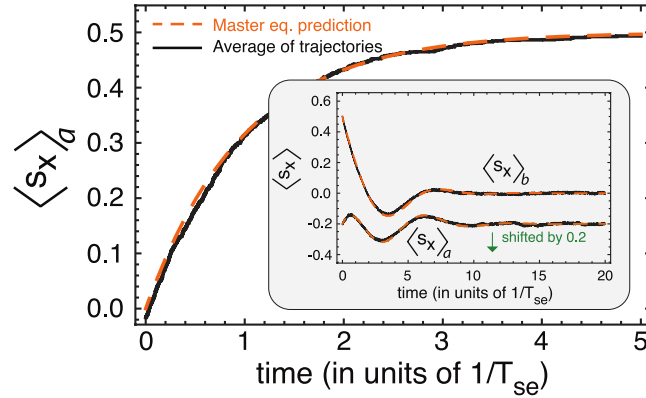


**Figure 5.8:** Spin transfer from 1000 atoms B ( $I = 5/2$ ), always kept in a  $+1/2$  eigenstate of  $s_z$ , to 1000 atoms A ( $I = 3/2$ ), initially unpolarized. The trajectory average (black solid line) is compared with Eq.(5.51), keeping only the cross-exchange term (dashed orange line). The inset shows a similar comparison with the B atoms initially in the  $|Fm_F\rangle = |33\rangle$  eigenstate of  $F_x$ . For both vapors we took  $A = 50$  and  $\omega = 5$ . The trace for  $\langle s_{xa} \rangle$  is shifted downward for clarity.

Having established the consistency of our trajectory approach with the coupled dynamics of Eqs. (5.51) and (5.52), we now move to analyze spin noise correlations that spontaneously build up in coupled vapors [100, 101]. Like in Fig.5.7 (a), we generate spin-noise time traces  $\langle s_x \rangle_a^{(j)}$  and  $\langle s_x \rangle_b^{(j)}$  in a dual-species vapor and do so for various magnetic fields  $\omega$ . The index  $j$  is in the range  $j = 1, \dots, j_{max}$ , where  $j_{max}dt$  is the total time interval considered. In Fig.5.9 we show the correlation coefficient  $\psi_{ab}^\omega$  for each magnetic field value  $\omega$ , where

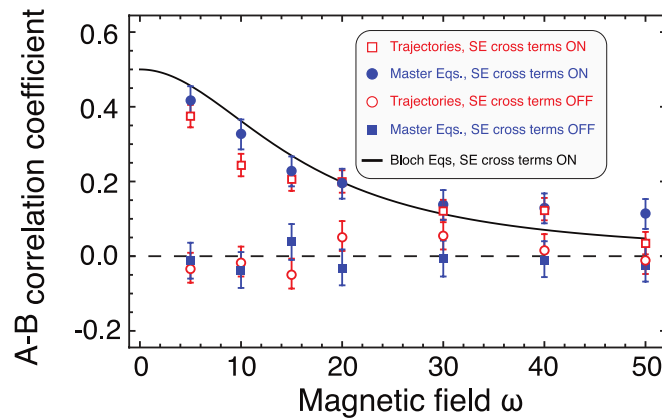


**Figure 5.9:** Spin-noise correlation coefficient  $\psi_{ab}^\omega$  for 400 atoms of type A and 400 atoms of type B. Time from  $t = 0$  to  $t = 20$  was split into  $2M$  steps. Initially, each atom is in a random eigenstate of  $\hat{F}_x$ . Every point is the mean of ten runs, and the error bar is the standard error of the mean. Shown are the trajectory average and the stochastic coupled master equation prediction, with and without cross exchange. The solid line is the prediction of the theory developed in [100].

$$\psi_{ab}^\omega = \frac{\sum_j (\langle s_x \rangle_a^{(j)} - \overline{\langle s_x \rangle_a}) (\langle s_x \rangle_b^{(j)} - \overline{\langle s_x \rangle_b})}{\sqrt{\sum_j (\langle s_x \rangle_a^{(j)} - \overline{\langle s_x \rangle_a})^2 \sum_j (\langle s_x \rangle_b^{(j)} - \overline{\langle s_x \rangle_b})^2}} \quad (5.53)$$

At low  $\omega$  we observe positive correlations, which then tend to zero as  $\omega$  increases. This effect was measured in [100] and was theoretically derived from the coupled Bloch equations augmented with noise generating terms. Here the positive correlation effect is demonstrated with a first principles quantum-trajectory analysis without any assumption. The coupled Bloch equations prediction is also shown in Fig.5.9 for completeness.

Importantly, we here move beyond the Bloch equations and further support the positive correlation effect using Eqs. (5.51) and (5.52). To do so, these equations need to be augmented with noise terms, which are operators acting in the relevant Hilbert space, whereas in the Bloch equations [100] the noise terms were just c-numbers. The first-principles derivation of these noise operators is not addressed here. Here we make an ad-hoc but physically realistic assumption about their form and show that the stochastic master equation prediction for  $\psi_{ab}^\omega$  agrees with the trajectory average. Explicitly, since spin noise produces spin polarization of order  $1/\sqrt{N} \ll 1$ , we assume that the atom's density matrix describing spin noise produced by SE collisions follows a spin-temperature distribution [108] with a fluctuating albeit high temperature, i.e.,  $\rho = e^{-\lambda F_x} / \text{Tr}(e^{-\lambda F_x})$ , with  $\lambda \ll 1$ . Expanding  $\rho$  around  $\lambda = 0$ , we find for the differential change  $\delta\rho \propto F_x$ . Hence we set for the stochastic terms added to (5.51) and (5.52)  $\delta_t \rho_a = \sqrt{\frac{\gamma_a}{N_a}} F_x d\xi_t^a$  and  $\delta_t \rho_b = \sqrt{\frac{\gamma_b}{N_b}} F_x d\xi_t^b$ <sup>12</sup>, respectively, where  $\gamma_a = \gamma_{aa} + \gamma_{ab}$  and  $\gamma_b = \gamma_{bb} + \gamma_{ba}$ <sup>13</sup>, while  $d\xi_t^a$  and  $d\xi_t^b$  are real and independent Wiener processes with zero mean and variance  $dt$ , i.e.,  $\langle\langle d\xi_t^a \rangle\rangle = \langle\langle d\xi_t^b \rangle\rangle = 0$  and  $\langle\langle d\xi_t^a d\xi_t^b \rangle\rangle = dt \delta_{ab} \delta(t - t')$ . The prediction of the stochastic master equations is shown in Fig.5.9 to reproduce the trajectory average.

As a systematic check, we turn off the cross-exchange process in the generation of trajectories, i.e., we do not perform A-B and B-A collisions. Similarly, we turn off the cross-exchange coupling terms in the stochastic coupled master equations. As shown in Fig.5.9,  $\psi_{ab}^\omega$  is consistent with zero for both cases.

Finally, the fact that the noise terms  $d\xi_t^a$  and  $d\xi_t^b$  should be independent can be further supported by the quantum trajectories, from which we calculate  $\chi_{aa}$ ,  $\chi_{bb}$ , and  $\chi_{ab}$ , where  $\chi_{ab} = \sum_j (\langle s_x \rangle_a^{(j+1)} - \langle s_x \rangle_a^j) (\langle s_x \rangle_b^{(j+1)} - \langle s_x \rangle_b^j)$ . We do this for 100 spin

<sup>12</sup>We note that the operator  $F_x$  is a different matrix in the two noise operators, since they refer to different atom species, i.e., with different nuclear spin, and hence different Hilbert spaces.

<sup>13</sup>The particular numerical value in front of the operator  $F_x$  in the noise terms is inconsequential for this work, since it drops out of the A-B correlation coefficient.

noise runs, with randomized rates  $\gamma_{ab}$  and magnetic field  $\omega$ . In Fig.5.10 it can be seen that  $\chi_{ab}$  is about three orders of magnitude less than  $\chi_a$  and  $\chi_b$ . Yet, a standard result [32] on the quadratic variation of an Ornstein-Uhlenbeck diffusion process is that (as  $dt \rightarrow 0$ )  $\chi_{ab} \propto \langle\langle d\xi_t^a d\xi_t^b \rangle\rangle$ . Thus, spin-noise correlations in dual species vapors are consistent with independent noise terms driving the master equations (5.51) and (5.52), the correlations being produced by the cross-couplings terms in (5.51) and (5.52) and not by any conspicuous choice of the noise terms.

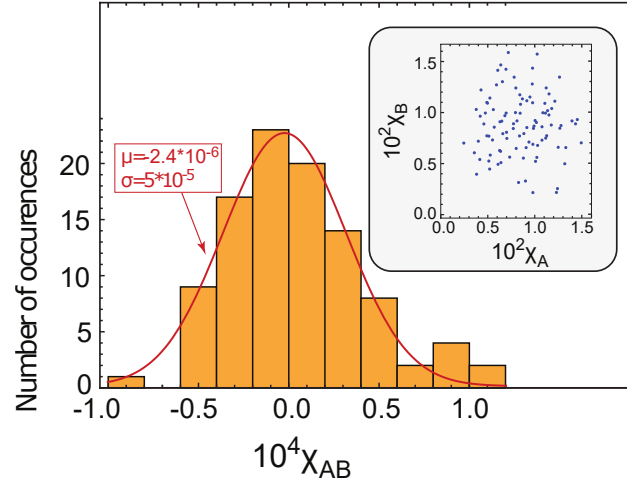


**Figure 5.10:** Distribution of  $\chi_{ab}$ ,  $\chi_a$ , and  $\chi_b$  for 100 spin noise runs with randomized  $5 \leq \omega \leq 50$  and  $0.1 \leq \gamma_{ab} \leq 1.5$ .

## 5.4 Lindblad dynamics for Alkali Spin-Exchange Interaction

The goal of this section is to investigate the conditions under which we can approach the master equation of spin-exchange dynamics by the Lindblad master equation. Lindblad master equation has been extensively studied in literature [230] and a plethora of interesting phenomena rely on the dissipative dynamics governed by this equation that may directly apply to the hot alkali vapor case. We begin the discussion by deriving the master equation from first principles as it is presented for example in [189]. As in Chapter 3 we define the SE operator  $P_e = 1/2 + 2 \sum_j s_j^a s_j^b$ , with properties  $P_e^\dagger = P_e$  and  $P_e^\dagger P_e = P_e P_e^\dagger = \hat{1}$  and the partial SE operator  $U = e^{-i\phi P_e} = \cos \phi - i \sin \phi P_e$  where  $\phi$  is the spin-exchange angle also discussed in previous chapters. We assume that initially the colliding partners are in the uncorrelated state  $\rho = \rho_a \otimes \rho_b$ . The evolution

of the state  $\rho$  using the partial SE operator is given by

$$\begin{aligned} U\rho U^\dagger &= (\cos\phi - i\sin\phi P_e)\rho(\cos\phi + i\sin\phi P_e^\dagger) \\ &= \rho - \frac{i}{2}\sin 2\phi[P_e, \rho] + \sin^2\phi(P_e\rho P_e^\dagger - \rho) \end{aligned} \quad (5.54)$$

Using the properties of the SE operator we can write the above equation as

$$U\rho U^\dagger = \rho - \frac{i}{2}\sin 2\phi[P_e, \rho] + \sin^2\phi(P_e\rho P_e^\dagger - \frac{1}{2}P_e^\dagger P_e\rho - \frac{1}{2}\rho P_e^\dagger P_e) \quad (5.55)$$

The term with the commutator<sup>14</sup>  $[P_e, \rho]$  can be written as

$$\frac{i}{2}\sin 2\phi[P_e, \rho] = i\sin 2\phi \sum_j [s_j^a s_j^b, \rho] \quad (5.56)$$

while after some algebra the last term of Eq.(5.55) can be written as

$$\begin{aligned} P_e\rho P_e^\dagger - \frac{1}{2}P_e^\dagger P_e\rho - \frac{1}{2}\rho P_e^\dagger P_e &= \\ = 4 \sum_{i,j} [s_j^a s_j^b \rho s_i^a s_i^b - \frac{1}{2}s_j^a s_j^b s_i^a s_i^b \rho - \frac{1}{2}\rho s_j^a s_j^b s_i^a s_i^b] \end{aligned} \quad (5.57)$$

The indices  $a, b$  denote the different Hilbert spaces between atom a and atom b. Putting everything together we obtain

$$U\rho U^\dagger = \rho - i\sin(2\phi) \sum_j [s_j^a s_j^b, \rho] + 4\sin^2\phi \sum_{i,j} [s_j^a s_j^b \rho s_i^a s_i^b - \frac{1}{2}s_j^a s_j^b s_i^a s_i^b \rho - \frac{1}{2}\rho s_j^a s_j^b s_i^a s_i^b] \quad (5.58)$$

Following the steps of the derivation of the SE master equation we trace-out the second atom and we obtain

$$\begin{aligned} \rho_e^a &= Tr_b[U\rho U^\dagger] = \rho^a - i\sin(2\phi) \sum_j \langle s_j^b \rangle [s_j^a, \rho^a] \\ &+ 4\sin^2\phi \sum_{i,j} \langle s_i^b s_j^b \rangle (s_i^a \rho^a s_j^a - \frac{1}{2}s_j^a s_i^a \rho^a - \frac{1}{2}\rho^a s_j^a s_i^a) \end{aligned} \quad (5.59)$$

Averaging over the ensemble of possible angle  $\phi$ , we define the SE rate and the SE frequency shift as

$$\frac{1}{T_{SE}} = \frac{\langle \sin^2\phi \rangle}{T} \quad (5.60)$$

$$\delta\omega_j = \frac{\langle \sin 2\phi \rangle}{T} \langle s_j^b \rangle \quad (5.61)$$

where  $\frac{1}{T}$  is the collision rate [172]. Therefore the time evolution of the spin density matrix for atoms a can be written as

$$\frac{d\rho^a}{dt} = \frac{1}{T}(\rho_e^a - \rho^a) \quad (5.62)$$

<sup>14</sup>This term is responsible for the spin-exchange rotation angle in the final form of the master equation and is also connected to the entanglement properties of the SE interaction.

resulting in

$$\frac{d\rho^a}{dt} = -i \sum_j \delta\omega_j [s_j^a, \rho^a] + \frac{4}{T_{SE}} \sum_{i,j} \langle s_i^b s_j^b \rangle (s_i^a \rho^a s_j^a - \frac{1}{2} s_j^a s_i^a \rho^a - \frac{1}{2} \rho^a s_j^a s_i^a) \quad (5.63)$$

For the moment, we are only interested in the decay term so we can ignore the frequency shift commutator term<sup>15</sup> and finally arrive at

$$\frac{d\rho^a}{dt} = \frac{4}{T_{SE}} \sum_{i,j} \langle s_i^b s_j^b \rangle (s_i^a \rho^a s_j^a - \frac{1}{2} s_j^a s_i^a \rho^a - \frac{1}{2} \rho^a s_j^a s_i^a) \quad (5.64)$$

Eq.(5.64) is going to be the starting point of the following discussion. First of all we notice that the relaxation of the first atom depends on the correlator  $\langle s_i^b s_j^b \rangle$  of the second atom. Secondly, we observe that Eq.(5.64) is of the most general form of a Lindblad master equation described by

$$\dot{\rho} = \sum_{n,m=1}^{N^2-1} h_{nm} (A_n \rho A_m^\dagger - \frac{1}{2} \{A_m^\dagger A_n, \rho\}) \quad (5.65)$$

Here  $\{a, b\} = ab + ba$  is the anti-commutator. The set of operators  $\{A_m\}$  is an arbitrary orthonormal basis of the Hilbert-Schmidt operators on the system's Hilbert space with the restriction that  $A_{N^2}$  is proportional to the identity operator. Our convention implies that the other  $A_m$  are traceless, and note that the summation only runs to  $N^2 - 1$  thus excluding the only basis-matrix with a non-zero trace. The coefficient matrix  $h$  determines the system dynamics. The matrix  $h$  must be positive semidefinite to ensure that the equation is trace-preserving and completely positive. Since the matrix  $h$  is positive semidefinite, it can be diagonalized with a unitary transformation  $u$ , resulting in the diagonal form  $u^\dagger h u$  with non-negative eigenvalues. Then we can define another orthonormal operator basis  $\{L_i\}$  where

$$L_i = \sum_{j=1}^{N^2-1} u_{ji} A_j \quad (5.66)$$

The new operators  $L_i$  are commonly called the Lindblad or jump operators of the system and the master equation can be re-written in diagonal form as

$$\dot{\rho} = \sum_{i=1}^{N^2-1} \lambda_i (L_i \rho L_i^\dagger - \frac{1}{2} \{L_i^\dagger L_i, \rho\}) \quad (5.67)$$

where  $\lambda_i$  are the eigenvalues of  $u^\dagger h u$  [8, 185].

Before applying the above formalism it is convenient to bring Eq.(5.64) into a more familiar form by making use of the identity  $\langle s_i^b s_j^b \rangle = \frac{1}{4} \delta_{ij} + \frac{i}{2} \epsilon_{ijk} \langle s_k^b \rangle$ . Eq.(5.64) then takes the form

$$\frac{d\rho^a}{dt} = \left[ \frac{d\rho^a}{dt} \right]_{eq} + \left[ \frac{d\rho^a}{dt} \right]_{neq} \quad (5.68)$$

<sup>15</sup>The frequency shift Hamiltonian term resembles a Zeeman interaction Hamiltonian with an effective magnetic field given by  $\langle s_j^b \rangle$  the expectation value of the spin operator of the second partner.

where

$$\left[\frac{d\rho^a}{dt}\right]_{eq} = \frac{1}{T_{SE}} \sum_i (s_i^a \rho^a s_i^a - \frac{1}{2} s_i^a s_i^a \rho^a - \frac{1}{2} \rho^a s_i^a s_i^a) \quad (5.69)$$

$$\left[\frac{d\rho^a}{dt}\right]_{neq} = \frac{1}{T_{SE}} \sum_{i,j} 2i\epsilon_{ijk} \langle s_k^b \rangle (s_i^a \rho^a s_j^a - \frac{1}{2} s_j^a s_i^a \rho^a - \frac{1}{2} \rho^a s_j^a s_i^a) \quad (5.70)$$

We find that we can write the SE master equation as a linear Lindblad form with Lindblad operators  $L_i = s_i^a$  and a second relaxation term that depends on the state of the second atom. In this form it is straightforward to observe that when  $\langle s_k^b \rangle = 0$  then the relaxation is linear and in Lindblad form describing the so-called spin-randomization collisions [33, 108, 172]. The non-linear relaxation term described by Eq.(5.70) reveals the non-equilibrium character of the SE-master equation, where the relaxation rate depends really on the spin-polarization of the second partner of the collision. The dynamics of the equilibrium term are trivial and are not going to be discussed here.

We note only that in the simplest case of a spin-1/2 system,  $s_x$  Lindblad operator correspond to a bit flip channel,  $s_z$  to a phase flip channel and  $s_y$  to a bit-phase flip channel. These relaxation channels might be generalized to the case of the full alkali atom resulting in an understanding of the dynamics taking place in the rich Hilbert space of combined electron and nuclear spin energy levels.

Focusing on the non-equilibrium term of Eq.(5.70), we define the matrix

$$h_{ij} = 2i\epsilon_{ijk} \langle s_k^b \rangle = \begin{pmatrix} 0 & 2i \langle s_z^b \rangle & -2i \langle s_y^b \rangle \\ -2i \langle s_z^b \rangle & 0 & 2i \langle s_x^b \rangle \\ 2i \langle s_y^b \rangle & -2i \langle s_x^b \rangle & 0 \end{pmatrix} \quad (5.71)$$

The eigenvalues  $\lambda_i$  of the above matrix  $h_{ij}$  are found to be

$$\lambda_1 = 0 \quad (5.72)$$

$$\lambda_2 = 2\sqrt{\langle s_x^b \rangle^2 + \langle s_y^b \rangle^2 + \langle s_z^b \rangle^2} \quad (5.73)$$

$$\lambda_3 = -2\sqrt{\langle s_x^b \rangle^2 + \langle s_y^b \rangle^2 + \langle s_z^b \rangle^2} \quad (5.74)$$

while the eigenstates are given by

$$\mu_1 = \begin{pmatrix} \langle s_x^b \rangle \\ \langle s_y^b \rangle \\ 1 \\ \langle s_z^b \rangle \\ \langle s_y^b \rangle \end{pmatrix} \quad (5.75)$$



$$\mu_2 = \begin{pmatrix} A \\ 1 \\ -\frac{i}{s}(\langle s_y^b \rangle A - \langle s_x^b \rangle) \end{pmatrix} \quad (5.76)$$

$$\mu_3 = \begin{pmatrix} A^* \\ 1 \\ \frac{i}{s}(\langle s_x^b \rangle - \langle s_y^b \rangle A^*) \end{pmatrix} \quad (5.77)$$

where we define  $s = \sqrt{\langle s_x^b \rangle^2 + \langle s_y^b \rangle^2 + \langle s_z^b \rangle^2}$  and  $A = \frac{\langle s_x^b \rangle \langle s_y^b \rangle - i s \langle s_z^b \rangle}{\langle s_y^b \rangle^2 - s^2}$ . Note that  $\mu_2^* = \mu_3$  and we also note that the eigenvectors are not normalized. The Lindblad operators are then given by [185]

$$L_i = \sqrt{\lambda_i} \sum_j \mu_{ij} s_j^a \quad (5.78)$$

where  $\mu_{ij}$  are normalized eigenvectors. Unfortunately, in the most general case the form of the eigenvectors is not straightforward in order to get a physical understanding of the complex SE dynamics, however it might be convenient in certain special cases<sup>16</sup>.

Although the analytical expression of the Lindblad operators in the most general case is not intuitive we can easily implement numerical calculations using these formulas. What is interesting is that we can clearly define quantum trajectories in that form and as an example we can have analytical calculations of such trajectories in the case of spin-1/2. Summarizing, we can write the master equation of SE as a sum of an linear Lindblad master equation and a non-linear one where the Lindblad operators in the later case depend on the state of the second partner of the collision

$$\begin{aligned} \frac{d\rho^a}{dt} = & \frac{1}{T_{SE}} \sum_i \left( L_i \rho^a L_i^\dagger - \frac{1}{2} L_i^\dagger L_i \rho^a - \frac{1}{2} \rho^a L_i^\dagger L_i \right) + \\ & + \frac{1}{T_{SE}} \sum_i \left( L(b)_i \rho^a L(b)_i^\dagger - \frac{1}{2} L(b)_i^\dagger L(b)_i \rho^a - \frac{1}{2} \rho^a L(b)_i^\dagger L(b)_i \right) \end{aligned} \quad (5.79)$$

where the notation  $L(b)_i$  indicates that the Lindblad operators depend on the state of the b-atom.

---

<sup>16</sup>The derivations presented above are by no means rigorous and complete. A lot of work needs to be done until we get to that point. However they provide a new approach to the SE master and a different perspective to the dynamics governed by it that might be a starting point for the interested theoretician.

# Chapter 6 Entanglement in Spin-Exchange Collisions

---

In this chapter we calculate and quantify the entanglement that a binary SE collision can generate from an interaction of two alkali vapors and then we calculate the lifetime of it. This entanglement is shown to have a lifetime at least as long as the spin-exchange relaxation time, and to directly affect measurable spin noise observables. To quantify entanglement we use the negativity which is a frequently used measure of bipartite entanglement that can be applied also to systems larger than spin-1/2. This is a formal theoretical demonstration that a hot and dense atomic vapor dominated by random spin-exchange collisions can support longlived bipartite and possibly higher-order entanglement.

The existing theoretical treatment [68, 172, 188] of alkali atom spin-exchange collisions treats the two atoms emerging from a binary collision as uncorrelated, and thus accounts for single-atom observables in an atomic vapor understood as consisting of uncorrelated atoms. This approach has been quite successful, because so far experiments probed mostly single-atom observables. However, recent years witnessed the exploration of collective quantum states in such vapors. In particular, measurement-induced multi-atom entanglement in hot alkali vapors was recently observed [83]. Moreover, quantum correlations in alkali or alkali/nobel gas vapors were theoretically discussed in [88, 90, 113].

Here we address the quantum foundations of alkali-alkali spin-exchange collisions and show that they produce strong bipartite (atom-atom) entanglement. We formally quantify this entanglement with the tools of quantum information science, and show it persists for at least another ten spin-exchange collision times. Hence we provide a formal demonstration, using the full alkali atom density matrix and the full spin-exchange interaction, that random spin-exchange collisions in a hot and dense vapor fundamentally allow for long-lived two-body entanglement. It is conceivable that these results hold true also for multi-body entanglement produced by a sequence of binary spin-exchange collisions. Here we terminate this sequence at the third collision partner, limiting this discussion to bipartite entanglement. We finally show how this entanglement can be revealed through binary spin correlations affecting measurable spin noise variances.

Spin-exchange (SE) collisions between two atoms, A and B, result from the different

potential curves [231–233] of the singlet and triplet total spin of the colliding partners. If  $\mathbf{s}_A$  and  $\mathbf{s}_B$  are the electron spins of the colliding atoms, the singlet and triplet projectors are  $P_S = \frac{1}{4} - \mathbf{s}_A \cdot \mathbf{s}_B$  and  $P_T = \frac{3}{4} + \mathbf{s}_A \cdot \mathbf{s}_B$ , respectively<sup>1</sup>. Introducing the exchange operator  $P_e = P_T - P_S$ , the SE interaction potential is written as [68]  $V_{se} = V_0 + V_1 P_e$ . Only the latter term drives the spin state evolution, expressed by the unitary operator  $U_\phi^{AB} = e^{-i \int dt V_1 P_e}$ , where  $\phi = \int dt V_1$  is the SE phase<sup>2</sup>. Noting that  $P_e^2 = \mathbb{1}$ , we find  $U_\phi^{AB} = \cos \phi \mathbb{1} - i \sin \phi P_e$ . Now let two uncorrelated atoms A and B enter a collision in the combined state  $\rho_0 = \rho_a \otimes \rho_b$ . The post-collision density matrix is  $\rho = U_\phi^{AB} \rho_0 (U_\phi^{AB})^\dagger = \cos^2 \phi \rho_0 + \sin^2 \phi P_e \rho_0 P_e - (i/2) \sin 2\phi [P_e, \rho_0]$ .

The next step in the standard derivation of SE relaxation [68, 172, 188] is to trace out atom B (A) in order to find the post-collision state of atom A (B), writing the combined post-collision state as  $\rho'_a \otimes \rho'_b$ , where  $\rho'_a = Tr_B\{\rho\}$  and  $\rho'_b = Tr_A\{\rho\}$ . With the post-collision state written as a tensor product of uncorrelated states, this approach is well suited for treating single-atom observables in a vapor described as consisting of uncorrelated atoms. Hence there is no need to keep track of the tensor-product notation and one is left with the single-atom density matrices (for single-species vapors one sets  $a = b$  and omits the atom indices altogether).

We will now extend this treatment and unravel the bipartite entanglement in the post-collision two-atom state  $\rho$  resulting from the action of  $U_\phi^{AB}$  on the initial state  $\rho_0$ . To facilitate this analysis, we write  $\rho$  as<sup>3</sup>

$$\rho = \left( \cos^2 \phi + \frac{1}{4} \sin^2 \phi \right) \rho_a \otimes \rho_b + \frac{1}{4} \sin^2 \phi \sum_j \sigma_j \rho_a \sigma_j \otimes \sigma_j \rho_b \sigma_j + \frac{\sin^2 \phi}{4} \left[ \sum_{i \neq j} \sigma_i \rho_a \sigma_j \otimes \sigma_i \rho_b \sigma_j + \sum_j (\rho_a \sigma_j \otimes \rho_b \sigma_j + \sigma_j \rho_a \otimes \sigma_j \rho_b) \right] \quad (6.1)$$

$$- \frac{i \sin 2\phi}{4} \sum_j (\sigma_j \rho_a \otimes \sigma_j \rho_b - \rho_a \sigma_j \otimes \rho_b \sigma_j) \quad (6.2)$$

We will first find a formal upper bound to the entanglement of  $\rho$ , which bound is independent of the SE phase  $\phi$  and the particular colliding states  $\rho_a$  and  $\rho_b$ . This will serve both as an indicative measure of entanglement and as a consistency check for the

<sup>1</sup>Regarding notation, operators like  $\mathbf{s}_A \cdot \mathbf{s}_B$  imply a tensor product  $\sum_j s_j \otimes s_j$ , the left (right) part of which refers to atom A (B), and  $s_j$  are the electron spin components,  $j = x, y, z$ . The tensor product space has dimension  $2(2I_a + 1)2(2I_b + 1)$ , where  $I_a$  and  $I_b$  are the nuclear spins of the colliding partners, which could be of the same or different species.

<sup>2</sup>The time dependence of  $V_1$  is implicit in its dependence on the internuclear distance, which changes with time along the collision trajectory.

<sup>3</sup>For ease in the following, instead of  $s_j$  we will use  $\sigma_j = 2s_j$ . The particular form of Eq.(6.2) is chosen to facilitate the entanglement calculations, and in any case is identically equal to existing derivations, see e.g. [68, 172].

numerical calculations following suit and demonstrating that several colliding states of practical interest lead to significant entanglement, in cases saturating the upper bound. Incidentally, a general lower bound other than the trivial one (zero) cannot be given, since the entanglement of  $\rho$  depends on  $\phi$ , and for  $\phi = 0$  or  $\phi = \pi$  it is  $\rho = \rho_0$ , in which case  $\rho$  has zero entanglement.

We first note that the first line in Eq.(6.2) is a separable density matrix, i.e. it is written as  $\sum_i p_i \rho_a^{(i)} \otimes \rho_b^{(i)}$ , with  $\sum_i p_i = 1$ . The form  $\rho_a^{(i)} \otimes \rho_b^{(i)}$  is obvious in the first term of the first line in Eq.(6.2). Regarding the second term, each term in the sum over  $j$  multiplied by  $\frac{1}{4} \sin^2 \phi$  is a physical tensor-product density matrix, because it is the result of acting on  $\rho_a \otimes \rho_b$  with a completely positive map consisting of  $\sigma_j$ , since  $\sigma_j$  is hermitian and  $\sigma_j^\dagger \sigma_j = \sigma_j^2 = \mathbb{1}$ . For example, the term  $j = x$  results from acting on  $\rho_a \otimes \rho_b$  with  $M_x = \sigma_x \otimes \sigma_x$ , i.e. from the operation  $M_x \rho_a \otimes \rho_b M_x^\dagger$ . Since all such  $M_j$  operators are local, the resulting density matrices in each of the three such terms ( $j = x, y, z$ ) are again of the separable form. Now, the second line in Eq.(6.2) is hermitian and traceless. If this second line was absent, the density matrix  $\rho$  would be separable. But as is, it generally exhibits bipartite entanglement.

Negativity is an entanglement measure [234] for bipartite systems, defined by  $\mathcal{N}(\rho) = (||\rho^{T_B}|| - 1)/2$ , where  $\rho^{T_B}$  is the partial transpose (PT) of  $\rho$ . The partial transpose of a bipartite density matrix  $\rho = \sum_{ijkl} \rho_{ij,kl} |i\rangle\langle j| \otimes |k\rangle\langle l|$  is  $\rho^{T_B} = \sum_{ijkl} \rho_{ij,kl} |i\rangle\langle j| \otimes |l\rangle\langle k|$ , i.e. the operator in the right position of the tensor product (party B) is transposed. The trace-norm  $||\rho^{T_B}|| \equiv Tr\{\sqrt{(\rho^{T_B})^\dagger \rho^{T_B}}\}$  is a special case ( $p = 1$ ) of the so-called Shatten-p norm. Since the PT of  $\rho$  in Eq.(6.2) is hermitian,  $||\rho^{T_B}||$  equals the sum of the absolute values of the eigenvalues of  $\rho^{T_B}$ .

To analytically calculate  $||\rho^{T_B}||$  in all generality presents an insurmountable difficulty. However, we can calculate an upper bound to  $||\rho^{T_B}||$ , using the triangle inequality  $||A_1 + A_2 + \dots A_n|| \leq ||A_1|| + ||A_2|| + \dots ||A_n||$ , and the fact that for any constant  $c$  it is  $||cA|| = |c| ||A||$ . First note that  $\sigma_x^T = \sigma_x$ ,  $\sigma_y^T = -\sigma_y$  and  $\sigma_z^T = \sigma_z$ . It follows that the effect of the PT operation on the first line of Eq.(6.2) is just to change  $\rho_b$  into  $\rho_b^*$ . However,  $\rho_b^*$  is also a physical density matrix having opposite phases compared to  $\rho_b$ . Hence after the PT, the first line is still a physical density matrix of unit trace, and hence its trace norm is 1.

For the terms in the second line of Eq.(6.2) we will use the identity  $||A_1 \otimes \dots \otimes A_n|| = ||A_1|| \dots ||A_n||$ , and the fact that the trace norm is unitarily invariant, i.e.  $||A|| = ||UAV||$  for unitary  $U$  and  $V$ . We appropriately choose  $U$  and  $V$  to be some Pauli operator  $\sigma_j$ , such that we rid all terms in the PT version of the second line of Eq.(6.2) from the  $\sigma_j$  operators, also using the fact that  $\sigma_j^2 = \mathbb{1}$ . For example, take the term  $A =$



$\sigma_x \rho_a \sigma_y \otimes \sigma_x \rho_b \sigma_y$ . Its partial transpose is  $A^{TB} = -\sigma_x \rho_a \sigma_y \otimes \sigma_y \rho_b^* \sigma_x$ . The trace norm of  $A^{TB}$  is  $\|A^{TB}\| = \|\sigma_x \rho_a \sigma_y\| \|\sigma_y \rho_b^* \sigma_x\|$ . For the first term in this product we take  $U = \sigma_x$  and  $V = \sigma_y$ , while for the second we choose  $U = \sigma_y$  and  $V = \sigma_x$ . Hence  $\|A^{TB}\| = \|\rho_a\| \|\rho_b^*\| = 1$ . We thus reduce all terms to expressions having unit trace norm. There are 12 such terms in the expression multiplied by  $(1/4) \sin^2 \phi$ , and 6 such terms in the one multiplied by  $-(i/4) \sin 2\phi$ . Thus the negativity of  $\rho$  given by Eq.(6.2) is bounded by

$$\mathcal{N}(\rho) \leq \frac{3}{2} \sin^2 \phi + \frac{3}{4} |\sin 2\phi| \quad (6.3)$$

We will next show numerically that states of experimental relevance lead to significant negativities, in cases saturating the bound of Eq.(6.3). We have performed an exact simulation for a  $^{87}\text{Rb}$  vapor (nuclear spin  $I = 3/2$ , 8-dimensional Hilbert space, 64-dimensional tensor product space). We use random pre-collision states  $\rho_a \otimes \rho_b$  and a random SE phase  $\phi$ . Writing down the most general random, hermitian and positive semidefinite 8-dimensional matrix is not trivial [235]. Therefore we use random coherent superpositions of the  $|FM\rangle$  basis states to create the most general random pure states  $|\psi_a\rangle$  and  $|\psi_b\rangle$ <sup>4</sup>.

The result is shown in Fig.6.1a. The largest negativity is produced for collisions of  $|20\rangle$  with  $|20\rangle$  and  $|10\rangle$  with  $|10\rangle$ , both of which saturate the bound for  $\phi = \pi/2$ . For those cases, which are relevant to frequency standards [236], we can find the exact result  $\mathcal{N}_{\text{hf}} = \frac{3}{4}(\sin^2 \phi + |\sin \phi| \sqrt{1 + 3 \cos^2 \phi})$  (dashed upper blue line in Fig.6.1a).

In contrast, collisions between the stretched states  $|22\rangle$  with  $|22\rangle$ , and  $|2-2\rangle$  with  $|2-2\rangle$  produce zero negativity,  $\mathcal{N}_{\text{stretched}} = 0$ . This is because stretched states are invariant under SE, so an initially uncorrelated product state of stretched states will remain invariant and uncorrelated.

Relevant to a highly spin-polarized vapor are mostly collisions between  $|22\rangle$  and  $|21\rangle$  states. In fact, such collisions produce the ubiquitous Zeeman frequency shift. Indeed, a *perfectly* spin-polarized vapor in the stretched state  $|22\rangle$  is invariant under SE, hence there is neither any entanglement nor any Zeeman shift produced. Considering an imperfectly polarized vapor with a population of  $|22\rangle$  significantly larger than the population of  $|21\rangle$ , it is collisions between  $|22\rangle$  and  $|21\rangle$  states that dominate the shift, since collisions of  $|21\rangle$  with  $|21\rangle$  are less frequent. The negativity for a collision of  $|22\rangle$  with  $|21\rangle$  (lower dashed blue line in Fig.6.1a) can also be found analytically, it is

<sup>4</sup>We can also create random mixed states by starting from random pure states and applying a random completely positive map, i.e. choose a set of operators satisfying  $\sum_j M_j^\dagger M_j = \mathbb{1}$ , and calculate  $\sum_j M_j |\psi\rangle\langle\psi| M_j^\dagger$ . For example, we can use the set  $M_j = \alpha_j \sigma_j$ , with random  $\alpha_j \geq 0$ ,  $j = x, y, z$ , and  $\sum_j \alpha_j^2 = 1$ . As expected, we obtain negativities on average smaller than for pure precollision states.

$$\mathcal{N}_Z = \frac{1}{4} |\sin \phi| \sqrt{3 + \cos^2 \phi}.$$

Based on Fig.6.1a and the exact results  $\mathcal{N}_{\text{hf}}$  and  $\mathcal{N}_Z$ , it appears that the entanglement produced by strong SE collisions, the phase of which is such [68] that the collisional average  $\overline{\sin^2 \phi} \approx 1$ , is rather significant. We next turn to explicitly quantify the lifetime of this entanglement. To this end, we will bring into the picture a third atom C, and consider the uncorrelated initial state  $\rho_a \otimes \rho_b \otimes \rho_c$ . We let atoms A and B collide with phase  $\phi$  as before, and then have atom B collide with atom C with phase  $\chi$ . We then trace out atom C, and find the negativity of the resulting A-B state

$$\rho' = \text{Tr}_C \{ U_\chi^{BC} U_\phi^{AB} \rho_a \otimes \rho_b \otimes \rho_c (U_\phi^{AB})^\dagger (U_\chi^{BC})^\dagger \}. \quad (6.4)$$

From the resulting expression we can ignore terms proportional to either  $\sin 2\phi$  or  $\sin 2\chi$ , the collisional averages of which express the collisional frequency shift and thus are very small [68], and thus we get

$$\begin{aligned} \rho' &\approx \cos^2 \chi \rho \\ &+ \cos^2 \phi \sin^2 \chi \rho_a \otimes \text{Tr}_C \{ P_e^{BC} \rho_b \otimes \rho_c P_e^{BC} \} \\ &+ \sin^2 \phi \sin^2 \chi \text{Tr}_C \{ P_e^{BC} P_e^{AB} \rho_a \otimes \rho_b \otimes \rho_c P_e^{AB} P_e^{BC} \} \end{aligned} \quad (6.5)$$

In Fig.6.1b we plot the exact ratio  $\mathcal{N}(\rho')/\mathcal{N}(\rho)$  as a function of  $\chi$ . It is seen that  $\mathcal{N}(\rho') \approx \cos^2 \chi \mathcal{N}(\rho)$ , i.e. the negativity of  $\rho'$  is approximately given by considering just the first term in Eq.(6.5). Since a binary SE collision happens every time interval  $T$ , related to  $T_{\text{se}}$  by [172]  $\overline{\sin^2 \chi}/T = 1/T_{\text{se}}$ , and since just one B-C collision reduces the A-B negativity by  $\cos^2 \chi$ , we can write

$$\frac{d\mathcal{N}(\rho)}{dt} \approx \frac{\mathcal{N}(\rho') - \mathcal{N}(\rho)}{T} \approx -\frac{\mathcal{N}(\rho)}{T_{\text{se}}} \quad (6.6)$$

Thus the negativity  $\mathcal{N}(\rho)$  is predicted to decay exponentially with time constant  $T_{\text{se}}$ . Indeed, this is explicitly shown in the example of Fig.6.1c. To produce this plot we let both atoms A and B initially collide in the state  $|20\rangle$  with phase  $\pi/2$ , thus producing a highly entangled state with negativity  $3/2$ . We then let either A or B collide with an atom C randomly chosen among the set of states  $|2m\rangle$ , and with phase sampled from a Cauchy distribution having zero mean and scale 10.0, producing an average  $\overline{\sin^2 \chi} \approx 0.5$ . We consider in total 15 collisions labelled by  $n = 0, 1, \dots, 14$  ( $n = 0$  is the initial A-B collision and the rest are A-C or B-C collisions). After each A-C or B-C collision atom C is traced out. We repeat this process for 100 times and plot the resulting average  $\overline{\mathcal{N}(\rho')}_n$  as a function of SE collision number  $n$ . We find a decay "time" (in terms of number of SE collisions) very close to  $1/\overline{\sin^2 \chi}$  as determined from the Cauchy distribution of the  $\chi$  values. In particular, it is observed that significant negativity ( $\geq 0.1$ ) survives for about  $7T_{\text{se}}$ .

It should be stressed that in all of the above considerations we have not specified the precise physical process realizing the tracing out of atom C. But our starting point was the existing single-atom derivation tracing out atom B (and A) when obtaining the single-atom density matrix under the assumption of *instant* A-B decorrelation. We found the natural timescale of this decorrelation by going into a deeper layer of the many-body spin dynamics and invoking the interaction with a third atom C. In fact, we forcefully and instantly decorrelate the dynamics at the third-collision partner (atom C). However, it is expected that atom C will gradually (through further collisions) extract information from the A-B state, rendering  $T_{\text{se}}$  a lower bound for the  $1/e$  entanglement lifetime.

Closing, we outline how the bipartite entanglement considered herein can manifest itself experimentally. Consider a spectroscopic measurement of the collective spin of  $N$  atoms,  $F_q = \sum_{j=1}^N f_q^j$ , where  $f_q^j$  the  $q$ -component of the  $j$ -th atom total spin, with  $q = x, y, z$ . The variance of  $F_q$  is in principle readily measurable, and is given by  $(\Delta F_q)^2 = \langle F_q^2 \rangle - \langle F_q \rangle^2 = \sum_{j=1}^N (\Delta f_q^j)^2 + \sum_{i \neq j} C_{f_q f_q}^{ij}$ , where  $C_{f_q f_q}^{ij} = \langle f_q^i f_q^j \rangle - \langle f_q^i \rangle \langle f_q^j \rangle$ . Clearly, for uncorrelated atoms it is  $C_{f_q f_q}^{ij} = 0$ , and the total variance equals the sum of the individual atom variances. Now, it is seen that a nonzero  $C_{f_q f_q}^{ab}$  is connected with the entanglement produced by an SE collision between atoms A and B. Indeed, using the post-collision state  $\rho$  of Eq.(6.2) we can find both terms entering  $C_{f_q f_q}^{ab}$ . It is  $\langle f_q^a f_q^b \rangle = \text{Tr}\{\rho f_q^a \otimes f_q^b\}$ ,  $\langle f_q^a \rangle = \text{Tr}\{\rho_a f_q^a\}$ , and  $\langle f_q^b \rangle = \text{Tr}\{\rho_b f_q^b\}$ , with  $\rho_a = \text{Tr}_B\{\rho\}$  and  $\rho_b = \text{Tr}_A\{\rho\}$ . In Fig.2 we plot examples of  $C_{f_q f_q}^{ab}$  for collisions within the  $F = 2$  manifold. It is evident that a large negativity  $\mathcal{N}(\rho)$  is connected with a large  $|C_{f_q f_q}^{ab}|$ .

To show the effect of  $C_{f_q f_q}^{ab}$  on spin variances we consider the following three cases of practical interest (in all examples we take  $\phi = \pi/2$ ): (i) a state having Zeeman coherence, e.g.  $|\psi\rangle = (|22\rangle + |21\rangle)/\sqrt{2}$ . After SE, the resulting variance of  $F_y$  for this state is 3.5, of which 21% comes from positive binary correlations. (ii) a state exhibiting alignment, e.g.  $|\psi\rangle = (|22\rangle + |2-2\rangle)/\sqrt{2}$ . Here the resulting variance of  $F_z$  is 8, of which 62.5% is the contribution of positive correlations. (iii) the state  $|20\rangle$  of interest to clock transitions. Here the resulting variance of  $F_z$  is zero. This is due to negative correlations (see Fig.2b) completely cancelling the variance's uncorrelated contribution.

For yet another example, a measurement of the projector to the lower  $F = 1$  manifold results in a variance of 0.75, of which 37.6% comes from correlations. Many other scenarios can similarly lead to significant effects on spin variances due to correlations established by the entanglement spontaneously produced by SE collisions. Such correlations will have to be fully understood in order to benchmark any metrological improvement of entangled states produced by external means (e.g. interaction with light, as in [83]) against the baseline variances determined by the underlying collisional

physics.



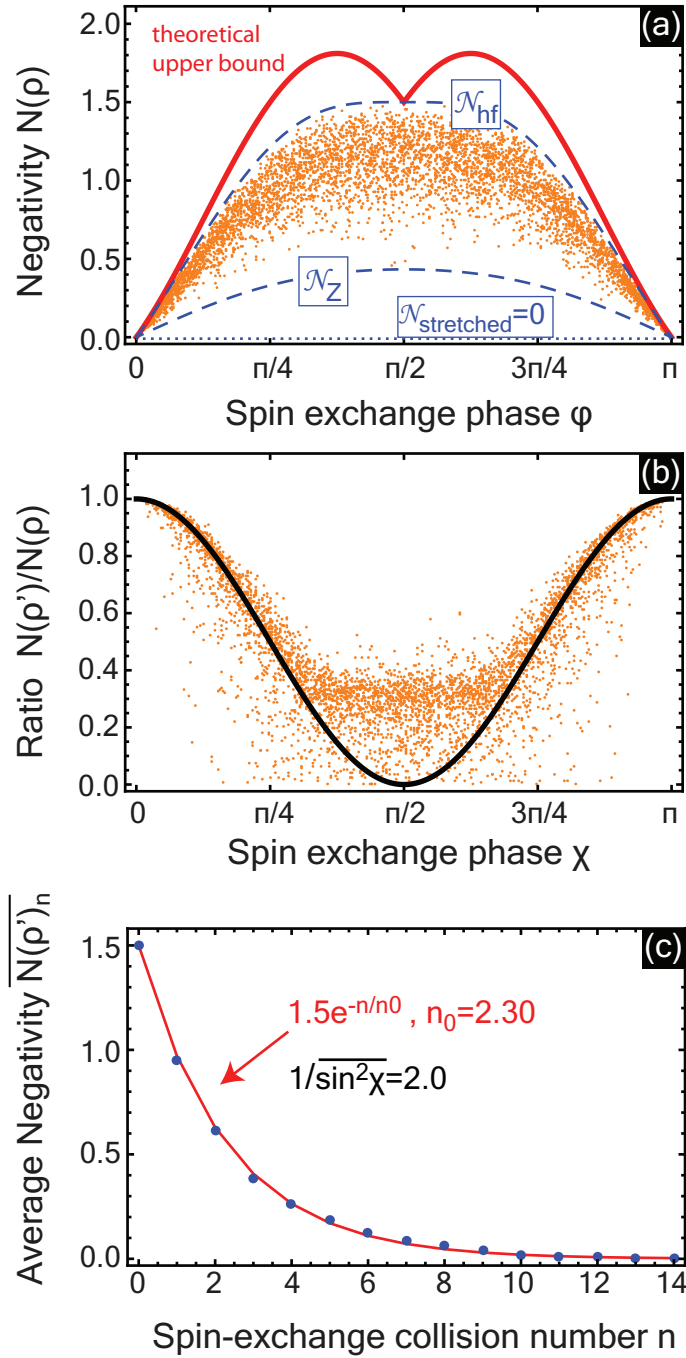


**Figure 6.1:** (a) Negativity of  $\rho$  in Eq.(6.2). Red solid line is the upper bound of Eq.(6.3). The 5000 orange dots correspond to random pure initial states  $|\psi_a\rangle$  and  $|\psi_b\rangle$  for  $^{87}\text{Rb}$  and random SE phase  $\phi$ . Upper (lower) dashed blue lines are the analytic negativities  $\mathcal{N}_{\text{hf}}$  ( $\mathcal{N}_{\text{Z}}$ ) for collisions of  $|20\rangle$  with  $|20\rangle$  ( $|22\rangle$  with  $|21\rangle$ ). Dotted curve at zero corresponds to collisions between stretched states,  $|22\rangle$  with  $|22\rangle$  and  $|2-2\rangle$  with  $|2-2\rangle$ . (b) Ratio of  $\mathcal{N}(\rho')$  with  $\mathcal{N}(\rho)$  for the same states corresponding to the orange dots in (a), where  $\rho'$  results from a B-C collision with random phase  $\chi$  and random C-atom state  $|\psi_c\rangle$ , after tracing out atom C. Solid line is  $\cos^2 \chi$ . (c) Evolution of A-B negativity (blue dots), starting out from a highly entangled A-B state with negativity 1.5, then A or B colliding with C atoms randomly chosen among  $|2m\rangle$  with random phase  $\chi$ . Red solid line is an exponential decay with constant  $n_0 = 2.3$ , close to  $1/\overline{\sin^2 \phi} \approx 2.0$  resulting from the Cauchy distribution of  $\chi$  having center 0.0 and scale 10.0.



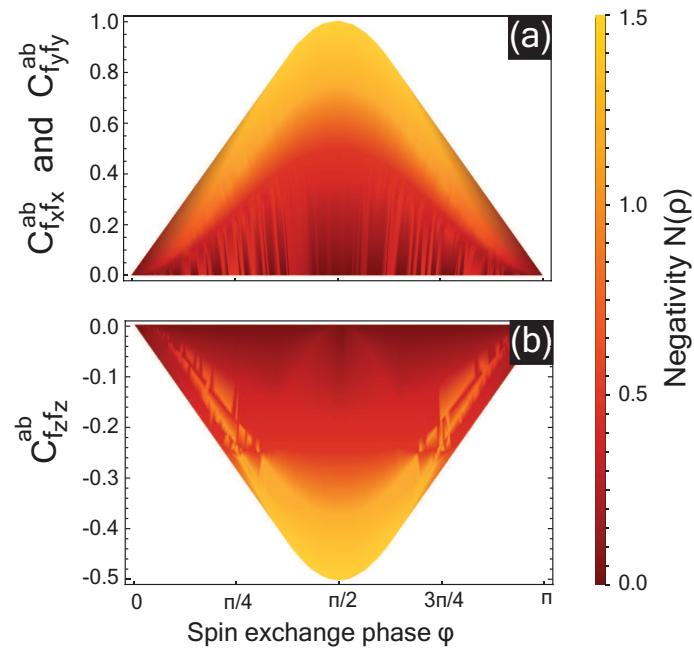


**Figure 6.2:** Binary spin correlations  $C_{f_q f_q}^{ab}$  for (a)  $q = x, y$ , and (b)  $q = z$ . The color-shaded negativity is that of the two-atom state  $\rho$  of Eq.(6.2) produced by an SE collision with phase  $\phi$  between  $|2m\rangle$  and  $|2m'\rangle$ , with  $m, m' = -2, -1, \dots, 2$ . As expected, strong binary spin correlations are seen to be connected with large absolute negativities. Correlation is positive and up to 1.0 for  $q = x, y$ , and negative down to -0.5 for  $q = z$ .

## Chapter 7 Conclusions

---

**W**e have developed and performed a precision experiment with the aim to study spin-noise correlations that spontaneously build-up due to rapid spin-exchange collisions in a vapor cell containing dual-species alkali vapors at room temperature and above. The  $^{87}\text{Rb}$ - $^{133}\text{Cs}$  experiment has interestingly shown non-zero spin-noise correlations leading to the conclusion that spin-exchange collisions in dual-species can generate and sustain spin-spin correlations as it has been demonstrated recently in [83, 100] but also theoretically in [89, 118].

We observe a coherence transfer effect between the two alkali species in equilibrium manifesting itself as an oscillation in the cross-correlation centered at the difference of the two Larmor frequencies in the time-domain. This spin-noise transfer effect is a result of the coupled spin-exchange dynamics that causes the two species to constantly exchange spin polarization, subsequently resulting in a spontaneous build-up of spin correlations.

Spin-noise correlations are more evident in the strong coupling regime where a large overlap of the spin-noise resonances in the Zeeman spectrum of the two vapors is observed. This effect was first demonstrated in [100]. Due to the large difference in the gyromagnetic ratios of  $^{87}\text{Rb}$  and  $^{133}\text{Cs}$  the strong overlap region is only limited to very small magnetic fields that are constrained by the omnipresent low frequency noise. A future experiment studying spin-noise correlations between  $^{87}\text{Rb}$  and  $^{39}\text{K}$ , would shine light upon these correlations in a broader range of magnetic fields, eliminating also the direct dependence of the spin-noise correlations on the magnetic field since the two species, naturally, have identical gyromagnetic ratios.

Moreover, on a theoretical point of view, we have developed a single-atom quantum trajectory picture of spin-exchange collisions consistent with the density matrix ensemble description used so far. This picture is ideally suited to understand quantum fluctuations of all sorts of spin observables, the fluctuations being driven by the incessant atomic collisions and the resulting binary spin-exchange interaction. As an application of the theory, we demonstrated from first principles that spin-exchange collisions spontaneously produce positive spin-noise correlations in hot vapors cells containing two atomic species.

Finally, we have explored the atom-atom entanglement generated by spin-exchange

collisions in hot alkali vapors. We show that spin-exchange collisions are capable to sustain bipartite entanglement at least for the spin-exchange lifetime. This entanglement might be generated either from the collisions themselves or from an external source like a collective QND measurement using the laser field. We have quantified the bipartite entanglement generated by spin-exchange collisions by extending the traditional spin-exchange theory in order to account for spin-spin correlations. Our results should be equally applicable to alkali-noble gas collisions and even to cold alkali-alkali collisions, and have the potential to further advance the understanding and design of non-trivial collective quantum states for use in quantum metrology and in quantum technology.

# Appendix Spin Operators and Density Matrix

---

## A.1 Spin Operators

Following the Appendix B of [50], we can use the general Clebsch-Gordan relations for an atom of unspecified nuclear spin  $I$  in order to generate the ground state spin operators in matrix form in the  $\{|F, m_F\rangle\}$  basis. The calculations are straightforward, therefore we present the matrices in the final form. The electronic spin operators in matrix form in the  $\{|F, m_F\rangle\}$  basis are

$$\begin{aligned}
 S_z = & \sum_{m=-a}^a \sum_{m'=-a}^a \frac{m}{[I]} \delta_{m',m} |a, m'\rangle \langle a, m| \\
 & + \sum_{m=-a}^a \sum_{m'=-b}^b \frac{\sqrt{a^2 - m^2}}{[I]} \delta_{m',m} |b, m'\rangle \langle a, m| \\
 & + \sum_{m=-b}^b \sum_{m'=-a}^a \frac{\sqrt{a^2 - m^2}}{[I]} \delta_{m',m} |a, m'\rangle \langle b, m| \\
 & + \sum_{m=-b}^b \sum_{m'=-b}^b \frac{(-m)}{[I]} \delta_{m',m} |b, m'\rangle \langle b, m|
 \end{aligned} \tag{A.1}$$

$$\begin{aligned}
 I_z = & \sum_{m=-a}^a \sum_{m'=-a}^a \frac{2Im}{[I]} \delta_{m',m} |a, m'\rangle \langle a, m| \\
 & - \sum_{m=-a}^a \sum_{m'=-b}^b \frac{\sqrt{a^2 - m^2}}{[I]} \delta_{m',m} |b, m'\rangle \langle a, m| \\
 & - \sum_{m=-b}^b \sum_{m'=-a}^a \frac{\sqrt{a^2 - m^2}}{[I]} \delta_{m',m} |a, m'\rangle \langle b, m| \\
 & + \sum_{m=-b}^b \sum_{m'=-b}^b \frac{(2I + 2)m}{[I]} \delta_{m',m} |b, m'\rangle \langle b, m|
 \end{aligned} \tag{A.2}$$

The matrix  $F_z$  can be calculated either by using  $F_z|F, m_F\rangle = m_F|F, m_F\rangle$  or simply by  $F_z = S_z + I_z$ . The ladder electron spin matrices  $S_+$  and  $S_-$  are given by

$$\begin{aligned}
S_+ = & \sum_{m=-a}^a \sum_{m'=-a}^a \frac{\sqrt{a-m}\sqrt{a+1+m}}{[I]} \delta_{m',m+1} |a, m'\rangle \langle a, m| \\
& + \sum_{m=-a}^a \sum_{m'=-b}^b \frac{\sqrt{a-m}\sqrt{b-m}}{[I]} \delta_{m',m+1} |b, m'\rangle \langle a, m| \\
& - \sum_{m=-b}^b \sum_{m'=-a}^a \frac{\sqrt{a+m}\sqrt{a+1+m}}{[I]} \delta_{m',m+1} |a, m'\rangle \langle b, m| \\
& - \sum_{m=-b}^b \sum_{m'=-b}^b \frac{\sqrt{a+m}\sqrt{b-m}}{[I]} \delta_{m',m+1} |b, m'\rangle \langle b, m|
\end{aligned} \tag{A.3}$$

$$\begin{aligned}
S_- = & \sum_{m=-a}^a \sum_{m'=-a}^a \frac{\sqrt{a+m}\sqrt{a+1-m}}{[I]} \delta_{m',m-1} |a, m'\rangle \langle a, m| \\
& - \sum_{m=-a}^a \sum_{m'=-b}^b \frac{\sqrt{a+m}\sqrt{b+m}}{[I]} \delta_{m',m-1} |b, m'\rangle \langle a, m| \\
& + \sum_{m=-b}^b \sum_{m'=-a}^a \frac{\sqrt{a-m}\sqrt{a+1-m}}{[I]} \delta_{m',m-1} |a, m'\rangle \langle b, m| \\
& - \sum_{m=-b}^b \sum_{m'=-b}^b \frac{\sqrt{a-m}\sqrt{b+m}}{[I]} \delta_{m',m-1} |b, m'\rangle \langle b, m|
\end{aligned} \tag{A.4}$$

The total alkali angular momentum operators are given by

$$\begin{aligned}
F_+ = & \sum_{m=-a}^a \sum_{m'=-a}^a \sqrt{a(a+1) - m(m+1)} \delta_{m',m+1} |a, m'\rangle \langle a, m| \\
& + \sum_{m=-b}^b \sum_{m'=-b}^b \sqrt{b(b+1) - m(m+1)} \delta_{m',m+1} |b, m'\rangle \langle b, m|
\end{aligned} \tag{A.5}$$

$$\begin{aligned}
F_- = & \sum_{m=-a}^a \sum_{m'=-a}^a \sqrt{a(a+1) - m(m-1)} \delta_{m',m-1} |a, m'\rangle \langle a, m| \\
& + \sum_{m=-b}^b \sum_{m'=-b}^b \sqrt{b(b+1) - m(m-1)} \delta_{m',m-1} |b, m'\rangle \langle b, m|
\end{aligned} \tag{A.6}$$

Note that the  $F$  matrices contain only diagonal elements in the two hyperfine manifolds, while the  $S$  and  $I$  operators contain also off-diagonal elements being able to produce hyperfine coherences in a possible interaction. The  $S_x$  and  $S_y$  are related to the previous



matrices via

$$S_x = \frac{S_+ + S_-}{2} \quad S_y = \frac{S_+ - S_-}{2i} \quad (\text{A.7})$$

while the same relations hold true for the  $F$  operators. Finally, we can write the nuclear spin matrices using the relations  $I_{x,y} = F_{x,y} - S_{x,y}$  and  $I_{\pm} = F_{\pm} - S_{\pm}$ . The definitions of the spin matrices presented here are completely equivalent with the definitions of the spin operators given in Chapter 2 using irreducible spherical tensor operators.

### A.1.1 Relations Between Spin Operators and Irreducible Spherical Tensor Operators

Using the definition of irreducible spherical operators defined in Chapter 2 we can prove that the irreducible components can be written in terms of the spin operators define above [135]

$$\begin{aligned} T_{00}(aa) &= \sum_{m,m'} (-1)^{a-m'} \begin{pmatrix} a & a & 0 \\ m' & -m & 0 \end{pmatrix} |am'\rangle\langle am| \\ &= \frac{1}{\sqrt{2a+1}} \sum_m |am\rangle\langle am| = \frac{1}{\sqrt{2a+1}} p(a) \end{aligned} \quad (\text{A.8})$$

and

$$\begin{aligned} T_{00}(bb) &= \sum_{m,m'} (-1)^{b-m'} \begin{pmatrix} b & b & 0 \\ m' & -m & 0 \end{pmatrix} |bm'\rangle\langle bm| \\ &= \frac{1}{\sqrt{2b+1}} \sum_m |bm\rangle\langle bm| = \frac{1}{\sqrt{2b+1}} p(b) \end{aligned} \quad (\text{A.9})$$

we also know that  $p(a) + p(b) = 1$  or equivalently

$$\sum_m |am\rangle\langle am| + \sum_m |bm\rangle\langle bm| = 1 \quad (\text{A.10})$$

Thus,

$$\begin{aligned} \mathbf{I} \cdot \mathbf{S} &= 1(\mathbf{I} \cdot \mathbf{S})1 \\ &= \left( \sum_m |am\rangle\langle am| + \sum_m |bm\rangle\langle bm| \right) \mathbf{I} \cdot \mathbf{S} \left( \sum_m |am\rangle\langle am| + \sum_m |bm\rangle\langle bm| \right) \\ &= \sum_m |am\rangle\langle am| \mathbf{I} \cdot \mathbf{S} |am\rangle\langle am| + \sum_m |bm\rangle\langle bm| \mathbf{I} \cdot \mathbf{S} |bm\rangle\langle bm| \end{aligned} \quad (\text{A.11})$$

The matrix elements  $\langle aM | \mathbf{I} \cdot \mathbf{S} | aM \rangle$  and  $\langle bM | \mathbf{I} \cdot \mathbf{S} | bM \rangle$  can be easily calculated resulting in

$$\begin{aligned} \langle aM | \mathbf{I} \cdot \mathbf{S} | aM \rangle &= \frac{1}{2} [a(a+1) - I(I+1) - 3/4] = \frac{I}{2} \\ \langle bM | \mathbf{I} \cdot \mathbf{S} | bM \rangle &= \frac{1}{2} [b(b+1) - I(I+1) - 3/4] = -\frac{I+1}{2} \end{aligned} \quad (\text{A.12})$$

Therefore we obtain

$$\begin{aligned}\mathbf{I} \cdot \mathbf{S} &= \frac{I}{2}p(a) - \frac{I+1}{2}p(b) \\ &= \frac{I}{2}\sqrt{2a+1}T_{00}(aa) - \frac{I+1}{2}\sqrt{2b+1}T_{00}(bb)\end{aligned}\quad (\text{A.13})$$

By solving the following system for  $p(a)$  and  $p(b)$

$$\begin{aligned}\mathbf{I} \cdot \mathbf{S} &= \frac{I}{2}p(a) - \frac{I+1}{2}p(b) \\ \mathbb{1} &= p(a) + p(b)\end{aligned}\quad (\text{A.14})$$

we obtain

$$\begin{aligned}p(a) &= \frac{I+1+2\mathbf{I} \cdot \mathbf{S}}{[I]} \\ p(b) &= \frac{I-2\mathbf{I} \cdot \mathbf{S}}{[I]}\end{aligned}\quad (\text{A.15})$$

Let's prove now how the total spin operator  $\mathbf{F}$  is related to the irreducible spherical tensor operators. The matrix element of  $F_0$  in a ground state manifold is given by

$$\langle Fm' | F_0 | Fm \rangle = m\delta_{m,m'} \quad (\text{A.16})$$

On the other hand, the matrix elements of the spherical basis tensor operators are given by

$$\langle F'm' | T_N^L(F, F') | Fm \rangle = (-1)^{F'-m'} \sqrt{2L+1} \begin{pmatrix} F' & F & L \\ m' & -m & -N \end{pmatrix} \quad (\text{A.17})$$

For  $L = 1$  and  $F' = F$  we get

$$\langle Fm' | T_N^1(F, F) | Fm \rangle = (-1)^{F-m'} \sqrt{3} \begin{pmatrix} F & F & 1 \\ m' & -m & -N \end{pmatrix} \quad (\text{A.18})$$

For the z-component i.e.  $N = 0$  the above relation reduces further to

$$\langle Fm' | T_0^1(F, F) | Fm \rangle = (-1)^{F-m'} \sqrt{3} \begin{pmatrix} F & F & 1 \\ m' & -m & 0 \end{pmatrix} \quad (\text{A.19})$$

Calculation of the 3J-Symbol yields

$$\langle Fm' | T_0^1(F, F) | Fm \rangle = \sqrt{\frac{3}{F(F+1)(2F+1)}} m\delta_{m,m'} \quad (\text{A.20})$$

Using Eq.(A.16) this result is equivalent to

$$\langle Fm' | T_0^1(F, F) | Fm \rangle = \sqrt{\frac{3}{F(F+1)(2F+1)}} \langle Fm' | F_0 | Fm \rangle \quad (\text{A.21})$$

or equivalently

$$T_0^1(F, F) = \sqrt{\frac{3}{F(F+1)(2F+1)}} F_0 \quad (\text{A.22})$$

Similarly, using the standard results from angular momentum theory we obtain

$$\langle Fm' | F_{\pm 1} | Fm \rangle = \mp \frac{1}{\sqrt{2}} \sqrt{(F \mp m)(F \pm m + 1)} \delta_{m', m \pm 1} \quad (\text{A.23})$$



whereas using again Eq.(A.18) results in

$$\langle Fm' | T_{\pm 1}^1(F, F) | Fm \rangle = (-1)^{F-m'} \sqrt{3} \begin{pmatrix} F & F & 1 \\ m' & -m & \mp 1 \end{pmatrix} \quad (\text{A.24})$$

or equivalently

$$\langle Fm' | T_{\pm 1}^1(F, F) | Fm \rangle = \mp \sqrt{\frac{3}{2}} \sqrt{\frac{(F \mp m)(F \pm m + 1)}{F(F+1)(2F+1)}} \delta_{m', m \pm 1} \quad (\text{A.25})$$

Therefore we obtain

$$T_N^1(F, F) = \sqrt{\frac{3}{F(F+1)(2F+1)}} F_N \quad (\text{A.26})$$

where  $N = 0, +1, -1$  are the angular momentum components in spherical basis. This result implies that the total angular momentum operator  $\mathbf{F} = \mathbf{I} + \mathbf{J}$  is equal to

$$\mathbf{F} = \sum_{N,F} (-1)^N \mathbf{e}_{-N} T_N^1(F, F) \sqrt{\frac{F(F+1)(2F+1)}{3}} \quad (\text{A.27})$$

or

$$\mathbf{F} = \sum_{N,F} (-1)^N \mathbf{e}_N T_{-N}^1(F, F) \sqrt{\frac{F(F+1)(2F+1)}{3}} \quad (\text{A.28})$$

Which is exactly the result presented in Chapter 2. In the same sense, one can show that the electronic angular momentum operator can be expressed as

$$\begin{aligned} \mathbf{J} &= \sum_{N,F,F_g} (-1)^N \mathbf{e}_{-N} T_N^1(F, F_g) W(1JFI; JF_g) \times \\ &\times \sqrt{\frac{J(2J+1)(F+1)(2F_g+1)}{3}} \end{aligned} \quad (\text{A.29})$$

For alkali atoms where  $J = 1/2$  and two hyperfine ground state manifolds are given by  $a = I + 1/2$  and  $b = I - 1/2$  hence, the above equation reduces to

$$\mathbf{J} = \sum_{N,F,F_g} (-1)^N \mathbf{e}_{-N} T_N^1(F, F_g) W(1\frac{1}{2}FI; \frac{1}{2}F_g) \sqrt{\frac{(F+1)(2F_g+1)}{2}} \quad (\text{A.30})$$

## A.2 Density Matrix Decomposition

Following [70] and as discussed in Chapter 2, we can expand the density matrix  $\rho$  in irreducible spherical basis operators using the uncoupled expansion

$$\rho = \sum_{K,L,M,N} (-1)^{M+N} \rho(K, -M; L, -N) T_{K,M}(II) T_{L,N}(JJ) \quad (\text{A.31})$$

Then, using the relations from the previous section of Appendix between the spin operators and the irreducible spherical tensor operators we obtain

$$T_{00}(JJ) = T_{00}(SS) = T_{00}\left(\frac{1}{2}\frac{1}{2}\right) = \frac{1}{\sqrt{2S+1}} = \frac{1}{\sqrt{2}} \quad (\text{A.32})$$



and

$$T_{1N}(SS) = T_{1N}\left(\frac{1}{2}\frac{1}{2}\right) = \sqrt{\frac{3}{(2S+1)(S+1)S}}S_N = \sqrt{2}S_N \quad (\text{A.33})$$

Making explicit summation on the density matrix expansion over the index  $L$  results in

$$\begin{aligned} \rho &= \sum_{K,M} (-1)^M \rho(K, -M; 00) T_{KM}(II) T_{00}\left(\frac{1}{2}\frac{1}{2}\right) \\ &+ \sum_{K,M,N} (-1)^{M+N} \rho(K, -M; 1, -N) T_{KM}(II) T_{1N}\left(\frac{1}{2}\frac{1}{2}\right) \\ &= \frac{1}{\sqrt{2}} \sum_{K,M} (-1)^M \rho(K, -M; 00) T_{KM}(II) \\ &+ \sqrt{2} \sum_{K,M,N} (-1)^{M+N} \rho(K, -M; 1, -N) T_{KM}(II) S_N \\ &\equiv \varphi + \Theta_N \cdot S_N \end{aligned} \quad (\text{A.34})$$

where  $\varphi$  and  $\Theta$  are purely nuclear operators given by

$$\varphi = \frac{1}{\sqrt{2}} \sum_{K,M} (-1)^M \rho(K, -M; 00) T_{KM}(II) \quad (\text{A.35})$$

$$\Theta_N = \sqrt{2} \sum_{K,M} (-1)^{M+N} \rho(K, -M; 1, -N) T_{KM}(II) \quad (\text{A.36})$$

We are going also to prove that  $\varphi$  and  $\Theta$  can be written in the form:

$$\varphi = \frac{\rho}{4} + \mathbf{S} \cdot \rho \mathbf{S} \quad (\text{A.37})$$

$$\Theta \cdot \mathbf{S} = \frac{3\rho}{4} - \mathbf{S} \cdot \rho \mathbf{S} \quad (\text{A.38})$$

which hold only for spin-1/2 particles. Starting from  $\mathbf{S} \cdot \rho \mathbf{S}$  and using  $\rho = \varphi + \Theta \cdot \mathbf{S}$  and keeping in mind that  $\varphi$  and  $\Theta$  are purely nuclear operators we obtain

$$\begin{aligned} \mathbf{S} \cdot \rho \mathbf{S} &= \mathbf{S} \cdot (\varphi + \Theta \cdot \mathbf{S}) \mathbf{S} = \mathbf{S} \cdot \varphi \mathbf{S} + \mathbf{S} \cdot (\Theta \cdot \mathbf{S}) \mathbf{S} = \varphi \mathbf{S} \cdot \mathbf{S} + \mathbf{S} \cdot (\Theta \cdot \mathbf{S}) \mathbf{S} = \\ &= \frac{3}{4} \varphi + \mathbf{S} \cdot (\Theta \cdot \mathbf{S}) \mathbf{S} \end{aligned} \quad (\text{A.39})$$

The second term can be subsequently simplified by applying the Einstein summation notation

$$\mathbf{S} \cdot (\Theta \cdot \mathbf{S}) \mathbf{S} = S_j \Theta_i S_i S_j = \Theta_i S_j S_i S_j \quad (\text{A.40})$$

$$= \Theta_i S_j S_j S_i + i \varepsilon_{ijk} \Theta_i S_j S_k \quad (\text{A.41})$$

where we make explicit use of the commutation relation for the spin operators

$$S_i S_j = S_j S_i + i \varepsilon_{ijk} S_k \quad (\text{A.42})$$

Noting that  $S_j S_j = \frac{3}{4}$  the above equation reads

$$= \frac{3}{4} \Theta \cdot \mathbf{S} + i \Theta \cdot (\mathbf{S} \times \mathbf{S}) = \frac{3}{4} \Theta \cdot \mathbf{S} + i \Theta \cdot (i \mathbf{S}) = \frac{3}{4} \Theta \cdot \mathbf{S} - \Theta \cdot \mathbf{S} = -\frac{1}{4} \Theta \cdot \mathbf{S} \quad (\text{A.43})$$



where we have make use of

$$(\mathbf{S} \times \mathbf{S}) = i\mathbf{S} \quad (\text{A.44})$$

Hence,

$$\mathbf{S} \cdot \rho \mathbf{S} = \frac{3}{4}\varphi - \frac{1}{4}\Theta \cdot \mathbf{S} \quad (\text{A.45})$$

combining this result with

$$\rho = \varphi + \Theta \cdot \mathbf{S} \quad (\text{A.46})$$

we arrive at

$$\varphi = \frac{\rho}{4} + \mathbf{S} \cdot \rho \mathbf{S} \quad (\text{A.47})$$

On the other hand we have shown

$$\varphi = \rho - \Theta \cdot \mathbf{S} \quad (\text{A.48})$$

Thus,

$$\mathbf{S} \cdot \rho \mathbf{S} = \frac{3}{4}\varphi - \frac{1}{4}\Theta \cdot \mathbf{S} = \frac{3}{4}(\rho - \Theta \cdot \mathbf{S}) - \frac{1}{4}\Theta \cdot \mathbf{S} \quad (\text{A.49})$$

Therefore we conclude the proof:

$$\Theta \cdot \mathbf{S} = \frac{3\rho}{4} - \mathbf{S} \cdot \rho \mathbf{S} \quad (\text{A.50})$$

# Appendix Gaussian Beams and Fresnel Equations

---

## B.1 Gaussian beams

Gaussian beams constitute the best description of the laser light field and they are very useful in many practical situations in a scientific laboratory. Frequently, a Gaussian beam description provides a more accurate description of the effects of the light than a plane-wave description. An example of such a system is a Fabry-Perot cavity and the description of the light-modes therein. The electric field of a TEM<sub>0,0</sub> Gaussian beam is given by [237]

$$\begin{aligned}
 E(x, y, z) = & E_0 \frac{w_0}{w(z)} \exp\left[-\frac{x^2 + y^2}{w^2(z)}\right] \\
 & \times \exp\left\{-i\left[kz - \tan^{-1}\left(\frac{z}{z_0}\right)\right]\right\} \\
 & \times \exp\left[-i\frac{kr^2}{2R(z)}\right]
 \end{aligned} \tag{B.1}$$

where

$$w^2(z) = w_0^2 \left[1 + \left(\frac{z}{z_0}\right)^2\right] \tag{B.2}$$

$$R(z) = z \left[1 + \left(\frac{z}{z_0}\right)^2\right] \tag{B.3}$$

$$z_0 = \frac{\pi w_0^2}{\lambda_0/n} \tag{B.4}$$

$\lambda_0$  is the free space wavelength,  $n$  is the index of refraction,  $r$  is the radial distance from the center axis of the beam,  $z$  is the axial distance from the beam's focus (or "waist"),  $w_0 = w(0)$  is the waist radius,  $R(z)$  is the radius of curvature of the beam's wavefronts at  $z$  and  $z_0$  is the Rayleigh range: at a distance from the waist equal to the Rayleigh range  $z_0$ , the width  $w$  of the beam is  $\sqrt{2}$  larger than it is at the focus where  $w = w_0$ .

Another useful quantity is the total angular spread of the beam far from the waist and is defined as:

$$\theta = \lim_{z \rightarrow \infty} \tan^{-1}\left(\frac{w(z)}{z}\right) \approx \frac{2\lambda_0/n}{\pi w_0} \tag{B.5}$$

## B.2 Fresnel Equations

When an electromagnetic wave approaches a surface which distinguishes two materials with different indices of refraction, from a medium with index of refraction  $n_1$  to a medium with index of refraction  $n_2$ , then the relations that relate the complex amplitude of the reflected and the transmitted electromagnetic waves with the amplitude of the incident wave are [238]:

$$r_{\perp} = \frac{\cos(\theta_i) - \sqrt{\left(\frac{n_2}{n_1}\right)^2 - \sin^2(\theta_i)}}{\cos(\theta_i) + \sqrt{\left(\frac{n_1}{n_2}\right)^2 - \sin^2(\theta_i)}} \quad (\text{B.6})$$

$$t_{\perp} = \frac{2 \cos(\theta_i)}{\cos(\theta_i) + \sqrt{\left(\frac{n_1}{n_2}\right)^2 - \sin^2(\theta_i)}} \quad (\text{B.7})$$

$$r_{\parallel} = \frac{\sqrt{\left(\frac{n_2}{n_1}\right)^2 - \sin^2(\theta_i)} - \left(\frac{n_2}{n_1}\right)^2 \cos(\theta_i)}{\left(\frac{n_2}{n_1}\right)^2 \cos(\theta_i) + \sqrt{\left(\frac{n_1}{n_2}\right)^2 - \sin^2(\theta_i)}} \quad (\text{B.8})$$

$$t_{\parallel} = 2 \frac{\frac{n_2}{n_1} \cos(\theta_i)}{\left(\frac{n_2}{n_1}\right)^2 \cos(\theta_i) + \sqrt{\left(\frac{n_1}{n_2}\right)^2 - \sin^2(\theta_i)}} \quad (\text{B.9})$$

The indices i,r,t are referred to the incident, the reflected and the transmitted waves respectively, while the indices  $\perp$  and  $\parallel$  are referred to the s (transverse) and p (horizontal) polarizations. s is the linear polarization perpendicular to the plane of incidence and p is the linear polarization parallel to the plane of incidence. Fluctuations in the air density can change the index of refraction between two different regions in the laser beam and can lead to a measurable rotation of the polarization that can be simulated using Fresnel equations.



# Appendix Atom-Light General Derivations



## C.1 The Wigner-Eckart Theorem

The Wigner-Eckart theorem has been invoked in many parts of this thesis. Here we present the particular notation and 0 conversion the we use throughout the thesis. We make use of the definition given in the book [239] by E.Rose. We are not going to write the formal definition Eq.(5.14) and Eq.(6.25) of [239], but we rather write an example of a matrix element that we often encounter and provides an intuitive understanding of the theorem. The matrix element of interest is

$$\begin{aligned}\langle F'm' | \mathbf{d} | Fm \rangle &= \sum_q (-1)^q \mathbf{e}_q \langle F'm' | d_{-q} | Fm \rangle \\ &= \sum_q (-1)^q \mathbf{e}_q \langle F'm' | 1 - q; Fm \rangle \langle F' || d || F \rangle\end{aligned}\quad (\text{C.1})$$

The reduced matrix element can be expressed in terms of the Racah-W Symbol as

$$\langle F' || d || F \rangle = \langle J' || d || J \rangle (-1)^{I+1+J'+F} \sqrt{(2J+1)(2F'+1)} W(J' F' J F; I 1) \quad (\text{C.2})$$

In many situations it is useful to express the Racah-W Symbol in terms of the Six-J Symbols using the relation

$$W(abcd; ef) = (-1)^{-(a+b+c+d)} \begin{Bmatrix} a & b & e \\ d & c & f \end{Bmatrix} \quad (\text{C.3})$$

Therefore, the reduced matrix element takes the form

$$\langle F' || d || F \rangle = \langle J' || d || J \rangle (-1)^{I+1-J-F} \sqrt{(2J+1)(2F'+1)} \begin{Bmatrix} J' & F' & I \\ F & J & 1 \end{Bmatrix} \quad (\text{C.4})$$

### C.1.1 Wigner-Eckart Expansion

In this section we show how the dipole interaction Hamiltonian Eq.(2.80) can be expressed in a form suitable for the application of the adiabatic elimination process. The derivation is taken from [117] and we represent it for reasons of completeness. Let's focus on the first term of Eq.(2.80) i.e.,  $P_{F'} \mathbf{d} P_F$ . Applying the Wigner-Eckart theorem

Eq.(C.1) we obtain

$$\begin{aligned} P_{F'} \mathbf{d} P_F &= \sum_{m', m} |F' m' \rangle \langle F' m' | \mathbf{d} | F m \rangle \langle F m | \\ &= \sum_{m', m} \sum_q (-1)^q \hat{\mathbf{e}}_q \langle F' m' | d_{-q} | F m \rangle | F' m' \rangle \langle F m | \end{aligned} \quad (\text{C.5})$$

where  $\hat{\mathbf{e}}_q$  represents the  $q_{th}$  component of the unit vector in spherical basis.

$$P_{F'} \mathbf{d} P_F = \sum_{m', m} \sum_q (-1)^q \hat{\mathbf{e}}_q \langle F' m' | 1 - q; F m \rangle \langle F' || d || F \rangle | F' m' \rangle \langle F m | \quad (\text{C.6})$$

An expansion of the reduced matrix element in terms of the six-J symbol Eq.(C.4) readily reads

$$\begin{aligned} P_{F'} \hat{\mathbf{d}} P_F &= \sum_{m', m} \sum_q (-1)^q \hat{\mathbf{e}}_q \langle F' m' | 1 - q; F m \rangle \langle J' || d || J \rangle \times \\ &\times (-1)^{I+1-J-F} \sqrt{(2J+1)(2F'+1)} \left\{ \begin{array}{ccc} J' & F' & I \\ F & J & 1 \end{array} \right\} | F' m' \rangle \langle F m | \end{aligned} \quad (\text{C.7})$$

To keep the notation compact we follow [117] and we define the following coefficients

$$o_{J, F'}^{J', F'} \equiv (-1)^{I+1-J-F} \sqrt{(2J+1)(2F'+1)} \left\{ \begin{array}{ccc} J' & F' & I \\ F & J & 1 \end{array} \right\} \quad (\text{C.8})$$

Thus the matrix element takes the form

$$P_{F'} \mathbf{d} P_F = \sum_{m', m} \sum_q (-1)^q \hat{\mathbf{e}}_q \langle F' m' | 1 - q; F m \rangle o_{J, F'}^{J', F'} \langle J' || d || J \rangle | F' m' \rangle \langle F m | \quad (\text{C.9})$$

A similar relation holds also for the second term of Eq.(2.80)

$$P_F \mathbf{d} P_{F'} = \sum_{m', m} \sum_q (-1)^q \hat{\mathbf{e}}_q \langle F m | 1 - q; F' m' \rangle o_{J, F'}^{J', F'} \langle J || d || J' \rangle | F m \rangle \langle F' m' | \quad (\text{C.10})$$

To simplify further the notation we define the characteristic Rabi frequency of the D1 or D2 line as

$$\Omega \equiv \frac{\langle J' || d || J \rangle E_0}{\hbar} \quad (\text{C.11})$$

we also define an effective dipole operator

$$\mathbf{D}_{F'F}^\dagger = \frac{P_{F'} \mathbf{d} P_F}{\langle J' || d || J \rangle} = \sum_{m', m} \sum_q (-1)^q \hat{\mathbf{e}}_q \langle F' m' | 1 - q; F m \rangle o_{J, F'}^{J', F'} | F' m' \rangle \langle F m | \quad (\text{C.12})$$

Finally, the dipole interaction of Eq.(2.80) can be compactly written as

$$\hat{\mathcal{H}}_{int}(t) = -\frac{\hbar \Omega}{2} \sum_{F, F'} (e^{-i(\mathbf{k} \cdot \mathbf{r} - \omega t)}) \hat{\mathbf{e}}^* \cdot \mathbf{D}_{F'F} + e^{i(\mathbf{k} \cdot \mathbf{r} - \omega t)} \hat{\mathbf{e}} \cdot \mathbf{D}_{F'F}^\dagger \quad (\text{C.13})$$

## C.2 Interaction Picture

For the application of the adiabatic elimination introduced in Chapter 2 it is useful to work in the interaction picture. Here we present some basic tools in interaction picture

that we are going to utilize. The interaction picture is useful when dealing with a system where a time-dependent interaction is added to the free Hamiltonian  $\mathcal{H} = \mathcal{H}_0 + V_I(t)$ . In this representation the wavefunction is given by evolving the wavefunction of the Schrodinger picture by the free Hamiltonian  $H_0$

$$|\psi_I(t)\rangle = e^{iH_0t/\hbar} |\psi_S(t)\rangle \quad (\text{C.14})$$

where  $|\psi_S(t)\rangle$  is the wavefunction in Schrödinger picture and  $|\psi_I(0)\rangle = |\psi_S(0)\rangle$ . In the interaction picture the Schrödinger equation yields

$$i\hbar\partial_t |\psi_I(t)\rangle = V_I(t) |\psi_I(t)\rangle \quad (\text{C.15})$$

with  $V_I(t)$  the interaction potential in the interaction picture is defined as

$$V_I(t) = e^{iH_0t/\hbar} V(t) e^{-iH_0t/\hbar} \quad (\text{C.16})$$

Expanding the wavefunction in terms of the eigenstates of the Hamiltonian  $|\psi_I(t)\rangle = \sum_n c_n(t) |n\rangle$  and multiplying by the right by a general state  $\langle n|$  we obtain an equation for the amplitude coefficients

$$i\hbar\dot{c}_m(t) = \sum_n V_{mn}(t) e^{i\omega_{mn}t} c_n(t) \quad (\text{C.17})$$

### C.2.1 Small Mathematical Trick

Given a system of first order linear differential equations

$$\begin{aligned} \dot{y}_1(t) &= -ay_1(t) + by_2(t) \\ \dot{y}_2(t) &= -cy_2(t) + dy_1(t) \end{aligned} \quad (\text{C.18})$$

it is a common trick to multiply both equations with  $e^{at}$ . The first equation can be written

$$\frac{d}{dt}(e^{at}y_1(t)) = be^{at}y_2(t) \quad (\text{C.19})$$

and by formal integration we arrive at

$$y_1(t) = e^{-at} \int dt' be^{at'} y_2(t') \quad (\text{C.20})$$

This trick is going to be useful in the following Appendix where the adiabatic elimination of the atomic dynamics is presented.



# Appendix Atomic Polarizability

---

## D.1 Adiabatic Elimination and Derivation of the Polarizability Tensor

The derivation we are going to describe below is taken from Ivan. H. Deutsch and Poul. S. Jessen (2010) [117] and I personally find it very enlightening and pedagogical. Here we repeat it for reasons of completeness. In the following derivation we are going also to adapt the Doppler and the pressure broadening mechanisms which are included in the seminal derivation by W. Happer and B. Mathur (1967) [135] and are excluded from the derivation of [117], since only cold atoms are assumed in the later. In that sense, the derivation is a mixture of the aforementioned articles. We note that the first approach to the interaction of a multi-level atom with a quantized radiation field was given by J. Barrat and Cohen-Tannoudji [240].

In the interaction picture (see the previous Appendix on the Interaction Picture) the interaction Hamiltonian Eq.(2.82) can be expressed as

$$\begin{aligned} \mathcal{H}_{int}(t) &= e^{i\mathcal{H}_0 t/\hbar} \mathcal{H}_{int}(t) e^{-i\mathcal{H}_0 t/\hbar} \\ &= -\frac{\hbar\Omega}{2} \sum_{F,F'} (e^{-i\mathbf{k}\cdot\mathbf{r}_0} e^{-i(\mathbf{k}\cdot\mathbf{v}-\Delta_{F'F})t} \hat{\mathbf{e}}^* \cdot \mathbf{D}_{F'F} + e^{i\mathbf{k}\cdot\mathbf{r}_0} e^{i(\mathbf{k}\cdot\mathbf{v}-\Delta_{F'F})t} \hat{\mathbf{e}} \cdot \mathbf{D}_{F'F}^\dagger) \end{aligned} \quad (\text{D.1})$$

where  $\Delta_{F'F} = \omega - \omega_{F'F} = \omega - \omega_{F'} + \omega_F$  is the detuning from a resonance between the states  $F'$  and  $F$ . Using again Appendix devoted to the interaction picture, the time evolution of the amplitude coefficients in the interaction picture take the form

$$\frac{d}{dt} c_{F',m'}^e(t) = -\frac{\Gamma}{2} c_{F',m'}^e(t) + i\frac{\Omega}{2} \sum_{F,m} e^{i\mathbf{k}\cdot\mathbf{r}_0} e^{i(\mathbf{k}\cdot\mathbf{v}-\Delta_{F'F})t} \langle F'm' | \hat{\mathbf{e}} \cdot \mathbf{D}_{F'F}^\dagger | Fm \rangle c_{F,m}^g(t) \quad (\text{D.2})$$

$$\frac{d}{dt} c_{F,m}^g(t) = i\frac{\Omega}{2} \sum_{F',m'} e^{-i\mathbf{k}\cdot\mathbf{r}_0} e^{-i(\mathbf{k}\cdot\mathbf{v}-\Delta_{F'F})t} \langle Fm | \hat{\mathbf{e}}^* \cdot \mathbf{D}_{F'F} | F'm' \rangle c_{F',m'}^e(t) \quad (\text{D.3})$$

where we phenomenologically introduce the decay rate of the excited  $J'$  state. This term describes a population loss process where the excited state amplitude decays to the ground state. Adiabatic elimination "slaves" the rapidly oscillating excited amplitude to the slowly varying ground state. This practically means that we can formally integrate the above equation and bring the ground state amplitude out of the integral since for the

timescales of the excited state dynamics, the ground state amplitude is to a very good approximation, constant. By formal integration and with the use of mathematical trick in the previous Appendix we arrive at

$$\begin{aligned} c_{F',m'}^e(t) &= i\frac{\Omega}{2}e^{-\frac{\Gamma}{2}t}e^{i\mathbf{k}\cdot\mathbf{r}_0}\sum_{F,m}\langle F'm'|\hat{\mathbf{e}}\cdot\mathbf{D}_{F'F}^\dagger|Fm\rangle\int_0^tdt'e^{i(\mathbf{k}\cdot\mathbf{v}-\Delta_{F'F}+i\frac{\Gamma}{2})t'}c_{F,m}^g(t') \\ &\approx -\frac{\Omega}{2}e^{i\mathbf{k}\cdot\mathbf{r}_0}\sum_{F,m}e^{-i(-\mathbf{k}\cdot\mathbf{v}+\Delta_{F'F})t}\frac{\langle F'm'|\hat{\mathbf{e}}\cdot\mathbf{D}_{F'F}^\dagger|Fm\rangle}{\Delta_{F'F}-\mathbf{k}\cdot\mathbf{v}+i\frac{\Gamma}{2}}c_{F,m}^g(t) \end{aligned} \quad (\text{D.4})$$

Plugging the above relation into the differential equation for the ground state amplitude we find

$$\begin{aligned} \frac{d}{dt}c_{F,m}^g(t) &= -\frac{i}{\hbar}\sum_{F',m'}\sum_{F_g,m_g}e^{i\Delta_{F'F}t}e^{-i\Delta_{F'F_g}t}\frac{\Omega^2/4}{\Delta_{F'F_g}-\mathbf{k}\cdot\mathbf{v}+i\frac{\Gamma}{2}}\times \\ &\times\langle Fm|\hat{\mathbf{e}}^*\cdot\hat{\mathbf{D}}_{F'F}|F'm'\rangle\langle F'm'|\hat{\mathbf{e}}\cdot\mathbf{D}_{F'F}^\dagger|F_gm_g\rangle c_{F_g,m_g}^g(t) \end{aligned} \quad (\text{D.5})$$

or

$$\begin{aligned} \frac{d}{dt}c_{F,m}^g(t) &= -\frac{i}{\hbar}\sum_{F',m'}\sum_{F_g,m_g}e^{i\Delta_{F_g,F}t}\frac{\Omega^2/4}{\Delta_{F'F_g}-\mathbf{k}\cdot\mathbf{v}+i\frac{\Gamma}{2}}\times \\ &\times\langle Fm|\hat{\mathbf{e}}^*\cdot\mathbf{D}_{F'F}|F'm'\rangle\langle F'm'|\hat{\mathbf{e}}\cdot\mathbf{D}_{F'F}^\dagger|F_gm_g\rangle c_{F_g,m_g}^g(t) \end{aligned} \quad (\text{D.6})$$

Written in a compact form, the effective light-shift interaction is then a block matrix in the two hyperfine manifolds with a non-Hermitian evolution given by

$$\frac{d}{dt}c_{F,m}^g(t) = -\frac{i}{\hbar}\sum_{F_g,m_g}\langle Fm|\mathcal{H}_{\text{eff}}|F_gm_g\rangle c_{F_g,m_g}^g(t) \quad (\text{D.7})$$

$$\mathcal{H}_{\text{eff}} \equiv -\frac{1}{4}\mathbf{E}_0^*\cdot\vec{a}\cdot\mathbf{E}_0 \quad \vec{a} = -\sum_{F,F',F_g}\frac{P_F\hat{\mathbf{d}}P_{F'}\mathbf{d}P_{F_g}}{\hbar(\Delta_{F'F}-\mathbf{k}\cdot\mathbf{v}+i\frac{\Gamma}{2})} \quad (\text{D.8})$$

We can account for the collisional broadening by making the replacement [135].

$$\Gamma/2 \rightarrow \Gamma/2 + \gamma_c \quad (\text{D.9})$$

We can also account for the collisional shift or pressure shift by replacing

$$\omega_{F'F} \rightarrow \omega_{F'F} + \delta\omega \quad (\text{D.10})$$

For a formal derivation of the pressure broadening we need to integrate the atomic polarizability over all collisional histories of the atom as it is presented in [70]. Hence we conclude that the atomic polarizability takes the final form

$$\vec{a} = -\sum_{F,F',F_g}\frac{P_F\mathbf{d}P_{F'}\mathbf{d}P_{F_g}}{\hbar(\Delta_{F'F}-\mathbf{k}\cdot\mathbf{v}+i(\frac{\Gamma}{2}+\gamma_c))} \quad (\text{D.11})$$



## D.2 Irreducible Components of the Polarizability Tensor

The scope of this section is to expand the polarizability tensor of Eq.(D.11) into irreducible components and then express each component in terms of the angular momentum operators in the ground state. This process provides a physical interpretation of the different components of the polarizability and allows each term to be expressed as effective known interactions like the hyperfine, Zeeman, Quadrupole, etc. In the following we adapt the derivation from [135]. Starting from the polarizability as derived in Eq.(2.96) and focusing on the dipole matrix elements we obtain

$$\begin{aligned} \sum_{F,F',F_g} P_F \mathbf{d} P_{F'} \mathbf{d} P_{F_g} &= \sum_{F,F',F_g} \sum_{m,m',m_g} |Fm\rangle \langle Fm| \mathbf{d} |F'm'\rangle \langle F'm'| \mathbf{d} |F_g m_g\rangle \langle F_g m_g| = \\ &= \sum_{F,F',F_g} \sum_{m,m',m_g} \sum_{q,q'} (-1)^{q+q'} \hat{e}_q \hat{e}_{q'} \langle Fm| d_{-q} |F'm'\rangle \langle F'm'| d_{-q'} |F_g m_g\rangle |Fm\rangle \langle F_g m_g| \end{aligned} \quad (\text{D.12})$$

Since we might have occasionally to deal with spatial tensors, such as the dielectric susceptibility of the vapor, we shall introduce a set of basis dyadics  $Q_M^L$

$$Q_M^L = \sum_q (-1)^{q-M-1} \hat{e}_q (\hat{e}_{q-M})^* C(11L; q, M - q) \quad (\text{D.13})$$

The inverse relation being

$$\hat{e}_q \hat{e}_{q'} = - \sum_L Q_{q+q'}^L C(11L; q, q') \quad (\text{D.14})$$

The basis dyadics are orthogonal and there are several special relationships involving the basis dyadics that are noteworthy, for example

$$\sqrt{3} Q_0^0 = \sum_q \hat{e}_q \hat{e}_q^* = \hat{e}_x \hat{e}_x + \hat{e}_y \hat{e}_y + \hat{e}_z \hat{e}_z \quad (\text{D.15})$$

The cross product of any pair of vectors  $\mathbf{A}$  and  $\mathbf{B}$  may be expressed as

$$\mathbf{A} \times \mathbf{B} = -i\sqrt{2} \sum_M (-1)^M A_{-M} Q_M^1 \cdot \mathbf{B} \quad (\text{D.16})$$

Thus we can use the inverse relation of the basis dyadics and replace  $\hat{e}_q \hat{e}_{q'}$  in Eq.(D.2). We can also use the inverse relationship of the irreducible spherical tensor operators defined in Eq.(2.8)

$$|Fm\rangle \langle F_g m_g| = \sum_{\Lambda} (-1)^{m_g - F_g} C(F F_g \Lambda; m, -m_g) T_{\Lambda, m - m_g} (F F_g) \quad (\text{D.17})$$

and we can use the Wigner-Eckart theorem from Appendix and apply it to the matrix elements of Eq.(D.2). Following these three steps the right hand side of Eq.(D.2) takes



the form

$$\sum (-1)^{q+q'+1+m_g-F_g} Q_{q+q'}^L T_{\Lambda, m-m_g}(F, F_g) C(11L; q, q') C(F F_g \Lambda; m, -m_g) \times C(F' 1F; m', -q, m) C(F_g 1F'; m_g, -q', m') \langle F || d || F' \rangle \langle F' || d || F_g \rangle \quad (\text{D.18})$$

where the summation extends over the whole set of indices  $\{\Lambda, L, F, F', F_g, m, m', m_g, q, q'\}$ .

The Clebsh-Gordan coefficients vanish unless the following rule of angular momentum conservation are implied. From the last two CG coefficients of Eq.(D.18) we get  $m = -q + m'$  and  $m' = -q' + m_g$  and a combination of both yields  $m - m_g = -(q + q')$ . From the first we have  $q + q' = M$  while from the second  $m - m_g = N$ , therefore,  $M = -N$  and  $\Lambda = L$ . Taking advantage of the above conservation relationships and by combining the four CG-coefficients [239] into a W-Racah Symbol using the following relation

$$\sum_{q, q'} C(11L; q, q', -N) C(F F_g L; m, -m_g, N) C(F' 1F; m', -q, m) C(F_g 1F'; m_g, -q', m') = (-1)^{F_g - m_g} \sqrt{(2F' + 1)(2F + 1)} W(11F F_g; L F') \quad (\text{D.19})$$

we arrive at

$$\sum_{L, N} \sum_{F, F', F_g} (-1)^{N+1} Q_{-N}^L T_{L, N}(F, F_g) W(11F F_g; L F') \times \sqrt{(2F' + 1)(2F + 1)} \langle F || d || F' \rangle \langle F' || d || F_g \rangle \quad (\text{D.20})$$

Once again, applying the Wigner-Eckart theorem (Appendix) for the reduced matrix elements we obtain

$$\langle F || d || F' \rangle \langle F' || d || F_g \rangle = (-1)^{F' - F_g + J' - J} \sqrt{(2F' + 1)(2F_g + 1)} \sqrt{(2J' + 1)(2J + 1)} \times W(J' F' J F; I 1) W(J' F' J F_g; I 1) \langle J || d || J' \rangle \langle J' || d || J \rangle \quad (\text{D.21})$$

We can express the reduced matrix elements in terms of the oscillator strength  $f_{ge}$  by noticing that the decay rate from the excited electronic state with angular momentum  $J'$  to the ground  $J$  is

$$\frac{1}{2} \Gamma = \frac{2\omega^3}{3\hbar c^3} \sqrt{\frac{2J + 1}{2J' + 1}} (-1)^{J' - J} \langle J || d || J' \rangle \langle J' || d || J \rangle \quad (\text{D.22})$$

and

$$\Gamma = \frac{2e^2 \omega^2}{m c^3} \frac{2J + 1}{2J' + 1} f_{ge} \quad (\text{D.23})$$

Combining the above equations the reduced matrix elements read

$$\langle F || d || F' \rangle \langle F' || d || F_g \rangle = \frac{3\hbar e^2 f_{ge}}{2m\omega} (-1)^{F' - F_g} \sqrt{(2F' + 1)(2F_g + 1)(2J + 1)} \times W(J' F' J F; I 1) W(J' F' J F_g; I 1) \quad (\text{D.24})$$



Hence Eq.(D.20) takes the form

$$\begin{aligned} & \sum_{L,N} \sum_{F,F',F_g} 3G(-1)^{N+1+F'-F_g} Q_{-N}^L T_{L,N}(F, F_g) \sqrt{(2F+1)(2F_g+1)} \\ & \quad \times (2F'+1)(2J+1) W(11FF_g; LF') W(J'F'JF; I1) W(J'F'JF_g; I1) \end{aligned} \quad (\text{D.25})$$

To simplify notation we have defined

$$G = \frac{e^2 f_{ge}}{2m\omega^2} \sqrt{\frac{Mc^2}{2k_B T}} = \frac{r_e c^2 f_{ge}}{2\omega^2} \sqrt{\frac{Mc^2}{2k_B T}} \quad (\text{D.26})$$

Note that we have also absorbed in  $G$  the constant terms in front of the polarizability tensor i.e.  $\frac{1}{\hbar k} \sqrt{\frac{M}{2k_B T}}$ . To simplify the notation further we also define

$$\begin{aligned} \xi^L(F, F_g; F') &= 3G(-1)^{F'-F_g+1} \sqrt{(2F+1)(2F_g+1)} \\ & \quad \times (2F'+1)(2J+1) W(11FF_g, LF') W(J'F'JF; I1) W(J'F'JF_g; I1) \end{aligned} \quad (\text{D.27})$$

Therefore Eq.(D.25) is simplified to

$$\sum_{L,N} \sum_{F,F',F_g} \xi^L(F, F_g; F') (-1)^N Q_{-N}^L T_{L,N}(F, F_g) \quad (\text{D.28})$$

Going back at the beginning (D.2) after all these simplifications the electric dipole matrix elements are finally written as

$$P_F \mathbf{d} P_{F'} \mathbf{d} P_{F_g} = \sum_{L,N} \sum_{F,F',F_g} \xi^L(F, F_g; F') (-1)^N Q_{-N}^L T_{L,N}(F, F_g) \quad (\text{D.29})$$

$\xi^L(F, F_g; F')$  can be further simplified using the following relation that combines the three W-Racah Symbols into two (eq.6.25 of [239] after some algebra).

$$\begin{aligned} & \sum_{F'} (-1)^{F'-F_g+1} (2F'+1) W(11FF_g, LF') W(J'F'JF; I1) W(J'F'JF_g; I1) \\ & \quad = (-1)^L W(FLIJ; F_g J) W(1LJ'J; 1J) \end{aligned} \quad (\text{D.30})$$

and  $\xi^L(F, F_g; F')$  takes its final form

$$\xi^L(F, F_g) = 3G(-1)^L \sqrt{(2F+1)(2F_g+1)(2J+1)} W(FLIJ; F_g J) W(1LJ'J; 1J) \quad (\text{D.31})$$

or in terms of Six-J Symbols

$$\begin{aligned} \xi^L(F, F_g) &= 3G(-1)^L \sqrt{(2F+1)(2F_g+1)(2J+1)} \\ & \quad \times (-1)^{-(I+F+J')} \left\{ \begin{matrix} F & L & F_g \\ & J & I & J \end{matrix} \right\} \left\{ \begin{matrix} 1 & L & 1 \\ & J & J' & J \end{matrix} \right\} \end{aligned} \quad (\text{D.32})$$

Therefore the matrix elements take the final form

$$P_F \mathbf{d} P_{F'} \mathbf{d} P_{F_g} = \sum_{L,N} \sum_{F,F_g} \xi^L(F, F_g) (-1)^N Q_{-N}^L T_{L,N}(F, F_g) \quad (\text{D.33})$$



# Bibliography

---

- [1] C. Gardiner and P. Zoller. *Quantum Noise: A Handbook of Markovian and Non-Markovian Quantum Stochastic Methods with Applications to Quantum Optics*. Springer Series in Synergetics. Springer, 2004. URL [https://books.google.gr/books?id=a\\_xST8oGhdgC](https://books.google.gr/books?id=a_xST8oGhdgC). 1
- [2] Vittorio Giovannetti, Seth Lloyd, and Lorenzo Maccone. Advances in quantum metrology. *Nature Photonics*, **5**, 2011. URL <https://doi.org/10.1038/nphoton.2011.35>. 1
- [3] F. Arute, K. Arya, and R. Babbush et al. Quantum supremacy using a programmable superconducting processor. *Nature*, **574**(7779), 2019. URL <https://doi.org/10.1038/s41586-019-1666-5>. 1
- [4] Han-Sen Zhong, Hui Wang, Yu-Hao Deng, Ming-Cheng Chen, Li-Chao Peng, Yi-Han Luo, Jian Qin, Dian Wu, Xing Ding, Yi Hu, et al. Quantum computational advantage using photons. *Science*, 2020. 1
- [5] Klemens Hammerer, Anders S. Sørensen, and Eugene S. Polzik. Quantum interface between light and atomic ensembles. *Rev. Mod. Phys.*, **82**, 2010. URL <https://link.aps.org/doi/10.1103/RevModPhys.82.1041>. 1, 44, 90, 91
- [6] Denis V Vasilyev, Klemens Hammerer, Nikolaj Korolev, and Anders Søndberg Sørensen. Quantum noise for faraday light–matter interfaces. *Journal of Physics B: Atomic, Molecular and Optical Physics*, **45**(12):124007, 2012. 1
- [7] John Kitching. Chip-scale atomic devices. *Applied Physics Reviews*, **5**(3):031302, 2018. URL <https://doi.org/10.1063/1.5026238>. 1
- [8] H.P. Breuer and F. Petruccione. *The Theory of Open Quantum Systems*. Oxford University Press, 2002. URL <https://books.google.gr/books?id=0Yx5VzaMYm8C>. 1, 161, 178
- [9] T. Baumgratz, M. Cramer, and M. B. Plenio. Quantifying coherence. *Phys. Rev. Lett.*, **113**:140401, 2014. URL <https://link.aps.org/doi/10.1103/PhysRevLett.113.140401>. 1
- [10] M. Auzinsh, D. Budker, D. F. Kimball, S. M. Rochester, J. E. Stalnaker, A. O. Sushkov, and V. V. Yashchuk. Can a quantum nondemolition measurement improve the sensitivity of an atomic magnetometer? *Phys. Rev. Lett.*, **93**:173002, 2004. URL <https://link.aps.org/doi/10.1103/PhysRevLett.93.173002>. 1
- [11] S. F. Huelga, C. Macchiavello, T. Pellizzari, A. K. Ekert, M. B. Plenio, and J.I. Cirac. Improvement of frequency standards with quantum entanglement. *Phys. Rev. Lett.*, **79**, 1997. URL <https://link.aps.org/doi/10.1103/PhysRevLett.79.3865>.
- [12] G Vasilakis, V Shah, and Michael V Romalis. Stroboscopic backaction evasion in a dense alkali-metal vapor. *Physical review letters*, **106**(14):143601, 2011. 1, 6, 44, 56
- [13] Martin van Exter. Noise and signal processing. Lecture Notes, 8 2003. Leiden University. 2
- [14] B. Johnson J. Thermal agitation of electricity in conductors. *Nature*, **119**(2984), 1927. URL <https://doi.org/10.1038/119050c0>. 2
- [15] H. Nyquist. Thermal agitation of electric charge in conductors. *Phys. Rev.*, **32**, 1928. URL <https://link.aps.org/doi/10.1103/PhysRev.32.110>. 2
- [16] W. Schottky. Über spontane stromschwankungen in verschiedenen elektrizitätsleitern. *Annalen*

- der Physik*, **362**(23), 1918. URL <https://onlinelibrary.wiley.com/doi/abs/10.1002/andp.19183622304>. 2, 84
- [17] Shlomo Engelberg. *Random signals and noise: a mathematical introduction*. CRC Press, 2018. 2, 83
- [18] D.K.C. (David Keith Chalmers) MacDonald. *Noise and fluctuations: an introduction*. New York, Wiley, 1962. 2
- [19] R. Kubo. The fluctuation-dissipation theorem. *Reports on Progress in Physics*, **29**(1), 1966. URL <https://ui.adsabs.harvard.edu/abs/1966RPPh...29..255K>. 2
- [20] Klaus Mølmer, Yvan Castin, and Jean Dalibard. Monte carlo wave-function method in quantum optics. *JOSA B*, **10**(3), 1993. 2
- [21] V. B. Braginsky and F. Ya. Khalili. Quantum nondemolition measurements: the route from toys to tools. *Rev. Mod. Phys.*, **68**, 1996. URL <https://link.aps.org/doi/10.1103/RevModPhys.68.1>. 2
- [22] Y. Takahashi, K. Honda, N. Tanaka, K. Toyoda, K. Ishikawa, and T. Yabuzaki. Quantum nondemolition measurement of spin via the paramagnetic faraday rotation. *Phys. Rev. A*, **60**, 1999. URL <https://link.aps.org/doi/10.1103/PhysRevA.60.4974>.
- [23] A Kuzmich, NP Bigelow, and L Mandel. Atomic quantum non-demolition measurements and squeezing. *EPL (Europhysics Letters)*, **42**(5):481, 1998.
- [24] Philippe Grangier, Juan Ariel Levenson, and Jean-Philippe Poizat. Quantum non-demolition measurements in optics. *Nature*, **396**(6711), 1998. URL <https://doi.org/10.1038/25059>.
- [25] A. Kuzmich, L. Mandel, J. Janis, Y. E. Young, R. Egnisman, and N. P. Bigelow. Quantum nondemolition measurements of collective atomic spin. *Phys. Rev. A*, **60**, 1999. URL <https://link.aps.org/doi/10.1103/PhysRevA.60.2346>. 2
- [26] A. Bachor Hans and C. Ralph Timothy. *A Guide to Experiments in Quantum Optics*. John Wiley & Sons, Ltd, 2019. URL <https://onlinelibrary.wiley.com/doi/abs/10.1002/9783527695805.fmatter>. 2, 156
- [27] E. S. Polzik, J. Carri, and H. J. Kimble. Spectroscopy with squeezed light. *Phys. Rev. Lett.*, **68**, 1992. URL <https://link.aps.org/doi/10.1103/PhysRevLett.68.3020>. 2
- [28] Vladimir B. Braginsky, Farid Ya Khalili, and Kip S. Thorne. *Quantum Measurement*. Cambridge University Press, 1992. 2
- [29] W. M. Itano, J. C. Bergquist, J. J. Bollinger, J. M. Gilligan, D. J. Heinzen, F. L. Moore, M. G. Raizen, and D. J. Wineland. Quantum projection noise: Population fluctuations in two-level systems. *Phys. Rev. A*, **47**, 1993. URL <https://link.aps.org/doi/10.1103/PhysRevA.47.3554>. 2, 42
- [30] Valerii S Zapasskii. Spin-noise spectroscopy: from proof of principle to applications. *Advances in Optics and Photonics*, **5**(2), 2013.
- [31] Nikolai Sinitsyn and Yuriy V. Pershin. The theory of spin noise spectroscopy: a review. *Reports on progress in physics. Physical Society*, **79** **10**:106501, 2016. 2
- [32] EB Aleksandrov and VS Zapasskii. Magnetic resonance in the faraday-rotation noise spectrum. *Zh. Eksp. Teor. Fiz*, **81**, 1981. 2
- [33] GE Katsoprinakis, AT Dellis, and IK Kominis. Measurement of transverse spin-relaxation rates in a rubidium vapor by use of spin-noise spectroscopy. *Physical Review A*, **75**(4):042502, 2007. 126, 167, 168, 179
- [34] SA Crooker, DG Rickel, AV Balatsky, and DL Smith. Spectroscopy of spontaneous spin noise as

- a probe of spin dynamics and magnetic resonance. *Nature*, **431**(7004):49, 2004. 33
- [35] Bogdan Mihaila, Scott A. Crooker, Dwight G. Rickel, Krastan B. Blagoev, Peter B. Littlewood, and Darryl L. Smith. Quantitative study of spin noise spectroscopy in a classical gas of  $^{41}\text{K}$  atoms. *Phys. Rev. A*, **74**:043819, 2006. URL <https://link.aps.org/doi/10.1103/PhysRevA.74.043819>.
- [36] John Kenton Stockton. *Continuous quantum measurement of cold alkali-atom spins*. PhD thesis, California Institute of Technology, 2007. 23, 27, 42
- [37] M. Koschorreck, M. Napolitano, B. Dubost, and M. W. Mitchell. Sub-projection-noise sensitivity in broadband atomic magnetometry. *Phys. Rev. Lett.*, **104**:093602, 2010. URL <https://link.aps.org/doi/10.1103/PhysRevLett.104.093602>. 2
- [38] M. Oestreich, M. Römer, R. J. Haug, and D. Hägele. Spin noise spectroscopy in gaas. *Phys. Rev. Lett.*, **95**:216603, 2005. URL <https://link.aps.org/doi/10.1103/PhysRevLett.95.216603>. 2
- [39] M. Römer, J. Hübner, and M. Oestreich. Spin noise spectroscopy in semiconductors. *Review of Scientific Instruments*, **78**(10):103903, 2007. URL <https://doi.org/10.1063/1.2794059>.
- [40] Fabian Berski, Hendrik Kuhn, Jan G. Lonnemann, Jens Hübner, and Michael Oestreich. Ultrahigh bandwidth spin noise spectroscopy: Detection of large  $g$ -factor fluctuations in highly- $n$ -doped gaas. *Phys. Rev. Lett.*, **111**:186602, 2013. URL <https://link.aps.org/doi/10.1103/PhysRevLett.111.186602>.
- [41] S. Cronenberger, C. Abbas, D. Scalbert, and H. Boukari. Spatiotemporal spin noise spectroscopy. *Phys. Rev. Lett.*, **123**:017401, 2019. URL <https://link.aps.org/doi/10.1103/PhysRevLett.123.017401>. 2
- [42] I. M. Savukov, S.-K. Lee, and M. V. Romalis. Optical detection of liquid-state nmr. *Nature*, 442 (7106), 2006. URL <https://doi.org/10.1038/nature05088>. 2
- [43] Min Jiang, Teng Wu, John W. Blanchard, Guanru Feng, Xinhua Peng, and Dmitry Budker. Experimental benchmarking of quantum control in zero-field nuclear magnetic resonance. *Science Advances*, **4**(6), 2018. URL <https://advances.sciencemag.org/content/4/6/eaar6327>.
- [44] J. Keeler. *Understanding NMR Spectroscopy*. Wiley, 2011. URL <https://books.google.gr/books?id=WUmCpq30pygC>. 2
- [45] F. Bloch. Nuclear induction. *Phys. Rev.*, **70**, 1946. URL <https://link.aps.org/doi/10.1103/PhysRev.70.460>. 2, 44
- [46] Tycho Sleator, Erwin L. Hahn, Claude Hilbert, and John Clarke. Nuclear-spin noise. *Phys. Rev. Lett.*, 55, 1985. URL <https://link.aps.org/doi/10.1103/PhysRevLett.55.1742>. 2
- [47] Dmitry Budker and Michael Romalis. Optical magnetometry. *Nature Physics*, **3**(4), 2007. URL <https://doi.org/10.1038/nphys566>. 3
- [48] D. Budker and Derek F. Jackson Kimball. *Optical Magnetometry*. Cambridge University Press, 2013. 3, 38, 40, 42, 45, 46, 47, 56, 111, 113, 114, 154
- [49] Vito Giovanni Lucivero. *Quantum metrology with high-density atomic vapors and squeezed states of light*. Universitat Politècnica de Catalunya, 2016. 3
- [50] Scott Jeffrey Seltzer. *Developments in alkali-metal atomic magnetometry*. Princeton University, 2008. 3, 11, 16, 17, 20, 29, 49, 69, 73, 74, 75, 76, 107, 110, 123, 127, 165, 168, 192
- [51] H. G. Dehmelt. Modulation of a light beam by precessing absorbing atoms. *Phys. Rev.*, **105**, 1957. URL <https://link.aps.org/doi/10.1103/PhysRev.105.1924>. 3



- [52] William E. Bell and Arnold L. Bloom. Optical detection of magnetic resonance in alkali metal vapor. *Phys. Rev.*, **107**, 1957. URL <https://link.aps.org/doi/10.1103/PhysRev.107.1559>. 3
- [53] D. Budker, D. F. Kimball, S. M. Rochester, V. V. Yashchuk, and M. Zolotarev. Sensitive magnetometry based on nonlinear magneto-optical rotation. *Phys. Rev. A*, **62**:043403, 2000. URL <https://link.aps.org/doi/10.1103/PhysRevA.62.043403>. 3
- [54] J. C. Allred, R. N. Lyman, T. W. Kornack, and M. V. Romalis. High-sensitivity atomic magnetometer unaffected by spin-exchange relaxation. *Phys. Rev. Lett.*, **89**:130801, 2002. URL <https://link.aps.org/doi/10.1103/PhysRevLett.89.130801>. 126
- [55] I. K. Kominis, T. W. Kornack, J. C. Allred, and M. V. Romalis. A subfemtotesla multichannel atomic magnetometer. *Nature*, **422**(6932), 2003. URL <https://doi.org/10.1038/nature01484>. 3, 5
- [56] J. M. Brown, S. J. Smullin, T. W. Kornack, and M. V. Romalis. New limit on lorentz- and *cpt*-violating neutron spin interactions. *Phys. Rev. Lett.*, **105**:151604, 2010. URL <https://link.aps.org/doi/10.1103/PhysRevLett.105.151604>. 3
- [57] Junyi Lee, Attaallah Almasi, and Michael Romalis. Improved limits on spin-mass interactions. *Phys. Rev. Lett.*, **120**:161801, 2018. URL <https://link.aps.org/doi/10.1103/PhysRevLett.120.161801>.
- [58] G. Vasilakis, J. M. Brown, T. W. Kornack, and M. V. Romalis. Limits on new long range nuclear spin-dependent forces set with a  $\text{K}-^3\text{He}$  comagnetometer. *Phys. Rev. Lett.*, **103**:261801, 2009. URL <https://link.aps.org/doi/10.1103/PhysRevLett.103.261801>. 45
- [59] Antoine Garcon, John W. Blanchard, Gary P. Centers, Nataniel L. Figueroa, Peter W. Graham, Derek F. Jackson Kimball, Surjeet Rajendran, Alexander O. Sushkov, Yevgeny V. Stadnik, Arne Wickenbrock, Teng Wu, and Dmitry Budker. Constraints on bosonic dark matter from ultralow-field nuclear magnetic resonance. *Science Advances*, **5**(10), 2019. URL <https://advances.sciencemag.org/content/5/10/eaax4539>. 3
- [60] T. H. Sander, J. Preusser, R. Mhaskar, J. Kitching, L. Trahms, and S. Knappe. Magnetoencephalography with a chip-scale atomic magnetometer. *Biomed. Opt. Express*, **3**(5), 2012. URL <http://www.osapublishing.org/boe/abstract.cfm?URI=boe-3-5-981>. 3
- [61] T. A. Bowen, E. Zhivun, A. Wickenbrock, V. Dumont, S. D. Bale, C. Pankow, G. Dobler, J. S. Wurtele, and D. Budker. A network of magnetometers for multi-scale urban science and informatics. *Geoscientific Instrumentation, Methods and Data Systems*, **8**(1), 2019. URL <https://www.geosci-instrum-method-data-syst.net/8/129/2019/>. 3
- [62] Hauke Müntinga, Hendrik Ahlers, M Krutzik, A Wenzlawski, S Arnold, D Becker, K Bongs, H Dittus, H Duncker, N Gaaloul, et al. Interferometry with bose-einstein condensates in microgravity. *Physical review letters*, **110**(9):093602, 2013. 3
- [63] Elena Boto, Niall Holmes, James Leggett, Gillian Roberts, Vishal Shah, Sofie S Meyer, Leonardo Duque Muñoz, Karen J Mullinger, Tim M Tierney, Sven Bestmann, et al. Moving magnetoencephalography towards real-world applications with a wearable system. *Nature*, **555**(7698):657, 2018. 3
- [64] Elena Boto, Ryan M Hill, Molly Rea, Niall Holmes, Zelekha A Seedat, James Leggett, Vishal Shah, James Osborne, Richard Bowtell, and Matthew J Brookes. Measuring functional connectivity with wearable meg. *bioRxiv*, 2020.
- [65] Dong Sheng, Abigail R Perry, Sean P Krzyzewski, Shawn Geller, John Kitching, and Svenja



- Knappe. A microfabricated optically-pumped magnetic gradiometer. *Applied physics letters*, **110**(3):031106, 2017.
- [66] M.E. Limes, E.L. Foley, T.W. Kornack, S. Caliga, S. McBride, A. Braun, W. Lee, V.G. Lucivero, and M.V. Romalis. Portable magnetometry for detection of biomagnetism in ambient environments. *Phys. Rev. Applied*, **14**:011002, 2020. URL <https://link.aps.org/doi/10.1103/PhysRevApplied.14.011002>. 3
- [67] Kasper Jensen, Mark Alexander Skarsfeldt, Hans Stærkind, Jens Arnbak, Mikhail V Balabas, Søren-Peter Olesen, Bo Hjorth Bentzen, and Eugene S Polzik. Magnetocardiography on an isolated animal heart with a room-temperature optically pumped magnetometer. *Scientific reports*, **8**(1):16218, 2018. 3
- [68] W. Happer, Y.Y. Jau, and T. Walker. *Optically Pumped Atoms*. Wiley, 2010. URL <https://books.google.gr/books?id=ycfaW6YjYe8C>. 3, 38, 39, 58, 59, 60, 69, 73, 168, 169, 170, 172, 181, 182, 185
- [69] I.I. Sobelman. *Atomic Spectra and Radiative Transitions*. Springer Series on Atomic, Optical, and Plasma Physics. Springer Berlin Heidelberg, 1996. URL <https://books.google.gr/books?id=nbHvAAAAAAAJ>. 3
- [70] W. Happer. Optical pumping. *Rev. Mod. Phys.*, **44**, 1972. URL <https://link.aps.org/doi/10.1103/RevModPhys.44.169>. 4, 14, 15, 28, 58, 59, 67, 70, 72, 153, 196, 205
- [71] Zoran D. Grujić and Antoine Weis. Atomic magnetic resonance induced by amplitude-, frequency-, or polarization-modulated light. *Physical Review A*, **88**(1):012508, 2013. 4
- [72] Georgios Vasilakis. *Precision measurements of spin interactions with high density atomic vapors*. Princeton University, 2011. 4, 11, 30, 32, 34, 35, 36, 38, 39, 40, 44, 46, 56, 73, 109, 167, 168
- [73] Elena Zhivun. *Vector AC Stark shift in  $^{133}\text{Cs}$  atomic magnetometers with antirelaxion coated cells*. PhD thesis, UC Berkeley, 2016. 6
- [74] Morgan W. Mitchell. Number-unconstrained quantum sensing. *Quantum Science and Technology*, **2**(4):044005, 2017. 6
- [75] Morgan W. Mitchell and Silvana Palacios Alvarez. Colloquium: Quantum limits to the energy resolution of magnetic field sensors. *Rev. Mod. Phys.*, **92**:021001, 2020. URL <https://link.aps.org/doi/10.1103/RevModPhys.92.021001>.
- [76] Morgan W Mitchell. Scale-invariant spin dynamics and the quantum limits of field sensing. *New Journal of Physics*, **22**(5):053041, 2020. 6
- [77] Géza Tóth and Morgan W Mitchell. Generation of macroscopic singlet states in atomic ensembles. *New Journal of Physics*, **12**(5):053007, 2010. 6
- [78] Brian Julsgaard, Alexander Kozhokin, and Eugene S Polzik. Experimental long-lived entanglement of two macroscopic objects. *Nature*, **413**(6854):400, 2001. 6
- [79] Brian Julsgaard. *Entanglement and Quantum Interactions with Macroscopic Gas Samples*. University of Aarhus, Denmark, 2003. 42, 81, 82, 86
- [80] Wojciech Wasilewski, Kasper Jensen, Hanna Krauter, Jelmer Jan Renema, MV Balabas, and Eugene Simon Polzik. Quantum noise limited and entanglement-assisted magnetometry. *Physical Review Letters*, **104**(13):133601, 2010. 6
- [81] V Shah, G Vasilakis, and Michael V Romalis. High bandwidth atomic magnetometry with continuous quantum nondemolition measurements. *Physical review letters*, **104**(1):013601, 2010. 6



- [82] R. J. Sewell, M. Koschorreck, M. Napolitano, B. Dubost, N. Behbood, and M. W. Mitchell. Magnetic sensitivity beyond the projection noise limit by spin squeezing. *Phys. Rev. Lett.*, **109**:253605, 2012. URL <https://link.aps.org/doi/10.1103/PhysRevLett.109.253605>. 6
- [83] Jia Kong, Ricardo Jiménez-Martínez, Charikleia Troullinou, Vito Giovanni Lucivero, Géza Tóth, and Morgan W. Mitchell. Measurement-induced, spatially-extended entanglement in a hot, strongly-interacting atomic system. *Nature Communications*, **11**(2415), 2020. 6, 42, 44, 65, 88, 133, 181, 186, 190
- [84] Vito Giovanni Lucivero, Aleksandra Dimic, Jia Kong, Ricardo Jiménez-Martínez, and Morgan W Mitchell. Sensitivity, quantum limits, and quantum enhancement of noise spectroscopies. *Physical Review A*, **95**(4):041803, 2017. 6, 140
- [85] Or Katz, Or Peleg, and Ofer Firstenberg. Coherent coupling of alkali atoms by random collisions. *Physical review letters*, **115**(11):113003, 2015. 6
- [86] Or Katz and Ofer Firstenberg. Synchronization of strongly interacting alkali-metal spins. *Phys. Rev. A*, **98**:012712, Jul 2018. URL <https://link.aps.org/doi/10.1103/PhysRevA.98.012712>.
- [87] Or Katz and Ofer Firstenberg. Transverse optical pumping of spin states. *Communications Physics*, **2**(1):58, 2019. 6
- [88] I. K. Kominis. Sub-shot-noise magnetometry with a correlated spin-relaxation dominated alkali-metal vapor. *Phys. Rev. Lett.*, **100**:073002, 2008. URL <https://link.aps.org/doi/10.1103/PhysRevLett.100.073002>. 6, 181
- [89] K. Mouloudakis, M. Loulakis, and I. K. Kominis. Quantum trajectories in spin-exchange collisions reveal the nature of spin-noise correlations in multispecies alkali-metal vapors. *Phys. Rev. Research*, **1**:033017, 2019. URL <https://link.aps.org/doi/10.1103/PhysRevResearch.1.033017>. 8, 51, 190
- [90] Or Katz, Roy Shaham, and Ofer Firstenberg. Quantum interface for noble-gas spins. *arXiv preprint arXiv:1905.12532*, 2019. 181
- [91] Roy Shaham, Or Katz, and Ofer Firstenberg. Quantum dynamics of collective spin states in a thermal gas. *Phys. Rev. A*, **102**:012822, 2020. URL <https://link.aps.org/doi/10.1103/PhysRevA.102.012822>. 6
- [92] Guiying Zhang, Ya Wen, Jian Qiu, and Kaifeng Zhao. Observing zero-field spin dynamics with spin noise in a pi-pulse modulated field. *arXiv preprint arXiv:1901.00714*, 2019. 6
- [93] AA Fomin, M Yu Petrov, GG Kozlov, MM Glazov, II Ryzhov, MV Balabas, and VS Zapasskii. Spin-alignment noise in atomic vapor. *arXiv preprint arXiv:1906.03163*, 2019. 6
- [94] Antoine Weis, Georg Bison, and Anatoly S. Pazgalev. Theory of double resonance magnetometers based on atomic alignment. *Phys. Rev. A*, **74**:033401, 2006. URL <https://link.aps.org/doi/10.1103/PhysRevA.74.033401>. 6
- [95] Matthias Braun and Jürgen König. Faraday-rotation fluctuation spectroscopy with static and oscillating magnetic fields. *Phys. Rev. B*, **75**:085310, 2007. URL <https://link.aps.org/doi/10.1103/PhysRevB.75.085310>. 6
- [96] AV Poshakinskiy and SA Tarasenko. Spin noise at electron paramagnetic resonance. *arXiv preprint arXiv:1910.13167*, 2019. 6
- [97] G. E. Katsoprinakis, M. Polis, A. Tavernarakis, A. T. Dellis, and I. K. Kominis. Quantum random number generator based on spin noise. *Phys. Rev. A*, **77**:054101, 2008. URL <https://link.aps.org/doi/10.1103/PhysRevA.77.054101>. 6



- [98] V. G. Lucivero, N. D. McDonough, N. Dural, and M. V. Romalis. Correlation function of spin noise due to atomic diffusion. *Phys. Rev. A*, **96**:062702, 2017. URL <https://link.aps.org/doi/10.1103/PhysRevA.96.062702>. 6, 101
- [99] Yuanjiang Tang, Ya Wen, Ling Cai, and Kaifeng Zhao. Spin-noise spectrum of hot vapor atoms in an anti-relaxation-coated cell. *Phys. Rev. A*, **101**:013821, 2020. URL <https://link.aps.org/doi/10.1103/PhysRevA.101.013821>. 6
- [100] A. T. Dellis, M. Loulakis, and I. K. Kominiis. Spin-noise correlations and spin-noise exchange driven by low-field spin-exchange collisions. *Phys. Rev. A*, **90**:032705, 2014. URL <https://link.aps.org/doi/10.1103/PhysRevA.90.032705>. 6, 8, 45, 46, 51, 128, 129, 174, 175, 190
- [101] Dibyendu Roy, Luyi Yang, Scott A Crooker, and Nikolai A Sinitsyn. Cross-correlation spin noise spectroscopy of heterogeneous interacting spin systems. *Scientific reports*, **5**:9573, 2015. 45, 51, 128, 129, 134, 174
- [102] Luyi Yang, P. Glasenapp, A. Greilich, D. Reuter, A. D. Wieck, D. R. Yakovlev, M. Bayer, and S. A. Crooker. Two-colour spin noise spectroscopy and fluctuation correlations reveal homogeneous linewidths within quantum-dot ensembles. *Nature Communications*, **5**(1):4949, 2014. URL <https://doi.org/10.1038/ncomms5949>.
- [103] Daniel A Thrasher, Susan S Sorensen, and Thad G Walker. Dual-species synchronous spin-exchange optical pumping. *arXiv preprint arXiv:1912.04991*, 2019.
- [104] G. G. Kozlov, I. I. Ryzhov, and V. S. Zapasskii. Spin-noise spectroscopy of randomly moving spins in the model of light scattering: Two-beam arrangement. *Phys. Rev. A*, **97**:013848, 2018. URL <https://link.aps.org/doi/10.1103/PhysRevA.97.013848>. 6
- [105] M. A. Bouchiat, T. R. Carver, and C. M. Varnum. Nuclear polarization in  $\text{he}^3$  gas induced by optical pumping and dipolar exchange. *Phys. Rev. Lett.*, **5**, 1960. URL <https://link.aps.org/doi/10.1103/PhysRevLett.5.373>. 7
- [106] Thad G. Walker and William Happer. Spin-exchange optical pumping of noble-gas nuclei. *Rev. Mod. Phys.*, **69**, 1997. URL <https://link.aps.org/doi/10.1103/RevModPhys.69.629>. 60, 64
- [107] W. Happer. Spin exchange, past, present and future. *Ann. Phys. Fr.*, **10**(6), 1985. URL <https://doi.org/10.1051/anphys:01985001006064500>.
- [108] S. Appelt, A. Ben-Amar Baranga, C. J. Erickson, M. V. Romalis, A. R. Young, and W. Happer. Theory of spin-exchange optical pumping of  $^3\text{He}$  and  $^{129}\text{Xe}$ . *Phys. Rev. A*, **58**, 1998. URL <https://link.aps.org/doi/10.1103/PhysRevA.58.1412>. 60, 76, 175, 179
- [109] Earl Babcock, Ian Nelson, Steve Kadlecsek, Bastiaan Driehuys, L. W. Anderson, F. W. Hersman, and Thad G. Walker. Hybrid spin-exchange optical pumping of  $^3\text{He}$ . *Phys. Rev. Lett.*, **91**:123003, 2003. URL <https://link.aps.org/doi/10.1103/PhysRevLett.91.123003>. 7
- [110] Rujie Li, Wenfeng Fan, Liwei Jiang, Lihong Duan, Wei Quan, and Jiancheng Fang. Rotation sensing using a  $\text{k-rb-}^{21}\text{Ne}$  comagnetometer. *Phys. Rev. A*, **94**:032109, 2016. URL <https://link.aps.org/doi/10.1103/PhysRevA.94.032109>. 7
- [111] M. Smicklas, J. M. Brown, L. W. Cheuk, S. J. Smullin, and M. V. Romalis. New test of local lorentz invariance using a  $^{21}\text{Ne-Rb-K}$  comagnetometer. *Phys. Rev. Lett.*, **107**:171604, 2011. URL <https://link.aps.org/doi/10.1103/PhysRevLett.107.171604>. 128
- [112] Kai Wei, Tian Zhao, Xiujie Fang, Hairong Li, Yueyang Zhai, Bangcheng Han, and Wei Quan.



- Simultaneous determination of the spin polarizations of noble-gas and alkali-metal atoms based on the dynamics of the spin ensembles. *Phys. Rev. Applied*, **13**:044027, 2020. URL <https://link.aps.org/doi/10.1103/PhysRevApplied.13.044027>. 7
- [113] Or Katz, Roy Shaham, Eugene S. Polzik, and Ofer Firstenberg. Long-lived entanglement generation of nuclear spins using coherent light. *Phys. Rev. Lett.*, **124**:043602, 2020. URL <https://link.aps.org/doi/10.1103/PhysRevLett.124.043602>. 7, 181
- [114] Or Katz, Reches Eran, Roy Shaham, Gorshkov Alexey V., and Ofer Firstenberg. Optical quantum memory with optically inaccessible noble-gas spins. *arXiv:2007.08770 [quant-ph]*, 2020.
- [115] Or Katz, Reches Eran, Roy Shaham, Gorshkov Alexey V., and Ofer Firstenberg. Optimal control of an optical quantum memory based on noble-gas spins. *arXiv:2007.10177 [quant-ph]*, 2020. 7
- [116] Florentin Reiter and Anders S. Sørensen. Effective operator formalism for open quantum systems. *Phys. Rev. A*, **85**:032111, 2012. URL <https://link.aps.org/doi/10.1103/PhysRevA.85.032111>. 7, 23
- [117] Deutsch Ivan H. and Jessen Poul S. Quantum control and measurement of atomic spins in polarization spectroscopy. *Optics Communications*, 283(5), 2010. ISSN 0030-4018. URL <http://www.sciencedirect.com/science/article/pii/S0030401809010517>. 7, 23, 27, 28, 41, 161, 201, 202, 204
- [118] K Mouloudakis and IK Kominis. Spin-exchange collisions in hot vapors create and sustain bipartite entanglement. *arXiv preprint arXiv:2004.11790*, 2020. 8, 65, 70, 190
- [119] Richard N. Zare. *Angular momentum: understanding spatial aspects in chemistry and physics*. J. Wiley & Sons, 1988. 10, 14
- [120] F. Verstraete, V. Murg, and J.I. Cirac. Matrix product states, projected entangled pair states, and variational renormalization group methods for quantum spin systems. *Advances in Physics*, **57**(2), 2008. URL <https://doi.org/10.1080/14789940801912366>. 12
- [121] Dmitry Budker, Derek Kimball, Derek F Kimball, and David P DeMille. *Atomic physics: an exploration through problems and solutions*. Oxford University Press USA, 2004. 12, 16, 72, 74, 114, 158
- [122] Karl Blum. *Density matrix theory and applications*, volume **64**. Springer Science & Business Media, 2012. 12, 13, 67
- [123] Marcis Auzinsh, Dmitry Budker, and Simon Rochester. *Optically polarized atoms: understanding light-atom interactions*. Oxford University Press, 2010. 12, 24
- [124] U. Fano. Description of states in quantum mechanics by density matrix and operator techniques. *Rev. Mod. Phys.*, **29**, 1957. URL <https://link.aps.org/doi/10.1103/RevModPhys.29.74>. 14
- [125] VM Acosta, M Auzinsh, W Gawlik, P Grisins, JM Higbie, DF Jackson Kimball, L Krzemien, MP Ledbetter, S Pustelny, SM Rochester, et al. Production and detection of atomic hexadecapole at earth's magnetic field. *Optics express*, **16**(15), 2008. 15
- [126] VK Khersonskii, AN Moskalev, and DA Varshalovich. *Quantum Theory Of Angular Momentum*. World Scientific, 1988. 16, 69
- [127] G. Breit and I. I. Rabi. Measurement of nuclear spin. *Phys. Rev.*, **38**, 1931. URL <https://link.aps.org/doi/10.1103/PhysRev.38.2082.2>. 16
- [128] E. Arimondo, M. Inguscio, and P. Violino. Experimental determinations of the hyperfine structure in the alkali atoms. *Rev. Mod. Phys.*, **49**, 1977. URL <https://link.aps.org/doi/10.1103/>



- [RevModPhys.49.31.16,17](#)
- [129] Fei Gong. *New physics and technology for spin-polarized alkali-metal atoms*. Princeton University, 2008. [17](#)
- [130] Junyi Lee. *New constraints on the axion's coupling to nucleons from a Spin Mass Interaction Limiting Experiment (SMILE)*. Princeton University, 2019. [17, 71](#)
- [131] D. M. Brink and G. R. Satchler. *Angular momentum*. Clarendon Press, 1968. [18](#)
- [132] Evgeniy B Alexandrov, Marcis Auzinsh, Dmitry Budker, Derek F Kimball, Simon M Rochester, and Valeriy V Yashchuk. Dynamic effects in nonlinear magneto-optics of atoms and molecules. *JOSA B*, **22**(1), 2005. [20](#)
- [133] S. J. Seltzer, P. J. Mearns, and M. V. Romalis. Synchronous optical pumping of quantum revival beats for atomic magnetometry. *Phys. Rev. A*, **75**:051407, May 2007. URL <https://link.aps.org/doi/10.1103/PhysRevA.75.051407>. [20](#)
- [134] W. Happer. Light propagation and light shifts in optical pumping experiments. *Progress in Quantum Electronics*, **1**, 1970. ISSN 0079-6727. URL <http://www.sciencedirect.com/science/article/pii/0079672770900029>. [22, 31](#)
- [135] W. Happer and B. S. Mathur. Effective operator formalism in optical pumping. *Phys. Rev.*, **163**, 1967. URL <https://link.aps.org/doi/10.1103/PhysRev.163.12>. [23, 27, 28, 35, 161, 194, 204, 205, 206](#)
- [136] W. Happer and B. S. Mathur. Off-resonant light as a probe of optically pumped alkali vapors. *Phys. Rev. Lett.*, **18**, 1967. URL <https://link.aps.org/doi/10.1103/PhysRevLett.18.577>. [30, 34](#)
- [137] B. S. Mathur, H. Y. Tang, and W. Happer. Light propagation in optically pumped alkali vapors. *Phys. Rev. A*, **2**, 1970. URL <https://link.aps.org/doi/10.1103/PhysRevA.2.648>.
- [138] SR de Echaniz, M Koschorreck, M Napolitano, M Kubasik, and MW Mitchell. Hamiltonian design in atom-light interactions with rubidium ensembles: A quantum-information toolbox. *Physical Review A*, **77**(3):032316, 2008.
- [139] DV Kupriyanov, OS Mishina, IM Sokolov, Brian Julsgaard, and Eugene Simon Polzik. Multimode entanglement of light and atomic ensembles via off-resonant coherent forward scattering. *Physical Review A*, **71**(3):032348, 2005.
- [140] Claude Cohen-Tannoudji, Jacques Dupont-Roc, and Gilbert Grynberg. Atom-photon interactions: basic processes and applications. *Atom-Photon Interactions: Basic Processes and Applications*, by Claude Cohen-Tannoudji, Jacques Dupont-Roc, Gilbert Grynberg, pp. 678. ISBN 0-471-29336-9. Wiley-VCH, March 1998., page 678, 1998.
- [141] Fam Le Kien, Philipp Schneeweiss, and Arno Rauschenbeutel. Dynamical polarizability of atoms in arbitrary light fields: general theory and application to cesium. *The European Physical Journal D*, **67**(5):92, 2013. [23](#)
- [142] Jun John Sakurai. *Advanced quantum mechanics*. Pearson Education India, 1967. [23](#)
- [143] Peter Lambropoulos and David Petrosyan. *Fundamentals of quantum optics and quantum information*, volume **23**. Springer, 2007. [23, 88](#)
- [144] B Shirinzadeh and Charles C Wang. Accurate determination of the vapor pressure of potassium using optical absorption. *Applied optics*, **22**(20), 1983. [25](#)
- [145] Christopher James Erickson. *Measurements of the magnetic field dependence of the spin relaxation rate in alkali metal vapors*. Princeton University, 2001. [25](#)



- [146] DA Van Baak. Resonant faraday rotation as a probe of atomic dispersion. *American Journal of Physics*, **64**(6), 1996. 25
- [147] Marlan O Scully and M Suhail Zubairy. Quantum optics, 1999. 27, 88, 159
- [148] Wolfgang Demtröder. *Laser spectroscopy: basic concepts and instrumentation*. Springer Science & Business Media, 2013. 29
- [149] Alan Corney. *Atomic and laser spectroscopy*. Clarendon Press Oxford, 1978. 29
- [150] C.J. Foot. *Atomic physics*. Oxford master series in physics. Oxford University Press, 2005. URL <https://books.google.gr/books?id=kXYpAQAAMAAJ>. 29
- [151] Paul Siddons, Charles S Adams, Chang Ge, and Ifan G Hughes. Absolute absorption on rubidium d lines: comparison between theory and experiment. *Journal of Physics B: Atomic, Molecular and Optical Physics*, **41**(15):155004, 2008. 30
- [152] Burton D Fried and Samuel D Conte. *The plasma dispersion function: the Hilbert transform of the Gaussian*. Academic Press, 2015. 30
- [153] John David Jackson. *Classical electrodynamics*. Wiley, New York, NY, 3rd ed. edition, 1999. URL <http://cdsweb.cern.ch/record/490457>. 35
- [154] Z Wu, Masao Kitano, William Happer, Mengyang Hou, and J Daniels. Optical determination of alkali metal vapor number density using faraday rotation. *Applied optics*, **25**:4483, 01 1987. 39, 41, 108, 140, 147, 148
- [155] Eugene Hecht. Hecht optics. *Addison Wesley*, **997**, 1998. 41
- [156] Serge Huard. Polarization of light. *Polarization of Light, by Serge Huard, pp. 348. ISBN 0-471-96536-7. Wiley-VCH, January 1997.*, page 348, 1997. 41
- [157] Jacob Sherson, Hanna Krauter, RK Olsson, Brian Julsgaard, and Eugene S Polzik. Quantum memory and teleportation using macroscopic gas samples. *Journal of Physics B: Atomic, Molecular and Optical Physics*, **41**(22):223001, 2008. 41, 86
- [158] Masahiro Kitagawa and Masahito Ueda. Squeezed spin states. *Phys. Rev. A*, **47**, 1993. URL <https://link.aps.org/doi/10.1103/PhysRevA.47.5138>. 44
- [159] D. J. Wineland, J. J. Bollinger, W. M. Itano, and D. J. Heinzen. Squeezed atomic states and projection noise in spectroscopy. *Phys. Rev. A*, **50**, 1994. URL <https://link.aps.org/doi/10.1103/PhysRevA.50.67>. 44
- [160] Xiaodong Qi, Yuan-Yu Jau, and Ivan H. Deutsch. Enhanced cooperativity for quantum-nondemolition-measurement-induced spin squeezing of atoms coupled to a nanophotonic waveguide. *Phys. Rev. A*, **97**:033829, 2018. URL <https://link.aps.org/doi/10.1103/PhysRevA.97.033829>. 44
- [161] Giuseppe Vitagliano, Philipp Hyllus, Iñigo L. Egusquiza, and Géza Tóth. Spin squeezing inequalities for arbitrary spin. *Phys. Rev. Lett.*, **107**:240502, 2011. URL <https://link.aps.org/doi/10.1103/PhysRevLett.107.240502>. 44
- [162] T. W. Kornack and M. V. Romalis. Dynamics of two overlapping spin ensembles interacting by spin exchange. *Phys. Rev. Lett.*, **89**:253002, 2002. URL <https://link.aps.org/doi/10.1103/PhysRevLett.89.253002>. 45
- [163] A. Abragam. *The Principles of Nuclear Magnetism*. Comparative Pathobiology - Studies in the Postmodern Theory of Education. Clarendon Press, 1961. URL [https://books.google.gr/books?id=9M8U\\_JK7K54C](https://books.google.gr/books?id=9M8U_JK7K54C). 45
- [164] I. M. Savukov and M. V. Romalis. Effects of spin-exchange collisions in a high-density alkali-metal



- vapor in low magnetic fields. *Phys. Rev. A*, 71:023405, 2005. URL <https://link.aps.org/doi/10.1103/PhysRevA.71.023405>. 46, 154, 170
- [165] Ulrich Weiss. *Quantum dissipative systems*, volume 13. World scientific, 2012. 46
- [166] Kurt Jacobs. *Stochastic processes for physicists: understanding noisy systems*. Cambridge University Press, 2010. 46
- [167] Don S Lemons and Paul Langevin. *An introduction to stochastic processes in physics*. JHU Press, 2002.
- [168] Don S Lemons, Anthony Gythiel, et al. On the theory of brownian motion. *Am. J. Phys*, 65(11), 1979.
- [169] Daniel T. Gillespie. The mathematics of brownian motion and johnson noise. *American Journal of Physics*, 64(3), 1996. URL <https://doi.org/10.1119/1.18210>. 46
- [170] Crispin Gardiner. *Stochastic methods*, volume 4. Springer Berlin, 2009. 47, 51
- [171] W.A. Gardner. *Introduction to Random Processes: With Applications to Signals and Systems*. Macmillan Publishing Company, 1986. URL <https://books.google.gr/books?id=3xfvAAAAAAAJ>. 49
- [172] W. Happer and W.A. Van Wijngaarden. An optical pumping primer. *Hyperfine Interact (1987)* 38: 435, 38:435, 1987. URL <https://doi.org/10.1007/BF02394855>. 52, 70, 173, 177, 179, 181, 182, 185
- [173] Christoffer B Møller, Rodrigo A Thomas, Georgios Vasilakis, Emil Zeuthen, Yeghishe Tsaturyan, Mikhail Balabas, Kasper Jensen, Albert Schliesser, Klemens Hammerer, and Eugene S Polzik. Quantum back-action-evading measurement of motion in a negative mass reference frame. *Nature*, 547(7662), 2017. 56
- [174] Georgios Vasilakis, Heng Shen, Kasper Jensen, Misha Balabas, Daniel Salart, Bing Chen, and Eugene Simon Polzik. Generation of a squeezed state of an oscillator by stroboscopic back-action-evading measurement. *Nature Physics*, 11(5), 2015.
- [175] C. Schori, B. Julsgaard, J. L. Sørensen, and E. S. Polzik. Recording quantum properties of light in a long-lived atomic spin state: Towards quantum memory. *Phys. Rev. Lett.*, 89:057903, 2002. URL <https://link.aps.org/doi/10.1103/PhysRevLett.89.057903>. 56
- [176] Robert L. Cook, Carlos A. Riofrío, and Ivan H. Deutsch. Single-shot quantum state estimation via a continuous measurement in the strong backaction regime. *Phys. Rev. A*, 90:032113, 2014. URL <https://link.aps.org/doi/10.1103/PhysRevA.90.032113>. 56
- [177] Kurt Jacobs. *Quantum measurement theory and its applications*. Cambridge University Press, 2014. 56, 159
- [178] Edward M. Purcell and George B. Field. Influence of collisions upon population of hyperfine states in hydrogen. *apj*, 124:542, 1956. URL <https://ui.adsabs.harvard.edu/abs/1956ApJ...124..542P>. 59
- [179] J. P. Wittke and R. H. Dicke. Redetermination of the hyperfine splitting in the ground state of atomic hydrogen. *Phys. Rev.*, 103, 1956. URL <https://link.aps.org/doi/10.1103/PhysRev.103.620>. 59
- [180] Alexander Dalgarno, M. R. H. Rudge, and David Robert Bates. Spin-change cross-sections for collisions between alkali atoms. *Proceedings of the Royal Society of London. Series A. Mathematical and Physical Sciences*, 286(1407), 1965. URL <https://royalsocietypublishing.org/doi/abs/10.1098/rspa.1965.0161>. 60



- [181] A. E. Glassgold. Spin exchange in collisions between atoms. *Phys. Rev.*, **132**, 1963. URL <https://link.aps.org/doi/10.1103/PhysRev.132.2144>. 60
- [182] A. E. Glassgold and James F. Walker. Spin-exchange scattering in uniform magnetic fields. *Phys. Rev.*, **160**, 1967. URL <https://link.aps.org/doi/10.1103/PhysRev.160.11>.
- [183] R.J. Knize, Z. Wu, and W. Happer. *Optical Pumping and Spin Exchange in Gas Cells*, volume **24** of *Advances in Atomic and Molecular Physics*. Academic Press, 1988. URL <http://www.sciencedirect.com/science/article/pii/S0065219908602328>.
- [184] Hyatt M. Gibbs and Robert J. Hull. Spin-exchange cross sections for  $\text{rb}^{87}\text{-rb}^{87}$  and  $\text{rb}^{87}\text{-cs}^{133}$  collisions. *Phys. Rev.*, **153**, 1967. URL <https://link.aps.org/doi/10.1103/PhysRev.153.132>. 60, 166
- [185] Todd A. Brun. A simple model of quantum trajectories. *American Journal of Physics*, **70**(7), 2002. URL <https://doi.org/10.1119/1.1475328>. 62, 178, 180
- [186] Michael A Nielsen and Isaac Chuang. Quantum computation and quantum information, 2002. 63, 160
- [187] Gerardo Adesso, Thomas R Bromley, and Marco Cianciaruso. Measures and applications of quantum correlations. *Journal of Physics A: Mathematical and Theoretical*, **49**(47):473001, 2016. 64, 161
- [188] Françoise Grossetête. Relaxation par collisions d'échange de spin. *Journal de Physique*, **25**(4), 1964. 68, 69, 70, 153, 169, 181, 182
- [189] W. Happer and A. C. Tam. Effect of rapid spin exchange on the magnetic-resonance spectrum of alkali vapors. *Phys. Rev. A*, **16**, 1977. URL <https://link.aps.org/doi/10.1103/PhysRevA.16.1877>. 69, 70, 71, 123, 153, 155, 156, 157, 176
- [190] W. Happer and H. Tang. Spin-exchange shift and narrowing of magnetic resonance lines in optically pumped alkali vapors. *Phys. Rev. Lett.*, **31**, 1973. URL <https://link.aps.org/doi/10.1103/PhysRevLett.31.273>. 69
- [191] Grossetête, F. Relaxation par collisions d'échange de spins. (ii). *J. Phys. France*, **29**(5-6), 1968. URL <https://doi.org/10.1051/jphys:01968002905-6045600>. 69, 153
- [192] L. Wilmer Anderson, Francis M. Pipkin, and James C. Baird. Precision determination of the hyperfine structure of the ground state of atomic hydrogen, deuterium, and tritium. *Phys. Rev. Lett.*, **4**, 1960. URL <https://link.aps.org/doi/10.1103/PhysRevLett.4.69>. 70
- [193] G. D. Cates, S. R. Schaefer, and W. Happer. Relaxation of spins due to field inhomogeneities in gaseous samples at low magnetic fields and low pressures. *Phys. Rev. A*, **37**, 1988. URL <https://link.aps.org/doi/10.1103/PhysRevA.37.2877>. 74
- [194] S. D. Stoller, W. Happer, and F. J. Dyson. Transverse spin relaxation in inhomogeneous magnetic fields. *Phys. Rev. A*, **44**, 1991. URL <https://link.aps.org/doi/10.1103/PhysRevA.44.7459>. 74, 75
- [195] Takahisa Mitsui. Spontaneous noise spectroscopy of an atomic magnetic resonance. *Phys. Rev. Lett.*, **84**, 2000. URL <https://link.aps.org/doi/10.1103/PhysRevLett.84.5292>. 75
- [196] M. Fleischhauer, A. B. Matsko, and M. O. Scully. Quantum limit of optical magnetometry in the presence of ac stark shifts. *Phys. Rev. A*, **62**:013808, 2000. URL <https://link.aps.org/doi/10.1103/PhysRevA.62.013808>. 75
- [197] A. Predojević, Z. Zhai, J. M. Caballero, and M. W. Mitchell. Rubidium resonant squeezed light from a diode-pumped optical-parametric oscillator. *Phys. Rev. A*, **78**:063820, 2008. URL



- <https://link.aps.org/doi/10.1103/PhysRevA.78.063820>. 82
- [198] Mark Fox. *Quantum optics: an introduction*, volume 15. OUP Oxford, 2006. 83
- [199] VS Zapasskii. Highly sensitive polarimetric techniques. *Journal of Applied Spectroscopy*, **37**(2), 1982. 83
- [200] P. Glasenapp, A. Greilich, I. I. Ryzhov, V. S. Zapasskii, D. R. Yakovlev, G. G. Kozlov, and M. Bayer. Resources of polarimetric sensitivity in spin noise spectroscopy. *Phys. Rev. B*, **88**:165314, Oct 2013. URL <https://link.aps.org/doi/10.1103/PhysRevB.88.165314>. 83
- [201] Vito Giovanni Lucivero, Ricardo Jiménez-Martínez, Jia Kong, and Morgan W. Mitchell. Squeezed-light spin noise spectroscopy. *Phys. Rev. A*, **93**:053802, 2016. URL <https://link.aps.org/doi/10.1103/PhysRevA.93.053802>. 85
- [202] Kasper Jensen. *Quantum information, entanglement and magnetometry with macroscopic gas samples and nonclassical light*. University of Copenhagen, Denmark, 2011. 86
- [203] G. Grynberg, A. Aspect, C. Fabre, and C. Cohen-Tannoudji. *Introduction to Quantum Optics: From the Semi-classical Approach to Quantized Light*. Cambridge University Press, 2010. URL <https://books.google.gr/books?id=l-10L8YInA0C>. 90
- [204] D.F. Walls and G.J. Milburn. *Quantum Optics*. Springer Berlin Heidelberg, 2008. URL <https://books.google.gr/books?id=LiWsc3Nlf0kC>. 90
- [205] Wirsching Paul H., L Paez Thomas, and Ortiz Keith. *Random vibrations. Theory and Practice*. Dover Publications, New York, 2006. URL <https://store.doverpublications.com/0486450155.html>. 92
- [206] Press William H., Teukolsky Saul A., Vetterling William T., and Flannery Brian P. *Numerical Recipes in FORTRAN; The Art of Scientific Computing*. Cambridge University Press, 40 W. 20 St. New York, NY, United States, 1993. 93
- [207] Singh Jaideep, Dolph Peter A. M., and Tobias William A. Alkali metal vapor pressures & number densities for hybrid spin exchange optical pumping. *Notes*, 2008. URL <https://people.nscf.msu.edu/~singhj/docs/vp195.pdf>. 95
- [208] David R Lide. *CRC handbook of chemistry and physics*, volume 85. CRC press, 2004. 100
- [209] Carl E. Wieman and Leo Hollberg. Using diode lasers for atomic physics. *Review of Scientific Instruments*, **62**(1), 1991. URL <https://doi.org/10.1063/1.1142305>. 101
- [210] Marcos A. de Araújo, Rubens Silva, Emerson de Lima, Daniel P. Pereira, and Paulo C. de Oliveira. Measurement of gaussian laser beam radius using the knife-edge technique: improvement on data analysis. *Appl. Opt.*, **48**(2), 2009. URL <http://ao.osa.org/abstract.cfm?URI=ao-48-2-393>. 101
- [211] A. Yoshida and T. Asakura. A simple technique for quickly measuring the spot size of gaussian laser beams. *Optics and Laser Technology*, **8**(6), 1976. URL <http://www.sciencedirect.com/science/article/pii/0030399276900426>. 101
- [212] Mikhail V. Romalis. *Laser Polarized <sup>3</sup>He Target Used For A Precision Measurement Of The Neutron Spin Structure*. Princeton University, 1997. 109
- [213] Dominic Hunter. *Chip-Scale Atomic Magnetometer Based on Free-Induction-Decay*. University of Strathclyde, 2019. 110, 111
- [214] Yuyan Liu, Jieli Lin, Guangming Huang, Yuanqing Guo, and Chuanxi Duan. Simple empirical analytical approximation to the voigt profile. *J. Opt. Soc. Am. B*, **18**(5), 2001. URL <http://josab.osa.org/abstract.cfm?URI=josab-18-5-666>. 110



- [215] J.J. Olivero and R.L. Longbothum. Empirical fits to the voigt line width: A brief review. *Journal of Quantitative Spectroscopy and Radiative Transfer*, **17**(2), 1977. URL <http://www.sciencedirect.com/science/article/pii/0022407377901613>. 111
- [216] David Jiles. *Introduction to magnetism and magnetic materials*. CRC press, 2015. 111
- [217] D. Budker, W. Gawlik, D. F. Kimball, S. M. Rochester, V. V. Yashchuk, and A. Weis. Resonant nonlinear magneto-optical effects in atoms. *Rev. Mod. Phys.*, **74**, 2002. URL <https://link.aps.org/doi/10.1103/RevModPhys.74.1153>. 111
- [218] EA Donley, E Hodby, L Hollberg, and J Kitching. Demonstration of high-performance compact magnetic shields for chip-scale atomic devices. *Review of Scientific Instruments*, **78**(8):083102, 2007. 111
- [219] S-K Lee and Michael V Romalis. Calculation of magnetic field noise from high-permeability magnetic shields and conducting objects with simple geometry. *Journal of Applied Physics*, **103**(8):084904, 2008. 113
- [220] Fritz Primdahl. The fluxgate magnetometer. *Journal of Physics E: Scientific Instruments*, **12**(4): 241, 1979. 116
- [221] J. Liu, D. Jing, L. Wang, and al. et. The polarization and the fundamental sensitivity of 39k (133cs)-85rb-4he hybrid optical pumping spin exchange relaxation free atomic magnetometers. *Sci Rep* 7, 6776, **75**, 2017. 127
- [222] Eric P Goodwin and James C Wyant. *Field guide to interferometric optical testing*. SPIE Bellingham, WA, 2006. 150
- [223] Boris Naydenov, Florian Dolde, Liam T. Hall, Chang Shin, Helmut Fedder, Lloyd C. L. Hollenberg, Fedor Jelezko, and Jörg Wrachtrup. Dynamical decoupling of a single-electron spin at room temperature. *Phys. Rev. B*, **83**, 2011. URL <https://link.aps.org/doi/10.1103/PhysRevB.83.081201>. 159
- [224] Maurice Goldman. Formal theory of spin-lattice relaxation. *Journal of Magnetic Resonance*, **149**(2), 2001.
- [225] D. Farfurnik, A. Jarmola, L. M. Pham, Z. H. Wang, V. V. Dobrovitski, R. L. Walsworth, D. Budker, and N. Bar-Gill. Optimizing a dynamical decoupling protocol for solid-state electronic spin ensembles in diamond. *Phys. Rev. B*, **92**:060301, 2015. URL <https://link.aps.org/doi/10.1103/PhysRevB.92.060301>. 159
- [226] Brian E Mischuck, Seth T Merkel, and Ivan H Deutsch. Control of inhomogeneous atomic ensembles of hyperfine qubits. *Physical Review A*, **85**(2):022302, 2012. URL [//journals.aps.org/pra/abstract/10.1103/PhysRevA.85.022302](https://journals.aps.org/pra/abstract/10.1103/PhysRevA.85.022302). 159
- [227] R. Loudon. *The Quantum Theory of Light*. OUP Oxford, 2000. URL <https://books.google.gr/books?id=AEkfajgqldoC>. 161
- [228] Hyatt Gibbs. Importance of nuclear-spin effects in extracting alkali spin-exchange cross sections from zeeman optical-pumping signals. *Phys. Rev.*, **139**, 1965. URL <https://link.aps.org/doi/10.1103/PhysRev.139.A1374>. 166
- [229] A.R. Edmonds. *Angular Momentum in Quantum Mechanics*. Investigations in Physics Series. Princeton University Press, 1996. URL <https://books.google.gr/books?id=OBS0g0oHhZ0C>. 166
- [230] Daniel Manzano. A short introduction to the lindblad master equation. *AIP Advances*, **10**(2): 025106, 2020. URL <https://doi.org/10.1063/1.5115323>. 176



- [231] VA Kartoshkin. Complex spin-exchange cross sections in collisions of rubidium isotopes in the ground state. *Optics and Spectroscopy*, **119**(4), 2015. 182
- [232] VA Kartoshkin. Spin exchange during collisions of potassium atoms: Complex cross sections. *Optics and Spectroscopy*, **111**(6), 2011.
- [233] Jing-Bo Xu and Dao-Xin Yao. Collisions between spin polarized alkali atoms. complex cross sections. In *Journal of Physics: Conference Series*, volume **635**, page 022041, 2015. 182
- [234] Martin B. Plenio and Shashank Virmani. An introduction to entanglement measures. *Quantum Info. Comput.*, **7**(1), 2007. 183
- [235] E. Brüning, H. Mäkelä, A. Messina, and F. Petruccione. Parametrizations of density matrices. *Journal of Modern Optics*, **59**(1), 2012. URL <https://doi.org/10.1080/09500340.2011.632097>. 184
- [236] Salvatore Micalizio, Aldo Godone, Filippo Levi, and Jacques Vanier. Spin-exchange frequency shift in alkali-metal-vapor cell frequency standards. *Phys. Rev. A*, **73**:033414, 2006. URL <https://link.aps.org/doi/10.1103/PhysRevA.73.033414>. 184
- [237] Joseph Thomas Verdeyen. *Laser electronics*, volume **3**. Prentice Hall Englewood Cliffs, NJ, 1995. 199
- [238] David J Griffiths. Introduction to electrodynamics, 2005. 200
- [239] Morris Edgar Rose. *Elementary theory of angular momentum*. Wiley, 1957. 201, 207, 208
- [240] JP Barrat and C Cohen-Tannoudji. Étude du pompage optique dans le formalisme de la matrice densité. *J. phys. radium*, **22**(6), 1961. 204

